Covalently cross-linked tetrafunctionalized *m*-THPC chitosan hydrogels as drug delivery platforms

Piotr Gierlich

M. Pharm.

Under the supervision of Prof. Dr. M. O. Senge

and Dr. Lígia C. Gomes-da-Silva

Submitted in fulfilment of the requirements for the degree of

Doctor of Philosophy

School of Chemistry,

Trinity College Dublin,

The University of Dublin

March 2022

Move. Get going. Blessed is he who leaves.

~ Olga Tokarczuk, *Flights*

Statement of authentication

I declare that this thesis has not been submitted as an exercise for a degree at this or any other university and it is entirely my own work.

I agree to deposit this thesis in the University's open access institutional repository or allow the Library to do so on my behalf, subject to Irish Copyright Legislation and Trinity College Library conditions of use and acknowledgement.

Furthermore, unpublished and/or published work of others, is duly acknowledged in the text wherever included.

I consent to the examiner retaining a copy of the thesis beyond the examining period, should they so wish (EU GDPR May 2018).

Signature:  _____

Piotr Gierlich

Date: _____31/03/2022_____

Summary of work

5,10,15,20-Tetrakis(3-hydroxyphenyl)chlorin (*m*-THPC, *temoporfin*), is a second generation PS that has been available on the market for over two decades under the commercial name Foscan. Practical limitations of PDT with Foscan are reflected in patient discomfort due to prolonged skin photosensitivity which causes skin burning and inflammation. Therefore, there is a constant need for the development of new pharmaceutical formulations that will allow these drawbacks to be overcome and improve quality of life for cancer patients. This body of work outlines the design of tetrafunctionalized *m*-THPC derivatives which exhibit improved photophysical and biological properties in comparison with the parent compound. We detail DDS s, specifically hydrogels, capable of controlling drug release through response to the altered pH of the tumor microenvironment. Hydrogels were produced, characterized, and tested under biological conditions with the results described across experimental chapters 2-5.

Chapter 1 provides a general introduction to Photodynamic Therapy (PDT) and highlights the importance of the immune system response for successful treatment of cancer. We explain the major drawbacks related with the clinical use of Foscan and highlight the advantages of hydrogels as promising platforms for delivery of hydrophobic molecules.

Chapter 2 focuses on synthetic strategies towards tetrafunctionalization of *m*-THPC derivatives. This approach aims to append different functionalities at the periphery which allows their use as suitable synthetic handles for the design of drug delivery platforms. For this, reliable, cost-efficient synthetic strategies were employed. Substitution, esterification, and Sonogashira coupling reactions produced tetrafunctionalized derivatives **PS 1**, **3** and **5**. The next part of this chapter focuses on the evaluation of the linear optical properties of *m*-THPC derivatives, including determination of their fluorescence quantum yield (Φ_F), fluorescence lifetime (τ) and singlet oxygen quantum yield (Φ_Δ). Finally, we assess the impact of substitution of *m*-THPC periphery for enhancement of non-linear properties of the dye using the two-photon excited fluorescence (TPEF) technique.

Chapter 3 highlights the synthesis and characterization of covalently cross-linked chitosan (CS) hydrogels formed by the reaction of CS chains with tetrafunctionalized *m*-THPC derivatives and difunctionalized PEG *via* amide and/ or imine bonds. Next, we provide rheological and macroscopic evaluation of the rheological properties of the obtained formulations. Finally, part of this chapter demonstrates a sustained release of the encapsulated PS upon decrease in pH. Mediation of this release is anticipated to be a result of progressive cleavage of the cross-link bonds between the CS and the PS.

Evaluation of the activity of tetrafunctionalized *m*-THPC derivatives *in vitro* against B16F10 and CT26 cancer cells with comparison to the activity to *m*-THPC is provided in chapter 4. For this we employ intra- and extracellular PDT protocols. The main mechanism of the extracellular phototoxicity was found to be caused *via* lipid peroxidation and confirmed by two methods – flow cytometry and confocal imaging using a ROS-sensitive BODIPY 581/591 probe. The final part of this chapter focuses on the determination of the primary cell death mechanism triggered by the activity of water-soluble derivative **PS 3**.

The last experimental section of this doctoral thesis, chapter 5, provides *in vivo* evaluation of the phototoxic activity of the lead derivative, **PS 3**, formulated and applied as a CS-based formulation. Intratumorally injected hydrogel formulations were applied towards CT26 colon carcinoma and B16F10 melanoma tumors. Moreover, we provide evaluation of the PS biodistribution using an *in vivo* fluorescence technique. Due to the prolonged release of the PS from the hydrogel at the site of injection, we compare the therapeutic efficacy upon two, single and multiple irradiation protocols. The final part of the thesis explores PDT-induced activation of the immune system *via* three protocols: 1) rechallenge of cured animals two months after PDT treatments, 2) evaluation of abscopal effects on a pseudo-metastatic model, and 3) evaluation of the PDT activity in immunocompetent *versus* immunocompromised mice.

Thesis outputs

1. Publications

B. Khurana, **P. Gierlich**, A. Meindl, L. C. Gomes-da-Silva, M. O. Senge, Hydrogels: soft matters in photomedicine, Photochem. Photobiol. Sci., **2019**, *18*, 2613–2656.

P. Gierlich, A. I. Mata, C. Donohoe, R. M. M. Brito, M. O. Senge, L. C. Gomes-da-Silva, Ligand-tageted delivery of photosensitizers for cancer treatment, *Molecules*, **2020**, *25*, 5317.

P. Gierlich, S. G. Mucha, E. Robbins, L. C. Gomes-da-Silva, K. Matczyszyn, M. O. Senge, One-Photon and Two-Photon Photophysical Properties of Tetrafunctionalized 5,10,15,20-tetrakis(m-hydroxyphenyl)chlorin (Temoporfin) Derivatives as Potential Two-Photon-Induced Photodynamic Therapy Agents, ChemPhotoChem, **2022**, e202100249.

2. Conference presentations

Oral presentation:

Gierlich, P.; Gomes-da-Silva, L. C.; Senge, M. O.; (**2019**): 'Covalently cross-linked tetrafunctionalized *m*-THPC chitosan hydrogels as delivery platforms', Polythea Summer School 2019 - Photodynamic Therapy Intersectorial Summer School, 07/15-19, Limoges, France.

Gierlich, P.; Callaghan, S.; Filatov, M. A.; Savoie, H.; Boyle, R. W.; Gomes-da-Silva, L. C.; Senge, M. O., (**2019**): 'BODIPY-based dyad photosensitizers for application in photodynamic therapy. *European Conference on Spectroscopy of Biological Molecules (ECSBM)*, 07/19-22, Dublin, Ireland.

Gierlich, P.; Donohoe, C.; Behan, K.; Gomes-da-Silva, L. C.; Kelly, D.; Senge, M. O., (**2021**): Covalently cross-linked tetrafunctionalized *m*-THPC chitosan hydrogels as delivery platforms. *Final of the 3 minutes thesis competition (3MT), University of Coimbra,* 03/5, online.

Gierlich, P.; Donohoe, C.; Behan, K.; Gomes-da-Silva, L. C.; Kelly, D.; Senge, M. O., (**2021**) Covalently cross-linked tetrafunctionalized *m*-THPC chitosan hydrogels as delivery platforms, 3rd year talk, Trinity College Dublin, Ireland, 09/02, online.

Gierlich, P.; Donohoe, C.; Behan, K.; Gomes-da-Silva, L. C.; Kelly, D.; Senge, M. O., (**2021**) Covalently cross-linked tetrafunctionalized *m*-THPC chitosan hydrogels as drug delivery platforms in the treatment of melanoma, 19th Congress of the European Society for Photobiology, Salzburg, Austria, 08/30 – 09/03, online. Abstract OC-7.3.4.

Poster presentation:

Gierlich, P.; Gomes-da-Silva, L. C.; Senge, M. O.; (**2019**): 'Covalently cross-linked tetrafunctionalized *m*-THPC chitosan hydrogels as delivery platforms', *2019 ESP – IUPB World Congress of Light and Life*, 08/25-30, Barcelona, Spain.

Gierlich, P.; Gomes-da-Silva, L. C.; Senge, M. O.; (**2019**): 'Covalently cross-linked tetrafunctionalized *m*-THPC chitosan hydrogels as delivery platforms', *Tetrapyrrole Discussion Group*, 09/16-17, Bristol, UK.

Gierlich, P.; Callaghan, S.; Filatov, M. A.; Savoie, H.; Boyle, R. W.; Gomes-da-Silva, L. C.; Senge, M. O., (**2019**): 'BODIPY-based dyad photosensitizers for application in photodynamic therapy, *11th International Cancer Conference 2019*, 09/24-25, Dublin, Ireland.

Gierlich, P.; Behan, K.; Gomes-da-Silva, L. C.; Kelly, D.; Senge, M. O., (**2020**): Covalently cross-linked tetrafunctionalized *m*-THPC chitosan hydrogels as drug delivery platforms. *27th Lecture Conference on Photochemistry*, 9/14–15, online, Abstract PP-05.

Gierlich, P.; Donohoe, C.; Behan, K.; Gomes-da-Silva, L. C.; Kelly, D.; Senge, M. O., (**2020**): Covalently cross-linked tetrafunctionalized *m*-THPC chitosan hydrogels as delivery platforms. *POLYTHEA Entrepreneurial school - 'From Academia to Industry' organized by the industrial partner of the project – BIOEMTECH,* 11/8-11, online.

Gierlich, P.; Donohoe, C.; Behan, K.; Gomes-da-Silva, L. C.; Kelly, D.; Senge, M. O., (**2021**): Covalently cross-linked tetrafunctionalized *m*-THPC chitosan hydrogels as delivery platforms. *ACS spring meeting,* 04/1-30, online, Technical division: POLY, Poster: 3553607.

Gierlich, P.; Donohoe, C.; Behan, K.; Gomes-da-Silva, L. C.; Kelly, D.; Senge, M. O., (**2021**): Covalently cross-linked tetrafunctionalized *m*-THPC chitosan hydrogels as delivery platforms. *The 5th Photodynamic Day,* 05/18, online, Abstract P-22.

Gierlich, P.; Donohoe, C.; Behan, K.; Gomes-da-Silva, L. C.; Kelly, D.; Senge, M. O., (**2021**): Covalently cross-linked tetrafunctionalized *m*-THPC chitosan hydrogels as delivery platforms. *1st HighLIGHTing Science Meeting organized by POLYTHEA students,* 05/27-28, online, ISBN 978-83-7493-169-4, page 76.

Gierlich, P.; Donohoe, C.; Behan, K.; Kelly, D.; Senge, M. O.; Gomes-da-Silva, L. C., (**2021**) Covalently cross-linked tetrafunctionalized *m*-THPC chitosan hydrogels as delivery platforms, Coimbra Chemistry Centre Day 2021, University of Coimbra, Coimbra, Portugal, 15/12.

Gierlich, P.; Donohoe, C.; Behan, K.; Gomes-da-Silva, L. C.; Kelly, D.; Senge, M. O., (**2022**) Covalently cross-linked tetrafunctionalized *m*-THPC chitosan hydrogels as delivery platforms, Frontiers in Medicinal Chemistry 2022, online, 14-16/03, Abstract-ID: 10994_29627.

Acknowledgements

First and foremost, I would like to thank my supervisors, Prof. Mathias O. Senge and Dr. Lígia C. Gomes-da-Silva for giving me the opportunity to carry out research in their groups and especially for constant guidance, advice, readiness to help with all kinds of questions and queries and faith in my abilities.

I would like to thank European Commission for supporting my PhD studies with European Union's Horizon 2020 research and innovation programme under the Marie Sklodowska-Curie Scholarship. I would like to thank everyone involved in the POLYTHEA project – PhD students and supervisors, for valuable advice and scientific discussions. Special thanks to Aurore for being a great and supportive project manager Furthermore, I would like to say thank you to my present and former colleagues from Senge group: (in no particular order): Nitika, Alina, Ganapathi, Chris, Keith, Jessica, Susan, Gemma, Marie, Marc, Jessica, Karolis, Harry, Zoi, Bhavya, Asterios and Grant for making the lab such an enjoyable place to work in, for their dependable help, useful input and encouragement. I would like to thank go to Nitika, Ganapathi and Susan, who helped me with the synthesis of several compounds during the projects and who inspired new ideas and approaches. Special thanks to Zoi (for millions of exchanged voice messages, trips, laughs, coffees, 'unexpected' Capitol evenings, *goals* and *conclusions*); Claire (for being the *leader*, best company to explore and rate the charms of the Portuguese land and all the laughs we had together); Jessica (for being the best hood-friend and all our discussions when running hours-lasting columns), Susan (for support in BODIPY synthesis, and always having time to check and proof-read my writings) Harry (for the support, being a great housemate and travel buddy, and not questioning my *silly* ideas).

I would like to thank Prof. Luís Arnaut from Coimbra University to giving me an opportunity to work in his group and constant support my work. I thank Dr. Fábio Schaberle for his scientific encouragement, guidance and help with $^1O_2$ measurements. I also thank Prof. Carlos Serpa for supporting my research. I would like to thank my colleagues from Coimbra University (in no particular order): Maria Inês, Catarina, Amilcar, Diogo, Daniela, Tiago, André,

Luís, Anita and Carolina. The atmosphere and support in the group truly made a big difference in day-to-day life. Special thanks to Maria Inês for all our fantastic dinner nights, trips to Lisbon, constant support, and care.

I would like to thank Prof. Dr. Katarzyna Matczyszyn for giving me the opportunity to carry out research in her lab during my secondment rotation in Poland. Your support, and our scientific and non-scientific discussion were always inspirational. Special thanks to Sebastian, Emma, and Krzysztof for their support during my internship and help in introducing me to the world of non-linear optics.

Moreover, I am very grateful to Dr. John O'Brien, Dr. Gary Hessman, Dr. Kevin Behan for carrying out NMR, mass spectrometry measurements and rheological characterization and for helping with the analysis of spectra.

I would like to thank to all my friends that constantly supported me during these challenging years of PhD. I thank Justyna, Zuza and Karolina who were always there for me and listened to all my dramas (for the last 20 years to be completely honest!). I thank Małgo and Dominika for always believing in me. Special thanks to Nidia for being the best neighbor in the world! The support from all of you is invaluable

I would like to thank Dr. Paulina Skupin-Mrugalska who inspired me to apply for such project as POLYTHEA. Without her guidance during my master's degree, I would never be here.

Last but not least, I would like to thank my family. Dziękuję rodzinie za nieustanne wsparcie. Dziękuję rodzicom za stworzenie najlepszych warunków, dzięki którym mam możliwość rozwijać swoje umiejętności i pasje, za wasze nieustanne wsparcie, miłość i zaufanie, bez których nigdy nie udałoby mi się doskonalić naukowo, ale przede wszystkim rozwinąć jako człowiek i otworzyć na świat.

Abbreviations

°C	Degree Celsius
3D	Three-dimensional
5-ALA	5-aminolevulinic acid
AK	Actinic keratosis
aPDT	Antimicrobial photodynamic therapy
Ar	Aryl
BPD	Benzoporphyrin monoacid ring A derivative
Calcd.	Calculated
CDAMP	Cell death-associated molecular pattern
CFU	Colony-forming unit
CRT	Calreticulin
CS	Chitosan
d	Doublet (NMR)
DAMP	Damage-associated molecular pattern
DC	Dendritic cells
dd	Doublet of doublets (NMR)
DDS	Drug delivery system
DLI	Drug-light interval
DMF	*N*,*N*'-dimethylformamide
DMSO	Dimethyl sulfoxide
DOX	Doxorubicin
DSB	Distyrylbenzene
EDC	1-Ethyl-3-(3-dimethylaminopropyl)carbodiimide

ε	Molar absorption coefficient
Em.	Emission
EMA	European Medicine Agency
EPR	Enhanced permeability and retention
equiv.	Equivalent(s)
ER	Endoplasmic reticulum
Ex.	Excitation
FCS	Fetal calf serum
FDA	Food and Drug Administration
FTIR	Fourier-transform infrared
G’	Storage modulus
G’’	Loss modulus
GA	Golgi apparatus
HA	Hyaluronic acid
HDL	High-density lipoprotein
HIF-1α	Hypoxia-inducible factor-1α
HOAt	1-Hydroxy-7-azabenzotriazole
HOMO	Highest occupied molecular orbital
HPD	Hematoporphyrin derivative
HPPH	2-[1-Hexyloxyethyl]-2-devinyl pyropheophorbide-*a*
HRMS	High resolution mass spectrometry
HSP	Heat shock proteins
I.P.	*Intraperitoneal*
I.V.	*Intravenous*
ICD	Immunogenic cell death

ICG	Indocyanine green
IL	Interleukin
ILC	Innate lymphoid cells
INF	Interferon
IR	Infrared
J	Coupling constant
LD	Light dose
LDL	Low density lipoprotein
LED	Light-emitting diode
LUMO	Lowest unoccupied molecular orbital
LVE	Linear viscoelastic region
m	Multiplet (NMR)
m-THPBC	5,10,15,20-Tetrakis(*meta*-hydroxyphenyl)bacteriochlorin
m-THPC	5,10,15,20-Tetrakis(*meta*-hydroxyphenyl)chlorin
m-THPP	5,10,15,20-Tetrakis(*meta*-hydroxyphenyl)porphyrin
m.p.	Melting point
MALDI	Matrix assisted laser desorption ionization
MB	Methylene blue
MMP	Matrix metalloproteinase
MOF	Metal-organic framework
MS	Mass spectrometry
NF-κB	Nuclear factor kappa-light-chain-enhancer of activated B cells
NHS	*N*-Hydroxysuccinimide

NIR	Near-infrared region
NK cells	Natural killer cells
NLO	Non-linear optics
NMR	Nuclear magnetic resonance
NP	Nanoparticle
Nu	Nude (mice)
OLED	Organic light-emitting diode
OPA	One-photon absorption
OPE	One-photon excitation
PAA	Poly(acrylamide)
PB	Prussian blue
PBS	Phosphate-buffer saline
PCI	Photochemical internalization
$Pd_2(dba)_3$	Tris(dibenzylideneacetone)dipalladium(0)
PDT	Photodynamic therapy
PEG	Polyethylene glycol
pHEMA	Poly(2-hydroxyethyl methacrylate)
PpIX	Protoporphyrin IX
PPa	Pyropheophorbide a
PS	Photosensitizer
PTT	Photothermal therapy
PTX	Paclitaxel
PVA	Poly(vinyl alcohol)
r.t.	Room temperature
R_f	Retention factor

ROS	Reactive oxygen species
S_0	Singlet ground state
S_1	First excited singlet state
SCC	Squamous cell carcinoma
SCID	Severe combined immunodeficiency
SOD	Superoxide dismutase
t	Triplet (NMR)
T_1	Excited triplet state
TAA	Tumor associated antigens
TAM	Tumor associated macrophages
TCSPC	Time correlated single photon counting
TEA	Triethylamine
THF	Tetrahydrofuran
TLC	Thin layer chromatography
TNF	Tumor necrosis factor
TPA	Two-photon absorption
TPE	Two-photon excitation
TPEF	Two-photon excited fluorescence
$TPPS_{2a}$	Tetraphenyl chlorin disulfonate
UV	Ultraviolet
UV/Vis	Ultraviolet/visible light
VEGF	Vascular endothelial growth factor
σ	Cross-section

Table of contents

Chapter 1. Introduction

1.1. Cancer – a multifactorial disease of our times

Cancer is a major public health problem throughout the world and therefore new and more effective treatment options are constantly required.[1] The current epidemiologic data predict an increasing cancer incidence in the next decades, with over 20 million new cancer cases annually expected by 2025. Moreover, it is predicted that in the next 40 years the burden of malignant diseases will significantly increase. Thyroid and prostate cancers have the best overall diagnosis, approximating 100% survival at 5 years, and 78% and 30% survival at 5 years for cancers with distant metastases. In contrast esophagus, liver, and especially pancreas cancers have the worst overall prognosis, typically less than 20%.[2] Increased efforts in the development of molecularly targeted therapies plays nowadays a crucial role to face challenges related with cancer treatment. Moreover, targeting the immune system and the antitumor immunity will be one of the main challenges and most promising strategies for cancer treatment in the future.[3] Clinical cancer treatments comprise conventional methods, which include surgical removal of tumors, chemotherapy, or radiotherapy. Surgery is the most effective procedure in the treatment of localized primary tumors. This is related with the whole population of cancer cells being removed. However recently, increasing number of clinical reports bring the evidence that surgery can increase the establishment of new metastases. This is related with the mechanical tissue trauma and inflammation that have been proved to enhance tumor growth.[4] Development of radiotherapy provided delivery of radiation with great precision to tumor lesions with substantial reduced injury to normal tissues. Suppression of tumor growth and metastasis can be achieved by cancer chemotherapy originally designed to directly destroy cancer cells.[5] Main problems are resistance to irradiation and chemotherapeutic agents, and the non-selective impact on healthy tissue that ends in significant side effects. PDT has emerged over 40 years ago as a promising approach for cancer treatment.[6] PDT involves the use of a pro-drug, known as photosensitizer (PS), that is activated by light of a certain wavelength. In the presence of oxygen, this triggers the formation of ROS that are highly toxic to the surrounding biological environment.

1.2. Photodynamic therapy

1.2.1. The roots of photodynamic therapy

Heliotherapy, the therapeutic exposure to sunlight, was known to the ancient Greeks, Egyptians, and Indians as a treatment for several skin disorders. The first mentions of phototherapy reach back to the ancient civilizations where it was noticed that light has a therapeutic effect towards diseases, including psoriasis and vitiligo.[7] However, development of phototherapy by western civilizations re-emerged only in the late 19th century. The crucial discovery that sunlight plays an important role in prevention of nutritional rickets was formed in 1890 by Theobald A. Palm.[8] Over the next years his observation allowed for understanding the impact of ultraviolet (UV) irradiation on vitamin D synthesis.[9] In 1899, Niels Finsen published a book entitled 'Phototherapy'.[10] Due to the discovery of red light activity towards *Lupus vulgaris* in 1903, Niels Finsen won the Nobel Prize in Medicine or Physiology. Established in 1896 the Finsen Light Institute carries on its activities to this day.[11] In the next years, von Tappeiner and Jesionek, continued the work and used photodynamic activity of eosin towards lupus and skin cancers.[12,13]

The first examples of use of tetrapyrrolic PSs appear in early 1900' when Hausmann and Pfeiffer published the biological activity of hematoporphyrin in mice and guinea pig models.[14–16] Although hematoporphyrin was first described by Scherer in 1841, its activity in the human body was observed for the first time in 1912, when Meyer-Betz injected himself with 200 mg of the PS and upon sunlight exposure observed photosensitization processes which occurred as blistering and swelling of the skin.[17] Next, the potential use of hematoporphyrin in the field of imaging was reported by Policard who discovered its fluorescence in tumors.[18] However, due to strong photosensitization, at that time the use of the PS in diagnostics was limited. Dougherty first successfully treated cancer with PDT in preclinical models in 1975. His studies involved treatment of tumors using hematoporphyrin derivative and resulted in long term cures.[19] Three years later, Dougherty *et al*. conducted the first controlled clinical study in humans. Study towards variety of tumor models was reported in 1978 allowing to observe response to the PDT treatment in 111 of the 113 patients.[20] Follow-up research led to the discovery of a water-soluble mixture of porphyrin molecules called

"hematoporphyrin derivative'' (HPD).[21–24] In 1994, HPD with its commercial name Photofrin, was approved by the Food and Drug Administration (FDA) for palliative PDT treatment of advanced esophageal cancer.[25] In the next years extensive research allowed the development of next generation PS that reached the clinical stage. The last half-century saw several advances in the development of PDT. PDT is a treatment method, which uses the combined effect of a photosensitizing drug, light, and oxygen to cause selective damage to the target tissue. The fundamental concept behind PDT involves the administration of a photosensitizing agent (pro-drug) and subsequent photoactivation by light of a specific wavelength to act against the target cells (**Figure 1.1**). Over the last three decades, PDT has been used in clinical practice to treat solid tumors.[26]

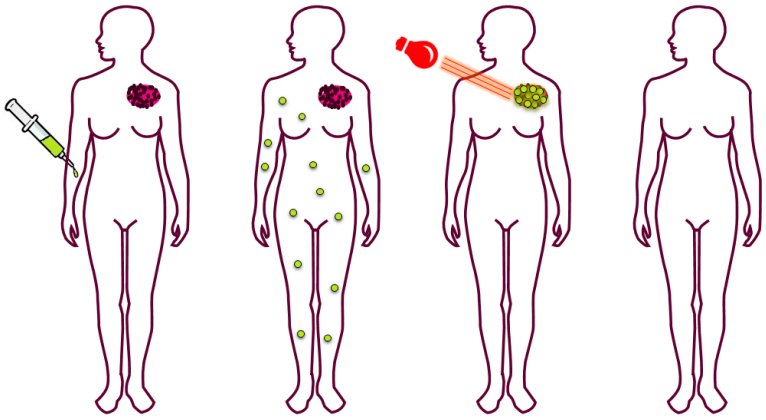

Figure 1.1. *Schematic representation of PDT treatment.*

1.2.2. Photosensitizers for photodynamic therapy

A PS is a chromophore that can access the triplet excited state and react with oxygen or surrounding biomolecules to produce highly toxic reactive oxygen species (ROS) after irradiation. Porphyrin-based molecules exhibit a unique absorption profile that contains two major areas – a strong band at 400 – 450 nm known as the Soret band and less intense bands between 500 and 800 nm defined as Q bands. Photophysical processes strongly depend on the structural properties of the PS. The Soret band reflects a strong electronic transition from the ground state to the second excited singlet state $S_0 \rightarrow S_2$, while and the Q bands arise from the transition to the first excited singlet state $S_0 \rightarrow S_1$.[27] Tetrapyrrolic PSs differ between each other in absorption profiles and intensities due to the destabilization of the highest occupied molecular orbitals

(HOMO). Therefore, changes of the energy gap between HOMO and lowest occupied molecular orbital (LUMO) can lead to the changes of the absorption spectra. This can be achieved by modifications of the macrocycle core (*e.g.*, reduction of the pyrrole ring) or on the molecule periphery (*e.g.*, introduction of functional motifs).[28,29] For instance, the two reduced pyrrole rings in the bacteriochlorin structure allow for a significant shift of the Q band towards the near-infrared region (NIR).[30]

The photophysical processes taking place during PDT are illustrated in **Figure 1.2**. Initially, the PS used in PDT is in the ground electronic singlet state (S_0) and after irradiation, with light of a suitable wavelength, it is excited to a short-lived singlet state (S_1). As the PS returns to the ground S_0 state, it emits the absorbed energy as fluorescence (useful for diagnosis and imaging). Alternatively, it can undergo intersystem crossing to the excited triplet state (T_1). This transition is spin-forbidden, indicating that PSs must have high triplet-state quantum yields. The T_1-state must also be sufficiently long-lived to take part in different chemical reactions; alternatively, the PS can return to the S_0-state *via* phosphorescence.[31] PDT can be classified into two types, depending on the reaction pathways leading to cause ROS. Type I reactions lead to energy transfer from the PS in the triplet excited state to molecular oxygen to form ROS like hydroxyl and superoxide radicals.[32,33] Type II reactions rely on energy transfer to molecular oxygen to form highly reactive $^1O_2$. The type II mechanism is the most important for the PDT effect.[34]

In recent years, scientists defined a set of properties for an ideal PS.[35,36] It should allow for cost-efficient, reliable manufacturing methods with easy purification procedure and good chemical stability. Moreover, compounds should maintain good solubility in biological media without affecting their phototoxic properties. From a photophysical point of view PSs should have the ability to generate a long-lived triplet state allowing for high quantum yields of ROS, especially singlet oxygen ($^1O_2$) generation.[37]

Moreover, PSs should have absorption maxima in the phototherapeutic window: between 650 and 800 nm. These wavelengths have deeper optical penetration into the target tissues while having enough energy to react with molecular oxygen.[38] From a biological perspective, an ideal PS should not be

toxic without light irradiation. Specific accumulation in the diseased tissue and relative rapid clearance from healthy tissues are also important features of promising PS. Drug administration should be straightforward, painless, and do not cause adverse reactions (**Figure 1.3**).[39,40] Although achieving all the above-mentioned PS properties is still challenging, great progress has been made in this direction over the past years. Most of the PSs used in the field of PDT are based on a tetrapyrrole structure, and include porphyrins, chlorins, bacteriochlorins or phthalocyanines.[41] Porphyrins are essential elements of metabolic processes and life. Therefore, many of the clinically approved PSs belong to the family of porphyrins and maintain structures similar to natural pigments such as chlorophylls or heme B.

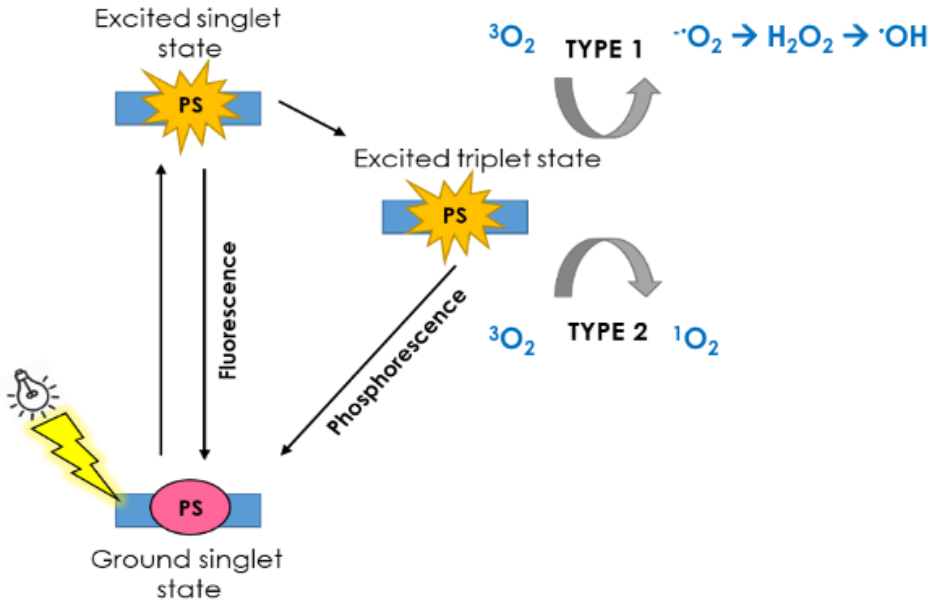

Figure 1.2. *Jabłoński diagram - an illustration of the main photophysical and photochemical processes involved in PDT.*

Porphyrin-derived PSs can be classified into first, second, and third generation ones. First generation PSs include HPD (Photofrin). Despite wide applications in PDT, this group exhibits several limitations on its clinical applications. Photofrin suffers from low solubility in aqueous media, requires high light doses owing to a low absorption at 630 nm and causes several side effects, including prolonged skin photosensitivity (during 4-6 weeks after PDT) due to the slow clearance of the PS. The disadvantages of the first-generation PSs necessitate investigating new compounds.[40,42]

Figure 1.3. *Properties of an ideal PS.*

The second-generation PSs were designed to overcome limitations of the first class. Therefore, these compounds exhibit better purity and enhanced photophysical properties, namely higher yields of $^1O_2$ generation. These new molecules were also characterized by absorption maxima in the wavelength range of 650–800 nm, allowing for a deeper tissue penetration, and shorter periods of skin photosensitivity.[43] Consequently, these PSs demonstrate less severe side effects due to the increased specificity towards diseased tissues and lower levels of non-specific accumulation. However, this class of PSs suffers from poor solubility in biological media, which reduces their application *via intravenous* (*I.V.*) administration; thus, opening the door for development of new drug delivery platforms.[44] This group involves a broad spectrum of compounds including 5-aminolevulinic acid (5-ALA), benzoporphyrin derivatives, texaphyrins, thiopurine derivatives, chlorin as well as bacteriochlorin analogues and phthalocyanines.[45] 5-ALA is the precursor of the natural protoporphyrin IX

(PpIX), which is then converted by ferrochelatase into heme.[46] Due to lower activity of ferrochelatase, PpIX exhibits high affinity towards tumor cells.[47] Other known molecules from this group are verteporfin (with the trade name Visudyne), talaporfin (Laserphyrin), padeliporfin (TOOKAD) and temoporfin (Foscan).[48–51] This doctoral thesis is mainly focused on temoporfin, which was approved for the treatment of head and neck cancer in 2001.[51] The PS allows for an excitation at 650 nm and it provides effective therapeutic response at very low doses (*e.g.*, 0.1 mg/kg).[52] A detailed description of properties of this compound will be given in **Section 1.3**.

Finally, third generation PSs relates to second generation PSs in combination with targeting motifs or encapsulated into nano drug delivery systems (DDS)s. The prime purpose of both approaches is to induce cancer-specific targeting to avoid toxicity towards healthy tissue; thus reducing adverse reactions.[53] The major advances regarding active targeting delivery of PSs, either by means of ligand-derived PS bioconjugates or by taking advantage of ligand-targeting nanocarriers, were recently discussed in a review by us.[54] Additionally, further improvements allowed to develop systems with controlled $^1O_2$ generation which enhances the therapeutic outcome.[55]

1.2.3. Clinically approved photosensitizers and current clinical trials

In 1994, porfimer sodium, with the commercial formulation Photofrin, became the first clinically approved PS intended for use for the palliative treatment of advanced esophageal cancer. Almost 30 years later, the number of PSs passing regulatory approval for clinical use had increased significantly. A list of clinically approved PSs available in the European Union is given in **Table 1.1**, while the chemical structures are presented in **Figure 1.4**.

5-ALA, the precursor of PpIX and heme, is a natural, nonproteogenic amino acid and component of the anabolic pathway of porphyrinoids. The mechanism of action involves accumulation in mitochondria and cytosol of tumor cells where it is metabolized to PpIX. A phototoxic effect towards tumor cells is achieved upon 635 nm irradiation. There are three clinically approved formylations of 5-ALA – Levulan, Alacare and Ameluz. However, in the EU only the last one has approval from the European Medicine Agency (EMA).

Ameluz is a gel formulation of 5-ALA used for the treatment of actinic keratosis (AK) of mild to moderate severity and basal cell carcinoma unsuitable for surgical treatment. Moreover, the 5-ALA derivative methyl aminolevulinate (Metvix) is a cream. Its mechanism of action is comparable with 5-ALA; however, the formulation allows for a deeper penetration of the PS to the skin lesions. A cytotoxic effect is achieved *via* 570 – 670 nm light irradiation. Finally, an intravesical solution of hexaaminolevulinic acid (Hexvis) has been approved for bladder cancer diagnostics. Cystoscopy examination is performed upon light illumination with the blue light (380 – 450 nm).

5,10,15,20-Tetrakis(*meta*-hydroxyphenyl)chlorin (*m*-THPC, *temoporfin*) is a second-generation PS approved for the treatment of squamous head and neck carcinoma. An extensive evaluation of *m*-THPC activity and applications will be given in **Section 1.3**. Padeliporfin, with the market formulation known as TOOKAD, is the first palladium-based PS approved for the prostate cancer treatment. *I.V*. administration of the drug is followed by 753 nm irradiation of the cancerous prostate tissue, which results in tumor necrosis.[50] The results of the clinical study concluded that TOOKAD exhibits good safety profile for localized prostate cancer.[56]

Verteporfin (Visudyne) is benzoporphyrin monoacid ring A derivative (BPD) approved for age-related macular degeneration and choroidal neovascularization caused by pathologic myopia.[57] The lipid-based formulation of verteporfin is administered by the venous route and activated *via* 690 nm laser irradiation. Verteporfin reaches the maximum plasma concentration after 30 min and the elimination half-time was reported to be 6 h, allowing for a rapid clearance, which reduced prolonged side effects.[48]

Redaporfin (LUZ11) has been approved for orphan designation for the treatment of biliary tract cancer. Orphan designation refers to a drug approved for diagnosis, prevention, or treatment of a life-threatening or chronically debilitating condition that is rare.[58] Redaporfin belongs to the family of bacteriochlorin and exhibits a strong absorption band at 749 nm, allowing for a deep tissue penetration. The PS is currently in ongoing clinical studies (phase I/II) for the treatment of head and neck cancers.[59,60]

Another PS with orphan designation and approved by EMA for the treatment of cutaneous T-cell lymphoma is synthetic hypericin derivative (SGX301). This hypericin-based PS, with the commercial name HyBryte, is administered topically, and irradiated with 5 J/cm^2 visible fluorescent light 12 to 24 h later. The PS triggers cell death *via* apoptotic processes due to the mitochondrial accumulation in the T-cells.[61] Considering the local application of SGX301-based ointment, the treatment targets only T-cells of the skin layer, allowing for reduced toxicity and less adverse reactions than upon systemic application.[62] Although the number of clinically approved PSs is still very limited, several new PS are in the clinical studies and under development.

Table 1.1. *List of clinically used PSs in the EU.*

PS	Trade name	λ_{max} [nm]	Disease	Ref
Porfimer sodium	Photobarr#	630	Bladder, esophageal, lung, and brain cancer; Barrett's esophageal cancer; cervical dysplasia	63
5-Aminolevulinic acid (HCl)	Ameluz Alacare	635	AK	64,65
Methyl aminolevulinate (HCl)	Metvix Metvixia Luxera Luxerm	570-670	AK, BCC, Bowen's disease	66
Hexaminolevulinate acid (HCl)	Hexvis	360-450	Bladder cancer diagnosis	67
Temoporfin	Foscan	652	Head and neck, lung, brain, skin, bile duct, prostate, bronchial, and pancreatic cancer	68
Padeliporfin	Tookad	762	Prostate cancer	69
Verteporfin	Visudyne	690	AMD, choroidal neovascularization caused by pathologic myopia.	70

withdrawn marketing authorization in the European Union

Hexaminolevulinate, a synthetic derivative of 5-ALA, is currently in phase III clinical studies towards oncogenic human papilloma virus and cervical lesions.[71] The drug formulation, commercially known as Cevira, is administered locally to the cervix and the treatment is expected to be delivered within 24 h (635 nm light irradiation). Cevira has been shown to be efficient and safe in patients.[72] (2-[1-Hexyloxyethyl]-2-devinyl-pyropheophorbide-*a*) – HPPH – a chlorophyll a derivative, has been investigated for the treatment of head and neck cancer. HPPH, with the commercial name Photochlor, reached II phase of clinical trials.[73] The clinical study involves *I.V.* administration of the drug *via* infusion and 665 nm light irradiation 24 or 48 h later. Clinical application of the HPPH towards other cancers, for instance lung or oral cavity carcinoma is under ongoing investigation.[74,75]

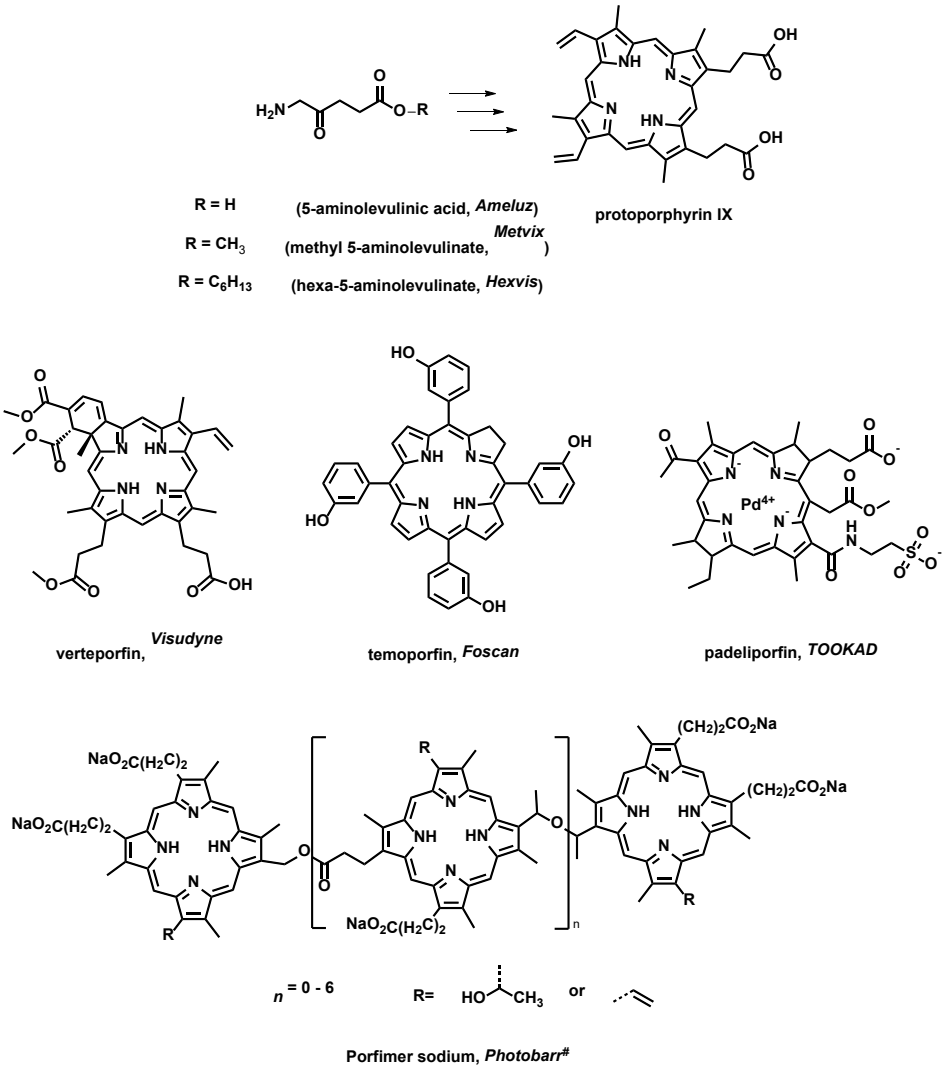

Figure 1.4. *Structures of clinically approved PSs available in the European Union.*

Furthermore, methylene blue (MB), as the commercially available product MB-MMX, reached phase III of clinical trials towards detection and visualization of adenomas and carcinomas in patients undergoing colonoscopy. The drug is administered orally, and due to the multimatrix structure of the tablet, the release of the PS occurs in the colon area. In the clinical study the MB formulation allowed a significant increase of tumor detection in comparison with conventional high-definition colonoscopy.[76] Another example of PSs currently undergoing clinical evaluation is tetraphenylchlorin disulfonate ($TPCS_{2a}$). This photosensitizer is not being used for PDT but for photochemical internalization (PCI) of bleomycin - a chemotherapeutic drug. PCI uses PSs that accumulate in endocytic vesicles and upon exposure to light release contents of vesicles into the cytosol in a functionally active form.[77] The PS was injected *I.V*. 72 hours prior treatment. After 30 mins post *I.V*. injection of bleomycin, the surface of the target tumor is illuminated with 652 nm laser light to enhance internalization of the chemotherapeutic at the target site. The combinatorial treatment of bleomycin and $TPCS_{2a}$ mediated PCI was safe and tolerated by all patients.[78] The PSs under current clinical development were published by Rodríguez-Amigo *et al*. in 2016 and more recently by Melissari *et al*. in 2021.[27,79]

1.2.4. Two-photon induced photodynamic therapy

Chromophores can be excited *via* one-photon absorption (OPA) or two-photon absorption (TPA) processes. In TPA, two lower energy photons, but equal with the transition energy, are simultaneously absorbed. For instance, a PS that absorbs at 400 nm, in two photon processes can be activated by two photons at 800 nm. While in one-photon processes, the rate of generation of the excited state exhibits a linear relationship with the light intensity, in two-photon processes the dependence is quadratic, thus requiring short and high energy laser pulses for the activation of the chromophore.[80] Similarly to one-photon processes, with a high enough energy level, the PS in the excited triplet state can interact with a molecular oxygen and produce highly reactive $^1O_2$ and other ROS. As the molar absorption coefficient in one-photon processes determines the probability of reaching the excited state upon light excitation, in two-photon processes, the cross-section (σ) is a quantitative measurement of such probability.[81] σ is expressed in Göppert–Mayer (GM, 1 GM = 10^{-50} cm^4 s $photon^{-1}$ $molecule^{-1}$) in honor of Maria Göppert–Mayer - the innovator of this technique.[82]

Development of two-photon activable dyes for application in PDT has allowed to increase the light penetration, which delivers better results in deep-seated tumors. The dependence between light wavelength and tissue penetration is shown in **Figure 1.5**. Moreover, it brings additional benefit of improving the spatial precision of the treatment. Excitation of PSs with long-wavelength at NIR reduces scattering from tissue components and reduces light-induced damage to tumor surroundings in comparison with PSs excited in the UV-Vis range. The process of simultaneous absorption of two photons by the molecule was for the first time analyzed by Göppert-Mayer in 1930s but only 30 years later, it was demonstrated experimentally in $CaF_2:Eu^{2+}$ crystal.[82,83] However, development of two-photon fluorescence microscopy by Webb *et al*. was a triggering point for extensive research of multiphoton processes.[84] To this day, this phenomenon found its application in many fields, including PDT, imaging, or optical data storage.[85–87]

The crucial factor that determines the applicability of a PS in two-photon PDT is its TPA σ. This quantity can be determined experimentally by Z-scan and Two-Photon Excited Fluorescence (TPEF) measurements. While Z-scan is based on the measurement of light intensity as the function of the sample position along the z-axis, the TPEF technique determines the intensity of the two-photon induced fluorescence as the function of the excitation intensity. However, both techniques have their limitations. When using the Z-scan technique, the TPA σ values tend to be larger compared with other techniques, which often correlates with the presence of non-linear scattering or defocusing of the sample during the measurements. In turn, TPFE can only be applied for fluorescent molecules and cannot overlap with the OPA regions. In the case of species with a reasonably high luminescence quantum yield, using TPEF is usually preferred. Typically, the experiment is carried out by comparing the signal from an investigated sample with that from a reference fluorescent dye, avoiding the need for exact knowledge of variables dependent on the laser beam.[88]

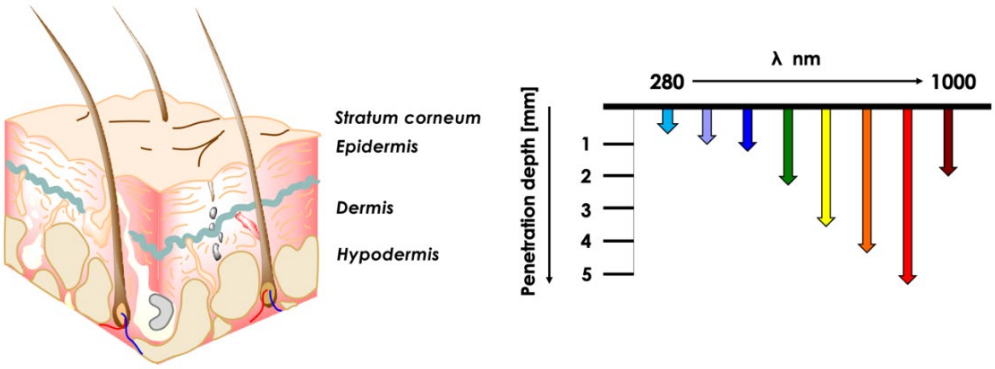

Figure 1.5. *Tissue penetration depth of various wavelength*

Several studies concerning the design and optimization of the PS structures to enhance their TPA properties can be found in the literature. In a recent review by Robbins *et al*., three main requirements for chromophores are listed to enhance TPA of the PS. Firstly, the presence of long π-conjugated systems or enforced co-planarity of the chromophore enhances delocalization of the π-electrons. Secondly, dipolar or multipolar units enhance transition dipole moments. This can be achieved by the presence of donor and acceptor groups at the center and periphery of the molecule. Finally, the molecules should present narrow OPA and TPA bands.[89] Moreover, combining the field of nanotechnology with TPA techniques, it was possible to achieve improvements

on two-photon performance of the PS, with additional benefits of enhanced accumulation in solid tumors. Additionally, modification of the surface of nanoparticles can allow site specific targeting (*e.g.*, attachment of ligands) of functional groups tuning TPA properties.[90] Most of the nanoparticles (NPs) involved in TPA studies belongs to the family of inorganic NP (carbon dots, silica, or gold nanoparticles), although polymer-based NPs play a functional role. The first example of the TPA efficacy *in vivo* using a mouse model, was reported by Collins *et al*. in 2008. The authors achieved blood-vessel closure upon 920 nm light irradiation using PSs engineered for two-photon excitation.[91] Since then significant progress have been made. For instance, Gary-Bobo *et al*. studied the utility of mannose-functionalized mesoporous silica nanoparticles towards subcutaneously established HCT-116 tumors. Laser light irradiation at 760 nm for three periods of 3 min on three different tumor areas allowed for *ca*. 70 % tumor mass reduction 30 days post treatment in comparison to the control group.[92] A tetraphenylethene derivative was used as photosensitizing agent in the design of these NPs. The antitumor efficacy of the NPs was evaluated *in vivo via* intratumoral injection into melanoma-bearing mice. Tumors were irradiated 2 h post injection using femtosecond-pulsed laser at 800 nm. NP-treated mice with laser irradiation showed a complete inhibition of the tumor growth within 18 days post-treatment in comparison with the non-irradiated group.[93]

Moreover, the differences between one- and two-photon excitation can be seen using two-photon fluorescence microscopy. In comparison with conventional microscopy techniques, two-photon fluorescence microscopy involves multiple photons for contrast generation. It gives a great advantage in generating of high-quality images opening the door for high-resolution imaging in various organs of living animals.[94] For instance, TPEF microscopy was introduced to monitor neural activity or coronary artery microstructure *in vivo*.[95,96] Two-photon fluorescence microscopy found its application in the field of PDT, mainly to detect and diagnose deep-seated tumors. Sun *et al*. utilized a "turn-on" fluorescence dye – a distyrylbenzene (DSB) derivative– for efficient TPEF imaging. Conversion of the dye from acetal-terminated DSB to aldehyde terminated molecules under physiological conditions (upon the addition of β-cyclodextrin) allows for a 26-fold enhancement of the σ values. For *in vivo*

imaging the PS was injected intratumorally in melanoma tumor bearing mice, and high-resolution images were recorded upon 760 nm excitation.[97] Although well-designed and optimized two-photon induced PDT can significantly increase the treatment efficacy in comparison to conventional methods, there are several drawbacks to overcome. Firstly, to allow efficient TPA processes the development of spatially designed PS, exhibiting high values of the TPA σ is required.[98] The second factor is the availability of laser systems. Despite the technological development in the field has progressed, laser systems, tailored to the properties of the PS and sufficiently reaching high intensities are relatively expensive.[99]

1.2.5. Biological effects of photosensitization

The efficiency of $^1O_2$ generation depends on many parameters, the most important being the yield and rate of triplet state formation, the stability of the chromophore, and the concentration of oxygen in a given environment. The quantification of $^1O_2$ quantum yields is challenging. This is mainly due to its high reactivity, short lifetime, and sensitivity towards environmental factors, which can cause significant errors.[100] $^1O_2$ exhibits a characteristic phosphorescence at 1275 nm, which can be detected directly. Alternatively, $^1O_2$ can be detected using fluorescent probes (such as Singlet Oxygen Sensor Green),[101] which change their properties in the presence of $^1O_2$.[102,103]

The long-term PDT activity is the combined effect of several mechanisms including: i) direct toxicity of ROS for target cells, ii) the damage to the tumor microvasculature, and iii) activation of the immune system against tumor cells. ROS can cause direct cell damage by generation of oxidative stress. Moreover, the species generated are highly reactive and cause oxidation of biomacromolecules in the diffusion range of the ROS, namely *via* reaction with proteins, lipids and DNA.[104] Oxidative stress may trigger several mechanisms of cell death such as necrosis or apoptosis. Moreover, understanding these mechanisms is important for maximizing the immune response and optimizing PDT as a treatment method.[105]

Biodistribution and thus, cellular localization of the PS plays a significant role for the photosensitizing activity as it coincides with the primary

site of photodamage. Cellular uptake depends on many factors, the most important of which are amphiphilicity, molecular weight, and environmental conditions, for instance pH of the cellular compartments. The balance between hydrophobicity and hydrophilicity is a crucial factor for cellular internalization by passive diffusion. Although, hydrophobic compounds tend to internalize cells more efficiently than hydrophilic ones, the excessive hydrophobicity limits applicability of the PS in biological conditions due to enhanced aggregation processes.[106] Low quantity of ROS generated in the cellular compartment can trigger protective processes in cells, namely *via* upregulation of molecules that play a role in long-term restoration of cell homeostasis. Moreover, toxic activity of ROS can be also quenched by the scavengers and the presence of antioxidants. Alternatively, overexpression of enzymes, for instance superoxide dismutase (SOD), has been shown to diminish the cytotoxic effect of PDT.[107] Considering the short lifetime and limited diffusion of ROS, the PS intracellular localization assumes an important role on the signaling pathways responsible for imitation of cell death processes. The most studied mechanisms of cell death initiated by the photosensitization are: apoptosis, necrosis, and autophagy-associated cell death.[108] Recently, immunogenic cell death (ICD) was established as an independent type of cell death mechanism that triggers release of a specific set of molecules, named as dander-associated molecular patterns (DAMPs) that contribute to trigger anti-tumor immune responses.[105,109,110] PDT activity can occur not only at the cellular level but can display a great activity towards tumor tissues and in the surrounding microenvironment. This is usually determined by the drug-light interval (DLI). The DLI and biodistribution of the PS determines vascular *versus* cellular regimen of the PDT treatment. For cellular PDT, DLI is usually longer (*e.g.*, > 24h), allowing for drug distribution and uptake by the cancerous cells. For vascular PDT, the DLI is usually short, and the treatment mainly affects the tumor vasculature as the PS is confined at the blood vessels.[60] It leads to direct destruction or endothelial cells and/or vessels walls causing blockage of the blood flow. For instance, irreversible damage to tumor microvasculature cuts the supply of oxygen and nutrients and consequently induces local hypoxia and tumor starvation.[111] Prolonged hypoxia can result in cancer cell death and lead to tumor necrosis.[112] Moreover, hypoxia induces upregulation transcription factors; namely, hypoxia-inducible factor-1α (HIF-

1α) which overexpression stimulates tumor cell proliferation.[113] Although the first observations of photodynamic perturbation of blood microcirculation were reported in 1963 by Castelani *et al*., the PDT-induced vascular shutdown was for only reported over 20 years later by Henderson *et al*.[114,115]

1.2.6. Photodynamic therapy-induced anti-tumor immunity

One unique property of PDT is its ability to trigger anti-tumor immune responses. The immune system is composed of cells and molecules with highly specialized, adaptive, and sensitive roles that combined effect allows to maintain homeostasis, namely in case of infection.[116] Immune cells originate in bone marrow where differentiate from pluripotent hematopoietic stem cells, differentiated subsequently into common myeloid or common lymphoid progenitor cells. The first ones give rise to neutrophils, eosinophils, basophils, dendritic cells (DCs), mast cells, monocytes/macrophages, platelets, and erythrocytes, while common lymphoid progenitor cells to T lymphocytes, B lymphocytes, natural killer cells (NK cells) and innate lymphoid cells (ILC).[117] Two types of immunity can be distinguished. Innate (natural) immunity is the first-line response towards infectious agent, while adaptive (acquired) immunity can be defined as a cellular memory of the repeated exposure to the infectious factor. The innate system includes phagocytic cells (neutrophils, monocytes, and macrophages), cells that release inflammatory mediators (basophils, mast cells, and eosinophils), and NK cells.[118] Adaptive immune system involves activity of antigen-specific B and T cells.[119] The hierarchy of the hematopoietic immune cells is shown in **Figure 1.6**.

The innate immune system is the body first line of the defense and include cellular (neutrophils, macrophages, and NK cells) and non-cellular (complement and antibacterial peptides) agents.[120] It first react against pathogens invaders and to tissue damage by activating inflammation. The main goal of the innate immune system is to restore normal tissue function and homeostasis. Oxidative stress generated by PDT triggers a rapid and acute local inflammation which appears as a local edema at the irradiation site. While chronic inflammation is typically perceived as an enemy for human healthy, the acute inflammation observed after PDT is recognized to be essential to mount subsequent anti-tumor immune responses.

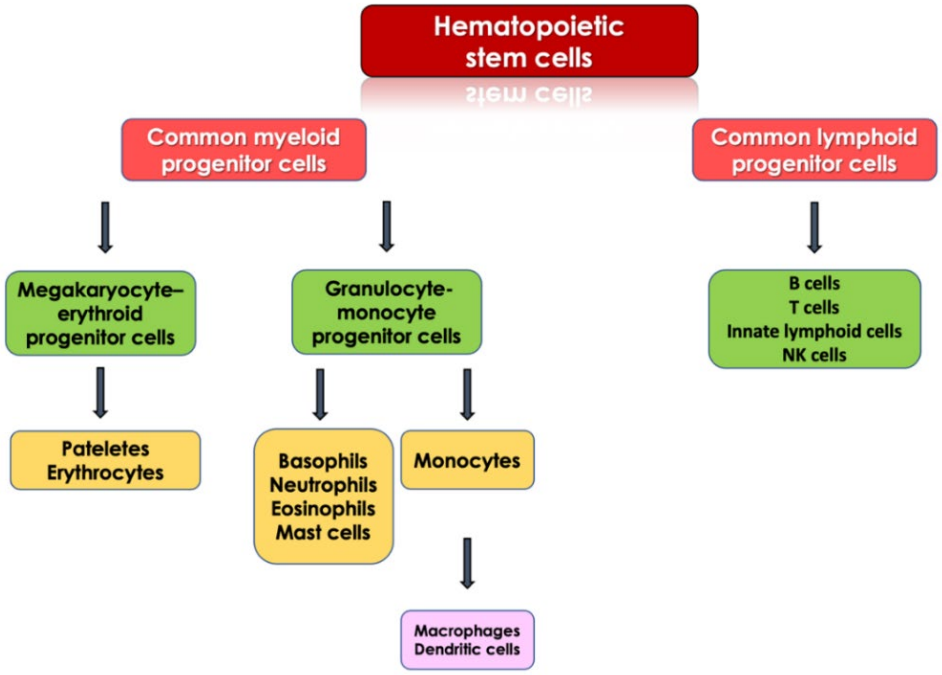

Figure 1.6. *Structure of the hematopoietic system.*

The inflammation mediated by PDT is subsequent to the release/ exposure of DAMPs by the tumor-dying cells. DAMPs originated from PDT may be categorized in three major groups: cell derived molecules, extracellular matrix degradation products and extravasated plasma proteins.[121] Release of DAMPs is followed by their recognition by the innate immune system receptors, which facilitates the recruitment of immune cells (*e.g.*, neutrophils) into the tumor bed. Inflammation causes significant changes in the tumor vasculature that become more permeable for complement proteins and immune cells. Neutrophils play an important role in immune system activation as they are one of the first cells of the innate immune system to enter PDT-treated tumors. They secrete leukotrienes, prostaglandins, and cytokines necessary for further propagation of inflammatory response.[122] Additionally, neutrophils are able to directly destroy pathogens and act as antigen presenting cells, presenting the antigens *via* major histocompatibility complex class II.[123] Recruitment of antigen-presenting cells, namely DCs, at tumor sites is of the utmost importance to trigger adaptive immune. This part of the immune system is highly specific to certain antigens and provides immunological memory. DCs engulf and process tumor antigens which is followed by their migration to lymph nodes. Tumor antigens at the surface of DC are them presented to T and B cells promoting their

maturation and proliferation. T cells, namely CD8+ T cells, then circulate through the host body being able to detect and destroy cancer cells. The PDT-induced stimulation of the immune system is presented on **Figure 1.7**.

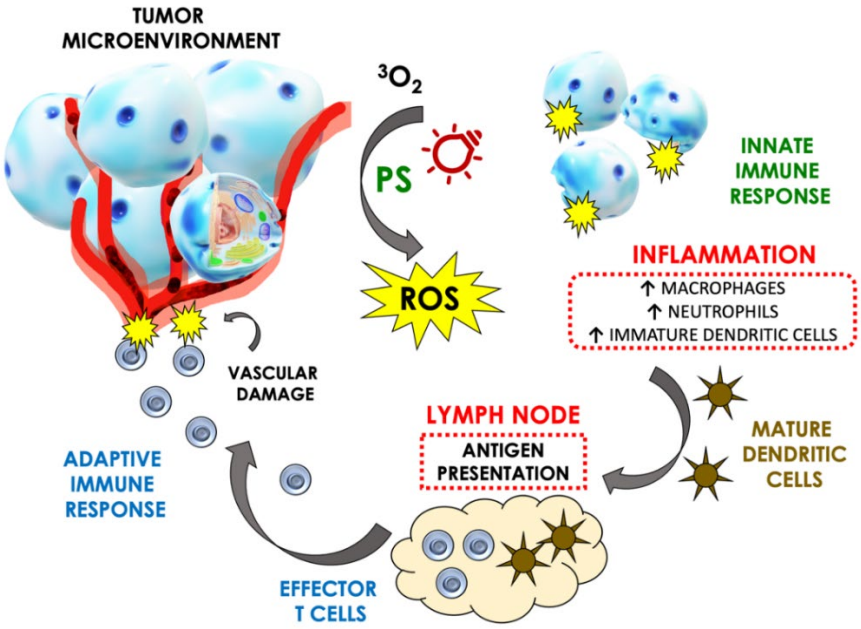

***Figure 1.7**. Antitumor immune mechanism triggered by PDT.*

1.3.Temoporfin

1.3.1. Photochemical properties of temoporfin

This doctoral thesis describes a new approach to overcome current limitation of temoporfin. 5,10,15,20-Tetrakis(3-hydroxyphenyl)chlorin (*m*-THPC, temoporfin), is a second generation PS that was discovered in early 1980s by Professor Ray Bonnett and has been available on the market for over two decades under the commercial name Foscan. *m*-THPC belongs to the family of reduced porphyrins and exhibits maximum absorption of the Q band at 652 nm.[51] The story of *m*-THPC began in 1980 when Bonnet *et al*. compared the photophysical properties and activity of 5,10,15,20-tetra(hydroxyphenyl)porphyrins, in which the *meta*-substituted derivative exhibited enhanced phototoxicity in comparison to Photofrin.[124] Therefore, hydroxyphenylporphyrins with substituents attached at the *meta* or *para* positions of the phenyl ring, exhibited enhanced phototoxicity towards subcutaneous tumors in comparison with *ortho*-substituted derivatives. In addition, these compounds induced less skin photosensitivity.[125] Although only

a 20 nm red-shift of the Q band was observed for the *meta* derivative, in comparison with HPD, a significant improvement (25-30 times) on the phototoxicity was obtained. This pointed *m*-THPC as a favorable candidate for further studies.[126]

The synthesis of *m*-THPC involves reduction of the pyrrole ring of the porphyrin derivative, 5,10,15,20-tetrakis(*meta*-hydroxyphenyl)porphyrin (*m*-THPP), *via* diimide reduction. The chemical evaluation was followed by the NMR, mass spectroscopy and spectral analysis of the PS and compared with *orto* and *para* derivatives.[127,128] Differently substituted derivatives exhibited similar photophysical properties: low fluorescence yields (0.1), comparable fluorescence lifetimes (10 ns), high triplet (0.7) and $^1O_2$ quantum yields (0.6).[129] Comparison of *meta* substituted chlorin derivative (*m*-THPC) with porphyrin (*m*-THPP) and bacteriochlorin (5,10,15,20-tetrakis(*meta*-hydroxyphenylbacteriochlorin, *m*-THPBC), **Figure 1.8**, demonstrated a progressive red-shift of the Q band - 644, 652 and 735 nm - for the porphyrin, chlorin, and bacteriochlorin, respectively. Although no significant changes in the fluorescence and $^1O_2$ quantum yields were observed, the poor stability of *m*-THPBC excluded further evaluation of the PS.[130]

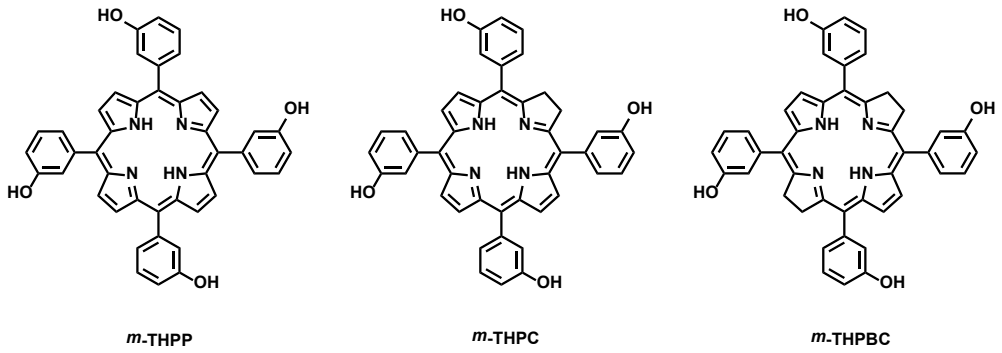

***Figure 1.8**. Chemical formulas of compounds of m-THPP (porphyrin), m-THPC (chlorin), and m-THPBC (bacteriochlorin).*

For *m*-THPC, two wavelengths – 514 nm and 652 nm – were found to be the most suitable for excitation of the chromophore. However, 652 nm is usually favored due to the deeper penetration.[131,132] Importantly, an optimization protocol reported by Coutier *et al*. showed that lower fluence rates of the applied light resulted in better therapeutic outcome. This is explained by limited oxygen depletion at the site of irradiation.[133]

1.3.2. Biological activity of *m*-THPC

Due to aggregation in aqueous environment, *m*-THPC internalizes cells in aggregated form, which is later followed by the monomerization processes in the biological membrane. The main cellular targets for *m*-THPC are the endoplasmic reticulum (ER), Golgi apparatus (GA) and mitochondria.[134–136] *m*-THPC uptake can be inhibited in the presence of serum proteins such as fetal calf serum (FCS). *In vitro* studies showed that the presence of FCS inhibits by 80-90% cellular uptake using T-47D cells.[137]

Photoactivation of *m*-THPC is flowed by release of cytochrome c and activation of caspase-3 as observed in several cancerous cell lines (M1 and WEHI3B myeloid leukemia cells). This was observed by treating cells with 0.8 μg/mL of *m*-THPC and 505-550 nm light intensity of 8.4 J/cm^2. Thus, apoptotic pathway is considered to be the primary mechanism of *m*-THPC-induced cancer cell death.[134] However, one must consider that the cell death mechanism is dependent on many factors, such as cell line, type and applied concentration of the PS, and other experimental conditions.[105] In another *in vitro* study using melanoma cells, it was demonstrated that inhibitors of apoptosis did not rescue cellular viability excluding apoptosis as the cell mode of killing.[138] However, in this study the applied treatment conditions were more severe (1-10 μg/mL of PS and LDs of 10 or 25 J/cm^2). Additionally, a recent study by Yuan *et al*. shown the ability of *m*-THPC to elicit ICD. This was confirmed by quantification of mature dendritic cells harvested from Balb/c mice, which were co-incubated with CT26 cells treated with NPs containing *m*-THPC. The authors observed increase in the percentage of mature DC from 38.94% (observed in the control group) to 55.65% after *m*-THPC-PDT.[139] Moreover, expression of DAMPs (*e.g*., surface exposed calreticulin (CRT), HMGB1, heat shock proteins (HSP) in *m*-THPC treated CT26 cells. Preclinical evaluation of *m*-THPC brought a clearer insight on the biodistribution and pharmacokinetics profile of the PS. Biodistribution and pharmacokinetic profile of a drug molecule are complex phenomena and depend on the species studied, treatment conditions, and biological interactions after administration. Garrier *et al*. reported that the highest level of *m*-THPC accumulation in EMT6 mammary carcinoma tumors occurs 24 h after *I.V*. application.[140]

In contrast, the highest *m*-THPC level in plasma was observed 3 h post injection, which allowed the use of a vascular PDT protocol *in vivo*.[141] PDT-induced vascular damage leads to tumor hypoxia, thus cuts the supply of nutrients, allowing to achieve long-term control of tumor growth. A good example of vascular-PDT using *m*-THPC was given by Triesscheijn, who compared the PDT efficacy against human squamous cell carcinoma SCC 3 and 48 h post PS application. Considering the high level of *m*-THPC in the circulatory system, complete tumor destruction was achieved at the 3 h timepoint, while tumor regrowth was observed at the 48 h timepoint.[142] An animal model was also used to gain a deeper understanding of *m*-THPC metabolism. It was shown that *m*-THPC is cleared from the body mainly in an unchanged form; however, fractions of the porphyrin-derivative were also detected by mass spectrometry.[143]

1.3.3. *m*-THPC in clinical practice

In the mid-1990s, *m*-THPC entered the clinical phase I for the treatment of different types of cancer including, prostate, bronchial and laryngeal. The pharmacokinetic study was based on biopsy and plasma analysis collected at different time points after *I.V.* administration of *m*-THPC.[144] The maximum concentration in plasma was observed 10 – 24 h post injection, while the half-life was established as 30 – 45 h. It is proven that the PS primarily accumulates in liver which is followed by the distribution to other tissues, including skin and muscles.[145] It was also demonstrated that *m*-THPC has a strong binding affinity towards serum proteins (albumin, high-density lipoprotein (HDL), low-density lipoprotein (LDL)) in the human plasma.[146] A phase III of clinical trials involved 128 patients and demonstrated a significantly improved quality of life in 53% of incurable cases of SCC of the head and neck cancer.[147] *m*-THPC received the first clinical approval in 2001 towards above-mentioned cancer.[148] The current recommendation of EMA states that Foscan is indicated for the palliative treatment of patients with advanced head and neck SCC failing prior therapies and unsuitable for radiotherapy, surgery or systemic chemotherapy. In clinical PDT, *m*-THPC is applied at low drug dose (0.15 mg/kg) and light intensity (in the order of 10 J/cm^2). In comparison with Photofrin (2 mg/kg), these conditions allow for over 10-fold decrease of the total drug dose.[149] Encouraged by this

promising therapeutic outcome initially obtained in clinical practice, in the following years *m*-THPC was tested towards several types of cancer including skin, prostate, and breast cancers.[150–152] The first approval of *m*-THPC by the FDA and EMA included a formulation based on a solution of temoporfin in ethanol anhydrous and propylene glycol, which was developed by Scotia Pharmaceuticals Ltd., UK. Although Foscan had granted a fast-track review status by the FDA, in 2000 the certification was withdrawn due to the insufficient data provided by Scotia. After initial problems with the certification, *m*-THPC returned to market in late 2001. Since 2002, *m*-THPC is distributed by the German manufacturer Biolitec Pharma. *m*-THPC (registered as Foscan) is used in the clinic after being dissolved in ethanol anhydrous and propylene glycol and the drug is administered *intravenously*. However, to avoid PS aggregation at the injection site it can be administered only *via* slow injection, which is often painful. Moreover, due to its high affinity to serum proteins or cellular membranes,[153] *m*-THPC exhibits a slow distribution to target cells. Therefore, an optimal DLI for Foscan can require several days.[154] Moreover, the slow distribution of the PS enhances non-specific targeting; namely, in the skin, resulting in post-treatment photosensitivity.[155] This means that Foscan-PDT is often burdened with the need to avoid exposure to sun irradiation for several consecutive weeks. Additional side effects include edema, headache, and hemorrhage.[156] However, these can be reduced by strict patient compliance and application of sun-protecting ointments to decrease activation of *m*-THPC that remains in the skin.[157] Mild to moderate pain in the treated area is also often reported by the patients. The above-mentioned side effects forced and stimulated further work on the improvement of the therapeutic formulation. To optimize the phototoxic response and reduce adverse reactions, two liposomal formulations – Foslip and Fospeg - were developed.[158] The latter formulation includes polyethylene glycol (PEG) on the liposome surface to decrease phagocytosis and enhance circulation time, thus allowing better tumor targeting. Both formulations exhibit lower level of dark toxicity *in vitro* and improved tumor selectivity *in vivo*.[159,160] Nevertheless, the major drawback of both formulations is related with the limited penetration of the liposome formulation into the tumor matrix and poor drug release.[161]

1.3.4. *m*-THPC – second or third generation PS?

Efforts to improve the activity of *m*-THPC continue. New formulations with high complexity and multifunctional have emerged, which has created a new generation of PSs. Typically, this third generation of PSs include a second-generation PS that is conjugated to or encapsulated in nanoparticles, which broadens the PS clinical potential by improving their pharmacokinetics, pharmacodynamics and biodistribution.[162] Several chemical modifications of the *m*-THPC structure have been reported.[163] Substitution pattern of hydroxyphenyl groups is important for the photoactivity and amphiphilicity of the PS. For instance, a study of Wiehe *et al*. showed, that replacement of one aryl substituents of *m*-THPC with an alkyl one significantly decreased the $^1O_2$ quantum yield studied in the liposome formulation.[164] Other advances include attachment of glycoproteins, or other targeting motifs such as bile acid, small non-steroid anti-inflammatory drugs or monoclonal antibodies.[165–168]

Over the last decades a constant developments of nanoparticle-based delivery systems of *m*-THPC have been made. An extensive review that substantively summarizes current development of *m*-THPC based DDS was recently published by Yakavets *et al*.[169] The authors reviewed nanoscale-based *m*-THPC formulations in terms of structural, photophysical and biopharmaceutical properties. Despite the success of nanosized formulations *in vitro* and *in vivo*, their translation into clinical practice remains limited. A common drawback of several examples from the above-mentioned review is that the NPs often suffer from insufficient drug release and limited penetration into the tumor tissues. Therefore, in order to maximize the benefits of nano-DDS, further improvements, *e.g*., design of stimuli-responsive platforms is required. Additionally, nanotechnology-based DDSs provide opportunities for active targeting and for application of combined therapies. The attachment of targeting moieties to the NPs' surfaces is a strategy widely used to enhance tumor accumulation and the treatment specificity.[54] However, the success of a targeted system is not straightforward, as many factors come into play. For instance, Moret *et al*. attached a folic acid moiety to the surface of the liposome containing *m*-THPC. *In vitro* results using A549, and KB cells showed a 2-fold enhanced uptake and phototoxicity in KB cells that express high levels of folate receptor

but not in A549 (negative to folate).[170] Recently, Liu *et al*. developed EGFR-Targeted EGa1 nanobody functionalized polymeric micelles loaded with *m*-THPC for the treatment of human epidermoid carcinoma A431. Phototoxicity experiments *in vitro* resulted in decrease of cellular viability to 20% upon 7 hours of incubation (18.6 μg/mL and 3.5 mW/cm^2) while no significant decrease of cell viability was observed for EGa-1 free formulation.[171] In summary, by taking advantage of the technological advances in drug delivery, significant improvements on PDT might be achieved. One promising approach relies on the use of hydrogel-based DDs, which will be discussed in the following sections.

1.4. Hydrogels

Three-dimensional (3D) polymer scaffolds with the ability to swell in aqueous media (known as hydrogels) are receiving increased interest by pharmaceutical engineering. The term hydrogel has its origin in the late 19th century and over the last decades they have been developed and widely used in many fields, including in drug delivery formulations.[172] The formation of hydrogel network requires the presence of at least three components: i) a monomer, ii) an initiator, and iii) a cross-linker. Initiator is defined as a source of chemical species that react with monomer to form an intermediate product capable to link with cross-linker or/ and other monomers and start polymerization process.[173] Cross-linkers that form the structure and prevent the hydrogels from dissolution can be attached to the polymer *via* physical or chemical interactions, which can be initiated by a variety of methods. Due to their porous structure, hydrogels retain water and swell in aqueous media. Moreover, polymer scaffolds protect the drug from degradation in a hostile environment, which impacts the pharmacokinetic profile and biodistribution of the drug.[174] Extensive research has led to the development of site-specific smart gels that can be tuned to respond to physiological fluctuations (thermoresponsive or pH-specific hydrogels)[175,176] or external stimuli, for instance ultrasound.

1.4.1. Historic development of hydrogels

The term 'hydrogel' was used for the first time in the late 19th century by Van Bemmelen for colloidal mixtures of inorganic salts forming a gel.[177,178] In the late 1940s, a hydrogel for human implants was the first hydrogel formulation entered in the market and was studied for several biomedical application including: skin replacement, or vascular prostheses.[179,180] The trade name "Ivalon" pertained to poly(vinyl alcohol) (PVA) cross-linked with formaldehyde.[181] A turning point for the development of hydrogels was achieved in 1960, when Wichterle and Lim reported a polymer system based on poly(2-hydroxyethyl methacrylate) (pHEMA). This material is in current use to manufacture soft contact lenses for eyes, representing the first successful marketed cross-linked material used in large scale in humans.[182] The polymeric network of pHEMA has similar characteristics of the modern-day hydrogels exhibiting swelling upon absorption of water without dissolution and retention of its shape.

First generation hydrogels (as the ones mentioned above) were established by chemical modifications and linking of monomeric and polymeric units using initiator molecules with the aim to develop a cross-linked material with good swelling ratios and mechanical properties which enhances their water retaining capacities.[183] Most polymeric networks utilized for the formation of hydrogels are of pHEMA, PVA, and PEG type.[184–186] This class found their application in ophthalmic and drug delivery applications.[187] These polymeric platforms were established by polymerization of water-soluble monomers using chain-addition reaction mechanisms.

Research on hydrogels for drug delivery has been focused on developing advanced DDS. These systems are based on the so-called smart hydrogels which respond to environmental changes such as temperature or pH, affecting the polymerization properties and the pore size of the hydrogels, thus potentiating drug-delivery activity.[172] For example, a pH-sensitive hydrogels are based on polymers that contain groups that either accept or release protons in response to changes in environmental pH. Polymers with a large number of ionizable groups are known as polyelectrolytes. pH-specific hydrogels display differences in swelling properties depending on the pH of the environment, which determines

kinetic of the drug release. Chitosan (CS) and *N*-(Hydroxypropyl)methyacrylamide (HPMA) are ones of commonly used polymers exhibiting pH-sensitive properties. For temperature-sensitive hydrogels, change of the solubility is induced by temperature changes that impact interaction between hydrophilic and hydrophobic segments in the polymer with water molecules, causing a sol-gel phase transition. Therefore, *in situ* hydrogel DDS has attracted attention in theremosensitive hydrogel drug delivery. In-situ hydrogel system can undergo phase change at the site of administration immediately after administration, making the solution or suspension transformed into a semi-solid or solid state.[188] Herein, *N*-Isopropylacrylamide is widely used thermosensitive polymer for biological applications due to its phase transition at 37°C.[189] Both, pH- and thermosensitive hydrogels found their use in cancer treatment. In the mid-1990s, physical interactions (*e.g.*, stereocomplexation, inclusion complex formation, metal–ligand coordination, and peptide interactions) were exploited to cross-link polymers (*e.g.*, poly(ethylene glycol)-poly(lactic acid), PEG-PLA cross-linked by cyclodextrin).[183] Such gel systems can be established by *in situ* cross-linking of the hydrogels, radical polymerization, formation of double-network hydrogels, by combination of natural and synthetic polymeric materials, or by forming composite hydrogels using small inorganic molecules. This provides platforms for biological applications such as controlled drug delivery to the target site, as potent PS carriers used in PDT.[190]

1.4.2. Classification of hydrogels

Hydrogels are broadly classified into different subtypes based on origin, durability, response to external stimuli, charges on the polymeric configurations, structural details, and composition of the polymers (**Figure 1.9**).[191]

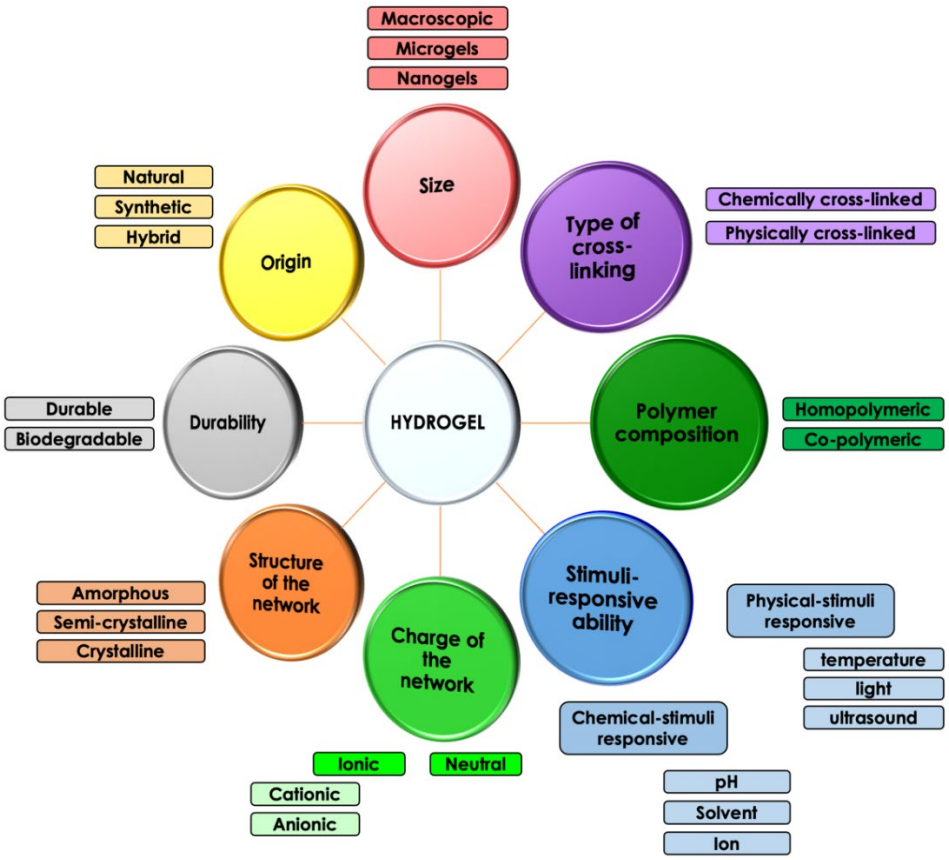

Figure 1.9. *Classification of hydrogels.*

1.4.2.1. Hydrogels based on origin

The polymeric material forming a hydrogel network can be originally derived from natural sources or can be synthetic or semi-synthetic. Naturally occurring systems are mainly based on polymeric materials such as agarose, alginates, gelatin, chitin, chitosan (CS), fibrin, hyaluronic (HA) acid or collagen.[192] Synthetic or man-made polymers, being more inert than the natural occurring polymeric materials, bear the advantage of longer shelf-life with a greater retention capacity. They can easily be modified to accommodate desirable properties for drug delivery (*e.g.*, cross-linking or encapsulation efficiency of the drug molecule).[193] Synthetic polymers, such as polyacrylamide (PAA) or PEG, provide better hydrogel-based platforms for the delivery of drugs or improvements in tissue engineering.

1.4.2.2. Hydrogels based on structure of the network

The durability of the hydrogel plays an important role in regulating the activity of the designed system. They have been sub-classified as durable (*e.g.*,

polyacrylate-based hydrogels suitable for potential applications in structural biomaterials and in biomedical engineering fields) and biodegradable (*e.g.*, polysaccharide-based, suitable for drug delivery applications) which further depend on their synthetic or natural origin.[194] Biodegradable systems have important uses in both biomedical and materials sciences. One advantage is their possible elimination from the body *via* a self-elimination degradation mechanism.[195]

1.4.2.3. Hydrogels based on structure of the network

Physical configurations of the polymers and the chemical composition of the subunits play an important role in determining the structure of hydrogel networks; thus, further classifications are amorphous, semi-crystalline and crystalline systems.[196]

1.4.2.4. Hydrogels based on charge of the network

Cross-linked polymeric networks might be neutral or carry electrical charges.[197] Nonionic or neutral hydrogels respond to change of external physical factors such as temperature, causing swelling and de-swelling, depending upon variation in the conditions. The linkages in these networks are irreversible. For ionic (anionic or cationic) hydrogels the amount of absorbed solvent depends on the electrostatic repulsions. For anionic cross-linked networks, the swelling of the network is enhanced at higher pH, due to an increase in electrostatic repulsion. For cationic networks, a lower pH enhances the swelling. Cross-linked networks carrying both acidic and basic monomers constitute an ampholytic hydrogel which activity is dependent on the ionic groups present in the polymeric chains. A hydrogel platform having both cationic and anionic monomeric groups, constitutes a zwitterionic system.

1.4.2.5. Hydrogels based on stimuli-responsive ability.

Physical or chemical stimuli might impact swelling or de-swelling of the networks. Physical stimuli are, for example, temperature, electric field, magnetic field, or light, while chemical stimuli typically include changes in the pH of the solvent systems, ionic strength, or solvent composition. This results in major changes in the network composition and their activity, both for smart and

conventional network platforms.[198] Examples of the stimuli responsive hydrogels used in the PDT field will be reviewed in **Chapter 3**.

1.4.2.6. Hydrogels based on polymer composition

Hydrogels can be classified as homo and co-polymeric structure. This depends on the number of polymer types involved in the formation of the hydrogel network. When a single species of a monomer is employed for the formation of the network, it forms a homo-polymeric hydrogel while use of two or more different monomeric units, either of which is hydrophilic, results in randomly or alternatingly arranged co-polymeric hydrogels.[199]

1.4.2.7. Hydrogels based on type of cross-linking.

When the polymeric structures are entangled *via* physical interactions such as, hydrogen or ionic bonds, or crystallization, physically cross-linked network, with relatively temporary and weak junctions are formed.[200] Examples of physically cross-linked hydrogels *via* hydrogen bonds are the ones based on PEG.[201] A hydrogel formed *via* ionic interaction can be achieved by incorporation of calcium ions at a certain pH with alginate derivatives.[202] Finally, crystallization was found to be a suitable method in the preparation of PVA-based hydrogels. In this case, repeated freeze-thaw cycles result in a tougher cross-linked network, with a higher crystalline nature of the gel as compared to the hydrogel obtained at room temperature conditions. The former confers enhanced mechanical strength and higher stability.[203]

Contrary to physically cross-linked hydrogels, chemically cross-linked ones yield permanently bonded networks.[204] Reactions of functional groups such as amine, carboxylic acid or aldehyde result in cross-linkage throughout the hydrogel network. For example, materials as chitosan and PVA are cross-linked using glutaraldehyde.[205,206] Chemical cross-linking is generally established by either addition reactions or condensation reactions of the cross-linkers with the polymeric hydrogel materials.[207] Alternatively, high-energy beams or gamma radiations can help to generate cross-linked hydrogels from unsaturated molecules.[208] Finally, free-radical polymerization involves an initiator and a monomer. The initiator molecules are converted to free radicals, which react with monomers by electron transfer.[209]

1.4.2.8. Hydrogels based on the size

Hydrogels can be classified based on their size into three groups: macroscopic hydrogels, microgels and nanogels.[210] The size of macroscopic hydrogels typically is in the range of millimeters to centimeters. Therefore, the route of administration usually requires local delivery *via* implantation.[211] Alternatively, if the gel exhibits suitable rheological properties, namely self-healing ability, this it can allow for local injections at the desired site – *e.g.*, transdermally or intratumorally. Local delivery of the formulation allows concentrating the drug release at the target site. Macroscopic hydrogels found broad application mainly in the field of tissue engineering as wound dressings.[212,213] Nevertheless, the intratumoral administration is gaining increasing attention in oncology due to the reduced systemic side effects.[214] Microgels and nanogels are hydrogels with dimensions on the order of micrometers and nanometers, respectively. These formulations are adequate for injection, even intravenous administration in the case of nanogels.[215] The size of nano and microgels can be controlled through the gelation conditions or the fabrication parameters (*e.g.*, nozzle size, flow rate).[216]

1.4.3. Hydrogels for drug delivery

Conventional drug formulations face a backlash due to their inefficiency to deliver drugs adequately to the site of action at a predetermined rate and over a predefined period. To mediate such temporal modulations, controlled site-specific targeting delivery platforms are required.[217] Hydrogels have been extensively investigated as effective, 'smart', and 'on-demand' DDSs.[218] They found their application in many branches of medicine, including oncology, wound healing and pain management (**Figure 1.10**).[210] This is especially important for hydrophobic drugs that aggregate and become non-active in an aqueous environment. Additionally, hydrogels protect the incorporated or conjugated molecule from enzymes of the surrounding microenvironment and physiological pH fluctuations in the body.[174] Moreover, the mechanical properties can be tuned allowing to obtain injectable hydrogels that are biocompatible with tissues. Depending on the type of hydrogel and route of administration, modulation of pharmacokinetics and biodistribution might also be achieved.

Oral, *I.V.*, intramuscular, or topical are the main routes of traditional drug administration, whereby the maximum dosage of the drug decreases rapidly with time.[219–221] However, hydrogels can be designed as "smart" drug carriers where there is an on-demand drug delivery over time. Controlled and site-specific drug release allows for a safer and higher bioavailability which might enhance therapeutic effects while reducing side-effects. This might be achieved by means of stimuli responsive hydrogels that are locally administered. This plays an important role in the field of oncology, where targeted and on demand delivery allows to reduce side effects related with the application of cytotoxic drugs.

The kinetics of drug release of pH-sensitive hydrogels are controlled by the degree of conformational changes, namely swelling capacity. For example, cationic hydrogels release the drug when swell at low pH and found their applications while anionic hydrogels release the drug at higher pH values. Therefore, anionic hydrogels are suitable for controlled intracellular drug delivery in tumor cells, and oppositely cationic ones at the extracellular matrix in tumor tissues.[222]

For instance, Paclitaxel (PTX)-loaded pH responsive hydrogel based on self-assembled FER-8 peptides was studied towards H22 tumor-bearing mice. The study performed by Raza *et al*. allowed for prolonged (96 h) and controlled release of PTX after intratumoral injection and increased antitumor efficacy compared to free PTX (2-fold lower tumor weight and volume for the hydrogel treated group) and lower toxicity (lower weight loss for hydrogel treated group).[223] In another study Zhao *et al*. tested locally applied amphiphilic copolymer hydrogel containing doxorubicin (DOX) and PTX. *In vitro* drug release study exhibited accelerated drug release for seven executive days in slightly acidic conditions (pH = 6.8). Next, hydrogel was injected intratumorally into subcutaneous melanoma tumor bearing mice. Combination therapy with DOX and PTX showed prolonged survival time compared with single drug administration and stronger inhibition (3-fold) of tumor growth.[224] Furthermore, an injectable, pH-sensitive L-alanine based hydrogel with covalently attached DOX showed promising anticancer activity in mice models towards CT26 and 4T1 tumors. Gel without DOX and intravenous injection of 'free' DOX were employed as control groups. For CT26 tumor model a 20% reduction of the

tumor volume and a 60% decrease in the tumor weight was observed for the DOX-Gel treatment as compared both control groups. In comparison, for 4T1 tumor animal model, a 4-fold and 2-fold reduction in tumor weight by DOX-Gel as compared to control and free DOX was observed, respectively.[225]

In summary, injectable and environment-sensitive properties of hydrogels make them excellent platforms for localized drug delivery applications. Given that the systemic administration of chemotherapeutic drugs is limited by toxicity, hydrogels provide a solution to avoid off-target drug delivery for cancer treatment.[226]

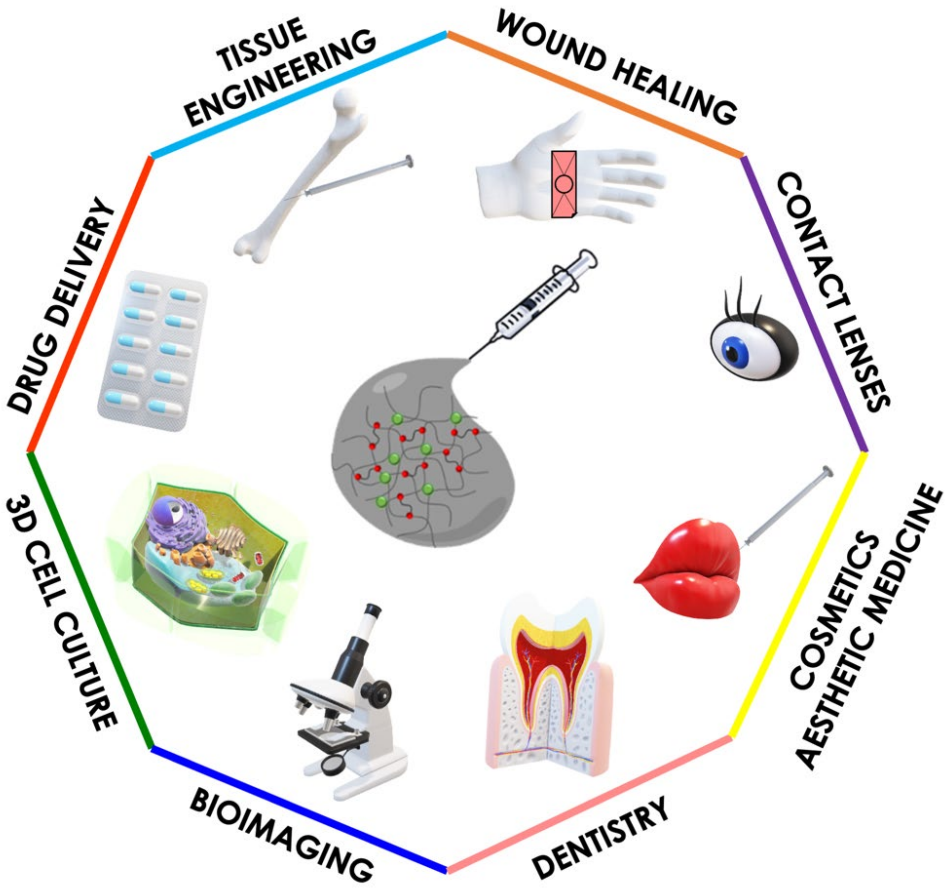

Figure 1.10. *Biomedical applications of hydrogels.*

1.4.4. Hydrogel-based drug delivery with application in PDT

Hydrogels constitute a potential platform for the delivery of various drugs, including PSs.[227] This requires incorporation of the PS into the hydrogel network and its local administration to the target tumor.

Controlled release of the PS might be achievable by designing hydrogels responsive to external stimulus (*e.g.*, light) or by taking advantage of the intrinsic properties of the tumor microenvironment (*e.g.*, acidic pH). The use of these "smart" hydrogel-based platforms provides several advantages such as the delivery of poor-water soluble PSs without further issues related to aggregation.

One Ps that can benefit for this technology is *m*-THPC which display poor water-solubility. The first *m*-THPC hydrogel formulation was reported in 2007 by Kopelman's group.[228] They prepared PAA particles using acrylamide monomer and *N*,*N*-methylenebis(acrylamide) as cross-linker. Polymerization was initiated with ammonium persulfate and *N*,*N*,*N*,*N*'-tetramethylethylenediamine in the presence of *m*-THPC to yield 2-3 nm sized nanoparticles. Aggregation of the PS was minimized with no significant leaching of the dye and the phototoxicities of free and hydrogel-bound *m*-THPC were comparable, although in the latter case, the PS was not internalized into the cell. Carbomer-based hydrogel containing *m*-THPC loaded into liposomes have also been investigated in detail. Various compositions of the hydrogels were tested showing that the elasticity of the gels correlated inversely with the PS concentration. Gels containing 0.75% weight/weight, carbomer (gelling agent) and lecithin (liposome stabilizing component) were considered to possess optimal rheological properties to deliver high amounts of *m*-THPC to the subcutaneous and deeper skin layers.[229] In a follow-up study such materials were found to be stable at 4 and 23 °C for over six months storage.[230]

In the context of PDT, most of the developed hydrogels are intended for local administration followed by sustained released of the PS, which might allow one to perform multi-illumination procedures. For instance, Zhu *et al*. developed an injectable nanozyme hydrogel as delivery platform of Prussian blue (PB) nanoparticles and an aggregation-induced emission luminogen (CQu) in agarose hydrogels. PB can drive the degradation of agarose hydrogel and decomposition of endogenous hydrogen peroxide end generate $^1O_2$. Considering that hydrogels can persist within tumors for a minimum of 48 h, they can facilitate multiple rounds of treatment following a single injection. Activity of the formulation was assessed towards 4T1 breast tumor bearing mice applying light irradiations at 0, 24 and 48 h post intatumoral injection of hydrogel. Results allowed for complete

inhibition of tumor growth for the mice irradiated with NIR and wight light which confirms integration of the benefits of PDT and photothermal therapy (PTT) to achieve better therapeutic outcomes.[231]

Enzymatic-responsive hydrogels, with synergistic photodynamic and chemotherapeutic mechanisms of action exhibiting enhanced activity, were recently reported for head and neck cancer. Indocyanine green (ICG) and DOX were incorporated in HA-acrylate-based hydrogels, which were further conjugated to matrix metalloproteinase (MMP).[232] Mice bearing SCC-15 tumors submitted to intratumoral injection of the developed multifunctional hydrogel exhibited strong tumor regression that was significantly higher than the one attained with hydrogels containing only ICG or DOX. However, the real contribution of MMP targeting is difficult to assess, as MPP free hydrogels were not tested.

An injectable thermosensitive hydrogel containing upconversion particles in the network was tested towards subcutaneously established 4T1 tumors. To enhance the tumor targeting efficacy, HA was modified on the surface of the scaffold. This thermosensitive hydrogel is formed in situ upon injection into the tumor site. The photodynamic activity was triggered upon near infrared (980 nm) irradiation. After 12 d of treatment, the tumor mass was significantly reduced and no side effects in normal tissues were observed. Significant inhibition of tumor growth was observed, resulting in the decrease of tumor volume of 50% in the first 12 days post-treatment, when continuous tumor growth was observed for the control group. Moreover, the strongest inhibition was observed for the ligand-targeted formulation.[233]

Another hydrogel for local-PDT treatment was studied by Loe *et al*. Pluronic-based hydrogel with encapsulated pyropheophorbide a (PPa) containing micelles and two-photon absorbing dye (imidazole derivative) was injected intratumorally. Such approach allowed for prolonged release of the PS at the tumor site. The signal of the PS was observed for 14 days post hydrogel injection, while signal of the PS was detected only during first four days of the study. Formulation allowed for tumor growth inhibition rate of 67.3% and 2 fold-stronger inhibition of tumor volume in comparison with free PPa polymeric micelles.[234]

Hydrogels of small size particles can penetrate across the target tissue allowing a more homogenous distribution. When the target disease is a solid tumor, hydrogel formulations in the nanoscale, can take advantage of the enhanced permeability and retention (EPR) effect (leaky tumor vasculature), which facilitates the diffusion of the PSs and their retention within the tumor tissue.[235] Only a few examples of hydrogel-based nanoparticles with proper features for systemic administration have been published. For instance, Hah *et al*. prepared PAA-based hydrogel conjugated to MB as the PS, and PEG chains aimed at prolonged NPs circulation in plasma.[236] The surface of the hydrogel was further decorated with the F3 peptide, which can selectively target tumor vasculature and cancer cells. Phototoxicity experiments carried out on MDA-MB-435 cells resulted in 90% cell death for the F3-targeted formulation, while the non-targeted particles only reached about 30% cell death.

1.4.5. Chitosan-based hydrogels

1.4.5.1. Properties of chitosan

The composition of the hydrogel is of the utmost importance as it impacts the chemical and biological properties of a certain formulation. A variety of polymers, of natural, semi-synthetic and synthetic nature, have been used. Natural polymers are known for their high biocompatibility. Among them, chitin, more precisely its derivative - chitosan - has been wide used for different biomedical application including drug delivery. Chitin, poly(β-(1→4)-N-acetyl-d-glucosamine), is a natural polysaccharide discovered in 1811 by Henri Braconnot and is the second most abundant natural polymer after cellulose.[237] Chitin has many sources in nature, among others it is a component of the exoskeleton of arthropods, but is also produced by plants.[238] Currently, the main sources of chitin are shells of shrimps and crabs.[239] Applications of chitin are limited by its highly hydrophobic, inelastic properties and insoluble in the majority of organic and inorganic solvents.[240]

N-deacetylation of chitin in the presence of acids and hot alkali ends in CS.[241] The degree of *N*-deacetylation often ranges from 40 to 95% and is a decisive factor of the properties of the final CS. Solubilization of this linear polysaccharide, CS, occurs by protonation of the amine group of the *d*-glucosamine unit, which leads to a formation of a polyelectrolyte in acidic media

and allows its use as a viscous solution, gel or polymeric film.[242] CS is soluble in dilute acidic solutions below pH 6.0 due to the quaternization of the amines. However, the solubility depends on many factors including the level of deacetylation, the ionic concentration, the pH, the nature of the acid used for protonation, and the distribution of acetyl groups along the chain.[243] Thus, solubility of CS may vary between different manufacturers. The viscosity of CS solution increases with its concentration and is inversely proportional to the temperature and level of deacetylation.[244]

CS has been widely used in drug delivery applications due to its biocompatible and biodegradable properties, together with its low toxicity.[245] Its enzymatic degradation mediated by lysozyme determines kinetic of the drug release from the polymer network. The later depends on many factors including molecular weight and degree of deacetylation.[246,247] It was found that CS with low level of deacetylation tends degrade rapidly, which can cause inflammatory response. In contrast, for highly deacetylated CS, this phenomenon is diminished due to slow degradation processes.[248]

CS is used in dietary applications and was approved by the FDA as a safe wound dressing material.[249,250] *In vivo* reports do not indicate significant toxicity.[251] Minor effects involve increase of lysosomal activity after *I.V.* injection.[252] Increased lysosomal activity results from lysozyme protease-involved degradation of CS. CS is degraded to oligosaccharides of variable length that can be further metabolized or excreted from the body.[244,253] Moreover, CS was found to impair tumor progression by stimulating macrophages and cytolytic T-lymphocytes.[254]

1.4.5.2. Chitosan for drug delivery

CS-based systems have been used for the delivery of different classes of pharmaceutical agents such as, chemotherapeutics, proteins, genes, antibiotics or even vaccines.[255–257] CS is being highly pursued for the preparation of hydrogels for sustained drug release. CS undergoes reactions typical for amines, mainly including *N*-acylation and Schiff reaction.[258] The multiple aliphatic amine and hydroxyl groups present in the CS chain can be used as synthetic handles for cross-linking during hydrogel formation. CS-based hydrogels easily

swollen which brings interested physical properties such as, variable consistencies and low interfacial tension with biological media. This contributes to reduce the immunological response of the body.[259] The swelling behavior can be tuned by adjusting the concentration of the CS solution and the amount of the cross-linker molecules. Moreover, protonation of the amine groups in the CS backbone, for instance at tumor acidic environment, can lead to the dissociation of the hydrogel structure with subsequent drug release.[258] CS-based drug delivery, such as hydrogels, are promising tools for oncological application, including in the field of PDT.[260]

Chitosan based hydrogel for local, intratumoral and controlled delivery of DOX was tested against CT26 tumors. Results of Liu *et al*. show that the formulation allowed for controlled release of the chemotherapeutic drug, reaching 80% release within 14 days. *In vivo* results proved advantage of the hydrogel formulation allowing to achieve the relative tumor growth inhibition of 74.99% in comparison with 50.30% and 0.05% calculated for intratumoral and *I.V*. injection of free DOX, respectively.[261]

Another example of CS-based hydrogel for local drug delivery was reported by Zhan *et al*. PEG-CS hydrogel allows for pH-specific release of the drug that occurs 5-fold faster at the pH = 5.6 in comparison with the pH of physiological conditions (7.4). Dox-loaded hydrogel was tested against human hepatocellular carcinoma tumors (HepG) established subcutaneously in the mice model. Dox-loaded hydrogels and pure hydrogels were injected subcutaneously in the tumor area, and the activity was compared with the PBS solution of DOX injected *I.V*. or at the tumor site. 2.3-fold smaller tumor size volume was observed on the 5th day post-treatment for DOX-hydrogel treated group in comparison with above mentioned control.[262]

The advantage of pH-responsive properties of CS hydrogels can be employed in the field of PDT. Herein, CS-based hydrogels are used for local delivery of PSs mostly *via* local, intratumoral injection. The above-mentioned benefits of localized and stimuli-responsive drug delivery were studied by Xia *et al*. *Meso*-tetrakis(1-methylpyridinium-4-yl)porphyrin (TMPyP), a water-soluble PS, was encapsulated into an injectable hydrogel composed of glycol chitosan and PEG derivative. These scaffolds allowed for efficient generation of

ROS, which was further confirmed in the animal study. Hydrogel was injected intratumorally in U14 tumor-bearing mice and 10 minutes later 532 nm light was applied. Obtained results indicate 5-fold stronger inhibition of the tumor growth in comparison with intratumorally injected PBS solution of free TMPyP.[263]

Belali *et al*. synthesized a folate-targeted and pH-sensitive CS -based hydrogel conjugated with 5,10,15,20-tetrakis(4-aminophenyl)porphyrin (NH_2-TPP).[223] With the highest tested concentration, about 80% MCF7 human breast cancer cell death was attained, which represented an increase of two times when compared with the non-targeted formulation (40% cancer cell death).[176]

Moreover, Azadikhah *et al*. developed antioxidant-photosensitizing hydrogel system. CS hydrogel was cross-linked using tannic acid, which also served as antioxidating agent. A water-soluble *N*,*N*′-di-(l-alanine)-3,4,9,10-perylene tetracarboxylic diimide (PDI-Ala) was used a PS. Hydrogel exhibited good $^1O_2$ generation efficacy and thus, its activity was tested in human melanoma cell line A375. Prior light irradiation, cells were co-incubated with hydrogels for 3 hours. Application of the formulation cause 60% cell death, while without light irradiation did not cause cytotoxicity at the same applied concentrations. In summary, phototoxic activity together with injectable properties of the formulation can serve as promising system for drug delivery *in vivo*.[264] Recently an extensive review summarizing CS-based DDS for PDT has been published by Calixto *et al*.[265] It can be concluded that the use of stimuli-responsive CS nanocarriers offers an opportunity for targeted drug delivery in the optimization of cancer therapy.

Chapter 2 Synthesis and characterization of tetrafunctionalized of *m*-THPC derivatives and evaluation of their linear and non-linear optical properties.

2.1. Introduction

Along the technological development of new laser systems and introduction of two-photon fluorescence microscopes to the market, the interest to introduce two-photon fluorescence techniques to the field of medicine, including PDT, has significantly increased. It grew demand to exploit new tools in order to allow for a better diagnosis and popularization of new therapeutic approaches.[266,84] This raises high expectations especially in the areas of neurology and ophthalmology where precise targeting and low level of invasiveness are highly desired. To this day, great progress has been made; however, a tremendous amount of work is still required to go beyond the stage of preclinical research and make two-photon-induced PDT a clinical procedure.[267]

One of the main obstacles of many available and extensively studied PSs is their absorption maximum in the UV-Visible region.[268] At these wavelengths the depth of light penetration into tissues is low, allowing for a cancer treatment very often just on the surface of the treated area. Moreover, UV region is harmful and mutagenic towards tissues.[269] This results in a poor therapeutic outcome, and side effects such as skin burn. For this reason, there is a constant impulse to develop molecules allowing for the excitation at the NIR region, increasing the clinical efficacy of PDT. The optical window for efficient tissue penetration covers the region from 800 to 1100 nm and is optimal to minimize absorption from endogenous chromophores and avoid light scattering by the surrounding microenvironment.[270] Excitation of molecules at these wavelengths can be achieved *via* rational design of molecules, leading to increased values of two-photon σ_2, and allowing their application for two-photon induced PDT.

Most of the clinically approved PSs do not allow for efficient excitation *via* TPA due to their low two-photon σ_2 values. This is impractical from the clinical point of view due to the risk of photodamage caused by high intensities of the applied laser light. Nevertheless, their photophysical properties can be tuned by change of axial ligand or peripheral substituents, leading to conformational distortion.[271] PSs used in two-photon excited (TPE) PDT offer the advantage of having the excitation maximum at the wavelengths twice longer in comparison with one-photon excited (OPE) processes. This allows for better penetration across tumor mass, allowing the cure of deep-seated tumors.[89] Nevertheless, design of chemically stable molecules meeting the requirements of both, high two photon $\sigma_2$values, where the triplet state energy is higher than the singlet energy level of the oxygen molecule, and maintaining the requirements of biosafety is still challenging.[28]

Chromophore can be excited *via* OPA or TPA processes. In TPA two, lower energy photons, but qual with the transition energy are concurrently absorbed (**Figure 2.1**). While in one-photon processes the rate of generation of the excited state exhibits a linear relationship with the light intensity, in two-photon processes the dependence is quadratic, thus requiring short and high energy laser pulses for the activation of the chromophore.[80]

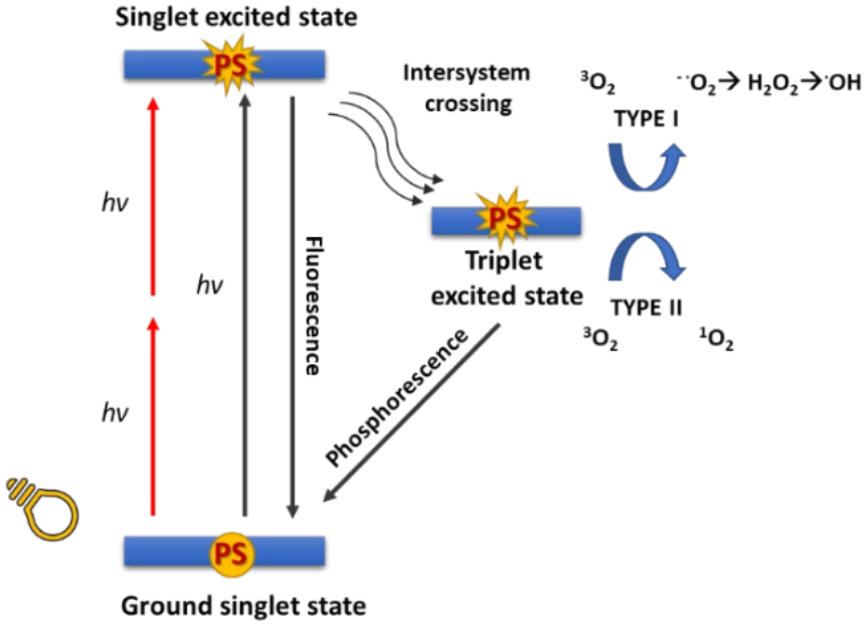

Figure 2.1*. Schematic representation of one-photon and two-photon (in red) excitation processes.*

To overcome listed limitations of conventional PDT and improve site-specific accumulation of the PS in the target area,[54] development of new DDS combine advances of TPA and nanotechnology. Therefore, TPA materials enhancing sensitization of encapsulated PS or increasing tumor targeting have been an object of pre-clinical research in recent years. Among them, hydrogels[227,234] or inorganic nanoparticles[272–275] opens promising possibilities for delivery of chromophores allowing for excitation at longer wavelengths and in consequences, improved therapeutic efficacy.

Several synthetic advances of the *m*-THPC structure which open the door for *m*-THPC to become a third generation PS have been reported.[163] This mainly involves bioconjugation of targeting moieties specifically recognized by cancer cells and/ or attachment or other molecules with additional therapeutic effects. Synthetic strategies were also successfully attempted by our group.[166,167,276,277] Rogers and co-workers previously expanded *m*-THPC structure by attaching bile acid – targeting motifs towards esophageal cancer cells.[166] Similarly, conjugation of non-steroid anti-inflammatory agents such as ibuprofen to the *m*-THPC core was introduced to reduce post-PDT inflammation involved in the tumor regrowth processes.[167] Finally, design of photocleavable *m*-THPC-conjugate systems or unsymmetrically substituted derivatives with potential use in non-linear optics has been successfully achieved.[277,278]

The desired properties of PSs for TPE PDT have been extensively reviewed in the literature.[98] One of the synthetic strategies to improve the TPA σ_2 values of a PS is the introduction of conjugated systems, donor or acceptor moieties and enhancement of molecular co-planarity.[279–281] The enhanced co-planarity leads to an improved delocalization of π-electrons of the conjugated system. Generally, large enhancements can be obtained by increasing the size of the π-electron system and the distance of a donor to an acceptor moiety.[282,283] Additionally, intramolecular charge transfer between the acceptor and donor motifs plays an important role to facilitate the enhancement of TPA σ_2 values. This can be quantified by the Δr index, which determines the distance of the intramolecular charge transfer.[284]

Over the last years, significant progress in application of two-photon induced PDT has been made allowing for improvement of conventional PDT modalities towards excitation of PSs at longer wavelengths. This permits a better therapeutic outcome of PDT-treated deep-seated tumors.[285,286] Tetrapyrroles, which include the families of porphyrins, chlorins and bacteriochlorins, extensively used in pre-clinical and clinical practice, were found a suitable target group to tune their photophysical properties.[85] Therefore, the potential use of *m*-THPC in TPE PDT has been reported. In a study performed by Hamed *et al.* excitation of *m*-THPC at 775 nm in DMSO was found to result in the magnitudes of 28 ± 8 GM.[287] Previously, Atif and co-workers, tested *m*-THPC as a potential TPE PDT molecule *in vitro* against epithelial cell line. They observed a significant decrease on the cell viability (>90%) when cells were treated with *m*-THPC followed by light irradiation with 800 nm laser (LD = 1.1×10^4 W m^{-2}). Importantly, light irradiation was found to not cause damage to cancer cells when being applied without PS.[288] In another study, methoxypolyethylene glycol derivative of *m*-THPC was studied against human colon carcinoma cells (HCT-116). Incubation of cells with *m*-THPC derivative was followed by laser irradiation at 784 nm (180 fs pulses, 400 mW for 900 s) and compared with single-photon laser excitation at 650 nm (LD = 10.8 J/cm^2). Although both approaches caused phototoxicity towards cancer cell, for two-photon PDT the anoxic energy transfer mechanism was found to be dominant mechanism responsible for cancer cell death.[289] Moreover, use of inorganic PSs such as ruthenium complexes was found to be suitable for TPA. They offer good properties for high energy irradiations due to their good stability and generation of long-lived excited triplet states.[290] Water-soluble ruthenium complexes reaching *ca.* 6800 GM at 750 nm have been recently developed by Karges *et al.* Published results showed a successful approach to treat resistant tumor *in vivo* upon clinically relevant two-photon (800 nm, 36 J/cm^2) and one-photon (500 nm, 36 J/cm^2) excitation without further signs of toxicity.[291] Measurement of tumor volumes 15 days post-treatment confirmed 2-fold stronger inhibition of tumor growth for TPE PDT treatment in comparison with OPE PDT. Nanotechnology is also being used to improve the efficacy of PSs namely by improving tumor selectively and tuning their photophysical properties (*e.g.* enhanced $^1O_2$ upon TPE). This topic has been reviewed in detail elsewhere.[90]

2.2. Objectives

Practical limitations of PDT with Foscan reflect in patient discomfort related with prolonged skin photosensitivity that causes skin burning and inflammation. Therefore, there is a constant need for a development of new pharmaceutical formulations that will allow to overcome these drawbacks and improve the quality of cancer patients. To address this, the first part of the current chapter will be focused on the development of reliable and cost-efficient synthetic procedures to access tetrafunctionalized *m*-THPC chromophores. Therefore, we aim to employ substitution,[292] esterification,[293] and Sonogashira coupling[294] reactions to append different functionalities at the periphery. Presence of aldehyde or carboxylic acid groups on the *m*-THPC skeleton is expected to provide suitable synthetic handle(s) for the design of DDS. Additionally, introduction of polar carboxylic acid groups aims to create the opportunity to improve poor-solubility of *m*-THPC in aqueous media. We expect that modification of the *m*-THPC periphery will allow to maintain the photophysical properties and biological activity of the *m*-THPC, while allow to improve optical properties suitable for TPA. Employment of the two-photon induced PDT for activation of tetrafunctionalized *m*-THPC derivatives **PS 1**, **3** and **5** is surmised to allow for their excitation at longer wavelengths and thus, allow for a better tissue penetration. The next part of this chapter will focus on evaluation of the linear optical properties of *m*-THPC derivatives, including a determination of their fluorescence quantum yield (Φ_F), fluorescence lifetime (τ) and singlet oxygen quantum yield (Φ_Δ). Finally, TPA σ_2 values will be determined in DMF using the TPE fluorescence technique. We aim those results obtained will confirm potential of tetrafunctionalized *m*-THPC derivatives **PS 1**, **3** and **5** for application in two-photon induced PDT.

2.3. Results and discussion

2.3.1. Synthesis and characterization of tetrafunctionalized *m*-THPC derivatives

With the goal to design novel DDS that overcome current limitations related with Foscan.[169] Simple *m*-THPC functionalizations were performed, expanding the *m*-THPC periphery, and providing aldehyde or carboxylic moieties – useful anchors in the design of novel platforms for drug delivery. Moreover, due to previously reported ability of *m*-THPC to perform TPE-PDT,[287] it was anticipated that the introduced modifications would have a positive impact on TPA σ_2 values, opening the door for potential application as TPE PDT dyes.

The first *m*-THPC derivative was synthesized following procedure previously described by Rogers and co-workers.[167] Hydroxyl groups of *m*-THPC were forced to react with carboxylic groups of 4-carboxybenzaldehyde *via* one-pot esterification reaction.[293] Therefore, to activate carboxylic acid groups of the 4-carboxybenzaldehyde, 1-ethyl-3-(3-dimethylaminopropyl)carbodiimide (EDC) hydrochloride and 1-hydroxy-7-azabenzotriazole (HOAt) were used. The advantage of using HOAt is related with its suppressive activity towards *N*-acylurea, a side product formed from EDC, being responsible to decrease reaction efficiency.[295] Moreover, these water-soluble components can be easily removed during the reaction workup. Derivative **PS 1** was formed in a 32% yield (**Scheme 2.1**).

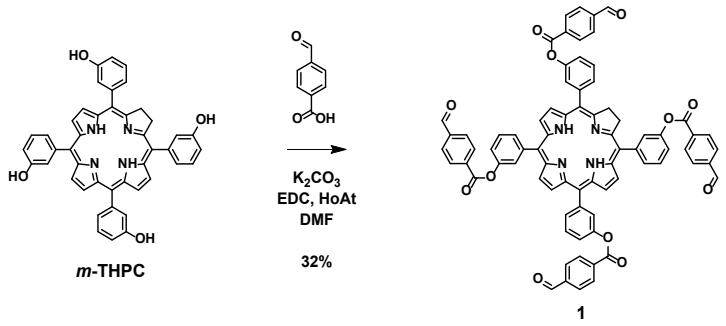

Scheme 2.1. *Synthesis of the derivative* ***PS 1***.

The second target, a *m*-THPC derivative containing carboxylic acid motifs, was synthesized employing a two-step protocol (**Scheme 2.2**). The first step involved a reaction of *m*-THPC with methyl bromoacetate in the presence

of potassium carbonate (K_2CO_3) which led to the formation of the derivative **2** in a 90% yield. Then, PS **2** was subjected to the basic hydrolysis using potassium hydroxide to access **PS 3** (85% yield).

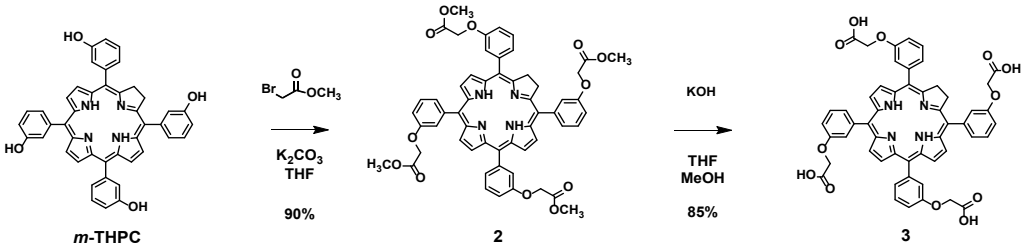

***Scheme 2.2**. Synthesis of **PS 3**.*

Finally, *m*-THPC derivative **PS 5** was synthesized in a two-step synthetic procedure. The first step included the reaction of *m*-THPC with propargyl bromide allowing for the nucleophilic substitution of the hydroxyl groups of *m*-THPC. By applying the conditions described by Rogers and co-workers the derivative PS **4** was synthesized in a 92% yield.[276] The second step was the reaction of propargyl groups with an aryl halide, 4-iodobenzaldeyde *via* Sonogashira coupling reaction. The coupling reaction was carried at 45°C in dry tetrahydrofuran (THF) in the presence of copper (CuI) and palladium (bis(triphenylphosphine)palladium(II) dichloride) ($Pd(PPh_3)_2Cl_2$) catalysts to access the desired product **5** in a 45% yield (**Scheme 2.3**).

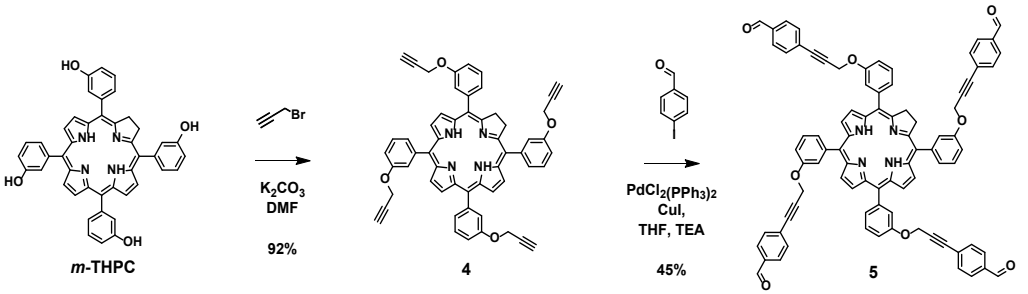

***Scheme 2.3.** Synthesis of the derivative **PS 5**.*

The *m*-THPC derivatives **PS 1**, **3** and **5** were characterized using H^1 and C^{13} NMR spectroscopy, MALDI-TOF mass spectrometry (MS), and UV/Vis and fluorescence spectroscopy. The NMR spectra in deuterated chloroform ($CDCl_3$) and deuterated dimethylsulphoxide (DMSO-d_6) and mass spectrometry (MS) data are included in the Appendix (**Figures A1-A19**).

The ^{1}H NMR spectra of compounds **1, 3** and **5** are consistent with the structure of *m*-THPC, which was originally evaluated in detail by Bonnett *et al.*[128] As presented on the NMR spectrum of **PS 1** (**Figure 2.2**), hydrogen atoms on the reduced pyrrole ring, characteristic for chlorins appear as a singlet at 4.15 – 4.25 ppm and the inner NH protons of the macrocycle appear as a singlet below -1.5 ppm. Moreover, the H^{1} NMR spectrum contains a signal at 10.12 ppm which is characteristic for the aldehyde motifs. However, the carboxylic signal of **3** recorded in DMSO-d_6 is not visible in the spectrum due to proton exchange with deuterium (**Figure A4**).[296] Moreover, the synthesis of the *m*-THPC derivatives and reaction intermediates was further confirmed by MS.

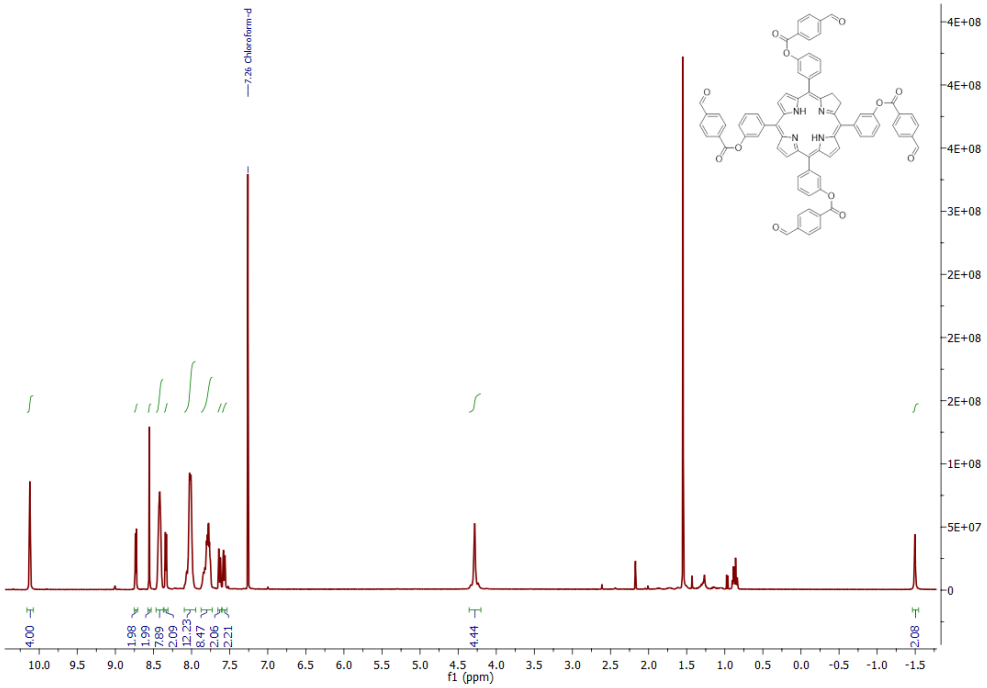

Figure 2.2. *H^{1} NMR spectrum of* ***PS 1*** *in $CDCl_3$.*

2.3.2. Absorption, excitation, and emission properties.

To compare the linear optical properties of *m*-THPC with the tetrafunctionalized derivatives, the absorption, excitation, and emission spectra were recorded. The obtained spectra have not shown significant changes in the absorption maxima of **PS 1**, **3** and **5** in comparison to those reported in the literature for *m*-THPC.[297] Moreover, Soret bands remained in the range from 420 to 422 nm, whereas the Q bands stayed in the range from 651 to 653 nm. As expected, the absorption and excitation spectra recorded for 650 nm wavelength overlap each other (**Figure 2.3, Figure A20-22**).

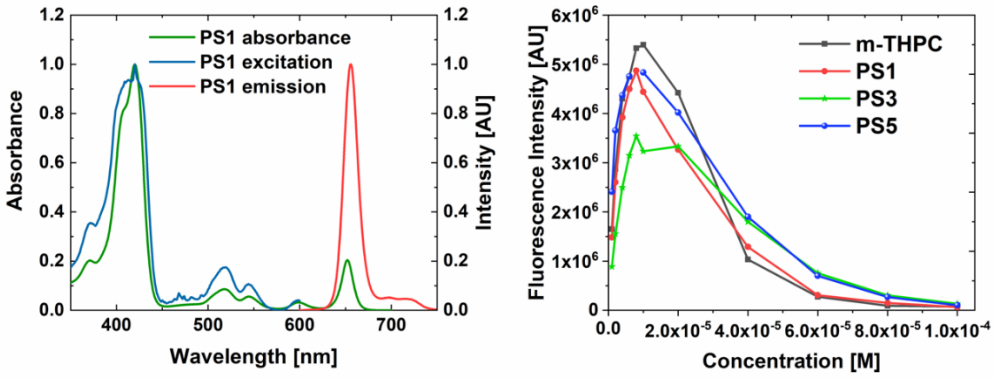

Figure 2.3. *Left: Normalized UV/Vis absorption spectra, excitation spectra (for 650 nm emission wavelength) and emission spectra (for the 420 nm excitation wavelength) of* ***PS 1*** *in air-saturated DMF at the concentration of 10^{-6} M. Right: Dependence of fluorescence intensity (at 650 nm) on concentration in DMF for m-THPC,* ***PS 1****,* ***3*** *and* ***5****.*

Furthermore, the red fluorescence spectrum of each PS was found to exhibit a sharp emission peak at 650 nm, with the full-width half-maximum values estimated to be *ca.* 18 nm, upon excitation in the wide wavelength range from in the near-ultraviolet and visible regions. However, the compounds differed in the emission efficiency. Recording 3D excitation – emission maps, we observed that the strongest red emission signal appeared upon excitation at 420 nm, which corresponds to the absorption maximum of the Soret band (**Figure 2.4**, **Figure A23**).

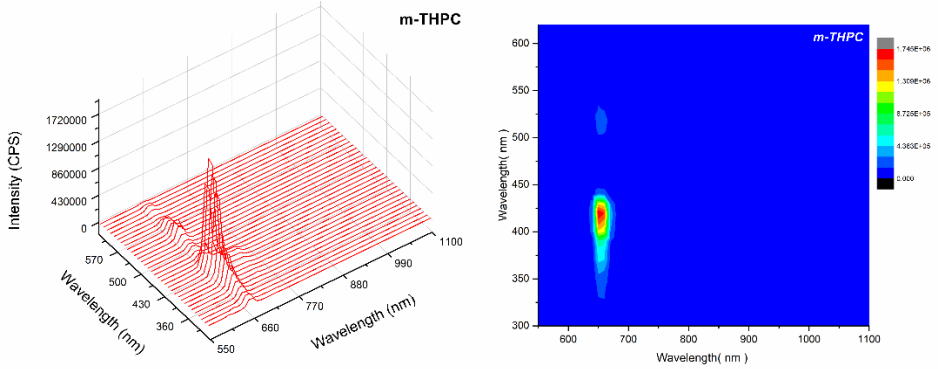

Figure 2.4. *One-photon excitation (350 – 600 nm) – emission (550 – 1100) spectra (left) and maps (right) of* ***PS 1****.*

Quenching of fluorescence was observed due to aggregation occurring with increasing concentration of the PS. This is a common phenomenon known for macrocycles and is caused when the interactions between the same molecules prevail in comparison with the interactions with a surrounding solvent.[298]

Bonnett *et al.* previously observed it for the *m*-THPC solution in methanol.[299] Importantly, aggregation of the PS is one of the factors reducing efficacy due to the decrease of $^1O_2$ generation and quenching of the emissive properties of the dye.[300] In our study we determined the optimal concentration of *m*-THPC and functionalized derivatives **1**, **3** and **5** in DMF. We noticed that the strongest fluorescence intensity signal for *m*-THPC was observed at the concentration of 10 μM, while for derivatives **1**, **3** and **5,** it was at 8 μM. Above these concentrations gradual decrease of fluorescence intensity was observed (**Figure 2.5**)

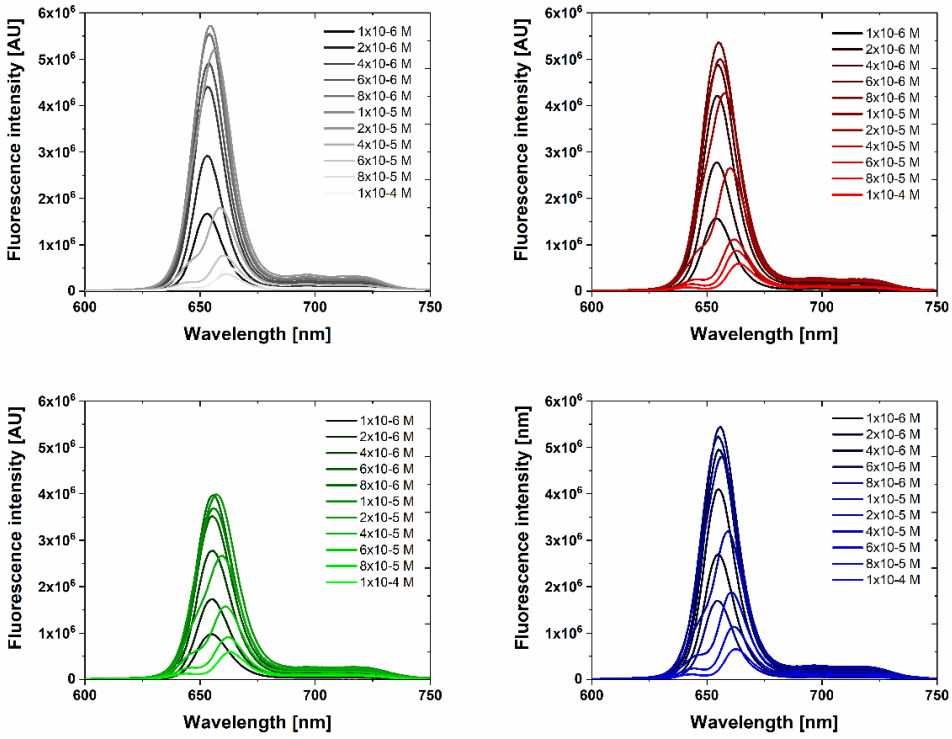

***Figure 2.5**. Fluorescence emission spectra of the **PS 1, 3, 5** and m-THPC in a range of concentrations from 10^{-6} to 10^{-4} M at an excitation wavelength 420 nm in DMF.*

Moreover, we observed red-shifting and broadening of the fluorescence band depending on the concentration of the PS. The fluorescence maximum, which for the non-aggregated form occurs at 652 nm, was shifted to 662 nm for *m*-THPC, 663 nm for **3,** and **5** and 664 nm for **1** when increasing the concentration to 100 μM. These spectral red-shifts arise from an aggregation processes and are typical for self-organization of organic dyes with dominating planar cores.[301]

2.3.3. Determination of molar absorption coefficient of derivatives

Determination of absorption coefficient of each derivative plays an important role in evaluating PS potency when applying light at specific wavelengths. The higher the values of molar absorption coefficient (**ε**) at the wavelength of irradiation, the lower light doses can be applied to excite the chromophore and in consequence, obtain a satisfactory therapeutic effect. Therefore, among all *m*-THPC derivatives, the **ε** values follow the trend *m*-THPC > **PS 1** > **PS 5** > **PS 3** (**Figure 2.6, Table 2.1**). Moreover, knowing the **ε** allows an accurate determination of the concentration of PS solutions, by applying the Lamber-Beer law.[302]

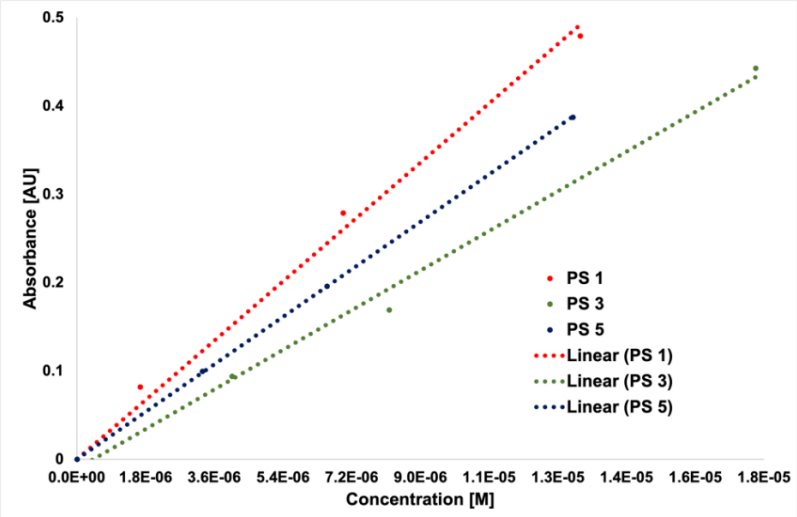

Figure 2.6. *Determination of the molar absorption coefficient of* ***PS 1****,* ***3*** *and* ***5*** *as a slope from the linear fitting of absorption as a function of the PS's concentration.*

Table 2.1. *Values of the molar absorption coefficient at 652 nm of m-THPC and* ***PS 1****,* ***3*** *and* ***5*** *in DMSO.*

PS	ε $_{\lambda 652}$ [L mol^{-1} cm^{-1}]
***m*-THPC**	39 800
PS 1	34 400 ± 1361
PS 3	25 970 ± 2348
PS 5	28 540 ± 81.93

2.3.4. Singlet oxygen quantum yield

Quantification of the singlet oxygen generation efficiency by PSs is one of the factors determining photodynamic activity of a certain molecule. Herein, we measured and compared the ability to generate singlet oxygen between *m*-THPC and its functionalized derivatives in two solvents, DMSO and DMF. The results gave no significant differences in the efficiencies of generation of $^1O_2$ between derivatives **1**, **3**, **5** and *m*-THPC. In DMSO, the highest quantum yield was obtained for the water-soluble derivative **3** resulting in 30.8%, followed by *m*-THPC, **PS 1** and **PS 5**, with 29.8%, 26.1% and 24.6%, respectively (**Table 2.2**). On the contrary, hydrophilic **PS 3** exhibited the lowest $^1O_2$ generation ability (64%) compared with other derivatives in DMF, reaching up to 76% for **PS 1**. These discrepancies were observed in both solvents and are related to different intensities of $^1O_2$ quenching in different solvents, an effect that is well described in the literature.[303–305] Nevertheless, we have proven that modifications of the *m*-THPC skeleton did not negatively affect the optical properties of the PS. The experimental values of Φ_Δ of *m*-THPC obtained in both solvents correspond with the literature data (68% in DMF and 40% in DMSO) whereas small discrepancies are in the range of experimental error.[306,307]

The value of the $^1O_2$ lifetime is determined by chemical and physical processes that remove $^1O_2$ from each system. In homogenous solutions the big impact on these processes has solvent quenching constant which depends on the properties of the solvent.[100] We calculated the average lifetime of $^1O_2$ in both DMSO and DMF and compared the obtained values with the literature data (**Figure 2.7**, **Table 2.2**). Calculated τ of 20 μs in DMF corresponds with the previously reported values of 18.9 and 14 μs.[308,309] An analogous situation was observed in DMSO, resulting in average lifetimes in the range of 6.9 – 9.6 μs, which corresponds with the literature value of 5.6 μs.[310,311] However, other reported values for DMSO are in a range up to 19 μs.[312] These discrepancies between $^1O_2$ lifetime were extensively discussed by Oelckers *et al.* and they might be caused by factors such as different measurement methods, apparatus sensitivity, solvent quality, temperature, or light source potency.[313] Nonetheless, the discrepancies of $^1O_2$ lifetime between *m*-THPC and tetrafunctionalized derivatives **PS 1**, **3** and **5** are in the range of available literature data.[308–312]

Table 2.2. *$^1O_2$ quantum yield (Φ_Δ) and $^1O_2$ lifetime data for m-THPC and tetrafunctionalized derivatives **PS 1**, **3** and **5** in DMSO and DMF. (Se=standard error).*

PS	Mean $^1O_2$ τ [s]	Se of mean	Φ_Δ (%)	Se of mean (%)
		DMSO		
***m*-THPC**	8.62E-06	2.16E-06	**29.8**	6.9
PS1	9.68E-06	7.64E-07	**26.1**	3.4
PS3	6.96E-06	4.31E-07	**30.8**	5.6
PS5	7.81E-06	1.50E-06	**24.6**	4.4
Rose Bengal	8.00E-06	1.58E-06	**16.0**	-
		DMF		
***m*-THPC**	1.91E-05	1.13E-06	**73.8**	3.7
PS1	2.04E-05	1.77E-06	**76.0**	2.4
PS3	2.02E-05	1.42E-06	**64.1**	4.6
PS5	2.03E-05	6.62E-07	**67.7**	4.6
Rose Bengal	2.05E-05	9.44E-07	**47.0**	-

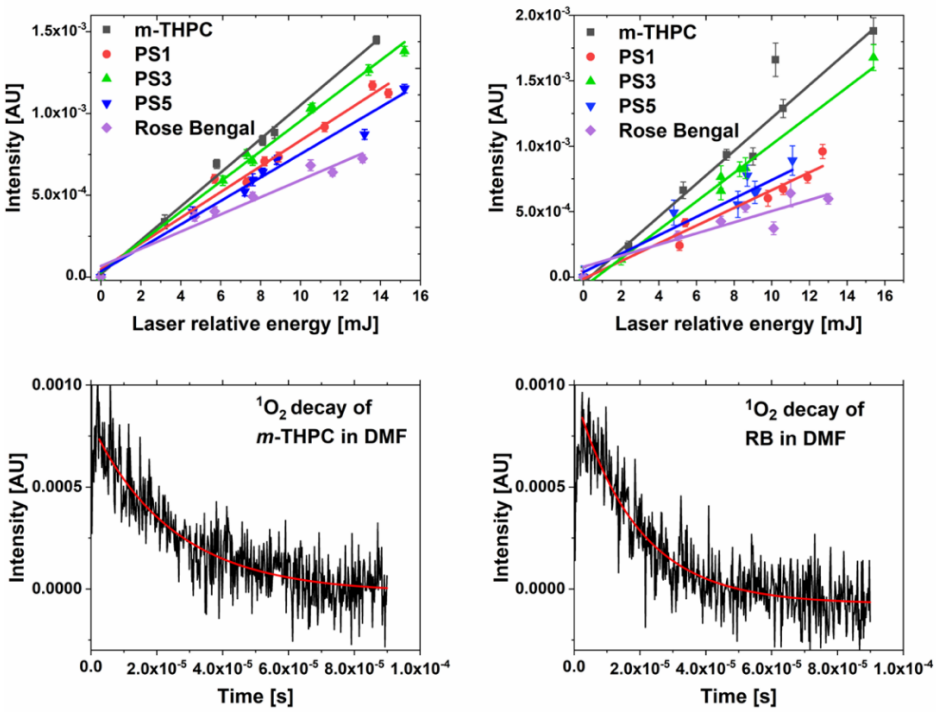

Figure 2.7. *$^1O_2$ phosphorescence intensities in DMF (top left) and DMSO (top right) as a function of the laser pulse energy. Representative $^1O_2$ phosphorescence decays of m-THPC (bottom left) and Rose Bengal (bottom right) recorded in DMF.*

2.3.5. Fluorescence quantum yields, fluorescence decay times and radiative and non-radiative constants

The absolute fluorescence quantum yields (Φ_F) measured in DMF were $\varphi_f \approx$ 44.7 %, 39.5 %, 38.1 % and 24.6 % for *m*-THPC, **PS 1**, **3**, and **5**, respectively. Fluorescence of *m*-THPC and its tetrafunctionalized derivatives was found to be enhanced in DMF in comparison with the data obtained in more polar solvents such as DMSO, or previously reported in ethanol (8.9%).[297] To our knowledge there is no Φ_F data of *m*-THPC reported in DMF. Although the difference between fluorescence intensity of *m*-THPC and derivatives **1** and **3** is not significant, a decrease of over 20% of the emission intensity can be observed for the **PS 5**. The decreased fluorescence intensity can be caused by the rigidity of the elongated substituents.

Although triple bond allows only for minimal conformational changes, the increased flexibility can be obtained by the bond between the methylene group and oxygen. This causes decrease of fluorescence and increase of contributions of non-radiative pathways that are often related to conformational

changes upon excitation. Nevertheless, these suggestions could be better explained with the support of quantum mechanics stimulations. Moreover, this is reflected in the increased value of the non-radiative constant k_{nr} (0.089) for **PS 5** in comparison with other derivatives (0.059 – 0.067).

The fluorescence decays of the *m*-THPC derivatives were recorded at 650 nm using time-correlated single-photon counting technique (TCSPC). Next, obtained decay curves were fitted using mono (*m*-THPC, **PS 1**, **PS 3**) or bi-exponential (**PS 5**) functions (**Figure 2.8**). Fluorescence τ values of *m*-THPC, **PS 1**, and **3** were found to be in the range from 9.2 to 9.3 ns (**Table 2.3**), while **PS 5** revealed two fluorescence τ components, denoted as T_1 and T_2, respectively. Although the T_2 component reaches a similar value to other derivatives (9.51 ns), the T_1 value was slightly lower (6.25 ns), and therefore, the as-calculated intensity-weighted average value was estimated to be 8.50 ns (**Table 2.4**).

The fluorescence τ depends on the intrinsic characteristics of the fluorophore itself and on the local environment. This plays a crucial role in the fluorescence τ imaging technique of the PSs using time resolved methods (*e.g.,* fluorescence τ imaging microscopy) and finds its application in biology (*e.g.*, for the evaluation of kinetic parameters of biological processes such as enzyme binding).[314] Collected data of Φ_F and long fluorescence τ allowed for a calculation of radiative (k_r) and non-radiative rate constants (**Table 2.3**). The ratio of k_{nr} to k_r indicates the predominance of non-radiative over radiative processes.

Table 2.3. *Fluorescence quantum yields (Φ_F), fluorescence decay times (τ) and radiative and non-radiative constants of m-THPC and tetrafunctionalized m-THPC derivatives **1**, **3** and **5**. (Se=standard error).*

PS	Φ_F (%)	Se of Φ_F (%)	Average τ (ns)	k_r (ns^{-1})	k_{nr} (ns^{-1})
***m*-THPC**	44.7	3.9	9.31	0.048	0.059
PS 1	39.5	1.4	9.26	0.043	0.065
PS 3	38.1	1.5	9.24	0.041	0.067
PS 5	24.6	1.5	8.50	0.029	0.089

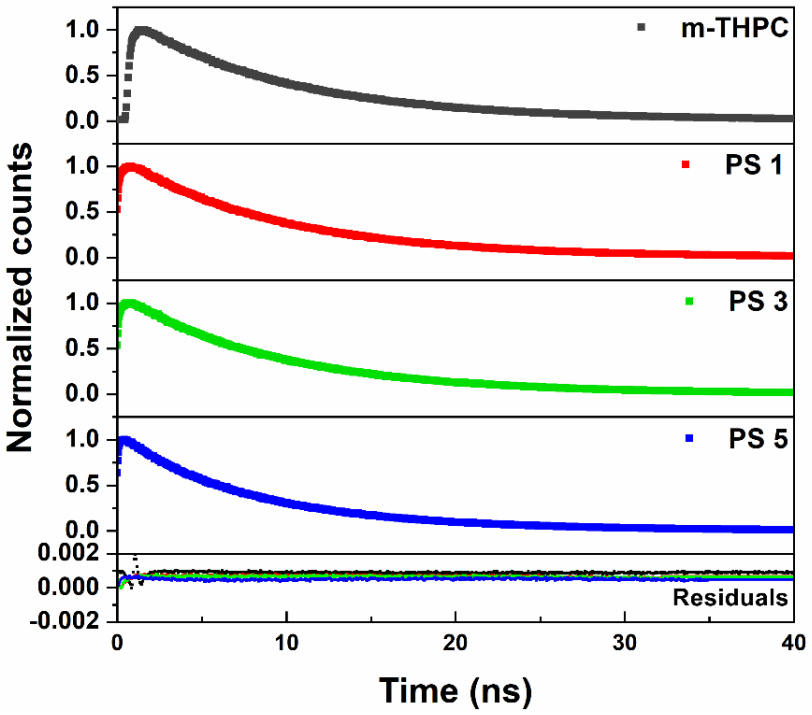

Figure 2.8. *Fluorescence decay of m-THPC and m-THPC derivatives **1**, **3** and **5**, after excitation at 377 nm in air-saturated DMF solution.*

Table 2.4. *Fluorescence τ parameters of* ***PS 5****: τ components (T_1 and T_2) and amplitude values (A_1 and A_2).*

PS	T_1 [ns]	A_1 [%]	T_2 [ns]	A_2 [%]	Average τ [ns]
PS 5	6.25	40.5	9.51	59.5	8.50

2.3.6. Nonlinear properties of *m*-THPC and *m*-THPC derivatives - Two-photon absorption and two-photon excited emission spectra

Power dependence measurements of emission intensities were performed ($\lambda_{exc.}$ = 840 nm) according to other studies.[315–317] The corresponding logarithmic plot of emission intensity *vs.* input power is shown in **Figure 2.9** with a slope value of 1.87 indicative of quadratic power relation. This indicates the fluorescence signal is proportional to the square of excitation light intensity, which confirms the TPA process.[318] Similar tendencies were previously noticed for *m*-THPC and its macromolecular modifications.[289,315] All *m*-THPC derivatives exhibited an intense emission upon femtosecond laser irradiation in the NIR region (**Figure 2.10** and **A24**).

Both, OPE and TPE emission spectra of *m*-THPC and tetrafunctionalized derivatives **1**, **3** and **5** in DMF exhibit a narrow emission profile in the red region ($\lambda_{max.}$ = 655 nm). To gain a better understanding of TPA properties of the derivatives, TPA σ_2 were estimated by TPEF measurements. σ_2 values were calculated using a commercially available dye LDS-698 in chloroform as a reference.[319] The most representative parameters at the TPA maxima are displayed in **Table 2.5.**

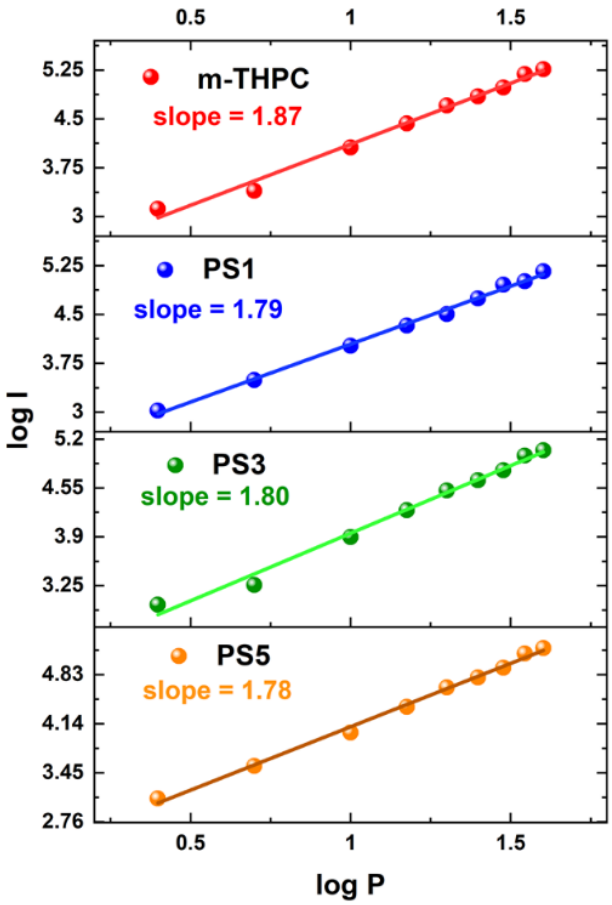

***Figure 2.9**. Power dependence relations of PSs in DMF excited at 880 nm.*

A good overlap of the Soret band (420 nm) with the major TPA peak (840 nm) was observed for *m*-THPC and derivatives **PS 1**, **3** and **5** (**Figure 2.11** and **A25)**. Considering that *m*-THPC and its derivatives exhibit a similar spectral behavior and a non-centrosymmetric design, it is then evidenced that OPA and TPA reach the same excited state. Noticeable red-shifting at the TPA spectra can correspond with the possible light reabsorption occurring during the OPA processes and is related with the different penetrating depth of the light beam.[320] Additionally, the compounds feature weaker TPA (~10-20 GM) in the longer wavelength region (>1000 nm) which are related to Q-bands from one-photon transitions.

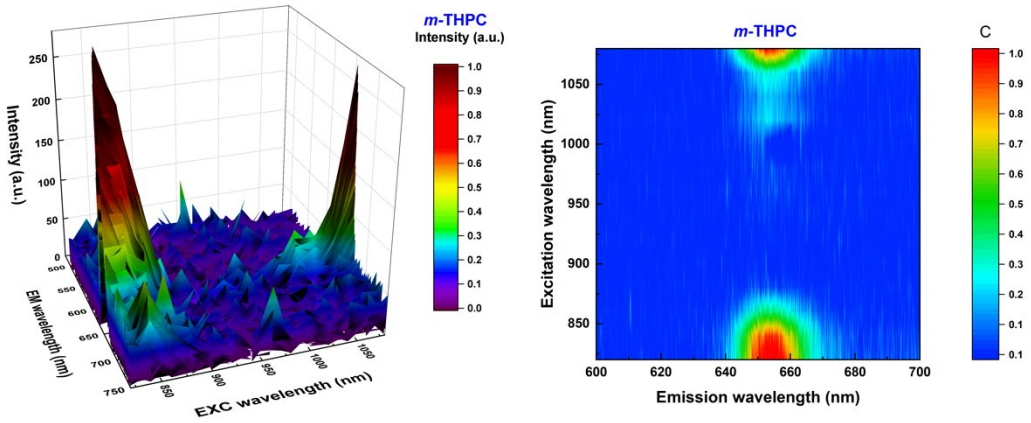

***Figure 2.10**. The TPE excitation-emission map of m-THPC in DMF. The relative molar concentration was adjusted so the corresponding absorbance value was kept below 0.1 in the emission region.*

Among all *m*-THPC derivatives, the TPA σ_2 values follow the trend **PS 5** > **PS 1** > **PS 3** > *m*-THPC (**Figure 2.12**, **Table 2.5**). It is well-known that extending the π-conjugation length of a molecule leads to an enhancement of the TPA σ_2.[272,321] This was observed with the change from carbonyl (**PS 1**) to alkyne linkers (**PS 5**). Considering the literature reports, direct meso-substitution of the functional groups to the porphyrin core has shown to have efficient enhancement of both the TPA σ_2 and brightness, despite hindering conjugation.[322] With electron accepting groups in the periphery of the molecules (**PS 1**, **PS 3**, and **PS 5**), in a donor-acceptor (D-A) motif, the extent of charge transfer from the center of the molecule is also increased.

***Table 2.5**. Non-linear optics parameters of m-THPC and derivatives in DMF ($\lambda_{exc.}$=840 nm).*

PS	σ_2 [GM]	Normalized σ_2 [GM/Da]	Brightness ($\phi \bullet \sigma_2$)
***m*-THPC**	26.7 ± 4.0	0.039	12.0
PS 1	32.7 ± 4.9	0.048	12.9
PS 3	30.0 ± 4.5	0.033	11.4
PS 5	69.3 ± 10.0	0.056	17.0

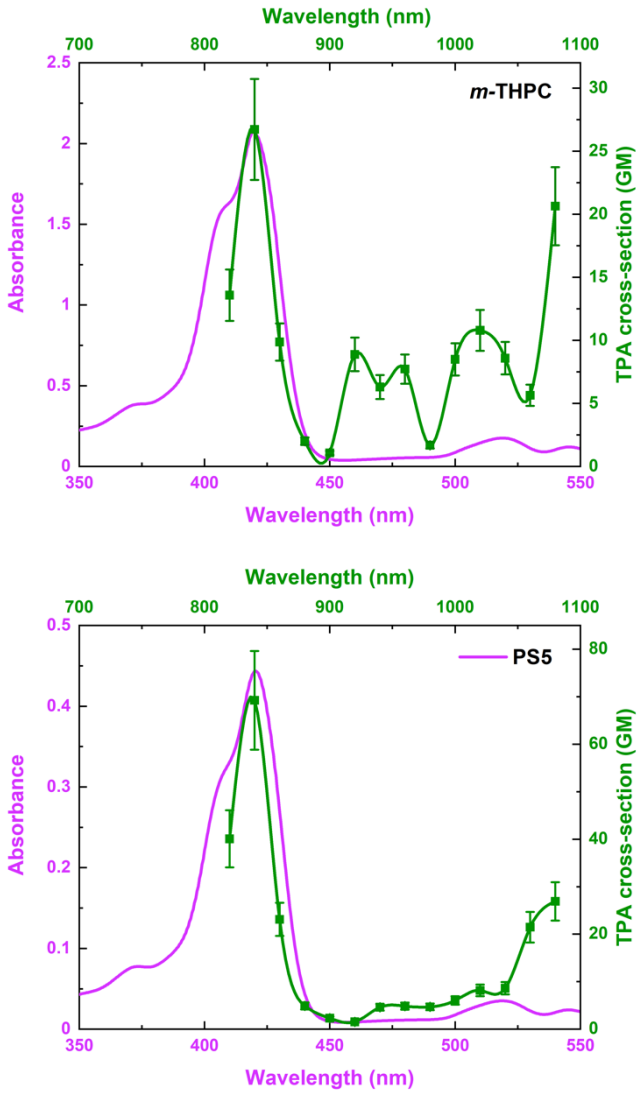

Figure 2.11. *OPA (pink) and TPA (green) spectra of m-THPC (top) and* ***PS 5*** *(bottom) in DMF. The relative molar concentrations were adjusted allowing the corresponding absorbance value being kept below 0.1 in the emission region.*

The observed difference in the TPA σ_2 is most likely due to the difference in the strengths of the electron-accepting end groups (ketone in **PS 1** and **PS 5** being more strongly electron-accepting than the carboxylic acid group in **PS 3**). It has been reported that the D-A architecture of **PS 1**, **3**, and **5**, leads not only to a significant enhancement of the TPA σ_2, but to increased brightness as well.[323] With these simple modifications we have managed to improve the TPA activity, indicating even a 2.6-fold enhancement at the TPA maximum of **PS 5** (69.3 ± 10.0 GM), compared to *m*-THPC (26.7 ± 4.0 GM). Varying molecular structures also induces different TPA peaks at the double wavelength of Q-bands regions (**Figure 2.12** and **A25**).

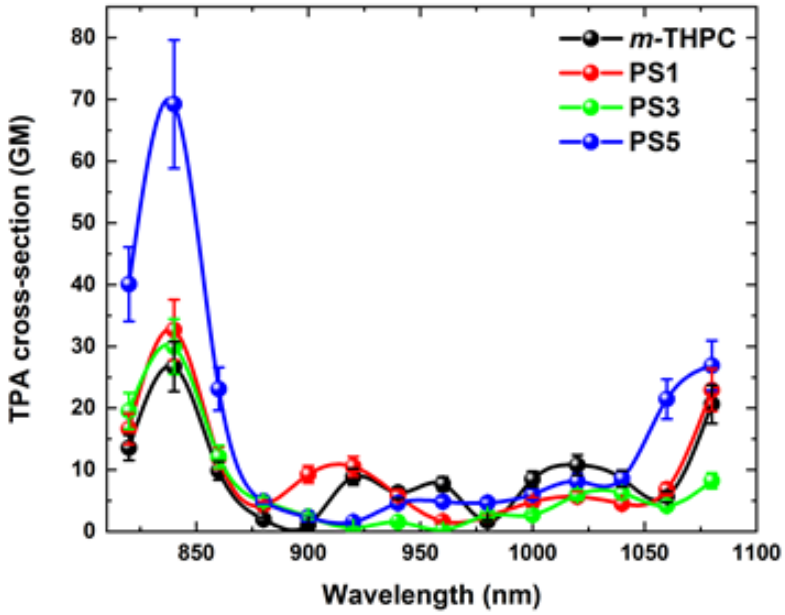

***Figure 2.12**. TPA spectra of all compounds in DMF. The relative molar concentration was adjusted allowing the corresponding absorbance value being kept below 0.1 in the emission region.*

Although *m*-THPC and its derivatives are known as fluorescent probes and superior PSs, their multiphoton-excited fluorescence and multiphoton absorption features have only found limited attention. Hamed *et al.* reported the TPA spectrum in the Q-band transition regime (1050-1450 nm) and around the Soret band using the open aperture Z-scan technique. TPA σ_2 of *m*-THPC in DMSO were measured to be around 20 GM at 1320 nm and 28 GM at 775 nm,[287] also showing similar spectral behavior in OPA and TPA spectra. Furthermore, TPE fluorescence at single excitation wavelength (800 nm) has been previously reported for *m*-THPC in a solvent mixture (20% ethanol, 30% polyethylene glycol, and 50% distilled water) to be 18 GM.[288]

2.3.7. Non-linear optical properties of PS 3 in aqueous solution

Intense fluorescence of the **PS 3** in the NIR region upon two-photon excitation, provides promising properties for TPE-fluorescence imaging in the range of the first biological optical window. Herein, introduction of the carboxylic acid groups to *meso*-phenyl ring of the **PS 3** confers water-solubility. Importantly, although no aggregation-induced fluorescence quenching was

observed, a significant shift of the fluorescence towards NIR region (~670 nm) in comparison with one recoded in DMF (~655 nm) was observed (**Figure 2.13**). Nevertheless, the existence of strong TPE red fluorescence at simulated physiological conditions reveals a great potential of **PS 3** in biomedical applications.

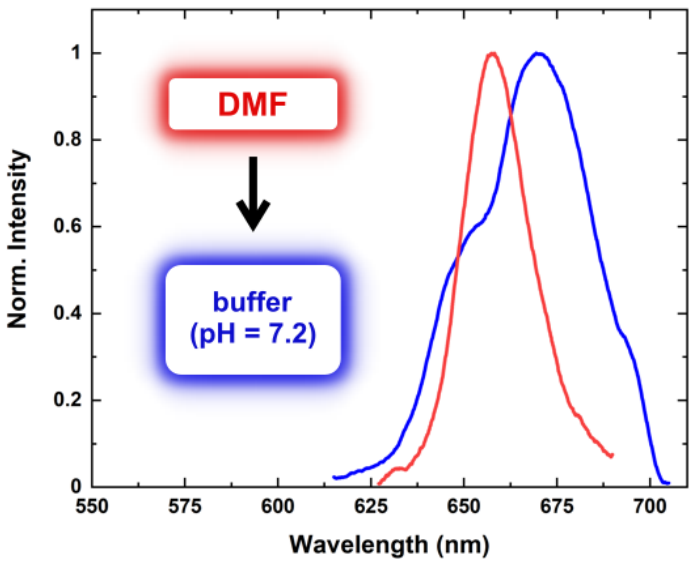

Figure 2.13. *Solvent dependent effect on TPE fluorescence spectra of* ***PS 3****.*

2.4. Conclusions and outlook

We reported convenient synthetic procedures to introduce aldehyde or carboxylic substituents into the skeleton of *m*-THPC and investigated the photophysical properties of the obtained *m*-THPC derivatives. Substitution, esterification and Sonogashira coupling reactions were used to display functional groups on the periphery of *m*-THPC. Employed synthetic strategies allow an efficient synthesis of **PS 1**, **3** and **5** derivatives with optimum reactions' yields. In addition, these strategies are expected to be feasible for a large-scale synthesis and might be used for other classes of PSs, opening the door for future design of libraries of chromophores meeting the requirements for two-photon induced PDT. The introduced aldehyde and carboxylic acid groups also create the opportunity for the development of more efficient drug delivery strategies.

Quantification of $^1O_2$ generation efficiency and fluorescence properties of derivatives demonstrated that **PS 1**, **3** and **5** derivatives have similar optical properties to the parent compound. This suggests that *m*-THPC derivatives will maintain the phototoxic activity and diagnostic properties of *m*-THPC under biological conditions, which gives us a promising outlook for further *in vitro* screening.

Next, the non-linear properties of *m*-THPC and derivatives were investigated using TPE fluorescence in DMF. Our results demonstrated increased TPA activities of *m*-THPC derivatives. This was further proven by determination of the two-photon σ_2. The best results were obtained with **PS 5** which shows a 2.6-fold enhancement at the TPA maximum when compared to *m*-THPC. However, **PS 3** appears as the most promising candidate for biological applications (PDT or *in vivo* imaging) considering its water solubility. In accordance, we recorded fluorescence emission at 670 nm of **PS 3** in phosphate buffer after two-photon excitation. Studies towards development of hydrogel-based DDSs are described in **Chapter 3**. In the next chapters we describe *in vitro* (**Chapter 4**) and *in vivo* (**Chapter 5**) screenings of *m*-THPC derivatives **PS 1**, **3** and **5** using two cancer cell lines.

2.5. Experimental

General information

Chemicals used for synthesis were purchased from *Merck*. Anhydrous solvents (DMF, THF) were purchased from commercial sources and used without further purification. Dry DMF and THF were purchased from *Acros Organics*. All air and/or water sensitive materials necessary for synthesis were handled using standard high vacuum procedures. Column chromatography was carried out using silica gel 60 (230-400 mesh; *Sigma-Aldrich*). Analytical thin-layer chromatography (TLC) was performed on precoated 60 F254 silica gel plates (0.2 mm thick; *Merck*). Melting points were measured using a Stuart SMP10 melting point apparatus. NMR spectra were recorded using Bruker AV 600, Bruker Advance III 400 MH or a Bruker DPX400 400 MHz or an Agilent 400 spectrometer. All NMR experiments were performed at room temperature. Mass spectrometry analysis (HRMS) was carried using Q-Tof Premier Waters MALDI quadrupole time-of-flight (Q-TOF) mass spectrometer connected with Z-spray electrospray ionization (ESI) and matrix assisted laser desorption ionization (MALDI) equipped in positive mode with trans-2-[3-(4-tert-butylphenyl)-2-methyl-2- propenylidene]malononitrile as the matrix. Absorption spectra were recorded using JASCO V-730 spectrophotometer. Emission/excitation spectra were measured using FluoroMax-4 spectrofluorometer (Horiba Jobin Yvon) and F-4500 Fluorescence Spectrophotometer (Hitachi). 10 mM phosphate buffer (pH = 7.2) was applied for PS3. Ultrapure distilled water (pH=7.0, Milli-Q) was used.

Synthesis of 5,10,15,20-Tetrakis[3-(4-formylbenzoate)phenyl]chlorin, 1

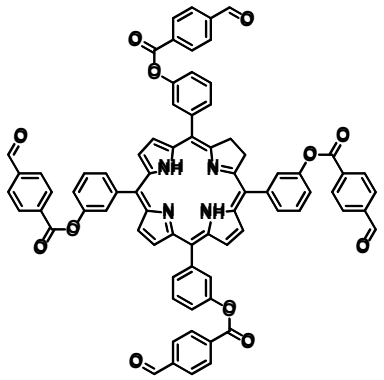

m-THPC (200 mg, 0.29 mmol.), K_2CO_3 (487 mg, 3.53 mmol.), HOAt (479 mg, 3.53 mmol.), EDC hydrochloride (676 mg, 3.53 mmol.), and 4-formylbenzoic acid (529 mg, 3.53 mmol) were added to a Schlenk flask. The reagents were stirred and dried under vacuum for 1 hour. Dry DMF (10 mL) was added to the flask and the reaction was stirred for 20 hours under argon. The reaction was monitored by TLC. When full conversion of the starting material was observed, the reaction was terminated by the addition of CH_2Cl_2 (50 mL). The reaction mixture was washed using distilled water (2×30 mL), $NaHCO_3$ (2×30 mL), NaCl (2×30 mL), and distilled water (2×30 mL). The organic phase was evaporated under reduced pressure. The product was purified on a silica gel column using CH_2Cl_2/n-hexane/methanol (3:1:0.1) as the eluent. The first purple band was collected and evaporated under reduced pressure and then recrystallized (CH_2Cl_2:hexane). The product was isolated as a purple solid (112 mg, 0.092 mmol, 32%). M.p. > 250 °C; R_f = 0.46 (SiO_2, CH_2Cl_2:hexane:methanol – 3:1:0.1); ^{1}H NMR (400 MHz, chloroform-*d*) δ = 10.12 (s, 4H, CHO), 8.73 (d, J = 4.9 Hz, 2H, Hβ), 8.56 (s, 2H, Hβ), 8.42 (d, J = 3.6 Hz, 8H, Ar-H), 8.34 (d, J = 4.9 Hz, 2H, Hβ), 8.10 – 7.95 (m, 12H, Ar-H), 7.79 (m, 8H, Ar-H), 7.63 (dd, J = 8.1, 1.6 Hz, 2H, Ar-H), 7.57 (dd, J = 8.1 Hz, 2H, Ar-H), 4.36 – 4.20 (s, 4H, Hβ), -1.50 (s, 2H, N-H) ppm; ^{13}C NMR (101 MHz, chloroform-*d*) δ = 191.4, 167.5, 164.3, 152.3, 150.4, 149.3, 144.3, 143.4, 140.5, 139.5, 135.0, 131.9, 130.7, 129.5, 127.8, 121.4, 111.3, 65.3, 42.0, 30.1, 29.1, 23.3, 23.1, 14.1, 11.1, 1.0 ppm; UV/Vis (chloroform): λ_{max} (log ε) = 421 (5.31), 519 (4.19), 547 (3.99), 601 (3.77), 654 nm (4.57); HRMS (MALDI) *m/z* calcd. for $C_{76}H_{48}N_4O_{12}$ $[M]^+$: 1208.3269, found 1208.3257.

Synthesis of 5,10,15,20-Tetrakis[3-(1-propan-2-one)phenyl]chlorin, 2

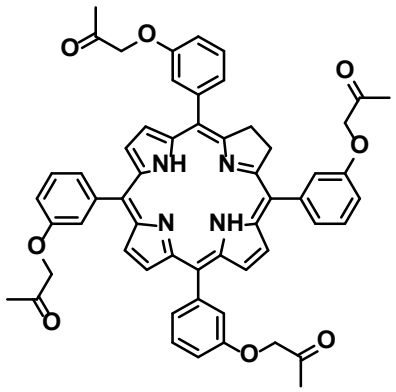

m-THPC (200 mg, 0.29 mmol.) and Cs_2CO_3 (449 mg, 2.94 mmol.) were weighted out and added to a Schlenk flask. The reagents were dried under vacuum for 1 hour. Dry DMF (10 mL) was added to the flask and the reaction was stirred for 15 minutes. Next, methyl bromoacetate (957 mg, 2.94 mmol.) was added and the reaction mixture was stirred for 20 hours at 45 °C under an argon atmosphere. The reaction was monitored by TLC. When full conversion of the starting material was observed, the reaction was terminated with the addition of CH_2Cl_2 (50 mL). The reaction mixture was washed using distilled water (2×30 mL), $NaHCO_3$ (2×30 mL), and NaCl (2×30 mL). The organic phase was evaporated under reduced pressure. The product was purified on silica gel column using CH_2Cl_2/n-hexane/methanol (3:1:0.1) as the eluent. The first purple band collected was evaporated under reduced pressure and recrystallized (CH_2Cl_2:hexane). The product was isolated as a purple solid (250 mg, 0.27 mmol, 90%). M.p.: >300 °C; R_f = 0.6 (SiO_2, CH_2Cl_2:hexane:methanol – 3:1:0.2); ^{1}H NMR (400 MHz, chloroform-*d*) δ = 8.59 (d, J = 4.9 Hz, 2H, H_β), 8.43 (s, 2H, H_β), 8.20 (d, J = 4.8 Hz, 2H, H_β), 7.75 (d, J = 7.6 Hz, 2H, Ar-H), 7.65 (s, 2H, Ar-H), 7.60 (q, J = 6.9 Hz, 4H, Ar-H), 7.51 (d, J = 7.4 Hz, 2H, Ar-H), 7.43 (s, 2H, Ar-H), 7.30 (dd, J = 8.4, 2.1 Hz, 2H, Ar-H), 7.23 (dd, J = 8.4 Hz, 2H, Ar-H), 4.79 (m, 8H, CH_2), 4.17 (s, 4H, H_β), 3.80 (s, 12H, CH_3), -1.51 (s, 2H, N-H) ppm; ^{13}C NMR (101 MHz, chloroform-*d*) δ = 169.3, 169.3, 167.1, 157.4, 156.2, 152.2, 144.3, 143.4, 140.4, 134.9, 131.9, 129.1, 128.0, 127.8, 127.6, 126.0, 123.4, 121.9, 120.1, 118.6, 114.3, 113.8, 111.7, 65.4, 63.7, 57.9, 52.2, 35.6 ppm; UV/Vis (chloroform): λ_{max} (log ε) = 420 (5.39), 519 (4.26), 547 (4.06), 600 (3.86), 654 nm (4.65); HRMS (MALDI) *m/z* calcd. for $C_{56}H_{48}N_4O_{12}$ $[M]^+$: 968.3269, found 968.3258.

Synthesis of 5,10,15,20-Tetrakis[3-(acetic acid)phenyl]chlorin, 3

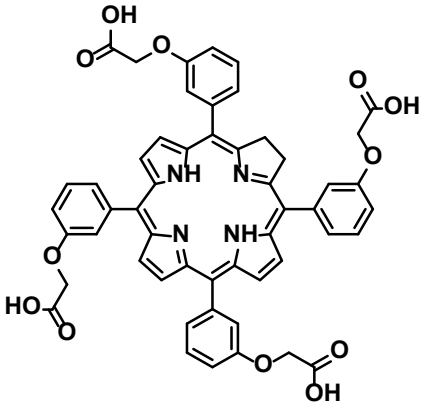

m-THPC derivative **2** (200 mg, 0.22 mmol.) was weighted out and added to a Schlenk flask. The reagents were dried under vacuum for 1 hour. THF (5 mL) and methanol (5 mL) were added to the flask and the reaction mixture was stirred for 15 min at room temperature. Next, KOH (148 mg, 2.63 mmol.) dissolved in distilled water (2 mL) was added to the flask and the reaction mixture was stirred overnight under reflux (80 °C). The reaction was monitored by TLC and, after full conversion, terminated. The solvent was evaporated, and distilled water (3 mL) was added to the reaction mixture. Next, the crude product was neutralized with an appropriate amount of 2 M HCl solution. The product was filtered using on a Büchner flask using and dried. The product was isolated as a purple solid (172 mg, 0.18 mmol, 85%). M.p. > 300 °C, ^{1}H NMR (400 MHz, dimethyl sulfoxide-d_6) δ = 8.62 (d, J = 4.7 Hz, 2H, Hβ), 8.36 (s, 2H, Hβ), 8.22 (d, J = 4.8 Hz, 2H, Hβ), 7.66 (d, J = 6.2 Hz, 4H, Ar-H), 7.63 (s, 2H, Ar-H), 7.47 (m, 4H, Ar-H), 7.32 (dd, J = 7.2 Hz, 2H, Ar-H), 7.25 (dd, J = 8.6 Hz, 2H), 4.84 (m, J = 11.0 Hz, 8H, CH_2), 4.16 (s, J = 29.3, 13.8 Hz, 4H, Hβ), -1.63 (s, 2H, N-H) ppm; ^{13}C NMR (101 MHz, methanol-d_4) δ = 171.5, 157.9, 156.9, 143.5, 142.4, 135.3, 128.8, 128.2, 127.7, 125.2, 123.9, 121.2, 120.7, 118.5, 114.2, 113.7, 113.0, 64.7, 38.9, 35.2 ppm; UV/Vis (methanol): λ_{max} (log ε) = 418 (5.18), 518 (4.10), 545 (3.92); 597 (3.77), 652 nm (4.44); HRMS (MALDI) *m/z* calcd. for $C_{52}H_{40}N_4O_{12}$ $[M]^+$: 912.2643, found 912.2650.

Synthesis of 5,10,15,20-Tetrakis[3-(prop-2-yn-1yloxy)phenyl]chlorin, **4**

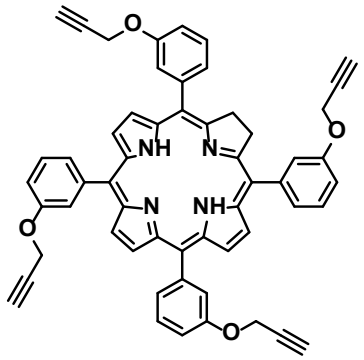

m-THPC (200 mg, 0.29 mmol.) and K_2CO_3 (406 mg, 2.94 mmol) added to a Schlenk flask. The reagents were dried under vacuum for 1 hour. Dry DMF (10 mL) was added to the flask and the reaction mixture was stirred for 15 minutes. Next, propargyl bromide (349 mg, 2.94 mmol.) was added and the reaction mixture was stirred for 20 hours under an argon atmosphere. The reaction was monitored by TLC. When full conversion of the starting material was observed, the reaction was terminated by the addition of CH_2Cl_2 (50 mL). The reaction mixture was washed using distilled water (2×30 mL), $NaHCO_3$ (2×30 mL), NaCl (2×30 mL) and distilled water (2×30mL). The organic phase was evaporated under reduced pressure. The product was purified on silica gel column using CH_2Cl_2/n-hexane/methanol (3:1:0.1) as the eluent. The first purple band collected was evaporated under reduced pressure and recrystallized (CH_2Cl_2:hexane). The product was isolated as a purple solid (225 mg, 0.27 mmol, 92%). ^{1}H NMR (400 MHz, chloroform-*d*) δ = 8.63 (d, J = 4.8 Hz, 2H, H_β), 8.47 (s, 2H, H_β), 8.24 (d, J = 4.9 Hz, 2H, H_β), 7.76 (m, 4H, Ar-H), 7.61 (m, 4H, Ar-H), 7.52 (m, 4H, Ar-H), 7.35 (dd, J = 8.3, 2.5 Hz, 2H, H_β), 7.29 (dd, J = 8.3, 2.5 Hz, 2H, H_β), 4.85 (m, 8H, CH_2), 4.27 – 4.11 (s, 4H, H_β), 2.57 (s, 4H, alkyne-*H*), -1.48 (s, 2H, N-H) ppm; HRMS (MALDI) *m/z* calc. for $C_{56}H_{40}N_4O_4$ $[M]^+$: 832.3050, found: 832.3040.

Synthesis of 5,10,15,20-Tetrakis[3'-(4''-ethynylbenzaldehyde)phenoxy]-chlorin, 5

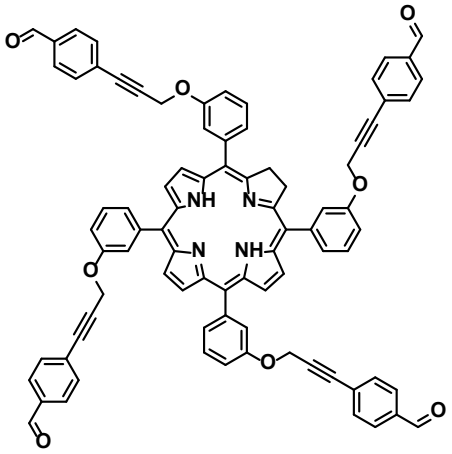

A Sonogashira coupling was performed under dry conditions. The *m*-THPC derivative **4** (100 mg, 0.12 mmol.) and 4-iodobenzaldehyde (278mg, 1.2 mmol) were weighted out and added to a Schlenk flask and dried for 1 hour under vacuum. Next, the compounds were dissolved in dry THF (6 mL) and TEA (3 mL) and stirred for 1 hour. Next, CuI (6.8 mg, 0.036 mmol) and $PdCl_2(PPh_3)_2$ (12 mg, 0.018 mmol) were added. The reaction was monitored by TLC. When full conversion of the starting material was observed, the reaction was terminated, filtered through celite and the crude product was purified on silica gel column (CH_2Cl_2:hexane:methanol – 3:1:0.1). Fraction of TEA (5 mL) was added to neutralize the silica and to reduce stacking of the compound. The first dark-red band collected was evaporated under reduced pressure and recrystallized. The product was isolated as a dark-red solid (67 mg, 0.053 mmol, 45%). M.p.: > 300°C; R_f = 0.7 (SiO_2, DCM:hexane:MeOH – 3:1:0.1); ^{1}H NMR (400 MHz, chloroform-*d*) δ = 10.08 – 9.88 (s, 4H, CHO), 8.56 (d, *J* = 4.8 Hz, 2H, Hβ), 8.41 (s, *J* = 3.3 Hz, 2H, Hβ), 8.16 (d, *J* = 3.9 Hz, 2H, Hβ), 7.93 – 7.78 (m, 4H, Ar-H), 7.71 (m, 8H, Ar-H), 7.67 – 7.61 (m, 4H, Ar-H), 7.60 – 7.51 (m, 4H, Ar-H), 7.50 (m, 8H, Ar-H), 7.41 (dd, *J* = 8.2, 1.9 Hz, 2H, Ar-H), 7.35 (dd, *J* = 8.2, 1.8 Hz, 2H, Ar-H), 5.09 (m, 8H, CH_2), 4.23 – 3.98 (s, 4H, Hβ), -1.49 (s, 2H, N-H) ppm, ^{13}C NMR (101 MHz, chloroform-*d*) δ = 191.4, 167.2, 157.0, 155.9, 143.2, 135.7, 132.4, 132.3, 129.4, 129.4, 129.2, 128.3, 127.8, 125.8, 123.5, 118.8, 87.9, 86.5, 56.5, 35.6 ppm; UV/Vis (chloroform): λ_{max} (log ε) = 423 (5.51), 521 (4.37), 548 (4.2), 600 (3.97), 654 nm (4.74); HRMS (MALDI) *m/z* calc. for $C_{84}H_{56}N_4O_8$ $[M]^+$: 1248.4098, found 1248.4124.

Determination of molar absorption coefficient of derivatives

Molar absorption coefficients (ε) at λ = 652 nm for *m*-THPC derivatives **PS 1**, **3** and **5** were determined. Three independent masses of **PS 1**, **3** and **5** were weighted, transformed to volumetric flasks, and dissolved in 1 mL of DMSO. Each mass of the compound was diluted 10, 20 or 40 times, maintaining the linear dependence between absorbance and concentration to fulfil the principle of the Lamber-Beer law, and the absorbance was recorded at 652 nm. The value of the absorption coefficient was determined as a slope obtained from the linear fitting of absorption as a function of the PS's concentration.

Fluorescence decay times and radiative and non-radiative constants

The photoluminescence decay profiles of *m*-THPC and tetrafunctionalized derivatives **PS 1**, **3** and **5** were measured through a conventional time correlated single-photon counting (TCSPC) setup, containing a BDL - 375 - SMN Picosecond Laser Diode (20 MHz, 377 nm), an Acton SpectraPro SP-2300 monochromator (Princeton Instruments), and a high-speed hybrid detector HPM-100-50 (Becker&Hickl GmbH) which was controlled by a DCC-100 card. The fluorescence τ values were calculated, after deconvolution procedure of the instrument response function (IRF).

Fluorescence quantum yields

The absolute fluorescence quantum yields Φ_F were determined using a FLS 980 Edinburgh Instruments spectrometer, equipped with an integrating sphere and a BDL-375-SMN Picosecond Laser Diode (20 MHz, 377 nm) as an excitation source. Compounds were dissolved in DMF to obtain 10 μM concentration, the sample in a 1 cm quartz cuvette was placed into the center of the integrating sphere. Absolute quantum yield was calculated based on the **equation 1**:

$$\Phi = \frac{E_b}{S_a - S_b} \qquad (Equation\ 1)$$

Where:

E_b – integrated fluorescence intensity of the PS sample (600-750 nm)
S_a – integrated excitation peak without presence of the PS (360-400 nm)
S_b – integrated excitation peak with presence of the PS (360-400 nm)

Singlet oxygen generation of PSs

The efficiency of singlet oxygen production was studied following the procedure previously described by Silva *et al.*[324] Briefly, $^1O_2$ phosphorescence was detected at 1270 nm at room temperature using a Hamamatsu R5509-42 photomultiplier (cooled with liquid nitrogen) after exciting the solutions of PSs using the second harmonic (532 nm) of a Nd:YAG pulsed laser (8 ns) Spectra-Physics model Quanta-Ray. In order to avoid scattered and fluorescence light Newport long pass filter 10LWF-1000-B were used before the photomultiplier. Solutions of *m*-THPC and tetrafunctionalized derivatives (**PS 1**, **3**, and **5**) were prepared in DMSO and DMF obtaining absorbance in a range of ~0.15-0.2 at 532 nm. Rose Bengal was used as a reference; the Φ_Δ for this dye is 0.47 and 0.16 in DMSO[325] and DMF[326], respectively. The $^1O_2$ phosphorescence decay was fitted using a monoexponential function. Pre-exponential factors I_0 were obtained selecting the same time interval for all compounds, then these intensities were plotted in function of the laser pulse energy. The Φ_Δ was determined using the slope, m_Δ, obtained from the linear fitting of I_0 *in* function of the laser pulse energy (**Equation. 2**). Two independent measurements were performed and the average Φ_Δ was calculated for *m*-THPC and tetrafunctionalized derivatives **PS 1**, **3** and **5**.

$$\Phi\Delta_x = \frac{(1-10^{-A_{ref}})}{(1-10^{-A_x})} * \frac{m_x}{m_{ref}} * \Phi_{ref} \qquad (Equation\ 2)$$

A_{ref} – absorbance of the reference at 532 nm.
A_x - absorbance of the compound *x* at 532 nm.
m_x – slope of the compound *x*
m_{ref} – slope of the reference
Φ_{ref} – Φ_Δ of the reference

Two-photon excited emission

TPE emission spectra were recorded on a custom-built experimental setup, consisting of a spectrometer (Shamrock 303i, Andor) equipped with an ultrasensitive camera (iDus camera, Andor). All samples were excited with Ti:Sapphire Chameleon laser (Coherent Inc.), operating from 800 nm to 1080 nm (the repetition rate 80 MHz and the pulse duration ≈120 fs). In order to minimize undesired re-absorption effects and aggregation processes, the relative molar concentrations were adjusted, so the corresponding absorbance values were kept below 0.1 in the emission region. Photostability of each compound was monitored throughout the experiments *via* absorption and OPE fluorescence measurements. All spectroscopic measurements were performed at room temperature.

Power-dependence measurements

TPE fluorescence spectra of *m*-THPC with the varying laser excitation power (from 2.5 mW to 40 mW) were recorded. The logarithmic emission intensity and laser power values were plotted and then, fitted with a linear function.

Two-photon absorption cross-section values

TPA cross-section values were calculated from the TPE emission measurements with the respect to **LDS 698** in chloroform,[327] following the **equation 3**:[328]

$$\sigma_{2PA,sam}[GM] = \sigma_{2PA,ref}\frac{I_{sam}C_{ref}\Phi_{ref}}{I_{ref}C_{sam}\Phi_{sam}} \qquad (Equation\ 3)$$

where *I* is the integrated emission intensity, *C* is the molar concentration, Φ is the OPE fluorescence quantum yield, and *n* is the refractive index of solvent (*sam* refers to sample and *ref* to reference). The normalized σ_2 values were estimated, following the **equation 4**, where M denotes the molecular weight of the compounds.

$$\sigma_{norm.2PA,sam}[GM/M] = \sigma_{2PA,sam}/M \qquad (Equation\ 4)$$

Brightness values were also determined as the products of TPA cross-sections and Φ_F.

3. Preparation and characterization of pH-responsive *m*-THPC chitosan hydrogels

3.1. Introduction

Although Foscan has been clinically approved for the palliative treatment of head and neck cancer, this formulation suffers from side effects such as skin photosensitivity.[329] Several nanosystems with improved properties allowing for exhibited high tumor selectivity and reduced toxicity in comparison to Foscan failed in the preclinical phase of trials.[169] This is often due to insufficient drug release of the PS in the target site and related poor penetration into tissue. Therefore, constant improvements of DDSs allowing not only for selective tumor targeting but also for controlled drug release at the tumor site is desirable. One strategy to improve the solubility of PSs is their encapsulation/formulation into nanocarriers such as: lipid-based or polymeric-based NPs, colloids, dendrimers, carbon nanotubes, micelles, among others.[330] Recently, three-dimensional (3D) polymer scaffolds with the ability to swell in aqueous media are of interest in pharmaceutical engineering. Over the last decades significant progress was made in the field and today, hydrogels can be found in many fields, including in drug delivery formulations.[172] The use of hydrogels for the delivery of therapeutic agents, including PSs, can positively impact the pharmacokinetic and biodistribution profile of the drug favoring its accumulation at the target tumors.[331]

Several hydrogels-based formulations for PS delivery have been reported exhibiting high therapeutic efficacy. In the field of photomedicine, the use of hydrogels allows to overcome the low solubility of PSs in polar media, without having an impact on photophysical properties of PS. This strategy has been used in antimicrobial,[332] antiviral,[333] and anticancer PDT treatments,[334] and was recently extensively reviewed by us.[227] One of the fundamental concepts behind the preparation of photoactive hydrogels is based on the linkage (physically or chemically) between the PS and an appropriate polymer. Cross-linking prevents dissolution of the polymer chains in aqueous environment. In chemically cross-linked, covalent bonds are formed between different polymer chains. They can be obtained by several mechanism including chemical reaction of

complementary groups, radical polymerization or using high energy irradiation. In terms of photodynamic hydrogels this often requires functionalization of the PS to allow its utility as a cross-linker. For physically hydrogels the linkage is obtained by physical interactions such as ionic interactions.[207] Moreover, hydrogels can be dependent on light to control chemical transformations within the network such as the initiation of the cross-linking process or activation of the PS.

CS is a linear polysaccharide that is produced by the deacetylation of chitin and is the second most abundant natural polymer after cellulose.[335] This polymer has been widely used in drug delivery applications due to its biocompatible and biodegradable properties, together with its low toxicity. The multiple aliphatic amine and hydroxyl groups present in the CS chain can be used as synthetic handles for cross-linking during hydrogel formation. Due to their porous structure, hydrogels can retain water and swell in aqueous media. Swollen hydrogels have interesting physical properties such as variable consistencies and low interfacial tension with biological media, that can reduce the immunological response in the body.[259] The swelling behavior of CS-based hydrogels can be tuned by adjusting the concentrations of the CS and of the cross-linker. In oncology, CS-based hydrogels have been explored for the delivery of different classes of anti-cancer agents, such as PSs, chemotherapeutic, radiotherapeutics, monoclonal antibodies, among others.[336] Moreover, protonation of the amine groups in the CS backbone can lead to the dissociation of the hydrogel structure and release of the encapsulated drug specifically at the acidic environment of tumors.[258] The need for stimuli-responsive DDSs that that efficiently target diseased areas in the body relates with non-specific interactions and thus biodistribution of the drug. This can lead to several alterations such as rapid drug clearance or in contrary – prolonged non-specific accumulation enhancing possibility of adverse reactions. Therefore, on-demand drug delivery is becoming feasible through the design of stimuli responsive systems. Their advantage offers dynamic reactivity towards stimulus (pH, temperature, enzyme) thus mimicking the responsiveness of living organisms. Stimuli-responsive systems should exhibit desired in vivo pharmacokinetic profile, target-specific accumulation and site-specific release

of the drug in a controllable manner.[337] To date, subcutaneous, transdermal, and oral administration are popular routes of administration of CS hydrogels.[260] Different sizes and structures determine the different functions of the hydrogels and the delivery route by which they are administered for cancer treatment. For instance, nanometer-sized hydrogels are often designed for *I.V*. administration, while macroscopic hydrogels with the centimeter sizes are suitable for transdermal delivery or in situ implantation.[211]

CS-based hydrogels have been reported as favorable carries of PSs, maintaining promising mechanical properties, and allowing for controlled drug delivery. Due to the antimicrobial properties of CS, many of hydrogel-based formulations for PS delivery have been directed towards applications in PACT.[338] A recent *in vivo* report using mouse model describes a CS-based hydrogel containing chlorophyll which was obtained from *Spirulina Platensis*. Hydrogel was locally applied at wounds infected with *S. Aureus* followed by 650 nm light irradiation. Enhanced healing process was observed in the presence of the hydrogel formulation.[339] Another study was reported by Wang *et al*, using a diabetic mouse model. Treatment of wounds was performed with titania nanoparticles incorporated into CS hydrogels. The combined effect of PTT and PDT allowed for enhanced wound healing in comparison with the control group.[340] Promising results were also obtained in PDT for cancer treatment. A CS-based hydrogel combining photo (PpIX) and chemotherapeutic (tegafur) activity was injected intratumorally into mice bearing breast tumors (4T1). Light-triggered tegafur release was observed which, combined with the PDT effects, ended in a strong anti-cancer activity that cause complete tumor eradication, reducing toxicity towards other tissues.[341] In another study, 5,10,15,20-tetrakis(1-methylpyridinium-4-yl)porphyrin (TMPyP) encapsulated into CS-based hydrogel was proposed as a theranostic tool. This formulation was tested in a mouse model of uterine cervical carcinoma (U14 cells). Intratumoral injection of hydrogels was followed by 532 nm light irradiation and led to complete inhibition of tumor growth without causing systemic toxicity.[342]

The physical properties exhibited by hydrogels after the application of forces include mechanical strength, stiffness, stress relaxation, self-healing, and degradation. These mechanical features are mainly dependent on the properties

of the polymer and cross-linking density. The more bonds are involved in formation of the hydrogel structure the more rigid the structure is. Tensile testing is commonly used to evaluate the *Young's modulus*, which is defined as the ratio of tensile stress to tensile strain, and *compressive modulus*, which is defined as the ratio of mechanical stress to strain in an elastic polymeric material under compression. These measurements give an indication of the material's durability.[343] For the characterization of a hydrogel formulation, compression testing is also often used. This test measures the stiffness of the material by mirroring the resistance of this platform against the deflection of the force applied to the system.[344]

The nature of cross-linking impacts the swelling ratio and consequently, the kinetics of drug release. It also determines the injectable properties of the gel. Injectable hydrogels exhibit adhesive properties and can attach to and cover surrounding tissues. Hydrogels with properties adequate for intra-tumoral injection are gaining considerable attention considering that direct delivery of anti-cancer drugs towards diseased tissue, significantly increasing bioavailability. This permits to increase the therapeutic effect while side effects or toxicity in healthy tissues is minimized.[345] Recently a dynamic covalent chemistry, which corresponds to chemical reactions carried out reversibly under conditions of equilibrium control, plays an important role in the design of injectable hydrogels.[346,347] For example, the reversible character of the Schiff-base bonds, which are defined as pseudo-covalent, allows recovery under applied forces that destroy the hydrogel structure. This means that the hydrogel can return to its integral form after crossing the lumen of a small needle used for the intratumoral injection. This phenomenon is defined as self-healing ability. CS, due to many amine groups present in the structure is an excellent polymer for preparation of Schiff-base hydrogels.[348] Dynamic Schiff-base hydrogels due to their versatile properties found a broad range of applications in the field of biomedicine, especially in tissue engineering, wound dressing, and anticancer treatment.[349–351] CS-based hydrogels with Schiff-base bonds have been successfully used owing to their injectable properties.

For example, Qu *et al*. designed antibacterial wound dressing CS-based hydrogel stimulating processes of healing due to antimicrobial properties of the

polymer and enhanced fibroblasts proliferation due to the presence of curcumin. Imine bonds involved in the cross-linking processes endowed injectable properties of the formulation and good mechanical properties, including adhesiveness at the site of application.[352] Another 'smart' gel was reported active towards hepatocellular carcinoma. This formulation was administered by subcutaneous injections and mediate an efficient delivery of the chemotherapeutic agent (DOX) at tumor sites with low pH.[353]

Drug release from hydrogels can be controlled by many factors such as swelling ratio, diffusion, or chemical cleavage of the cross-linking bonds.[345] PSs can be physically incorporated within the hydrogel structure or covalently attached to the polymer backbone. In the first case, the drug molecule is stabilized in the hydrogel network *via* physical interactions. As these secondary forces are defined as weak, the drug release is usually rapid.[200] In comparison, covalent cross-linking impairs the burst release of the drug molecule. Therefore, the release ratio is mainly controlled by the rate of the cleavage of covalent bonds.[354] The extensive research into the dynamics of the hydrogel formation has led to the development of the so-called 'smart-gels'.[355] These are polymeric cross-linked hydrophilic networks possessing tunable properties which can be triggered by varied stimuli-specific physiological responses. Driving forces of these processes can be distinguished as physically or chemically induced. Physical stimuli include temperature[175,356] or ultrasounds,[357] whereas fluctuations in pH[176,358] and enzyme-triggered[359] chances are classified as chemically based stimuli. Going a step further, development of multi-stimuli responsive hydrogels has been reported, too.[360] It is known that tumor growth processes can lead to several fluctuations in the body such as changes of the pH or development of the hypoxic conditions in the tumor microenvironment. The limited oxygen delivery to the tumor site, combined with increased oxygen metabolism leading to production of CO_2 and release of H^+, lowers the pH in the tumor microenvironment to values close to 7.0 - 6.4. The acidic nature of tumors is being explored to the design of formulations resulting in controlled and sustained release of anti-cancer drugs at the tumor.[361] This strategy is also being used with CS-based formulations.[362–364]

3.2. Objectives

The work in this chapter will focus on development of new injectable CS-based hydrogels for the sustained release of *m*-THPC. The latter is expected to permit multiple steps of irradiation without the need of further PS injections. Additionally, introduction of the dynamic, reversible Schiff-base bonds in the cross-linking of hydrogels is expected to endow injectable properties of the formulation. We aim to apply the CS-based hydrogel formulation *via* intratumoral injection, which will allow to increase biodistribution of the PS in target tissue, thus achieve better therapeutic response. For this, we will take the advantage of the tetrafunctionalized *m*-THPC derivatives, **PS 1**, **3** and **5,** described in **Chapter 2**. These derivatives were designed to contain suitable functional groups to covalently bind to the CS backbone *via* Schiff-base reaction or amide bond. We expect that the synthetic procedures will allow for efficient and homogenous conjugation of the PS to the CS backbone. Moreover, difunctionalized PEG bearing aldehyde groups will be added to obtain the desired rheological properties of the formulation by increasing cross-linking density within the scaffold. We aim to confirm self-healing ability of the polymer formulation macroscopically and *via* rheological analysis. In this chapter, we will describe the development and characterization of three injectable pH-sensitive CS-based hydrogels for photodynamic application. We aim to demonstrate a sustained release of the encapsulated PS upon decrease of the pH value, which we anticipate being mediated by the progressive cleavage of the cross-link bonds between the CS and the PS. These formulations aim to allow an efficient photodynamic activity towards cancer cells while reducing toxicity towards healthy tissues.

3.3. Results and discussion

3.3.1. Synthesis and characterization of hydrogels

To address the poor water-solubility of *m*-THPC, novel CS-based hydrogel formulations were prepared by taking the advantage of the tetrafunctionalized derivatives (**PS 1**, **3**, **5**) previously described on **Chapter 2.** The developed hydrogels are composed of three major components – CS, difunctionalized PEG and PS. CS, as a natural polymer, can vary in molecular weight and degree of deacetylation depending on the source and method of preparation.[365] To allow water solubility, the degree of deacetylation should be above 85%. In our case, a commercially available CS chloride salt in which the level of deacetylation is more than 90% was used. Such high deacetylation allows for solubility in aqueous media without the addition of acids.[366,367] Difunctionalized PEG containing two aldehyde groups was used to obtain desirable viscoelastic properties of the formulation and to enhance cross-linking density within the structure. Chemical structures of difunctionalized PEG and CS (Protasan UP CL 241) are shown in **Figure 3.1**.

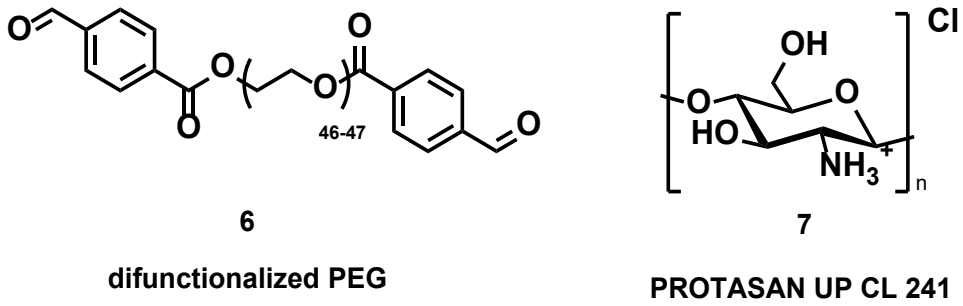

Figure 3.1. *Structures of difunctionalized PEG and commercially available CS salt – PROTASAN UP CL 241.*

Zhang *et al*. reported a 20% solution of PEG being used to form hydrogel structures; nevertheless, in our case 1.2% solution of difunctionalized PEG (10% of the CS amount) was sufficient to form hydrogel with desirable mechanical strength and swelling degree.[348] The general procedure of hydrogel preparation involves mixing of the 3% (*w/w*) CS solution in phosphate-buffered saline (PBS) with 0.5% (*w/w*) of the PS dissolved in DMSO and 1.2% (*w/w*) of the difunctionalized PEG dissolved in distilled water until gelation occurs (**Scheme 3.2**). **PS 1** and **PS 5** hydrogels are formed by cross-linking *via* an imine bond

while amide bond takes place for **PS 3 (Figure 3.3)**. We expect that different cross-link bonds can result in different drug release profile.

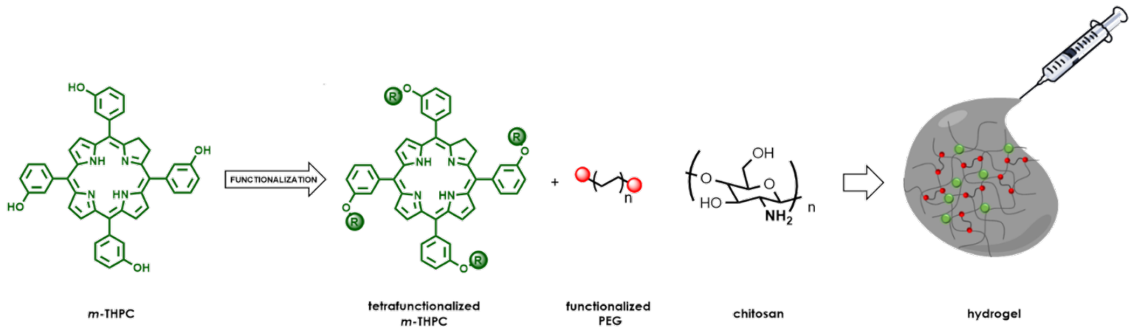

Scheme 3.2. *Synthesis of PS-PEG-CS hydrogels.*

Hydrogels were prepared using a one-pot reaction between CS, **1** or **5**, and difunctionalized PEG to cross-link the hydrogels with imine bonds resulting in formation of two polymer networks – **PS1-PEG-CS** and **PS5-PEG-CS**. In contrast, **PS 3** required an initial step of activation of the carboxylic acid groups, which was achieved by adding *N*-hydroxysuccinimide (NHS) and EDC hydrochloride.[368] Then, activated **PS 3** was added to CS, which was followed by addition of PEG to yield **PS3-PEG-CS**. With vigorous mixing, gelation of **PS1-PEG-CS**, **PS3-PEG-CS** and **PS5-PEG-CS** occurred within two minutes (**Figure 3.4)**. Next, the hydrogels were washed in ethanol (40 %) to allow for removal of unreacted monomers, PS, and solvents.

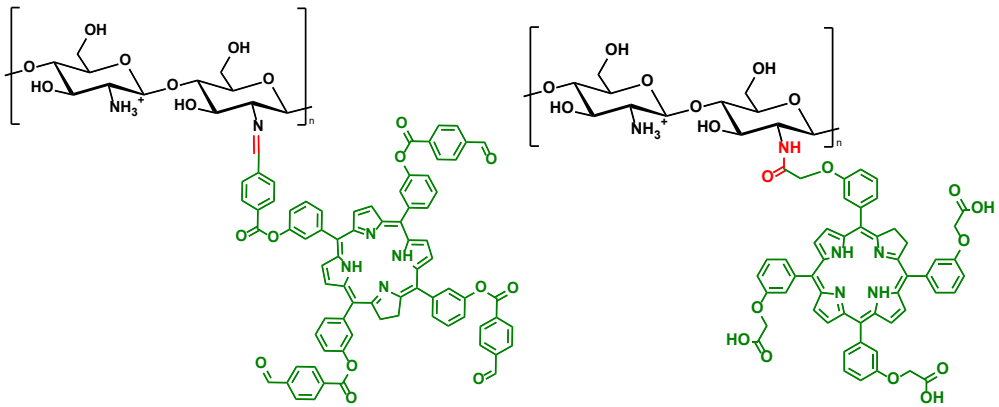

Figure 3.3. *Formation of the cross-link bonds between the* ***PS 3*** *(left) and* ***PS 1*** *(right) to the CS backbone.*

The composition of the formulation was optimized based on the available literature. For the design of injectable hydrogels, 3% (*w/w*) solution of CS offers favorable viscosity.[369,370] This allows the desired cross-linking density to be

obtained, which is expected to enable sustained drug release from the scaffold. The lower the concentration of CS solution, the faster hydrolysis of the hydrogel scaffolds is observed.[370] The amount of the PS varies significantly across different types of hydrogels and photosensitizer. Typically, it does not overcome 10% (*w/w*) of the hydrogel composition.

Our preliminary studies testing 0.25% and 0.5% (*w/w*) concentrations of the PS did not show major differences in the physical properties of the formulations. However, higher concentrations of the PS allow for a better hydrogel stability, and release of the drug molecule in a more controlled manner, without affecting the swelling degree of the formulation. Higher concentrations of the PS were not tested as this could cause problems of aggregation in the aqueous medium before the formation of cross-link bonds.

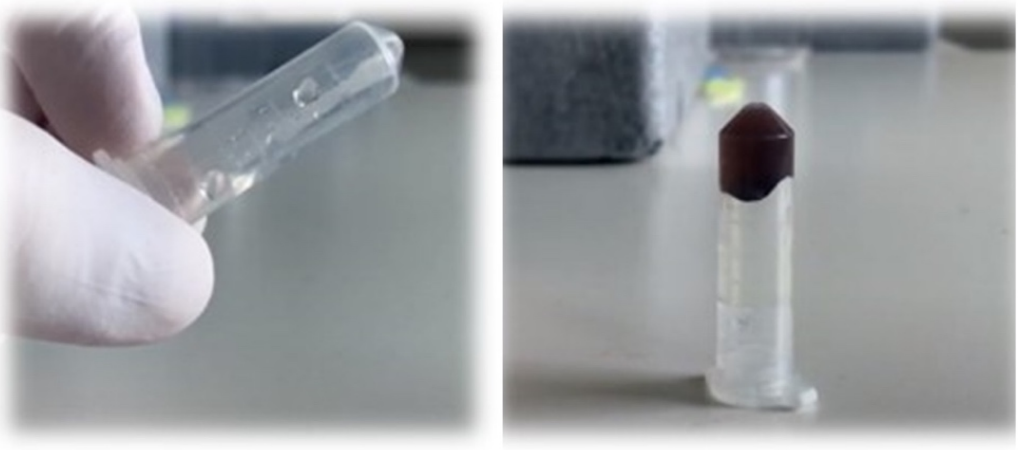

Figure 3.4. *Cross-linking of hydrogels – (left) – viscous solution of CS, (right) – cross-linked gel.*

The obtained hydrogels were characterized using FT-IR spectroscopy, while viscoelastic properties were studied using a rheometer. The IR spectra of CS, PEG and the hydrogels cross-linked with imine bonds (**PS1-PEG-CS** and **PS5-PEG-CS**) were overlaid and are shown in **Figure 3.5**. The absorption band specific to aldehyde bending vibrations (1750-1700 cm^{-1})[371] is observed in the functionalized PEG structure and was absent in the hydrogel spectra, which indicates that effective cross-linking of the polymer occurred in the hydrogel network. A new peak between 1650-1600 cm^{-1} is attributed to an imine bond (C=N)[372] which is indicates cross-link bonds between CS and the PS.

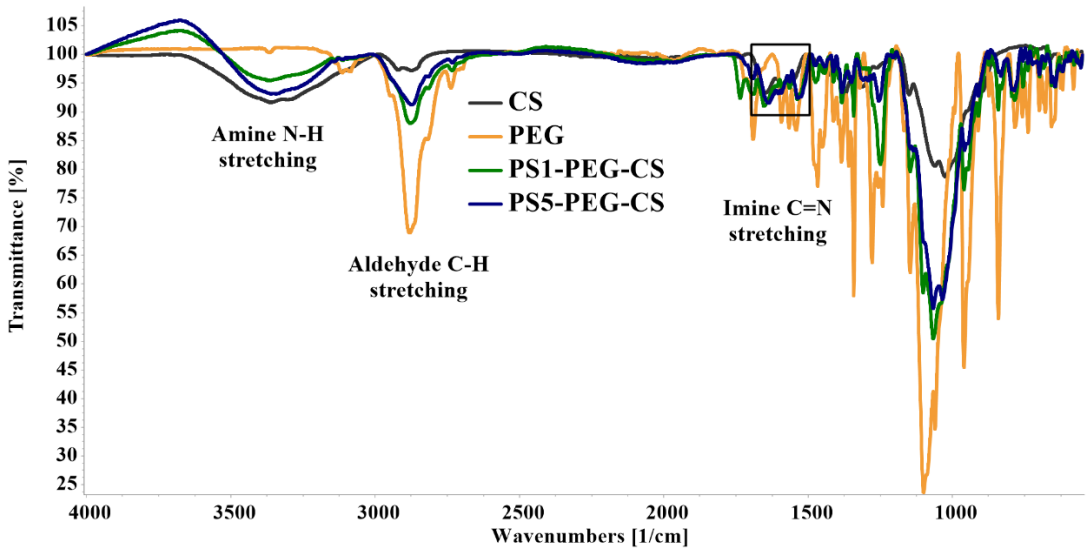

Figure 3.5. *Overlaid IR spectra of CS (black), PEG (yellow),* ***PS1-PEG-CS*** *(green) and* ***PS5-PEG-CS*** *(blue).*

FT-IR analysis was also used to confirm the cross-link *via* amide bonds in **PS3-PEG-CS**. The spectra of CS, PEG, and hydrogel **PS3-PEG-CS** are presented in **Figure 3.6**. New absorption bands between 3200-3600 cm^{-1} and 1650-1700 cm^{-1} (hydrogel spectrum) relate to an amide bond, which is the main bond cross-linking the network.[373] Moreover, as before, the aldehyde group of the functionalized PEG was absent in the hydrogel spectra, indicating effective cross-linking of the polymer within the network.

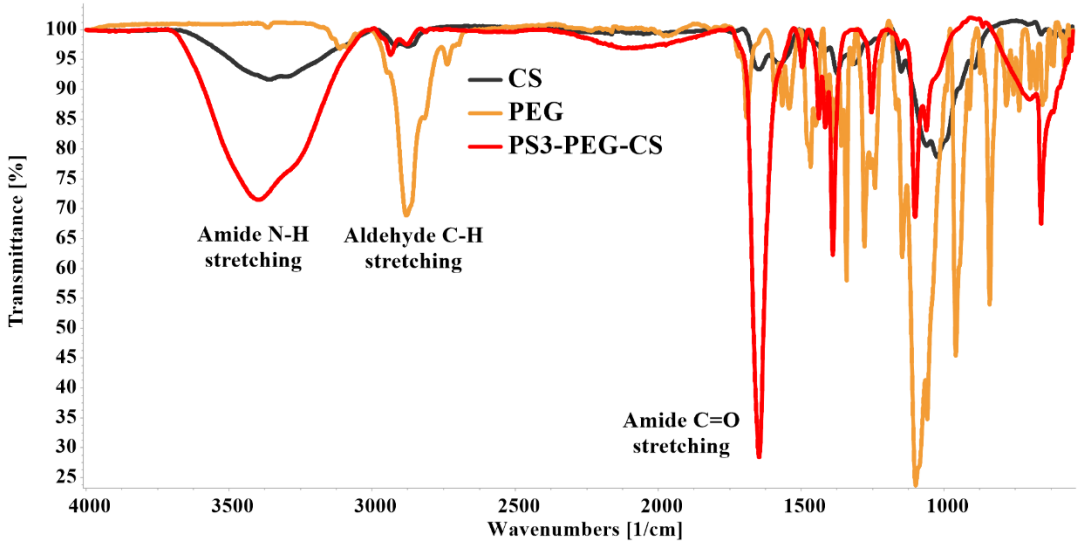

Figure 3.6. *Overlaid IR spectra of CS (black), PEG (yellow) and* ***PS3-PEG-CS*** *(red).*

3.3.2. Evaluation of the viscoelastic properties of hydrogels.

The self-healing ability of the hydrogel formulations was tested macroscopically. First, hydrogels were cut into pieces and the divided fragments were put together and the healing process was observed over time. Within one-hour, full recovery to the original shape was observed (**Figure 3.7**). Next, hydrogels were loaded into a syringe barrel and extruded through the needle. After injection, the hydrogel structure appears deformed due to the applied stress; however, fully reforms to the homogenous formulation within one hour. The results obtained confirm that the hydrogel formulations possess self-healing abilities and can be used as an injectable DDS.

Figure 3.7. *Macroscopical evaluation of hydrogels. (left) - self-healing ability of the* ***PS1-PEG-CS*** *hydrogel within 1 hour observation, (right) - injectable properties of* ***PS3-PEG-CS*** *hydrogel.*

Rheological characterization defines the flow and mechanical properties of hydrogels under applied external forces.[374,375] Self-healing and shear-thinning properties make hydrogels good candidates for injectable drug delivery platforms, with the ability to retain active agents (such as PSs) and protect them against *in vivo* biological forces.[376] Storage and loss moduli are used to define the energy that is stored or released during the applied shear stress. Storage modulus (G') represents the elastic behavior of the material, while loss modulus (G'') described the viscous behavior. When the elastic behavior of the network is stronger than the viscous behavior (G'>G'') and the G'' to G' ratio (tan delta) is < 1, the material is considered elastic. Conversely, when the tan delta value is > 1, the material behaves more like a liquid and usually is not stable under strong flow conditions.[377] Several conditions have an impact on the mechanical strength

of hydrogels. Nevertheless, one of the most important factors that should be taken into consideration when designing the formulation is the ratio between the polymer and cross-linker used to form hydrogel. Azadikhah *et al*. evaluated and compared variety of cross-linker concentrations (8, 12 and 16% tannic acid) on the viscoelastic properties of CS-based hydrogel. The increase in mechanical strength, determined by rheological characterization, was proportional to the concentration of the tannic acid.[264] Therefore, in the field of PDT, where a PS is very often used as a cross-linker in the formation of hydrogels, determination of the polymer-PS ratio is a crucial step. This ratio has an impact on several factors, ranging from mechanical strength, injectable properties, to the kinetics of drug release. Frequency sweep measurements were preformed to evaluate and compare the viscoelastic properties of the hydrogels, which are defined by storage and loss moduli.[378] This study describes the hydrogel behavior in the linear viscoelastic region (LVE) region and is presented as G' and G'' as a function of the angular frequency at a fixed constant strain (**Figure 3.8**). The fixed constant strain was defined using the amplitude sweeps measurements and is 5%. Low frequencies help to characterize the behavior of the network during slow changes of stress, while high frequencies investigate fast motion during short timescales.

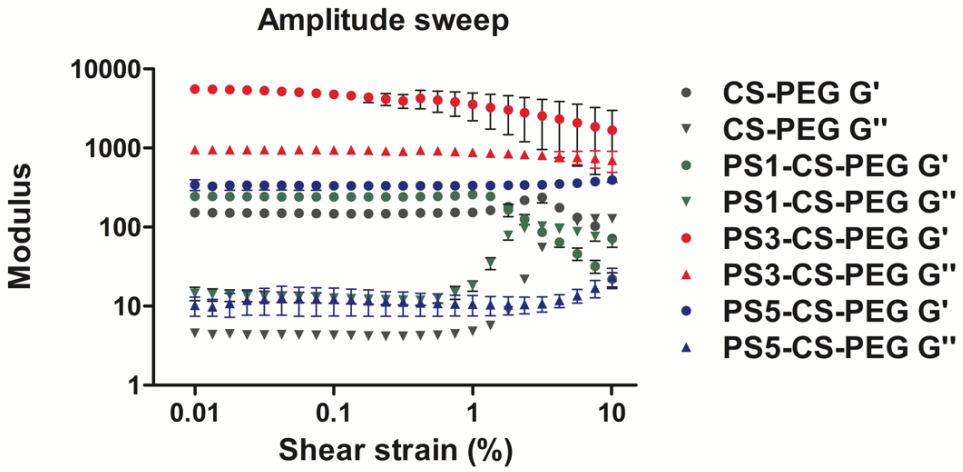

Figure 3.8. *Loss (G'') and storage (G') moduli of the hydrogels with a strain amplitude sweep (strain = 1% − 1000%) at a fixed angular frequency (1Hz). n=3*

The storage modulus of the CS-based hydrogels was higher than the loss modulus, which confirms the formation of a 3D hydrogel network. Moreover, the higher values of G' (~ 1000 and more) and G'' (> 10) for all hydrogels containing PS in comparison to the blank formulation (~100 for the G' and lower than 10 for the G'') indicate the impact of the PS on the hydrogel network, resulting in higher rigidity of the scaffold (**Figure 3.9**).

Comparable results were also observed by Bayat *et al.* In their work, increasing concentration of the PS, tetraamino-(phthalocyaninato)zinc(II) (ZnTAPc), was correlated with higher values of the G'.[379] Although both **PS1-PEG-CS** and **PS5-PEG-CS** form dynamic imine bonds with the CS chains, the **PS5-PEG-CS** network is more elastic (G' is 100 times bigger for the **PS 5** than **1**) which means that **PS 5** does generate more cross-links than **PS 1**.

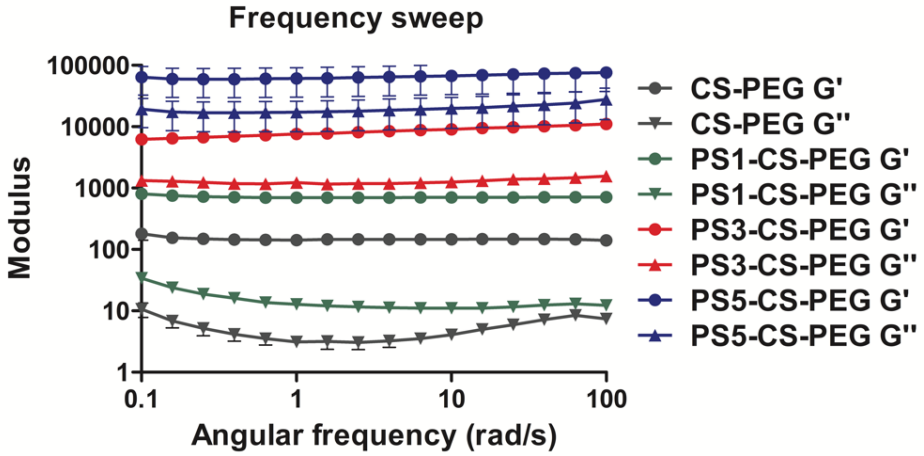

Figure 3.9. *Storage (G') and loss (G'') moduli of the hydrogel formulations as a function of angular frequency at a fixed strain of 5%. n=3*

Rheology analysis was used to study the self-healing properties of the hydrogel 3D networks, using the recovery test.[176] Strain (5, 300 and 600%) was applied in relation to time. The hydrogel formulations were stable at a strain of 5%, while the network is disrupted at higher strain values (300 and 600%). Storage and loss moduli values of tested hydrogels recovered to the original values after removal of the applied strain. For hydrogel cross-linked *via* amide bonds (**PS3-PEG-CS**), the self-healing process requires more time than the timeframe of the study (> 3.5 min). Moreover, with higher applied strain the structure was destroyed - G' vales decline close to the 0 value. This was in

contrast to the hydrogels cross-linked *via* dynamic imine bonds (**PS1-PEG-CS** and **PS5-PEG-CS**) - G' values were in the range 10 – 100 of the applied strain. For the **PS3-PEG-CS**, G' values after removal of the applied strain recover to the original values at the lowest amount of strain. The storage modulus does not decrease lower than 10 values after applied strain. This indicates the impact of the additional Schiff-base bonds in the network (**Figure 3.10**).

Comparable results were also observed by Belali *et al.*[176] The authors developed an injectable CS-based hydrogel conjugated with 5,10,15,20-tetrakis(4-aminophenyl)porphyrin (NH_2-TPP) and cross-linked *via* an imine bond. Self-healing ability was evaluated in a recovery study applying various strain forces (1, 300 and 600%). Similarly, the G' were higher than G'' values at the lowest applied strain, however the opposite situation occurred with the increased strain values (300 and 600 %) leading to the destruction of the forming bonds.

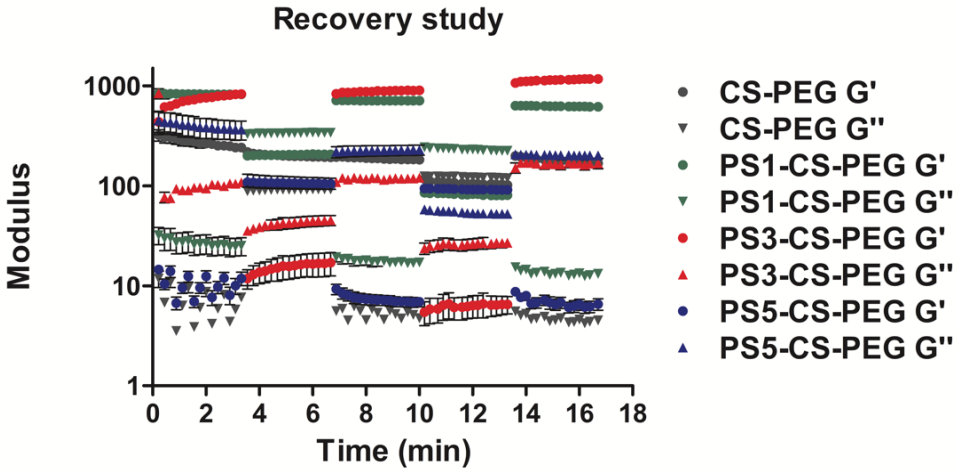

Figure 3.10. *The self-healing properties of all hydrogel formulations demonstrated by continuous step strain (5% strain → 300% strain → 5% strain → 600% strain → 5% strain) measurements. n=3*

3.3.3. Drug content and cross-linking efficiency

Two general methods for drug loading into the hydrogel structure can be distinguished. The first one considers addition of the active pharmaceutical ingredient before the cross-linking process occurs, while the second one involves trapping the drug molecule into a swollen, already formed hydrogel. However, both methods are affected by several limitations such as drug-polymer

interactions or amount of polymer groups available for covalent attachment.[380] Drug loading is especially important for biological applications, where the exact amount of the drug in the pharmaceutical formulation must be known in order to establish dosage. The cross-linking efficiency determines several factors of the hydrogel, including viscoelastic properties, drug loading and release efficiency.[381] The cross-linking or drug loading efficiency can be calculated as a ratio of the drug molecule determined in the hydrogel structure to the amount added for preparation of the formulation.[382] Therefore, cross-linking efficiency of **PS 1**, **3** or **5** in the hydrogel structure was evaluated spectroscopically. After destruction of three independent samples of each hydrogel structure *via* hydrolysis under acidic conditions, the obtained solution was diluted by a factor of 10 in DMSO and the absorption spectrum of PS was recorded at 652 nm. The accurate concentration of the PS was determined using the molar absorption coefficient and considering the Lambert-Beer law. Based on the obtained results, we conclude that the cross-linking efficiency (70 – 80%) is similar in all hydrogel formulations (**Table 3.1**). In addition, the cross-linking efficiencies of different samples of the same hydrogel batch were very similar, not exceeding 10%. This means that the PS is distributed equally within the network, which reduces the risk of drug over- or underdose in potential hydrogel application.

Table 3.1. *Cross-linking efficiency of hydrogels. (n = 2)*

Hydrogel	Cross-linking efficiency (%) + Standard deviation
PS1-PEG-CS	80.15 + 5.73
PS3-PEG-CS	70.00 + 7.32
PS5-PEG-CS	79.95 + 4.27

3.3.4. pH-responsive PS release from hydrogel scaffolds.

The use of CS and the imine or amide cross-linked bonds in the developed hydrogels is expected to give a pH-responsive behavior to the developed formulations. The pH-dependent release of the PS from the hydrogel

scaffold contributes the protonation of the amine groups in the CS backbone and dissociation of the imine bond in the acidic environment. Herein, the stability of hydrogels **PS1-PEG-CS**, **PS3-PEG-CS** and **PS5-PEG-CS** was evaluated at different pH values – 7.5, 6.5 and 5.0. An accelerated drug release was observed for hydrogel scaffolds incubated in the most acidic buffer (pH = 5). Under these conditions, over 50% PSs release was observed within three hours of incubation. A slower release profiles of PSs were observed at pH = 6.5 reaching approximately 50% within 10 hours of incubation. In contrast, at pH = 7.5 maximally 1% PS release was observed after 24 hours of incubation (**Figure 3.11**).

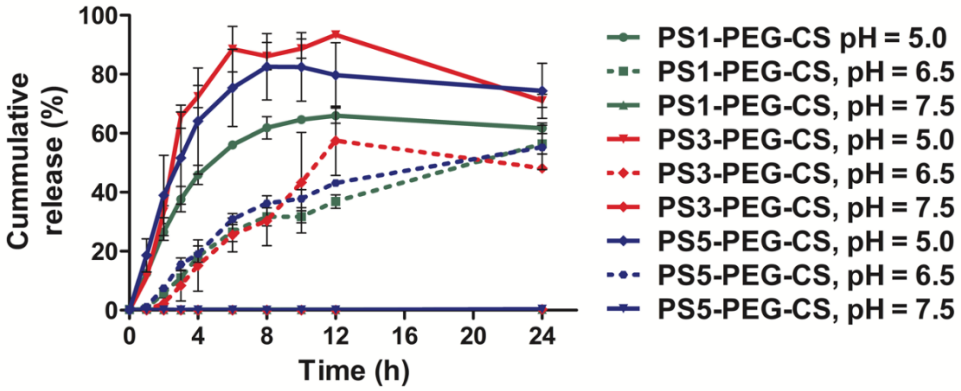

Figure 3.11. *pH-dependent drug (**PS 1**, **3** and **5**) release from hydrogel scaffolds.*

The data confirms that hydrogels can be used as a favorable delivery system for the *m*-THPC-based PS, protecting the drug from premature release and aggregation, while allowing for a site, pH-dependent delivery of the PS. This data is satisfying considering our aim of intratumoral application of these systems. Therefore, the hydrogels obtained should allow a controlled release of the PS at place of injection, facilitating enhanced treatment efficacy due to higher bioavailability at tumors sites.

3.3.5. Aggregation of the PS in aqueous media

Aggregation of the PS in aqueous media affect the photophysical properties of the PS such as ability to generate singlet oxygen, triplet state lifetime or fluorescence, reducing the photoactivity of PSs.[383] Therefore, design of the DDSs allowing for an application of the PS in non-aggregated state and reducing its aggregation on the target site is very important to increase treatment

efficacy.[384] Alternatively, it can be achieved by the chemical modifications of PS and design of chromophores containing groups allowing for water-solubility or inhibiting aggregation processes by the steric hindrance.[385] Therefore, aiming to use tetrafunctionalized derivatives **PS 1**, **3** and **5** for in vitro studies we tested their behavior in PBS buffer by measuring their absorption spectra.

Considering this, aggregation studies were performed to predict the behavior of the released PS in biological conditions. For aggregated forms of the tetrapyrrolic PS it is expected to observe decrease of intensity and red-shifting of the Soret and Q-bands.[301,386] Here, the spectra of *m*-THPC, **PS 1** and **PS 5** exhibited a 2-fold decrease of the Soret band intensity. This can be related with the hydrophobic properties of the PS, which are insoluble in water, leading to the immediate formation on the aggregates. Nevertheless, **PS 1** and **5** still are potential candidates as potent PS as the determining factor will be the ratio of aggregates/monomers inside cancer cells.[106] The opposite situation was observed for the water-soluble derivative **PS 3**. Herein, no significant changes in the absorption spectra recorded in DMSO and PBS were observed making **PS 3** the most promising candidate for PDT (**Figure 3.12**).

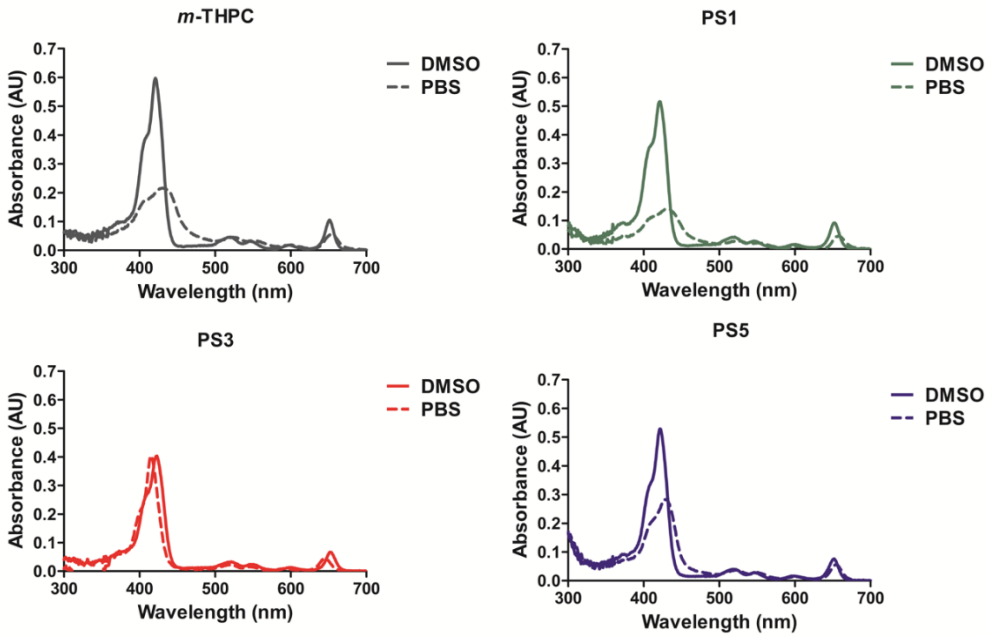

Figure 3.12. *Overlaid and normalized absorption spectra of m-THPC (grey),* ***PS 1*** *(green),* ***3*** *(red) and* ***5*** *(purple) recorded in DMSO and PBS.*

3.4. Conclusions and outlook

In this chapter we reported synthetic procedures for the quick and efficient synthesis of CS-based hydrogels. CS, as a natural and non-toxic polymer has been previously used in several PDT-involved formulation, allowing for protection of the encapsulated PS and providing stimuli responsive properties. Functional groups of tetrafunctionalized *m*-THPC derivatives **PS 1**, **3** and **5** were used as synthetic handles in cross-linking processes with the amine groups of the CS chain. Therefore, aldehyde groups of **PS 1** and **5** formed dynamic Schiff-base bonds, whereas carboxylic acid groups of **PS 3** were cross-linked to the polymer *via* more stable amide bond. Moreover, addition of difunctionalized PEG increased the cross-linking density resulting in desirable viscoelastic properties. Characterization of the hydrogel confirmed covalent attachment of the PS into the hydrogel scaffold. This was demonstrated *via* FT-IR analysis, where formation of imine and amide bonds withing hydrogel structure was observed. Due to the dominant influence of the Schiff-base bonds involved in the formation of hydrogel and their dynamic and reversible properties it was possible to obtain injectable properties of the polymer-based formulation. We confirmed that macroscopically and by rheological measurements. After extruding hydrogels through a needle, the hydrogel structure reformed to the original shape within one hour. Similar behavior was observed when pieces of hydrogel were cut in half and observed over time. Within one-hour, a homogenous, uniform structure was rebuilt. Confirmed injectable properties of the formulation will allow for intratumoral drug delivery. This route of administration allows to reduce metabolic site related with systemic administration, increase the drug concentration at the target site and prevent from systemic side effect.

The cross-linking efficiency experiments confirmed satisfying drug loading efficiency resulting in an average 70-80% encapsulation of the active molecule. Importantly, the PS was distributed homogenously within the network. One of our main goals was to obtain formulations that would enable intratumoral injection of the PS with subsequent sustained release. To confirm our assumptions a drug release study was performed. We observed prolonged release of the PS from hydrogel scaffold when incubating formulation in

medium at pH = 6.5, reaching the maximum (60%) within 24 hours of incubation. In comparison, enhanced release was observed in the pH = 5.0, where the plateau state (100% release) was reached within 12 hours of incubation. Importantly, we did not observe the release of PS at the pH of 7.5, which prevents premature release. Based on the drug release study it is expected that pH-specific drug delivery of the PS using CS-based hydrogel will allow for controllable and sustained drug release and distribution at the target site. This approach is expected to ensure sufficient drug delivery into cancerous tissue.

Finally, the aggregation study was performed to predict the behavior of the released PS in biological conditions. Therefore, spectra recorded in DMSO were compared with ones measured in PBS (0.4% DMSO). We observed a significant decrease of *m*-THPC and derivatives **PS 1** and **5** absorbances. This is in line with their more hydrophobic properties which is a result of an attachment of aldehyde groups, changing the polarity of the molecule. Opposite properties were exhibited by **PS 3**, where no significant changes in absorption spectra were observed in both solvents. This is due to carboxylic acid groups endowing water-solubility; therefore, no aggregation was observed in PBS.

In summary, we reported quick and reproducible synthesis of photoactive hydrogels will allow for efficient drug delivery. Due to the pH-sensitivity of the CS and desirable mechanical properties of synthesized hydrogels we aim for controlled and site-specific drug delivery. These systems are expected to allow for enhanced PS bioavailability and reduce common side-effects related to Foscan treatment. The biological activity of free *m*-THPC derivatives **PS 1**, **3** and **5** will be discussed in **Chapter 4**.

3.5. Experimental

Materials

Reagents and solvents were of analytical grade and commercially acquired. Unless stated otherwise, they were used without further purification. Difunctionalized PEG was kindly provided by Prof. Daniel Kelly's group, Institute of Biomedical Engineering, Trinity College Dublin, Ireland and synthesized according to the literature protocol.[21] Chitosan PROTASAN UP CL 214 was purchased from *NovaMatrix*. The cationic polymer is a highly purified and well-characterized water-soluble chloride salt which functional properties are described by the molecular weight (150000-400000 g/mol) and the degree of deacetylation >90%. Solvents (DMSO) were purchased from from *Acros Organics*. The rheological experiments were performed using a modular compact rheometer (Anton Paar, Graz, Austria). Fluorescence of PS in the drug release study was measured using microplate reader (Agilent Technologies, USA). Absorption spectra were recorded using JASCO V-730 spectrophotometer. Fourier transform infrared (FT-IR) data was recorded on a Digilab FTS-6000 spectrometer in the range of 4000–400 cm^{-1} at room temperature (25 °C).

Preparation of PS1-PEG-CS and PS5-PEG-CS hydrogels

CS (120 mg) was dissolved in phosphate buffer saline (PBS) (4 mL) and stirred for 24 hours to completely dissolve the polymer. CS solution (0.4 mL) was transferred to an Eppendorf and mixed with 0.765 mg of the **PS 1 or PS 5**) previously dissolved in DMSO (0.17 mL). Next, the functionalized PEG (1.2 mg) dissolved in distilled water (0.1 mL) was transferred to the Eppendorf and vortexed to form the hydrogel. Gelation occurred within 2 minutes with vigorous mixing of the solution. The hydrogel was immersed in PBS (pH = 7.5) to remove unreacted materials and excess DMF.

Preparation of PS3-PEG-CS hydrogel

CS (120 mg) was dissolved in phosphate buffer saline (PBS) (4 mL) and stirred for 24 hours to completely dissolve the polymer. CS solution (0.4 mL) was transferred to the Eppendorf and mixed with 0.765 mg of the **PS 3** dissolved in DMSO (0.17 mL). **PS 3** was previously stirred with NHS (0.5 mg) and EDC

hydrochloride (0.5 mg) for 30 minutes to activate the carboxylic acid moieties. Next, the functionalized PEG (1.2 mg) dissolved in distilled water (0.1 mL) was transferred to the Eppendorf and vortexed to form the hydrogel. Gelation occurred within 2 minutes with vigorous mixing of the solution. The hydrogel was immersed in PBS (pH = 7.5) to remove unreacted materials and excess DMF.

Preparation of PEG-CS (blank) hydrogel

CS (120 mg) was dissolved in PBS (4 mL) and stirred for 24 hours to completely dissolve the polymer. CS solution (0.4 mL) was transferred to an Eppendorf and vortexed with DMSO (0.17 mL). Next, the functionalized PEG (1.2 mg), dissolved in distilled water (0.1 mL) was transferred to the Eppendorf, and mixed to form the hydrogel. Gelation occurred within 2 minutes of vigorous mixing of the solution. The hydrogel was immersed in PBS (pH = 7.5) to remove unreacted materials and excess DMF.

Rheological analysis

The rheological experiments (amplitude sweep, frequency sweep and the recovery study of the hydrogels) were performed using a modular compact rheometer in the parallel plate mode. For this measurements, 25 mm diameter parallel plates were used, with a measuring gap of 1.0 mm at room temperature (25 °C). The hydrogel was placed between the parallel plate and a solvent trap was added to the platform to avoid evaporation of water. The experiments were performed in the linear viscoelastic (LVE) region, which was determined for each hydrogel by an amplitude sweep study in the range of frequencies between 0.1 and 10 Hz.

Macroscopical evaluation of self-healing properties

The self-healing ability of the **PS1-PEG-CS** and **PS3-PEG-CS** hydrogels was evaluated after cut each hydrogel in half. Then, the two samples were placed together during 60 min at room temperature. Photographs were taken to record the healing process to the original shape. Moreover, both hydrogels were independently loaded into syringe and extruded through the needle into a vial. The re-healing process was monitored macroscopically in time.

Determination of cross-linking efficiency

The amount of the **PS 1**, **3** or **5** cross-linked into hydrogel structure was quantified. Three independent samples (m = ~30 mg) of each hydrogel were destroyed by adding 200 µL of an acidic solution (1:1 PBS/acetic acid). A dilution of each hydrogel sample was prepared in DMSO, and the absorbance was measured at 652 nm. The concentration of the PS was calculated considering the molar absorption coefficient of each PS.

pH-dependent PS release from CS-based hydrogel scaffold

The cumulative release of **PS 1**, **3** and **5** from hydrogel structure was quantified *via* fluorescence intensity measurements, at different time points (0 to 24 h) after incubation with 2 mL of PBS at different pH (7.5, 6.5 and 5.0) at 37 °C. At the indicated time points, 50 µL of the release buffer was withdrawn and followed by 10 x dilution (10 µL in 90 µL of DMSO) to guarantee good PS solubilization. For each PS, a calibration curve was performed in PBS/DMSO (1:10 ratio) at concentrations ranging from 0 to 8 µM (**Figure 3.13**). The cumulative release of *m*-THPC derivatives from the hydrogel structures was inferred from the PS fluorescence intensity measurements that was measured in a microplate reader (excitation: 420/40, emission: 645/20). A sample of each hydrogel was then totally disrupted by addition of an acidic solution to entirely release the entrapped PS which was assumed as 100% of release.

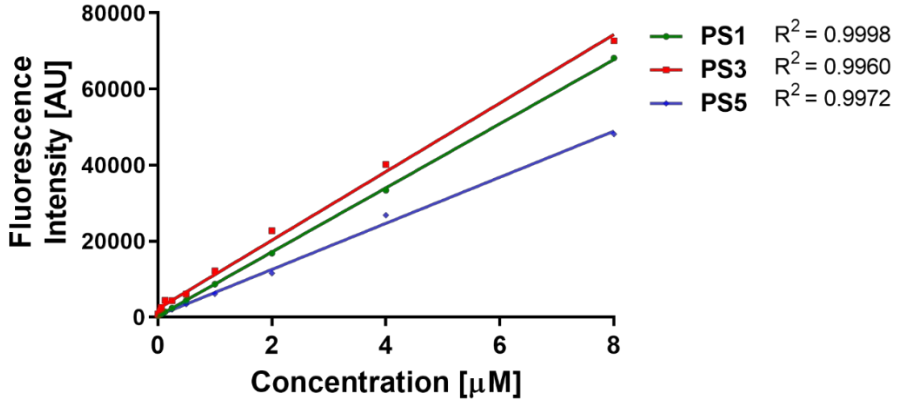

Figure 3.13. *Calibration curve of* ***PS 1****,* ***3*** *and* ***5*** *recorded in PBS/DMSO (1:10 ratio) at concentrations ranging from 0 to 8 µM*

Aggregation study

An equal volume of each PS stock solution (in DMSO) was diluted in PBS (0.4% DMSO) and DMSO, respectively, to evaluate the level of PSs aggregation in an aqueous solution. Stock solutions of *m*-THPC, **PS 1**, **3** and **5** varied in a range of 1.04 – 1.1 mM. Next, absorption spectra of each PS were recorded and overlayed to compare the level of aggregation by the observation of changes in the Soret and Q band.

Chapter 4 *In vitro* evaluation of tetrafunctionalized *m*-THPC derivatives

4.1. Introduction

The efficacy of anti-cancer PDT depends on the combined effect of three actions: 1) direct phototoxicity as a result of ROS production and the generation of oxidative stress, 2) destruction of the tumor vasculature and 3) activation of anti-tumor immune responses.[6] This chapter is focused on the action 1) as it provides the *in vitro* evaluation of *m*-THPC, and its derivatives, **PS 1**, **3** and **5**, on two cancer cells lines. The intracellular sphere of activity of $^1O_2$ is very limited as it can only diffuse ~ 0.3 μm from where it is produced, therefore it can only affect surrounding macromolecules.[100,387,388] Organelle components such as nucleic acids, proteins and especially lipids, which allow for increased oxygen solubility, are targets for ROS leading to the generation of oxidative stress.[389] This indicates that the intracellular localization of the PS at the time of irradiation is an important factor for the PDT effect.[390]

Hydrophobic PSs, such as *m*-THPC, have a tendency to accumulate in the mitochondria, GA and/ or ER, whereas hydrophilic molecules, *e.g.*, padeliporfin, accumulate in lysosomes as a result of endocytosis.[26] Organelle tropism determines impacts PSs activity and the cell death mechanisms. For example, PSs localized in the mitochondria and/or ER/GA compartments are often associated with higher damage to cancer cells.[391] In PDT, necrosis, apoptosis and autophagy have been the most studied mechanisms of cell death (**Figure 4.1**).[105] Accidental necrosis is a form of non-regulated cell dead and is characterized by the loss of the cellular membrane, swelling of the cells owing to water influx and often release of the cellular content, which *in vivo* stimulates an inflammatory response.[392] Apoptosis is a regulated and highly complex cell death mechanism dependent on the activation of different caspases.[393] Autophagy is a catabolic process that causes the degradation of cellular components and can damage larger structures such as organelles or protein aggregates. Depending on the intensity of the stress stimulus, autophagy can act as a pro-survival mechanism or as a type of cell death.[394] The cell death field is advancing at an unprecedent pace. Other forms of cell demise and their

mechanisms and signaling pathways are continuously being discovered.[395–397] Finally, ICD is a type of cell demise that has been described in the context of multiple PDT protocols. It assumes particular importance considering its ability to activate the immune system to recognize and kill cancer cells. to.[105,109]

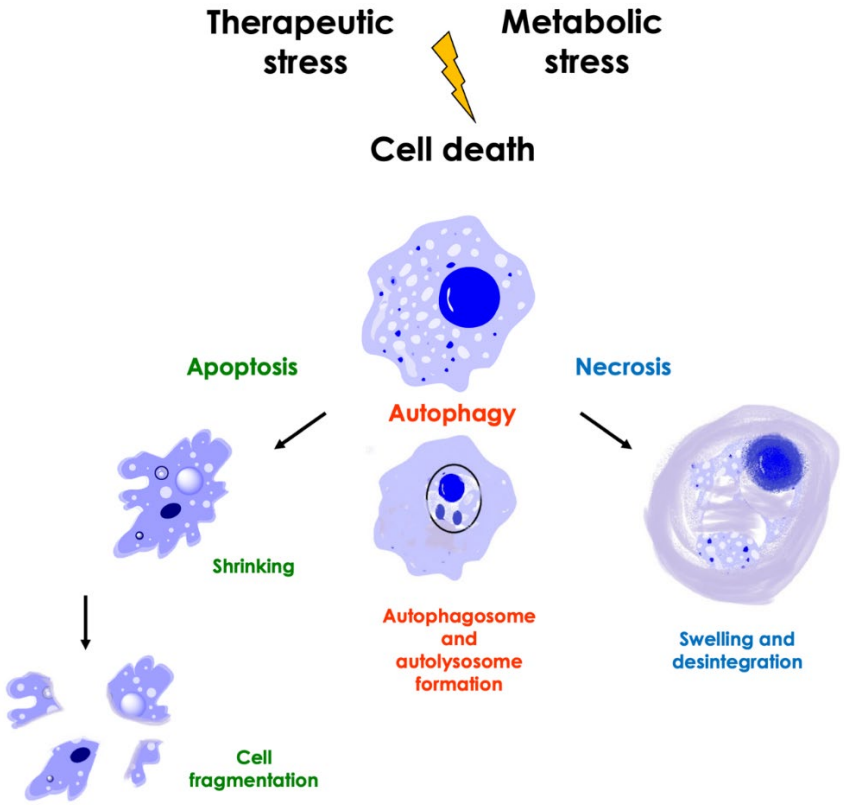

Figure 4.1. *Schematic representation of the most common cell death mechanisms.*

To this day, the activity of *m*-THPC, and numerous derivatives, has been extensively studied using a variety of cancerous and non-cancerous cell lines. The work of Rezzoug *et al*. indicated that although the uptake of *m*-THPC occurs with it in an aggregated state, this is followed by slow monomerization at the cellular membranes.[398] After internalization, the main target of *m*-THPC is the ER and GA compartments.[136] *m*-THPC can also colocalize in lysosomes and mitochondria, albeit to a lesser extent.[136] Numerous studies shown that light activation of *m*-THPC ends in elevated toxicity. IC_{50} in the range of 0.75 to 100 nM have been reported in cancer cells of different histological origin (*e.g.*, A-427, BHY, KYSE-70, RT-4, SISO, C6 or 22A cells).[168,399,400] The mode of cell killing of photo-activated *m*-THPC has also been deeply investigated. Several studies in different cell lines show that *m*-THPC induced PDT triggers the release of cytochrome c and caspase-3 activation, causing apoptotic cell death.[134]

PDT-induced inactivation of GA and ER enzymes was observed, which reflects its tropism for these organelles. Damage at the ER/GA is likely the starting point for the indirect activation of the mitochondrial apoptotic processes. As mentioned earlier, the cell death mechanism is dependent on the severity of the PDT treatment.[401] In accordance, for *m*-THPC, necrosis was also reported for high concentrations while autophagy has been observed at low drug concentrations.[402]

4.2. Objectives

In this chapter we investigate the activity of tetrafunctionalized *m*-THPC derivatives *in vitro* against B16F10 and CT26 cancer cells and compare this activity to *m*-THPC. CT26 is a colon carcinoma cell line that is extensively used as a tumor model for screening new anti-cancer compounds, including PSs. It is known to be highly immunogenic which justifies it use in immunotherapy protocols and studies involving anti-tumor immunity.[60] B16F10, a murine melanoma, is a highly metastatic cancer cell line that has a lower immunogenic profile in comparison to CT26.[403] Cytotoxicity and phototoxicity experiments will be performed to select the most potent and promising *m*-THPC derivative for further hydrogel preparation and *in vivo* applications. Moreover, the cellular uptake of these PSs will be investigated to determine if the chemical modifications and consequently, the changes in polarity impact the intracellular levels of the PS in comparison to *m*-THPC. The mechanism of action of the lead PS derivative will be evaluated using inhibitors of the cell death pathways more relevant in the context of PDT. Finally, lipid peroxidation will be evaluated *via* flow cytometry and confocal microscopy by means of the BODIPY 581/591 probe.[404] Considering the improved photo-physical properties of the *m*-THPC derivatives, we anticipate that these molecules would deliver better biological activity than the *m*-THPC counterpart.

4.3. Results and discussion

4.3.1. Cytotoxicity of *m*-THPC and tetrafunctionalized *m*-THPC derivatives

Dark toxicity experiments using *m*-THPC and tetrafunctionalized derivatives **PS 1**, **3** and **5** were performed on CT26 and B16F10 cell lines. PSs, at concentrations ranging from 2.5 to 80 μM, were incubated with cells for 24 hours and the cell viability was determined applying the Alamar Blue (resazurin) assay.[405] Resazurin is a cell permeable nonfluorescent probe that upon cell internalization is reduced *via* cellular redox enzymes to resorufin.[406] This process results in a color change from blue to red, which can be measured by fluorometry at 590 nm, allowing for a quantitative measurement of cell viability. A previously reported comparative study of *m*-THPC with other PSs using human epidermoid carcinoma cells demonstrated that the half maximal inhibitory concentration (cytotoxicity in 50% of the cell population - IC_{50}) was found to be *ca.* 9 μM. Moreover, a comparative study by Kiesslich *et al*. showed that at doses below 1 μM significant toxicity of *m*-THPC towards different biliary tract cancer cell lines was not observed. Nevertheless, it should be considered that the activity of PSs between different cell lines may vary and is dependent on cellular mechanics.[407] Our results indicate that tetrafunctionalized *m*-THPC derivatives **PS 1**, **3** and **5** do not cause cytotoxicity in the applied range of concentrations (up to 80 μM) (**Figure 4.2**). Significant toxicity of *m*-THPC was observed at 20 μM, resulting in decreased cellular viability (~ 50% on B16F10 cells and ~100% on CT26 cells).

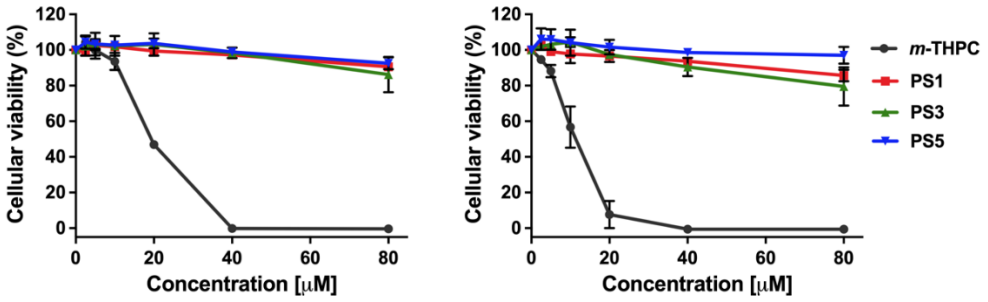

Figure 4.2. *Cytotoxicity of m-THPC and tetrafunctionalized derivatives towards B16F10 (left, n=3) and CT26 (right, n=2) cancer cells.*

The IC_{50} values of *m*-THPC in both cell lines does not differ significantly and was calculated to be 19.39 µM for B16F10 and 11.19 µM for CT26 cells. These results give a promising outlook for further studies because one of the requirements for PSs is a lack of dark toxicity. This property avoids non-specific toxicity towards healthy tissue, thus reducing side effects and improving treatment efficacies. The lack of dark toxicity observed for the *m*-THPC derivatives in comparison to *m*-THPC will result in a better safety profile.

4.3.2. Photocytotoxicity of *m*-THPC and tetrafunctionalized *m*-THPC derivatives after a period of incubation of 24 h – intracellular protocol

The general biological requirements for an ideal PS are strong internalization, minimal dark toxicity, high levels of photoactivity and relatively long excitation wavelengths.[408] Therefore, after determining the biocompatibility of derivatives **1**, **3** and **5**, phototoxicity experiments were performed to evaluate their potential applicability in PDT-induced treatments. The PSs were applied over a range of concentrations from 1.25 µM to 10 µM, staying below cytotoxic concentrations. After 24 hours of incubation, the B16F10 cells were washed and irradiated with 660 nm light at a dose of 0.4 or 2 J/cm^2. Under these conditions, we did not observe signs of cell death for derivatives **1**, **3** and **5** (**Figure 4.3**).

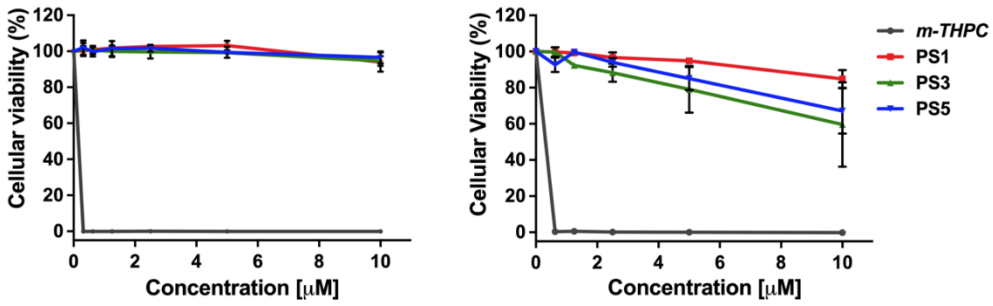

Figure 4.3. *Phototoxicity of m-THPC and tetrafunctionalized derivatives* ***PS 1****,* ***3*** *and* ***5*** *incubated with B16F10 melanoma cells for 24 hours and irradiated with 660 nm light at a LD of 0.4 J/cm^2 (left, n=3) or 2 J/cm^2 (right, n=2).*

In contrast, *m*-THPC caused 100% cell death even at the lowest applied concentration (1.25 µM). Results of this study led us to increase the LD from 0.4 to 2 J/cm^2, while maintaining a non-cytotoxic PS concentration range.

Similar to the previous experiment, the *m*-THPC derivatives did not exhibit significant phototoxicity towards the melanoma cells, while *m*-THPC caused 100% cell death at the lowest applied concentration (**Figure 4.4**).

Next, we decided to implement even more severe PDT conditions. The concentration range of the PSs was increased from 1.25 – 10 μM to 1.25 – 40 μM and the LD was increased from 2 to 4 J/cm^2. In B16F10 cells, strong phototoxic activity was observed at the highest concentration of **PS 3** (40 μM), reaching over 90% of cell death (**Figure 4.4**). **PS 1** and **5** did not exhibit phototoxicity under the applied conditions.

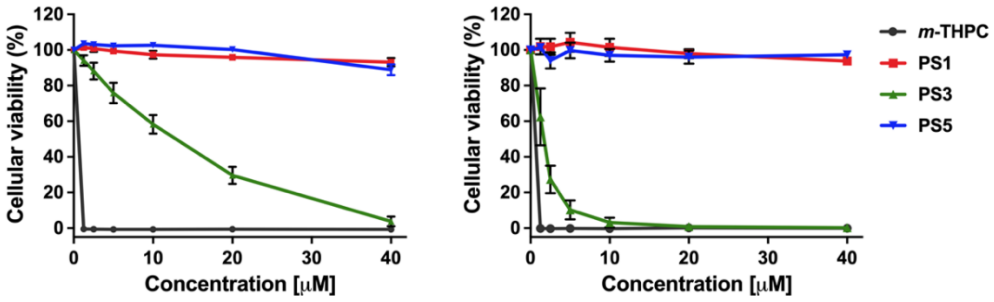

Figure 4.4. *Phototoxicity of m-THPC and tetrafunctionalized derivatives* ***PS 1****,* ***3*** *and* ***5*** *incubated with B16F10 melanoma cells (left, n=3) or CT26 colon carcinoma cells (right, n=3) for 24 hours and irradiated with 660 nm light at a LD of 4 J/cm^2.*

Similar results were obtained in CT26 cells; however, a stronger PDT effect was observed. For **PS 3**, 70% cell death was observed at a 10-fold lower concentration than in the case of the B16F10 cells. This is also reflected in the calculated IC_{50} for **PS 3** in both experiments. The IC_{50} value was over 20 times lower for the CT26 (0.88 μM) cells than for that of the B16F10 cells (19.99 μM). The limited phototoxicity of *m*-THPC derivatives was unexpected considering the similarity of their photophysical properties with the ones of *m*-THPC. As extensively described in **Chapter 1**, derivatives **PS 1**, **3** and **5** and *m*-THPC exhibited very similar $^1O_2$ quantum yields in both solvents, DMF and DMSO. Poor biological activity was then anticipated to be caused by inefficient cellular uptake of the PSs. To confirm this hypothesis, cellular internalization studies were conducted by taking advantage of the inherent fluorescence of the PSs.

4.3.3. Cellular uptake of *m*-THPC and tetrafunctionalized derivatives 1, 3 and 5.

Herein, an evaluation of the cellular uptake of derivatives **1**, **3** and **5** in comparison to *m*-THPC was performed using a cell lysis protocol. Based on the results obtained from three independent experiments, we observed that the cellular uptake of derivatives **PS 1**, **3** and **5** is ~10-fold lower comparison to *m*-THPC (**Figure 4.5**). These results explain the limited phototoxicity of the derivatives described earlier.

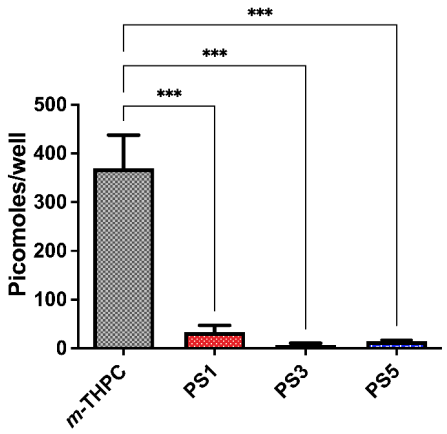

Figure 4.5. *Cellular uptake of m-THPC and derivatives* ***PS 1****,* ***3*** *and* ***5*** *following 24 hours of incubation with B16F10 melanoma cells Results are expressed as the mean values of 3 independent experiments: two-way ANOVA in comparison with untreated cells, p < 0.001 for* ***.

Cellular uptake and organelle tropism of a PS is strongly dependent on the ratio of hydro- or lipophilic moieties and charge distribution within the PS. Thus, we propose that differences on the polarity and amphiphilicity of the tetrafunctionalized derivatives might be a differentiating factor.[409] We observed in the aggregation study (**Chapter 3, Section 3.3.5**) that the introduction of aldehyde groups decreased the solubility of the PS in aqueous media. Nevertheless, similar to *m*-THPC and other known PSs, the hydrophobic character of the PS should allow for permeation of the compound through the biological membrane. Therefore, activity of the PS would be dependent on the aggregate/non-aggregate ratio at the time of irradiation. However, the opposite could be expected for **PS 3** where the introduction of carboxylic acid groups endowed water-solubility. This could potentially inhibit permeation through the lipid bilayer.

4.3.4. Photocytotoxicity of *m*-THPC and tetrafunctionalized *m*-THPC derivatives activated in the extracellular medium – extracellular protocol.

Peter R. Ogilby and co-workers have shown that singlet oxygen produced outside of cells (in the cell culture medium) is also capable of inducing cell death.[410,411] Due to the cellular uptake results indicating low internalization of the tetrafunctionalized derivatives **1**, **3** and **5,** in comparison to *m*-THPC, we then evaluated the PSs phototoxicity by using an extracellular photodynamic protocol. Herein, light irradiation was performed immediately after the addition of the PS solution to the cells. The PSs were applied in concentrations from 2.5 µM to 80 µM, and directly irradiated with 660 nm light at a LD of 15 J/cm^2. After irradiation, cells were washed to avoid bias of *m*-THPC dark toxicity. Next, cell viability was determined after 24 hours *via* the Alamar blue assay. We expected that upon light irradiation, the generation of ROS will allow for the destruction of the lipid bilayer *via* lipid peroxidation processes, resulting in cell death. We observed significant phototoxicity with *m*-THPC and **PS 3** but not with the **PS 1** and **PS 5** counterparts. However, *m*-THPC demonstrates a stronger therapeutic response at lower concentrations (40 and 20 µM) than the **PS 3** derivative (**Figure 4.6**). Interestingly, the CT26 cells were more sensitive towards *m*-THPC activity, resulting in over 90% cell death at the highest applied concentration, while 50% of the cells were viable after treatment with **PS 3** at the same condition. Further evaluation of the PSs ability to generate $^1O_2$ in aqueous media was performed to understand if the lack of toxicity is impacted by chromophore aggregation.

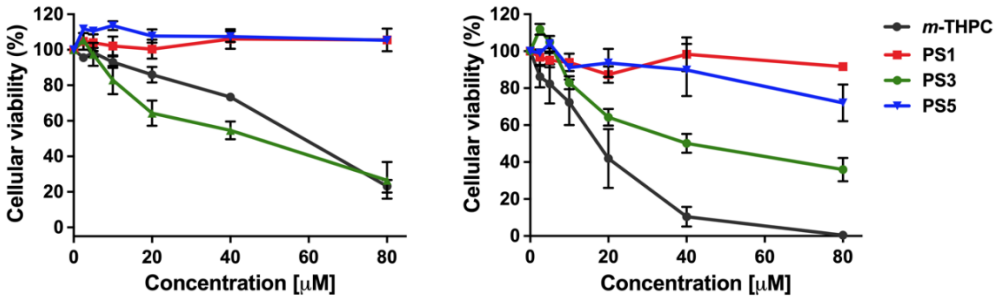

Figure 4.6. *Phototoxicity of m-THPC and tetrafunctionalized derivatives* ***PS 1****,* ***3*** *and* ***5*** *added to B16F10 melanoma (left, n=3) or CT26 colon carcinoma cells (right, n=3) and immediately irradiated at 660 nm with a LD of 15 J/cm^2.*

4.3.5. $^1O_2$ generation efficiency of *m*-THPC derivatives, PS 1, 3 and 5, in aqueous medium.

We evaluated the ability of **PS 1**, **3** and **5** to generate $^1O_2$ in polar solvents. For this, the PSs were dissolved in a 1:10 (v/v) DMSO/ethanol mixture and the ability of the compounds to generate $^1O_2$ was tested *via* direct detection of the $^1O_2$ phosphorescence signal at 1270 nm. The excitation wavelength was 532 nm for all compounds. We observed that **PS 1** and **5** displayed low $^1O_2$ generating efficiencies in polar solvents possibly due to the strong aggregation of the chromophores.[34] A negligible signal of the phosphorescence intensity at the 1270 nm was observed upon excitation of **PS 1** and **PS 5** (**Figure 4.7**). In contrary, **PS 3**, which contains carboxylic acid groups, efficiently generated $^1O_2$ (**Figure 4.7**). This means that **PS 3**, assumes a non-aggregated state in the cell culture medium allowing for the generation of longer-lived triplet states and consequently, ROS. Thus, further experiments were focused on the **PS 3** derivative which was considered as our lead compound.

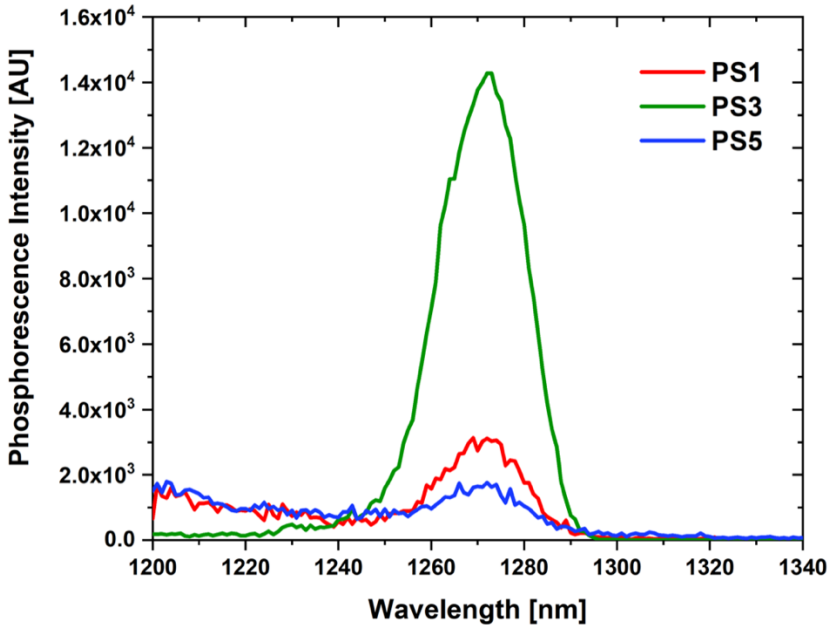

Figure 4.7. *Phosphorescence intensity of $^1O_2$ generated upon 532 nm laser irradiation of 10^{-4} M solutions of m-THPC and derivatives **PS 1**, **3** and **5** dissolved in an DMSO/ethanol mixture (1:10).*

4.3.6. Evaluation of lipid peroxidation after photo-activation of extracellular *m*-THPC and PS 3 using flow cytometry.

To evaluate the intensity of lipid peroxidation, we used a commercial kit (The Image-iT® lipid peroxidation kit) based on the BODIPY® 581⁄591 C11. This reagent localizes in lipid membranes throughout live cells and upon oxidation by lipid hydroperoxides, displays a shift in peak fluorescence emission from ~590 nm (red) to ~510 nm (green) providing a ratiometric indication of lipid peroxidation. Herein, B16F10 cells were treated with *m*-THPC, **PS 3** and cumene hydroperoxide (positive control). Cumene hydroperoxide can cause peroxidation of endogenous lipids in cytochrome P-450-containing systems.[412] Light irradiation (660 nm) at a dose of 15 J/cm^2 was immediately applied after the addition of the PSs to evaluate the extracellular effect of the generated ROS on the lipid membrane. Cells incubated with the lipid peroxidation sensor without any additional treatment were included as negative control. The obtained results indicate that the extracellular PDT protocol leads to lipid peroxidation in melanoma cells. This process was concentration dependent being observed higher fluorescence intensity for the *m*-THPC and **PS 3** at 40 μM than at 20 μM (**Figure 4.8**). **PS 3** induced slightly more lipid oxidation which is in line with the data obtained from the extracellular phototoxicity assay (**Figure 4.8**).

The obtained results help to explain the *in vitro* phototoxicity of **PS 3** in comparison to *m*-THPC. For the PDT-treated cells with higher lipid peroxidation levels, lower cell viability was observed. Moreover, different cell morphology was observed between cells treated with PSs and cumene hydroperoxide. Based on the obtained cell histograms, it is evident that oxidative stress caused by the positive control causes more severe changes in cell morphology than PDT-induced ROS (**Figure 4.8**). Interestingly, a large debris of cells observed only in the groups undergoing PDT treatment may suggest that the cell death processes are more complex and that the observed rapid cell death is a result of several processes, including necrotic cell death.[413]

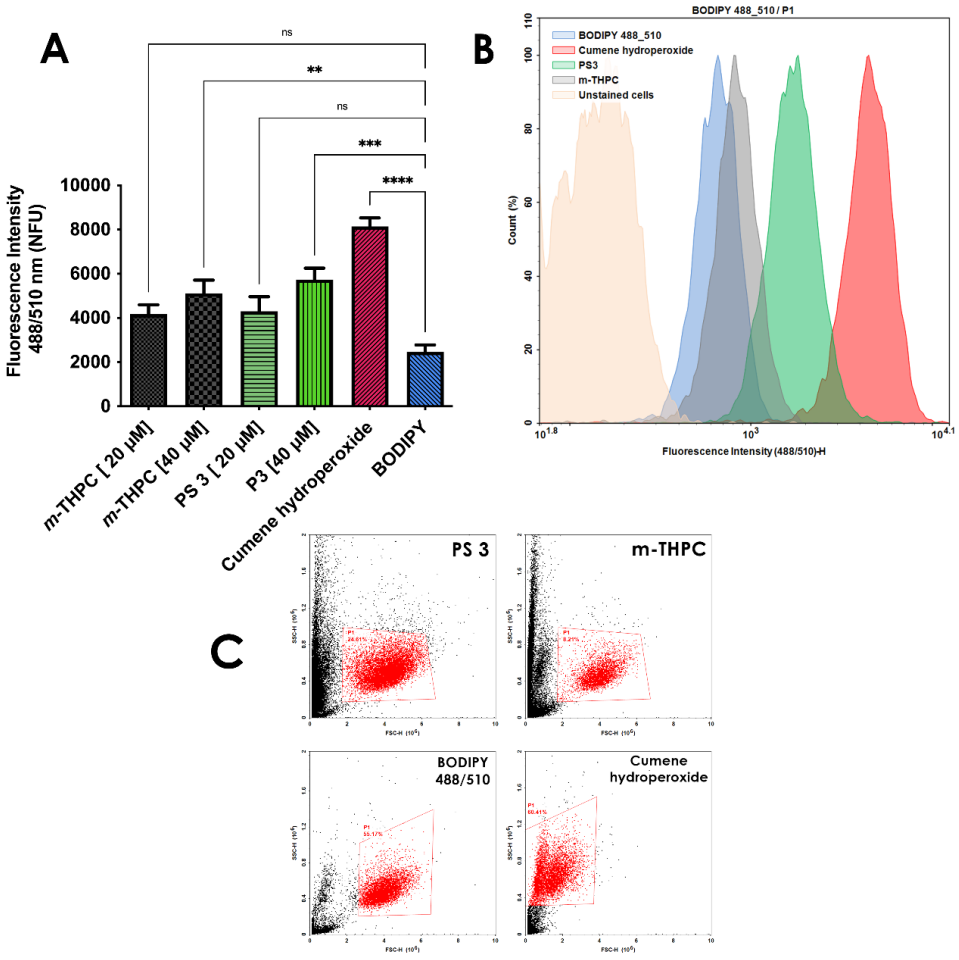

Figure 4.8. *(**A**) Lipid peroxidation of B16F10 cancer cells caused by photo-activated **PS 3** (20 and 40 µM), m-THPC (20 and 40 µM) and cumene hydroperoxide (10 µM). Results are expressed as the mean values of 3 independent experiments; two-way ANOVA in comparison with untreated cells; (**B**) Histogram of the fluorescence intensities of the lipid peroxidation caused by **PS 3** (40 µM), m-THPC (40 µM) and cumene hydroperoxide (10 µM); (**C**) Representation of flow cytometry dot plots of **PS 3** (top, left), m-THPC (top, right) and cumene hydroperoxide (bottom, right) treated B16F10 cells co-incubated with the BODIPY 581/591 probe (bottom, left). Lipid peroxidation was determined using a BODIPY® 581/591 probe and quantified via flow cytometry**** $p<0.0001$ *** $p< 0.001$, ** $p < 0.01$.*

4.3.7. Evaluation of lipid peroxidation caused by photo-activated extracellular *m*-THPC and PS 3 *via* confocal microscopy

A follow up study to confirm the lipid peroxidation upon extracellular PDT treatment, using **PS 3** and *m*-THPC, was performed by confocal microscopy. Cells were treated as mentioned on the previous section. After irradiation, cells were washed with PBS and images were immediately recorded using confocal microcopy. In this study, both the reduced (581/591) and the

oxidized (488/510) forms of the BODIPY were recorded. This provides a ratiometric, and consequently a more accurate indication of the lipid peroxidation process in B16F10 cells. According to the confocal images, peroxidation of lipids occurs not only on the surface of the cellular membrane (**Figure 4.9**).

The quantification of the fluorescence intensity ratio from the region of interest (ROI) from both channels, red (reduced) and green (oxidized), permit to quantify the intensity of the occurring peroxidation. Therefore, the stronger the fluorescence intensity signal of the oxidized form (green), the lower the ratio between the reduced and oxidized species. Obtained results from three independent measurements confirm the results from the flow cytometry analysis (**Figure 4.8**). Strong oxidation and a low fold-change of the fluorescence intensity was observed for the cumene hydroperoxide indicating the formation of lipid peroxides (**Figure 4.10**).

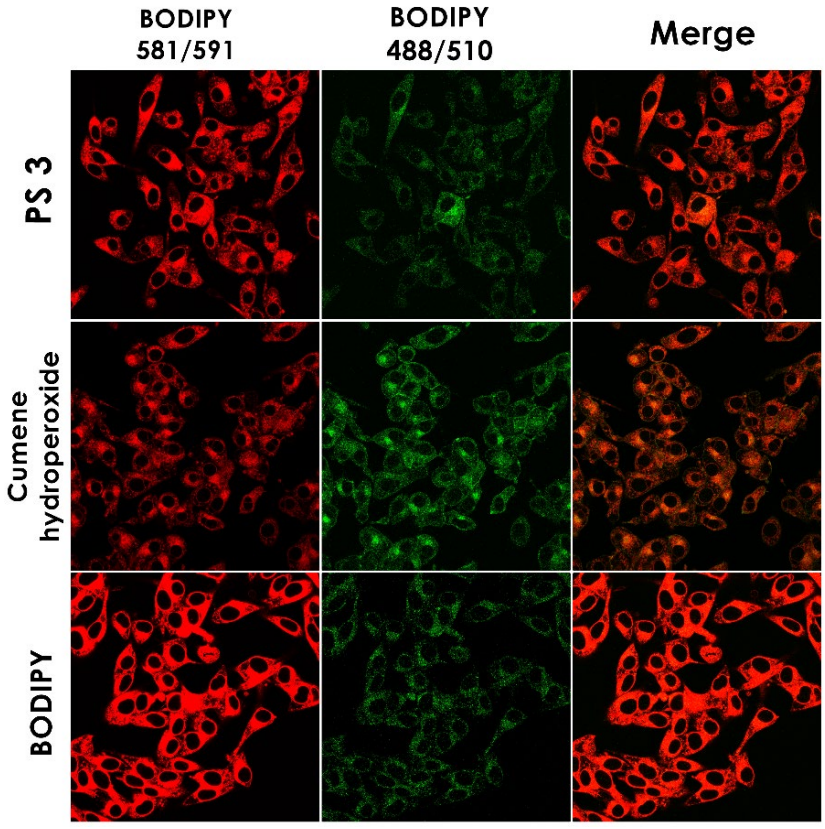

Figure 4.9. *Representative images of lipid peroxidation on B16F10 cancer cells caused by photo-activated* ***PS 3*** *(40 µM) Reduced (red) and oxidized (green) forms of the BODIPY® 581/591 probe were obtained via confocal microscopy. Cumene hydroperoxide (10 µM) was used as positive control.*

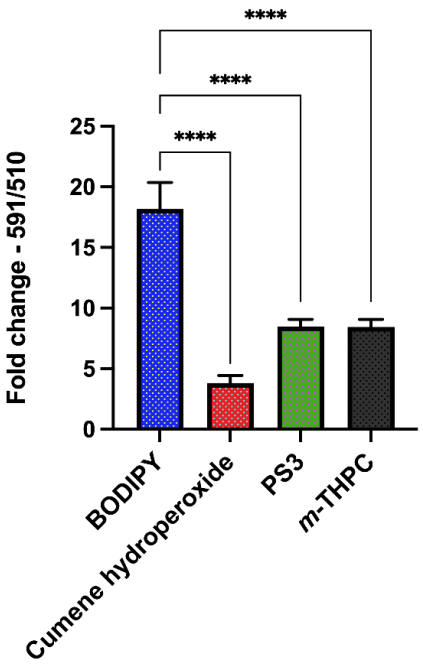

Figure 4.10. *Quantitative analysis of lipid peroxidation on B16F10 cancer cells caused by photo-activated* ***PS 3*** *(40 µM) Reduced (red) and oxidized (green) forms of the BODIPY® 581/591 probe were obtained via confocal microscopy. Cumene hydroperoxide (10 µM) was used as positive control. **** $p < 0.0001$*

4.3.8. Evaluation of the cell death mechanism.

The imbalance between the toxicity of ROS and the ability of cells to maintain homeostasis results in oxidative stress which ultimately triggers cell death. Differences modalities of regulated cell death have been described. Most of them are highly complex and their signaling pathways can partially overlap, which makes their identification a difficult task. To obtain a deeper understanding of the cancer cell death modalities caused by the phototoxic activity of **PS 3**, we took advantage of specific cell death inhibitors. Therefore, Z-VAD, BAPTA-AM, ferrostatin, and necrostatin (Nec-1) were incubated with cells 3 h in advance to PDT treatment. Z-VAD is a caspase inhibitor that has the ability to stop apoptotic processes.[414] BAPTA-AM is a membrane-permeable calcium chelator. Increased levels of calcium ions can lead to the activation of degradative enzymes responsible for apoptotic cell death.[415] Ferrostatin is a selective inhibitor for ferroptosis that, *via* reductive properties, can prevent damage of the cell membrane caused by oxidative processes.[416] Finally, Nec-1 inhibiting RIPK1 kinase activity, which is responsible for necroptosis cell death, was evaluated.[417]

Our results did not show significant differences of the cell viability when the different inhibitors were applied, which excludes apoptosis, ferroptosis and necroptosis as the main modalities of cell death trigger by PDT-**PS3** (**Figure 4.11**). These observations were unexpected considering that ferroptosis and apoptosis are the two main cell death pathways triggered by lipid peroxidation processes. Moreover, another possible mechanism of cell death can involve non-regulated pathways. It was previously shown by Sato *et al*. that PSs that target cellular membrane induce phototoxic effect by stimulation of accidental necrosis. One of the examples is monoclonal antibody-targeted dye, IR700, which accumulates in cell membranes.[418] Upon light exposure PS releases and accumulates in the membrane which causes physical stress within the membrane, leading to its rupture and consequently, necrotic cell death. The cell death is preceded by morphological changes of cells, resulting in swelling and blebbing. Therefore, to gain a deeper understanding of the cell death mechanism, evaluation of morphological changes induced by extracellular PDT protocol using **PS 3** and *m*-THPC was evaluated.

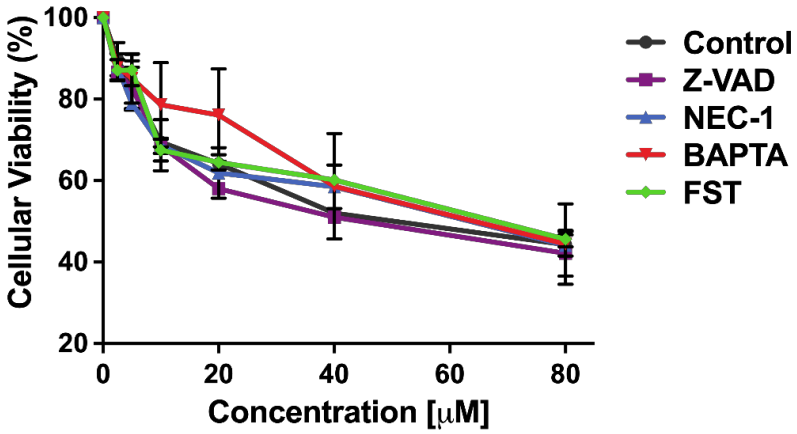

Figure 4.11. *Impact of cell death inhibitors on the viability of B16F10 melanoma cells after photoactivation of* ***PS 3*** *(40 μM) with irradiation at 660 nm with a LD of 15 J/cm^2 (n=2).*

4.3.9. Evaluation of morphological changes induced by extracellular PDT with PS 3.

Light transmission and fluorescence microscopy experiments were performed to obtain additional information about the mode of action of **PS 3**-based PDT. For this, cells were incubated with Hoechst and Propidium iodide 24 h after activation of extracellular **PS 3**. Hoechst 33342 is a cell-permeable

blue-fluorescent probe used for chromosome staining and allows us to observe changes on chromatin such as condensation and fragmentation.[419] Propidium iodide is not permeant to live cells, therefore is commonly used to detect dead cells in a population.[420] Herein, they were used together to give a broader overlook of the cell morphology and death processes caused by *m*-THPC and **PS 3**. For the control group, we observed that the morphology of melanoma cells takes the shape of the spindle- and epithelial-like cells with homogenous Hoechst distribution on the cell nuclei. As expected, a negligible signal for propidium iodide was observed confirming that the population of cells does not exhibit signs of death processes (**Figure 4.12**). In contrast, cell swelling was observed after *m*-THPC-PDT. These cells do not exhibit significant changes on Hoechst staining but a strong fluorescence signal for proprium iodide was observed. This staining profile is typical of necrotic cells. Similar conclusions can be drawn by analyzing the images of **PS 3** treated cells. The morphology of the cells is similar for the *m*-THPC treatment, however lower number of proprium iodide positive cells were observed, indicating lower toxicity when compared to *m*-THPC.

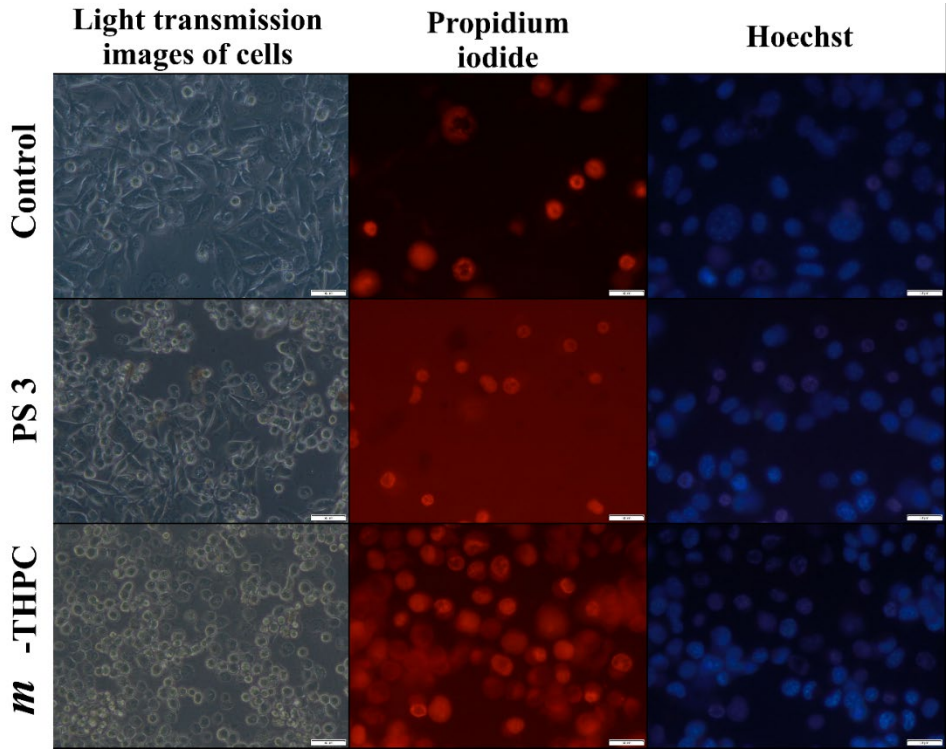

Figure 4.12. Representative images of *fluorescence microscopy of B16F10 melanoma cells recorded 24 hours post-treatment with* ***PS 3*** *(40 μM) or m-THPC (40 μM) - direct irradiation with 660 nm light with a LD of 15 J/cm^2. Cells were stained with propidium iodide and Hoechst. Untreated cells were used as a control group.*

4.4. Conclusions and outlook

In this chapter we reported the evaluation of the biological activity of *m*-THPC and tetrafunctionalized *m*-THPC derivatives, named **PS 1**, **3** and **5**, towards B16F10 melanoma and CT26 colon carcinoma cells. We observed that the derivatives exhibited a better safety profile in comparison to the mother compound and did not cause cytotoxicity up to 80 μM without light application. In comparison, the IC_{50} of *m*-THPC was found to be 19.39 μM and 11.19 μM for B16F10 and CT26 cell lines, respectively. Next, we tested the phototoxic activity of our compounds. Photo-activated *m*-THPC caused damage to cells leading to over 100% cell death at the lowest applied concentrations (1.25 μM and 0.4 J/cm^2). In contrast, phototoxic activity of **PS 3** was only observed when the LD was increased 10 times (4 J/cm^2). The calculated IC_{50} for **PS 3** was 19.99 and 0.88 μM towards B16F10 and CT26 cells, respectively. No phototoxicity was attained with **PS 1** and **PS 5** derivatives. The poor activity of these derivatives was unexpected considering the similarity of their photophysical properties with the ones of *m*-THPC. To deeper understand the poor phototoxicity of *m*-THPC derivatives, a cellular uptake study was performed. We observed that internalization of the derivatives within 24 hours of incubation is strongly inhibited, which explains the limited phototoxicity in comparison to *m*-THPC.

Photoactivation of *m*-THPC and its derivatives at the extracellular medium revealed significant phototoxicity for *m*-THPC and **PS 3**. The lack of phototoxicity observed for **PS 1** and **5** is likely explained by their aggregation in aqueous mediums. In accordance, direct measurement of the $^1O_2$ phosphorescence signal generated by the derivatives in more polar environments (1:10 solution of DMSO and ethanol) revealed insignificant signals for **PS 1** and **5**, while a strong signal was observed for **PS 3**. The limited internalization and strong aggregation of **PS 1** and **5** excluded their further application in PDT. Therefore, we focused on understanding the mechanism of action of **PS 3**. Due to the low level of PS internalization and good phototherapeutic response using the extracellular PDT protocol, lipid peroxidation was one of the mechanisms predicted to be responsible for the observed activity. Therefore, a lipid peroxidation assay was performed using flow cytometry and confocal

microscopy imaging. Both experiments confirmed that **PS 3** and *m*-THPC cause oxidation of the extracellular and intracellular lipid membranes. Considering the fact that lipid peroxidation can stimulate several signaling pathways leading to cell death, experiments using inhibitors of different regulated cell death mechanisms were tested. The obtained results did not allow us to clearly identify one main mechanism and the processes seem to be complex. Moreover, due to low cellular uptake of **PS 3** and yet phototoxic activity applying extracellular PDT protocol it can be surmised that accidental necrosis can be considered as one of the mechanism responsible for cell death. It is known that short incubation times favor PS tropism towards cell membrane and upon photoactivation can induce disruption of membrane integrity thus led to accidental necrosis.[105] It was shown by Kessel *et al*. that accumulation of chlorin e_6 in the plasma membrane a photosensitization process caused loss of membrane integrity and depletion of intracellular ATP leading to necrotic cell death.[421] In another example, a PDT effect, preceded by 2 hours of PS (ZnPc) incubation resulted in alterations of the cytoplasmic organelles and the plasma membrane indicating necrotic cell death mechanism.[422] Therefore, the distribution of the nucleus-targeted probe (propidium iodide) and swelling of the *m*-THPC or **PS 3** treated cells, strongly suggest accidental necrosis as the main mechanism of cell death. Our extensive evaluation of the biological properties of functionalized derivatives **1**, **3** and **5** in comparison to *m*-THPC allowed us selection of **PS 3** for further *in vivo* evaluation.

In summary, although several previously published reports focused on modification of the *m*-THPC structure to tune its photophysical properties and biological activity, no *temoporfin*-loaded hydrogels were reported for intratumoral drug delivery towards cancer. The activity of our lead compound, **PS 3,** differs from the parent compound. Due to the low level of internalization, the $^1O_2$ produced extracellularly by **PS 3** has been shown to trigger accidental necrosis likely through its action on the cell membrane, which often is followed by the release of DAMPs. However, the mechanism underlying immunogenic cell death in the context of PDT are still poorly understood and deserve further investigation. Additionally, **PS 3** in comparison with the parent compound lacks toxicity in the dark and exhibits water-solubility, which are desired properties of

the PS. Although new generation of PS is being tailored to specifically target overexpressed biomarkers of tumors, we expect that the lack of cytotoxicity in the broad range of PS concentrations, together with localized drug delivery *via* intratumoral injection of the stimuli-responsive hydrogel will allow for the reduction of the systemic side effects related with the treatment of Foscan and a therapeutic response towards melanoma and colon carcinoma tumors.

4.5. Experimental

General information

Unless otherwise specified, all chemicals were commercially sourced and used without further purification. CT26 cells (ATCC CRL-2638) and B16F10 (gently given by IPO, Porto, Portugal) were cultured in Dulbecco's Modified Eagle's medium (DMEM, Sigma-Aldrich) supplemented with 10% (v/v) heat-inactivated fetal bovine serum, 100 U/mL penicillin and 100 ng/ml streptomycin (Invitrogen). The Image-iT lipid peroxidation kits for live cells analysis were obtained from Thermofisher. Cellular viability analysis was performed using a synergy HT Multi-mode microplate reader (Biotek). Phototoxicity experiments were performed using a 660 nm LED lamp (Wolezek).

Cytotoxicity of *m*-THPC and tetrafunctionalized derivatives PS 1, 3 and 5.

B16F10 (6000 cells/ well) or CT26 (6000 cells/ well) cancer cells were seeded in 96-well plates to achieve a monolayer configuration. After 24 hours of incubation, a volume of 200 µL of the relevant concentration of *m*-THPC or **PS 1**, **3** and **5** was pipetted into the appropriate triplicate wells. The final concentrations of *m*-THPC and derivatives were from 2.5 to 80 µM. The stock solutions were diluted with culture medium (DMEM) maintaining the final concentration of DMSO below 1%. Cells were incubated with the PS solution for 24 hours, and after that time, washed with medium. Next, the plates were incubated for 24 hours at 37 °C. A Resazurin assay (Alamr blue) was used to assess the cytotoxicity of the tested PSs at various concentrations.

Phototoxicity experiments of *m*-THPC and tetrafunctionalized derivatives PS 1, 3 and 5– extracellular protocol.

B16F10 (6000 cells/ well) were seeded in 96-well plates to achieve a monolayer configuration. After 24 hours of incubation, a volume of 200 µL of the relevant concentration of *m*-THPC or **PS 1**, **3** and **5** was pipetted into the appropriate triplicate wells. The final concentrations of *m*-THPC and tetrafunctionalized derivatives was from 0.625 to 10 (for 0.4 and 2 J/cm^2) and from 1.25 to 40 µM (for 4 J/cm^2). The stock solutions were diluted with culture medium (DMEM) maintaining the final concentration of DMSO below 1%.

Cells were incubated with the PS solution for 24 hours, and after a washing step to remove non-internalized compound, cells were irradiated with a LD of 0.4, 2 or 4 J/cm^2. The correction factor from the overlap of the absorption spectra between the LED and each photosensitizer was calculated and applied in order to achieve accurate light doses.[423] The plates were then incubated for an additional period of 24 hours at 37 °C. Finally, the Resazurin assay was used to assess the cytotoxicity of each PS.

Phototoxicity experiments of *m*-THPC and tetrafunctionalized derivatives PS 1, 3 and 5 – extracellular protocol

B16F10 (6000 cells/ well) were plated in 96-well plates to achieve a monolayer configuration. After 24 hours of incubation, a volume of 200 µL of the relevant concentration of *m*-THPC or **PS 1**, **3** and **5** was pipetted into the appropriate triplicate wells and cells were immediately irradiated. The final concentrations of *m*-THPC and tetrafunctionalized *m*-THPC derivatives ranged from 2.5 to 80 µM. The stock solutions of *m*-THPC, **1**, **3** and **5** were diluted with cell culture medium (DMEM) maintaining the final concentration of DMSO below 1%. LD of 4 or 15 J/cm^2 were delivered to the cells. After 15 mins, cells were washed with medium to remove non-internalized compound and incubated for an additional period of 24 hours. Finally, the Resazurin assay was applied to evaluate the cell viability.

Singlet oxygen generation study in DMSO/Ethanol

PS 1, **3** and **5** were dissolved in a 1:10 (v/v) DMSO/ethanol mixture at the final concentration of 10^{-4} M and the ability of the compounds to generate $^1O_2$ was tested *via* direct detection of the $^1O_2$ phosphorescence signal at 1270 nm. The excitation wavelength was 532 nm for all compounds. For this, a home-built setup constructed from an Omni-l 300 Zolix spectrograph with a mounted cooled infrared detector module (Hamamatsu), and excitation from a fractionated fiber coupled 532 nm laser system (Optoelectronics Tech.) was used. Signals from the excitation source and the detector were fed to a Lock-in Amplifier (SciTec Instrument), and the spectra were collected by the dedicated Zolix software.

Cellular uptake

The cellular uptake of the PSs was performed by measuring the fluorescence of the supernatant obtained after cell lysis. B16F10 melanoma cancer cells were seeded in 24-well plates to obtain a seeding density 35 000 cells per well. On the next day, solutions of *m*-THPC, **PS 1**, **3** and **5** were added to the cells at a concentration of 8 µM in DMEM and incubated for 24 hours. Afterwards, cells were washed twice with DMEM followed by the addition of 200 µL of the lysis buffer (DMSO + 10% triton). Cell lysis was facilitated by scratching the bottom of each well. The cell lysate was transferred to a 1.5 mL tube and centrifuged (2000 rpm, 5 min). The supernatant was collected and 100 µL were transferred to a 96-well plate. A calibration curve of each PS in lysis buffer was prepared with concentrations ranging from 8 µM to 0 µM. Fluorescence measurements were carried out using a microplate reader (excitation: 460/40, emission: 645/20). Concentrations of the PSs were calculated based on the calibration curve (**Figure 4.13**).

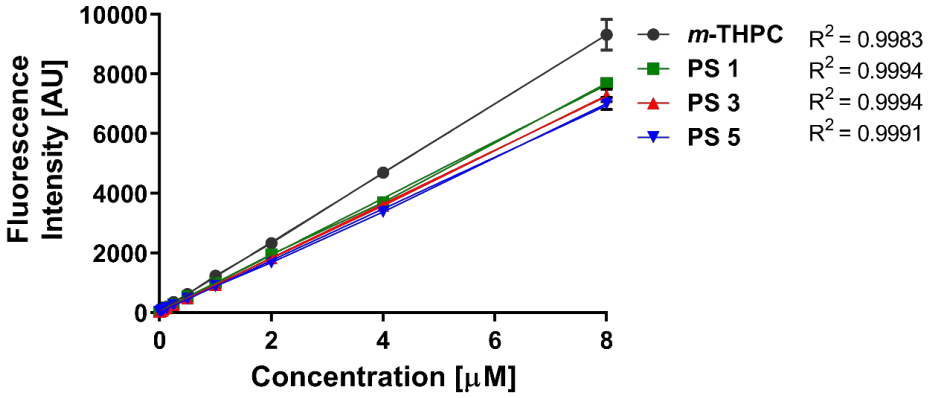

Figure 4.13. *Calibration curve of m-THPC,* ***PS 1****,* ***3*** *and* ***5*** *in lysis buffer in the range of concentrations from 8 µM to 0 µM*

Lipid peroxidation evaluated by flow cytometry.

The Image-iT® lipid peroxidation kit is based on C11 reagent and is a sensitive fluorescent reporter for lipid peroxidation. Upon oxidation in live cells, fluorescence shifts from red to green, providing a ratiometric indication of lipid peroxidation by flow cytometry (Novocyte® TM 3000 ACEA). Therefore, B16F10 cells were seeded in 24-well plates to obtain a seeding density of 50 000 cells per well. After 24 hours, the cells were incubated with 40 µM of cumene

hydroperoxide (positive control). The Image-IT kit at the final concentration of 10 µM was added to the cells 30 minutes prior to incubation with the PS and was present during the treatment. *m*-THPC and **PS 3** were added to the cells at a concentration of 40 µM and directly irradiated with a LD of 15 J/cm^2. Next, the fluorescence intensity of the oxidized BODIPY probe was detected on flow cytometry at an excitation/emission of 488/510 nm.

Lipid peroxidation evaluated by confocal microscopy

B16F10 (4000 cells/well) were seeded with a final volume of 250 µL in 8-well iBidi plates. After 24 hours, the cells were incubated with 40 µM of cumene hydroperoxide (positive control). The BODIPY® 581⁄591 from the Image iT Lipid peroxidation kit (ThermoFisher) at the final concentration of 10 µM was added to the cells 30 minutes prior to incubation with the PSs and was presented during the entire treatment. *m*-THPC and **PS 3** were added to the cells at a concentration of 40 µM and immediately irradiated with a LD of 15 J/cm^2. Images of lipid peroxidation were acquired on a Carl Zeiss LSM 710 confocal microscope using excitation laser at 488 for the BODIPY probe. Cell segmentation was performed using ImageJ software and the ratios of the signal from the 590 (reduced form) to 510 (oxidized form) channels were used to quantify lipid peroxidation in cells.

Evaluation of cancer cells death mechanism.

7000 B16F10 cancer cells (7000 cells/ well) were plated in 96-well plates to achieve a monolayer configuration. After 24 hours of incubation, cell death inhibitors, namely Z-VAD (25 µM), BAPTA-AM (5 µM), ferrostatin (5 µM), and Nec-1 (25 µM) were incubated of cell death were pipetted into cells in triplicate and incubated for 3 hours. Z-VAD and BAPTA-AM are inhibitors of apoptosis, while ferrostatin and necrostatin inhibit ferroptotic and necroptotic processes, respectively. The inhibitors were removed and 200 µL of **PS 3** was pipetted at concentrations of 80, 40, 20, 10, 5 and 2.5 µM into appropriate triplicate wells, followed by irradiation (LD = 15 J/cm^2). Cells were washed fresh medium, containing each inhibitor was added. After 24 hours of incubation, the Resazurin assay was applied to evaluate the cell viability. Inhibitors and applied concentrations are listed below:

Microscopic evaluation of the morphological changes induced by photo-activated PS 3 and *m*-THPC

4T1 cells (70 000 cells/ well) were seeded in 24-well plates at a final volume of 500 µL of DMEM. 24 hours later, *m*-THPC (40 µM) and **PS 3** (40 µM) were added. The cells were immediately irradiated with a LD of 15 J/cm^2 and then washed with PBS. Finally, Hoechst (3,24 µM) and propidium iodide (0,002 mg/mL) were added, incubated for 2 hours and 24 h and observed under a fluorescence microscope.

Statistical analysis.

The results are presented as the mean ± standard error (SEM). One-way ANOVA with Dunnett´s post-test was used to determine statistically significant differences of the means between the control group and the treated groups. Statistical differences were presented at probability levels of $p < 0.05$ *, $p < 0.01$ **, $p < 0.001$ *** and $p < 0.0001$.

Chapter 5 *In vivo* evaluation of PS 3 tetrafunctionalized *m*-THPC derivative, formulated in CS-based hydrogel, against melanoma (B16F10) and colon carcinoma (CT26) tumors

5.1. Introduction

Animal models are a tool to enrich our understanding on the mechanisms and etiology of human diseases. Considering the large amount of promising *iv* results being reported in the literature and the complexity of PDT treatments, animal models are necessary to prove and optimize the activity of novel PDT systems during the preclinical stage.[424,425] Although the number of *in vivo* experiments being performed each year continuously increases in the field of PDT, the number of new PSs and DDS reaching the clinical phase continues to fall.[426] Considering that large clinical trials for regulatory approval are dependent on pharmaceutical companies, PDT constantly stuffers from low acceptance by the pharmaceutical industry and the medical community that considers PDT field as a therapeutic niche and complex treatment due to the need for both a drug and a medical device.[427] Thus, PDT must be simple, successful and cost effective. The selection of cancer cell lines is another factor that requires consideration. The specific syngeneic tumor model used in animal studies is important for the immunological evaluation of the treatment but might be considered less relevant than cancer cell lines of human origin. Subcutaneous tumor models are routinely used in preclinical PDT owing to their high tumor accessibility to the irradiation process. Animal models allow to test and optimize a broad spectrum of treatment parameters. For instance, *in vivo* biodistribution studies allow to predict DLI, which correspond to the time between formulations administrations and irradiation. The DLI and biodistribution of the PS determines vascular versus cellular regimen of the PDT treatment. For vascular PDT, the DLI is usually short, and the treatment mainly affects the tumor vasculature as the PS is confined at the blood vessels. For cellular PDT, DLI is usually longer (*e.g.*, > 24h), allowing for drug distribution and uptake by the

cancerous cells.[428] The response to PDT differs for both approaches; however, in both cases edema and necrosis of the irradiated tissue is typically observed.

Due to the intensive development and increased application of hydrogel formulations as drug carriers, our motivation considered their evaluation at the preclinical stage. Recently several reports confirmed the benefits of using hydrogel-based delivery of PS towards tumors in the *in vivo* models. For instance, Zhou *et al*. was proposed a prolonged oxygen-generating chlorin e_6-poloxamer hydrogel to alleviate tumor hypoxia and induce immune response. PDT-induced activity suppressed the growth of primary 4T1 tumors and inhibited metastasis *via* stimulation of immune response. This was confirmed by increased level of IFN-γ produced by CD8+ cytotoxic T lymphocytes in mouse serum.[429]

It has been reported that many photo-activated PSs induce ICD and anti-tumor immunity.[105] Canti *et al*. demonstrated that rechallenged mice (that were previously cured from cancer by disulfonated phthalocyaninato)aluminium(III)-PDT treatment) were able to suppress tumor growth and remained tumor free for 100 days post rechallange.[430] This was further confirmed by several studies involving animal models with intact immune systems.[431–433] PDT engages both innate and adaptive immune system responses. The innate immune system responds immediately upon non-specific changes in the cellular microenvironment. It involves immune agents that take part in the first line of defense and includes cellular (neutrophils, macrophages, and natural killer cells) and non-cellular (complement and antibacterial peptides) agents.[120] Importantly, the innate immune system response is not followed by the formation of immunological memory.

The activation of innate immunity is often caused by PDT-induced local inflammation, which is caused by the release of inflammatory cytokines and lipid membrane derived arachidonic acid metabolites.[434] Furthermore, several reports highlight the link between PDT-induced inflammation and immune system activity.[435] The main goal of the innate immune system is to restore normal tissue function and homeostasis. In contrast, the adaptive immune system is highly specific to certain antigens and provides immunological memory. The activity is induced by antigen specific B and T cells. B cells are responsible for

the production of immunoglobulins, while T cells are divided into several populations with different functions.[436] Adaptive immunity can be divided into two types. Briefly, type 1 involves $CD4^+$ T cells that stimulate the activity of IL-12 and IFN-gamma and activation of $CD8^+$ T cells, while type 2 stimulates $CD4^+$ T cells that express IL-4, inducing the production of antibodies by B cells.[437] The debate on whether the immune response inhibits or promotes cancer progression continues. This is mainly due to the reported inter-dependence between inflammatory processes and cancer progression.[438] Moreover, paradoxically, activity of innate immunity was reported to exhibit ability to stimulate tumor angiogenesis (*via* production of growth factors, cytokines, chemokines) and suppress activity of the adaptive immune system.[439,440] Nevertheless, processes activated by the innate immune system are crucial for the initiation of the adaptive immune system.

In addition to *intravenous* (*I.V.*) and *intraperitoneal* (*I.P.*) drug administration, increased use of intratumoral injections is being observed namely with a variety of nanoformulations and multifunctional polymer structures.[441,442] Intratumoral drug delivery allows for a local, controlled and sustained PS distribution to the tumor site, avoiding non-specific drug accumulation in non-cancerous tissues, thus minimizing toxicity.[443] This allows to achieve high concentrations of the PS at the target side and improved therapeutic efficacy. Finally, intratumoral DDSs enable the loading and release of poorly soluble PS that exhibit tendency to aggregate upon *I.V.* administration.[444] This is a major obstacle causing prolonged side effects related with Foscan treatment.

In recent years, investigations of the antitumor immune response prompted by PDT have been reported for many PSs. These approaches involve: i) rechallenge experiments, ii) vaccination experiments, iii) disease progression in immunocompetent vs immunocompromised mice and, iv) evaluation and characterization of the immune mechanisms. Several reports using different tumor and animal models involve studies with *m*-THPC. For instance, in 1999 Coutier *et al*. showed that macrophage-like cells improve PDT effects. This was shown using the U937 human monocyte cell line and the best conditions for macrophage activation were reported when sublethal LDs were used.[445] Cecic *et*

al. showed that *m*-THPC- and Photofrin-PDT treatment of mammary sarcoma (EMT6) and SCC (SCCVII) tumors results in neutrophilia, which appeared essential for maintaining the elicited antitumor activity of these cells.[446] Follow up studies with *m*-THPC demonstrated that IL-1β is one of the critical mediator responsible for the therapeutic outcome of PDT in a SCCVII tumor model.[447] Moreover, Mitra *et. al.*, demonstrated that lower doses of *m*-THPC *in vitro* and *in vivo* lead to the stimulation of heat shock protein expression, which is responsible for suppressing properties due to their ability to stimulate the activity of innate immune system towards the tumor cells.[448–450]

Importantly, the ability of *m*-THPC to stimulate the immune response was recently confirmed in clinical practice. The study group contained nine patients with head and neck SCC that underwent *m*-THPC induced PDT treatment *via I.V.* injection, according to the regulatory protocol.[451] The data was based on blood sample analysis collected at different timepoints: 24 h before PDT, 24 h after PDT, one week after PDT, and four to six weeks after PDT. The results obtained indicate an increase in pro-inflammatory cytokines including IL-6 and IL-10, NK cells, and HMGB1 proteins. The links between PDT and immunology have been attentively elaborated in a recent review by the Oliveira group.[452] Moreover, the recent discovery of immune checkpoint inhibitors by James Allison and Tauku Honjo (2018 Nobel Prize in Physiology or Medicine) stimulated researchers to intensify work towards combination cancer and immune- therapies.[453]

5.2. Objectives

Herein, the activity of **PS3-PEG-CS** hydrogels will be tested towards melanoma and colon carcinoma tumors. Hydrogel formulation will be injected intratumorally towards CT26 colon carcinoma and B16F10 melanoma tumors. We aim that local administration of the PS will allow for controlled and sustained PS distribution to the tumor site, avoiding non-specific drug accumulation in non-cancerous tissues, thus minimizing toxicity related with the *I.V.* treatment with Foscan. Advantage of the **PS3-PEG-CS** hydrogel formulation will be compared with the PBS solution of **PS 3**. First, biodistribution studies will be performed to evaluate the best DLI for the treatment. Next, based on the results from a preliminary screening of optimizations, we aim to select the best PDT conditions. As shown in **Chapter 2**, *in vitro* drug release study proved pH-dependent, prolonged release of the PS from CS-based hydrogel. Therefore, taking into consideration the expected prolonged release of the PS from the hydrogel at the site of injection, further improvements in the therapeutic efficacy will be achieved by exploring a multiple irradiation protocol. Additionally, we expect that multiround light stimulation will allow for enhanced stimulation of the immune system. As referred in the **Chapter 1**, immune responses elicited by PDT are extremely important for the outcome of the treatment. Therefore, we aim to explore PDT-induced activation of the immune system *via* three protocols: 1) rechallenge of cured animals two months after PDT treatments, 2) evaluation of abscopal effects on a pseudo-metastatic model and 3) evaluation of the PDT activity in immunocompetent *versus* immunocompromised mice. We aim that obtained results will contribute to better understand the mechanisms behind the **PS3-PEG-CS** localized therapy into a systemic therapeutic response. We expect that our therapeutic approach will allow to inhibit growth of primary tumors and allow to control distant metastasis while being safer that the commercial counterpart, *m*-THPC

5.3. Results and discussion

5.3.1. Biodistribution study

The biodistribution of a PS affects the efficacy and safety of the treatment, which are deciding factors of the formulation applicability in the clinic. For example, non-specific accumulation of a PS in healthy tissues (*e.g.*, skin) can cause unintended toxicity (*e.g.*, skin photosensitivity), reducing the safety profile of the applied formulation. One possible approach to overcome this limitation relies on the use of injectable hydrogels with controlled and low release of the PS, as the ones mentioned in **Chapter 3**. The biodistribution study of **PS 3** released from the hydrogel matrix was carried out with in two subcutaneous tumor models: B16F10-tumors in C57BL/6J mice and CT26-tumors in Balb/c mice. **PS3-PEG-CS** hydrogel and **PS3-PBS** solution were injected intratumorally when the tumor volume reached 5 mm in diameter. An experimental group which was given an intratumoral injection of the **PEG-CS** hydrogel, without the PS in the network, was used as control group. Slow, pH-specific, prolonged release of the PS from the **PS3-PEG-CS** hydrogel scaffold at the tumor site was monitored by measuring the fluorescence of the **PS 3** (**Figure 5.1**). Directly after injection, negligible fluorescence was detected, indicating that the PS was quenched in the hydrogel network. As the **PS 3** was being release, increased **PS 3** associated signal was measured. The strongest signal was observed 6 and 24 h post injection in both tumor models. Sustained drug release was observed for three days (72 h) as shown in **Figure 5.2**. This confirmed our assumption that pH-dependent cleavage of the cross-link bonds occurs in the slightly acidic tumor microenvironment. In contrary, for the **PS3-PBS** solution, the fluorescence signal was observed immediately after injection. However, significant signal intensity of the 'free' PS was only detected 24 h post-injection. This indicates that the majority of **PS 3** is cleared from the tumor site within the first 24 h. Based on the quantification of the fluorescence intensity signal from the established region of interest (ROI) we observed a statistically significant difference in the fluorescence intensity signal of **PS3-PEG-CS** and **PS3-PBS** for the 6, 48, and 72 h time points in the CT26 tumor model (**Figure 5.1**). Smaller differences were observed for the B16F10 tumor model, which may indicate that **PS 3** exhibit different release kinetics or clearance rates in the

two tumor models. *In vivo* release profiles might be impacted by differences in the tumor microenvironment between the two models, for instance a different pH value or the advancement of the tumor vasculature. One of the characteristic properties related with human melanoma tumors is the acidification of the tumor microenvironment.[454] De Milito *et al*. using CB-17 SCID/SCID female mouse model showed that the extracellular pH value of engrafted Mel501 melanoma tumors was 6.42 ± 0.19.[455] In contrast, the intracellular pH of CT26 cells was found to be 7.19 ± 0.14.[456]

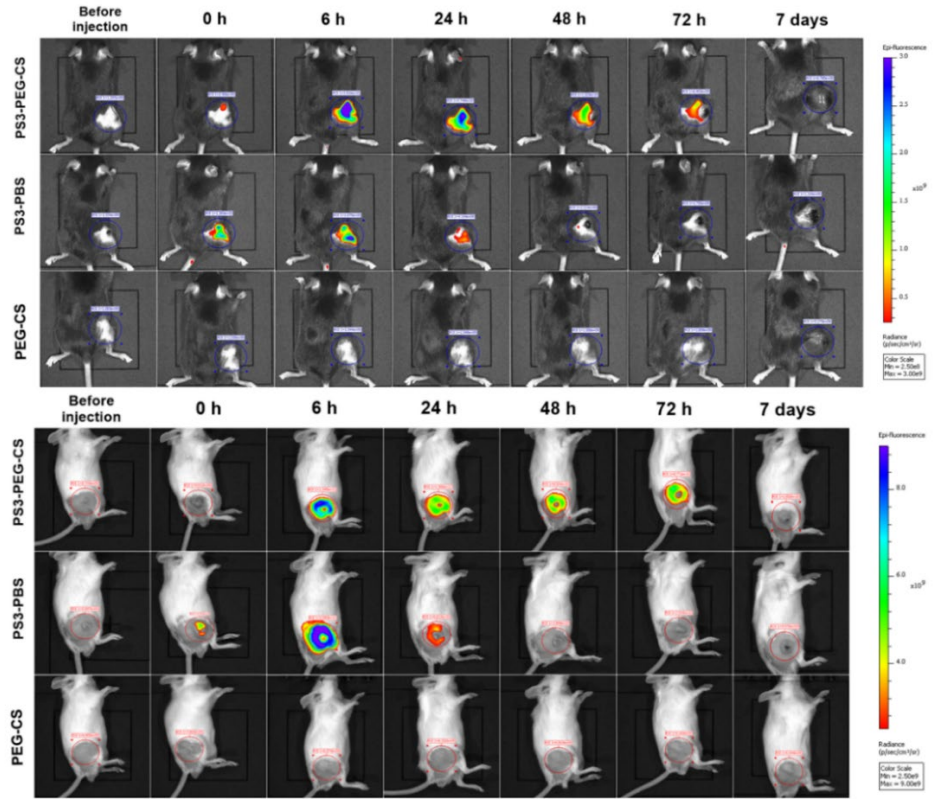

Figure 5. 1. *Representative in vivo fluorescence images of C57BL/6J (**top**) and Balb/c (**bottom**) mice at the indicated time points after intratumoral injection of **PS3-PEG-CS**, **PS3-PBS**, and **PEG-CS** ($\lambda_{ex.}$ = 420 nm, $\lambda_{em.}$ = 600-700 nm, dose of PS **3** = 0.08 mg).*

On the 7th day of the experiment, **PS 3** was not detected at tumor sites and the animals were sacrificed. The main organs (bladder, tumor, spleen, liver, muscle, and kidneys) were collected for *ex vivo* detection of **PS 3** (**Figure 5.3**). No specific accumulation of **PS 3** was observed in any organ in comparison to the control group. Trace amounts of **PS 3** were observed in the bladder, which corresponds to the water-soluble nature of the PS, indicted by its presence in the urine. The data obtained indicate that **PS 3** is completely cleared from the body

within one week. This is particularly important in PDT to avoid skin photosensitivity. Moreover, we did not observe any major differences in organ morphology, which is a clear sign that **PS 3** did not cause toxicity towards healthy tissues without light irradiation.

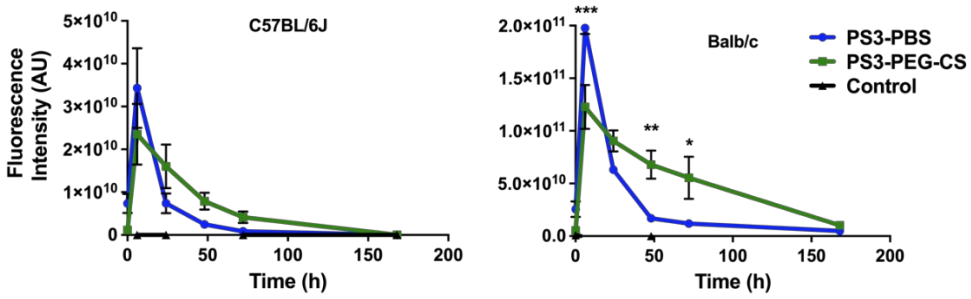

Figure 5.2. *Time dependent fluorescence intensities of the* ***PS 3*** *quantified in vivo upon intratumoral injection of* ***PS3-PEG-CS***, ***PS3-PBS*** *or* ***PEG-CS*** *formulations in melanoma (left) or colon carcinoma (right) tumors.* $\lambda_{ex.}$ *= 420 nm,* $\lambda_{em.}$ *= 600-700 nm, dose of* ***PS 3*** *= 0.08 mg, n=3. *** p<0.001, ** p<0.01, * p<0.05.*

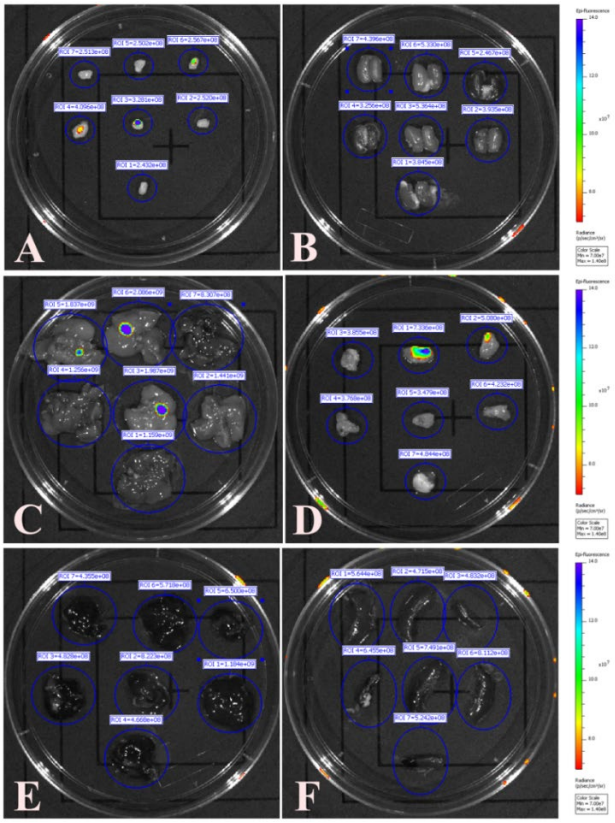

Figure 5.3*. In vivo fluorescence images of organs collected from C57BL/6J mice after intratumoral injection of* ***PS3-PEG-CS*** *(first line on the Petri dish),* ***PS3-PBS*** *(Second row on the Petri dish) and* ***PEG-CS*** *(The third row on the Petri dish). Muscle (A), kidneys (B), liver (C), bladder (D), tumors (E) and spleen (F).* $\lambda_{ex.}$ *= 420 nm,* $\lambda_{em.}$ *= 600-700 nm, dose of* ***PS 3*** *= 0.08 mg.*

5.3.2. CT26 colon carcinoma tumor model

5.3.2.1. Optimization of the PDT protocol

An optimization study was performed using the CT26 tumor model, which was inoculated subcutaneously into Balb/c mice. We selected LD of 20 and 30 J/cm^2 which was applied 24 h after **PS3-PEG-CS** hydrogel injection. However, considering the results of the *in vitro* study described in **Chapter 4**, **Section 4.3.2**, where **PS 3** exhibited 10 times stronger phototoxicity towards CT26 cells in comparison to the melanoma cell line, and higher immunogenicity in the melanoma CT26 tumors, we decided to apply lower drug doses for the *in vivo* evaluation. Therefore, drug doses of 0.04 or 0.07 mg and LDs of 20 or 30 J/cm^2 were evaluated. Contrary to the melanoma model, a strong phototoxic response was observed across all applied treatment conditions. Extensive edema at the tumor site was observed within two days post-treatment, indicating strong local inflammation. In the case of the higher applied doses (0.07 mg and 30 J/cm^2), strong inflammation of the treated area was followed by the appearance of necrosis, which led to formation of large wounds (**Figure 5.4**). This resulted in long recovery times of 3 – 4 weeks post treatment for the animals.

A good therapeutic outcome was obtained for the dose combination of 0.04 mg - 30 J/cm^2 and 0.07 mg - 20 and 30 J/cm^2. Survival analysis showed an increase in animal survival in the first 2 to 3 weeks post treatment owing to inhibited tumor growth (**Figure 5.5**). Moreover, full animal recovery without tumor recurrence was achieved in 50% of mice of both groups up to 60 days. In contrast, doses of 0.04 mg and 20 J/cm^2 were insufficient to inhibit tumor growth. Although cases of tumor regrowth occurred under all treatment conditions applied it was significantly delayed and correlated with the treatment conditions. Higher drug doses are related to larger hydrogel injection volumes, which can cover larger areas and consequently increase the number of cancer cells affected by the treatment. Importantly, in our case the signs of regrowth often occurred at the borders of the illuminated area, indicating that the injected volumes of the hydrogel, especially at lower doses, are insufficient to cover the tumor site. Nevertheless, in contrary to the melanoma tumor model, it was possible to obtain cures in 3 out of the 4 treatment groups.

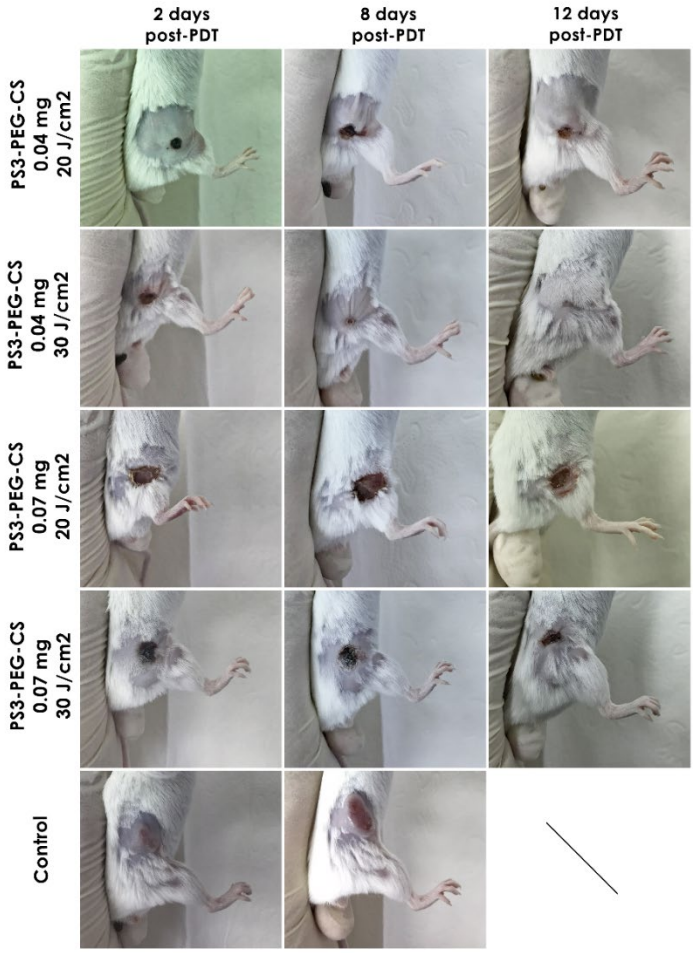

Figure 5.4. *Post PDT images of Balb/c mice undergoing optimization treatment using* ***PS3-PEG-CS*** *(DLI = 24 h, drug dose = 0.04 – 0.07 mg, LD = 20 – 30 J/cm^2, λ = 660 nm).*

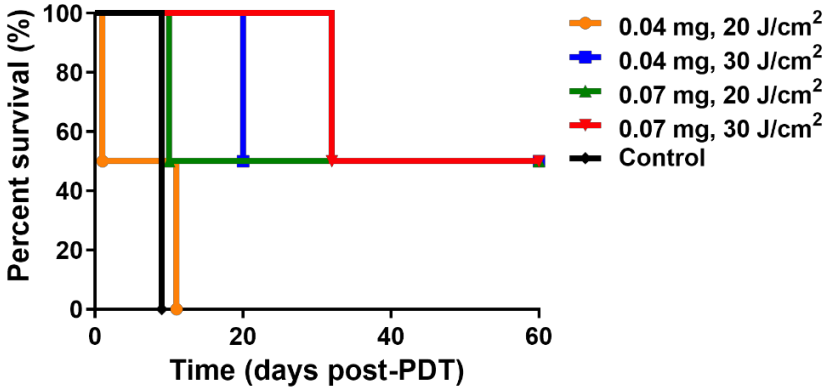

Figure 5.5. *Kaplan–Meier survival analysis of male Balb/c mice bearing CT26 tumors. An optimization study of the PDT treatment using the* ***PS3-PEG-CS*** *hydrogel. Each treatment groups contains of 1 – 2 mice. (DLI = 24 h, drug dose = 0.04 – 0.07 mg, LD = 20 – 30 J/cm^2, λ = 660 nm).*

5.3.2.2. Single treatment protocol

The best treatment conditions selected in **Section 5.3.2.1** were then applied to larger groups. The average drug dose used for the treatment was 0.07 mg of **PS 3** which was followed by irradiation (20 J/cm^2) 24 h post-injection. In this study, we included another treatment group, which received 'free' **PS 3** dissolved in PBS. Our goal was to compare the impact of the PS distribution at the injection site on the treatment efficacy and to evaluate the risk of unwanted side effects including toxicity towards healthy tissue. The **PS3-PBS** formulation was injected intratumorally, maintaining the same volume of the formulation as **PS3-PEG-CS**. Similar to the melanoma model, strong edema of the irradiated area was observed directly after the treatment and lasted up to 48 h (**Figure 5.6**). Finally, progressive necrosis and formation of a scab was observed in the first week post-treatment.

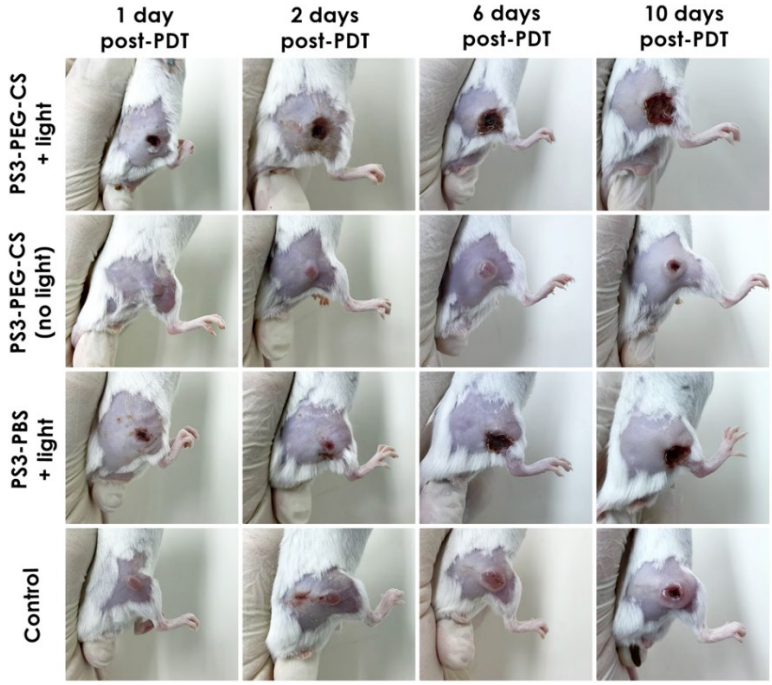

Figure 5.6. *Post PDT images of Balb/c mice undergoing single irradiation protocol using the* ***PS3-PEG-CS*** *or* ***PS3-PBS*** *formulation (DLI = 24 h, drug dose 0.07 mg, LD = 20 J/cm^2, λ = 660 nm).*

The results obtained show a small advantage of the hydrogel formulation over free PS. This is reflected in the survival analysis which allowed to obtain 50% survival rate of the treated group, while survival in the **PS3-PBS** group was below 40% (**Figure 5.7**). A better therapeutic response at the 24 h timepoint was

achieved for the hydrogel as it allows for a homogenous distribution of the formulation at the injection site and sustained release of the PS from the network. **PS3-PEG-CS** hydrogel without light irradiation led to a higher survival rate in comparison to the control group, which might be explained by the mechanical destruction of the tumor at the injection site.

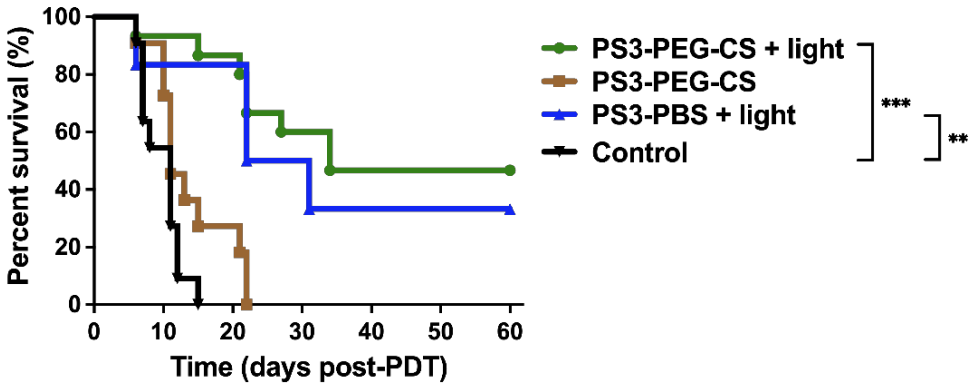

Figure 5.7. *Kaplan–Meier survival analysis of male Balb/c mice bearing CT26 tumors. A single irradiation protocol for the PDT treatment using the* ***PS3-PEG-CS*** *or* ***PS3-PBS*** *formulation. Each treatment groups contains 6-15 mice (DLI = 24 h, drug dose 0.07 mg, LD = 20 J/cm^2, λ = 660 nm). *** p<0.001, ** p<0.01.*

5.3.2.3. Multiple treatment protocol

Considering the good therapeutic response from the study performed previously using single irradiation of the tumor site (**Section 5.3.2.2**), for the multiple irradiation protocol we decided to include an additional group that received a lower dose of **PS 3** (0.04 mg). These conditions allow to verify if the multiple irradiation protocol allows for a better therapeutic response at reduced doses due to the efficient stimulation of the immune system. Moreover, a reduction of the drug dose will increase the safety profile of the formulation and decrease the injection volume of the hydrogel.

A significant improvement of the animal survival rate was observed for the protocol involving multiple light irradiations. Interestingly, the results confirmed our hypothesis and a survival rate of 67% for both applied doses of the PS was observed. The survival rate at 60 days post-PDT for the multiple irradiation protocol was over 60%, compared to 50% for the single irradiation protocol (**Figure 5.8, 5.9**). Again, a weaker effect was achieved for the **PS3-PBS** group.

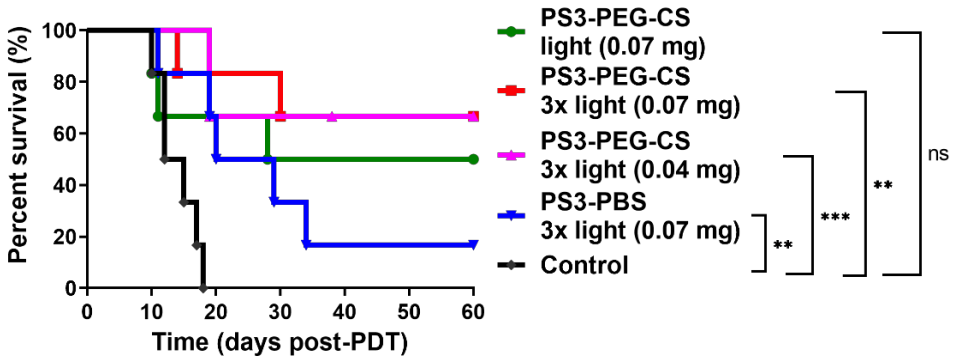

Figure 5.8. *Kaplan–Meier survival analysis of male Balb/c mice bearing CT26 tumors. A comparison between the single and multiple irradiation protocol for the PDT treatment using the* ***PS3-PEG-CS*** *or* ***PS3-PBS*** *formulation. Each treatment groups contains 6 mice (DLI = 24–72 h, drug dose = 0.04 or 0.07 mg, LD = 20 J/cm^2, λ = 660 nm). *** p<0.001, ** p<0.01, * p<0.05, ns – p>0.05.*

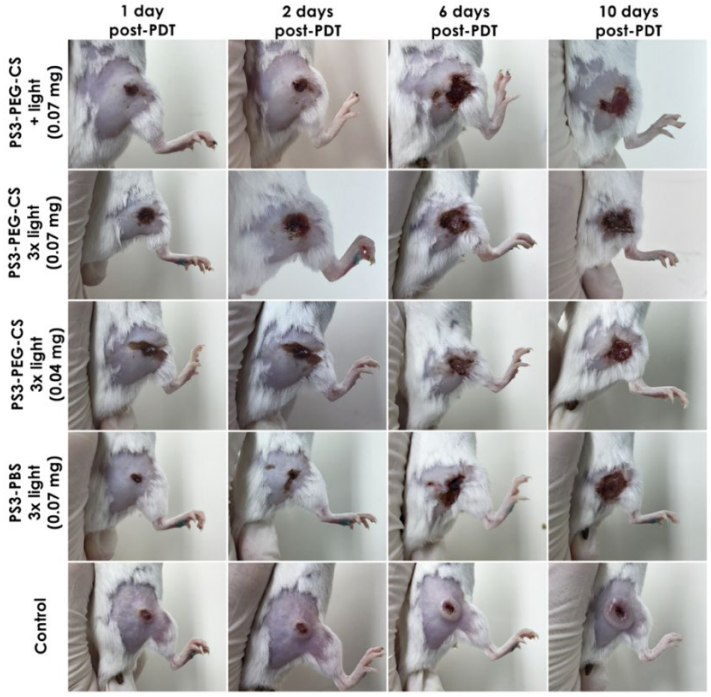

Figure 5.9. *Post-PDT images of Balb/c mice undergoing single and multiple irradiation protocols using the* ***PS3-PEG-CS*** *or* ***PS3-PBS*** *formulation (DLI = 24–72 h, drug dose = 0.04 or 0.07 mg, LD = 20 J/cm^2, λ = 660 nm).*

The results prove that a multiple irradiation protocol against the CT26 tumor model can enhance treatment efficacy. Although at the beginning progressive necroses and oedema were observed (**Figure 5.9**), tumor regrowth was mainly observed for the **PS3-PBS** formulation. This is probably explained by the faster tumor clearance of **PS 3** when administered in its free form.

5.3.3. Melanoma tumor model

5.3.3.1. Optimization of the PDT protocol

Melanoma is a type of skin cancer characterized by high pigmentation due to high melanin production. The selected tumor model, B16F10 cells, is syngeneic to C57BL/6 mice which have high pigmented skin. Melanin absorbs light in UV and visible regions meaning that it can have a negative impact during PDT.[457] Secondly, hyperactivity of melanocyte-based enzymes can cause posttranslational modifications, resulting in inhibition of apoptogenic signaling and leading to resistance to the targeted therapies.[458] Previous work with *redaporfin-PDT* also showed that CT26 tumors respond better to PDT than the B16F10 melanoma tumor model.[459] The different therapeutic outcome observed in each cancer model may be due to the differences in the immunogenicity of CT26 tumors and the melanoma model. It was shown in a comprehensive immune profiling study of eight murine solid tumors (CT26, B16F10, 4T1, MAD109, LLC, RENCA) that the CT26 colon tumor model exhibited high immunogenic profile while the B16F10 melanoma model was the least immunogenic.[460] Although PDT has potential as a treatment of melanoma, a deeper understanding of PDT-induced processes is required to optimize effective treatment conditions.

Our first attempt to selecting the best condition to treat B16F10 tumors, included varied PS doses (0.03 – 0.08 mg) and LDs (20 – 36 J/cm^2) The area of the irradiation was 15 mm. The hydrogel was injected intratumorally when the tumor size reached ca. 6 mm diameter and was followed by illumination at 660 nm 24 h later. An assessment of the treatment efficacy was performed by monitoring tumor growth kinetic post-treatment until the animals reached the experimental endpoint (12 mm diameter). The treatment efficacy was further evaluated using a Kaplan-Meier survival plot, which is presented in **Figure 5.10**. The experimental results show that for **PS3-PEG-CS** at 0.055 mg and LDs of 20 and 30 J/cm^2, no signs of phototoxic activity towards melanoma tumors were observed. The Kaplan-Meier analysis presented in **Figure 5.10.** shows that survival of these groups were not significantly different from the untreated group. However, by increasing the dose to 0.08 mg and 36 J/cm^2, it was possible to obtain a PDT response and tumor damage. Although formation of the edema

at the irradiation site was observed for all protocols, its intensity was dependent on the severity of the applied treatment conditions. This means that for LDs of 20 and 30 J/cm^2, the edema had a temporary effect that lasted during the first few hours post-treatment, when in contrary when a LD of 36 J/cm^2 was used the effect lasted 24 h. This suggests that **PS 3** can trigger local inflammatory processes, which are a driving factor for activation of antitumor immunity.[121] Moreover, although signs of necrosis were observed at the highest applied treatment conditions, the processes were insufficiently severe to inhibit the growth of primary tumors. Thus, continuous growth of melanoma tumors was observed up to the endpoint of 8 days post-treatment. We surmise that this treatment is unable to regress tumors over 6 mm in diameter due to their advanced stage. Moreover, considering that 660 nm light can achieve approximately 5 mm tissue penetration, the efficacy of treatment on advanced and pigmented tumors is decreased.

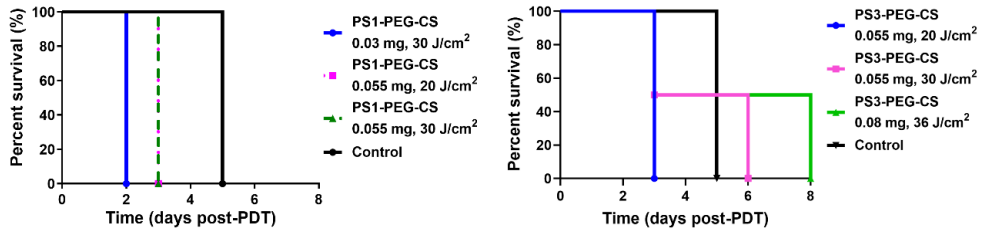

Figure 5.10. *Kaplan–Meier survival analysis of female C57BL/6J mice bearing B16F10 melanoma tumors. An optimization study of the PDT treatment using* ***PS1-PEG-CS (left)*** *or* ***PS3-PEG-CS (right)*** *hydrogels. Each treatment groups contains 1 mouse. (DLI = 24 h, drug dose = 0.03 – 0.08 mg, LD = 20 – 36 J/cm^2, λ = 660 nm).*

In this study, **PS1-PEG-CS** was also used to test whether the formulation *in vivo* will result in improved treatment efficacy in contrary to the *in vitro* results. It was expected that upon cleavage of the cross-link bonds of the hydrogel network, the PS remains partially conjugated to the polymer, resulting in enhanced PS uptake and activity.[461] We did not observe a response to treatment with the **PS1-PEG-CS** formulation. No signs of local inflammation nor necrosis were noted. Due to the promising therapeutic response at the highest applied treatment conditions for the **PS3-PEG-CS** formulation, doses of 0.08 mg and 36 J/cm^2 were selected for further evaluation towards smaller, less advanced melanoma tumors. Summarizing obtained results allow to conclude

that the PDT effect of the intratumorally injected **PS3-PEG-CS** formulation is insufficient to treat larger tumors at the applied light and drug conditions. Next, considering the results of the biodistribution study (**Section 5.3.1**), which showed that the highest **PS 3** release was attained 6 and 24 h after the hydrogel injection, we sought to investigate the impact of different DLI on the PDT efficacy. It was expected that PSs cross-linked within a hydrogel formulation remain in a non-aggregated state. Therefore, the PS entrapped in the hydrogel is expected to generate ROS and cause damage to the surrounding tissues.[462] Then, we expected that by applying different DLIs, we could observe differences in the activity of the formulation.

Herein, **PS1-PEG-CS** and **PS3-PEG-CS** hydrogels (0.08 mg) were injected intratumorally and tumor irradiation (36 J/cm^2) was performed at different timepoints – directly after hydrogel injection (0 h) and 7 or 24 h post injection. Survival analysis presented in **Figure 5.11** indicates that the most efficient therapeutic outcome was obtained for the **PS3-PEG-CS** formulation at the 24 h timepoint. Under these conditions, we observed the formation of a local edema, suggesting the activation of inflammatory processes. Moreover, during the first four days post-treatment local inflammation was followed by tumor necrosis, which indicated the destruction of tumor cells. The survival rate was extended to 18 days post-treatment compared to five days of the untreated group. Although for **PS3-PEG-CS**, local inflammation was also observed when tumor illumination was performed at the 7 h timepoint, PDT-induced toxicity was insufficient to inhibit tumor growth. The maximum survival rate in this group was 11 days. We did not observe any signs of PDT when light irradiation was performed directly after **PS3-PEG-CS** application, thus the animals reached the endpoint within five days post-PDT. Finally, no signs of PDT effects were observed at any of the applied conditions for **PS1-PEG-CS**, thus excluding the use of the formulation for further *in vivo* evaluation. Overall, the results confirm our predictions that the PS is only effective upon released from the polymeric network into the tumor interstitium. We expect that although it might be possible to generate $^1O_2$ inside or on the surface of the hydrogel, the distance between $^1O_2$ and the tumor cells is too large to cause a cytotoxic effect.

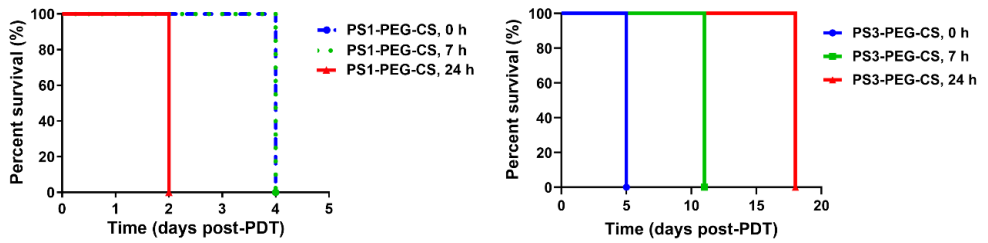

Figure 5.11. *Kaplan–Meier survival analysis of female C67BL/6J mice bearing B16F10 tumors melanoma tumors. An optimization study of the PDT treatment using the* ***PS3-PEG-CS*** *hydrogel. Each treatment group contains 1 mouse. (DLI = 0, 7 or 24 h, drug dose = 0.08 mg, LD = 36 J/cm^2, λ = 660 nm).*

5.3.3.2. Single treatment protocol

The preliminary screening described above allowed to test varied condition of PDT using **PS3-PEG-CS**. The most promising conditions were then tested in larger groups of animals (n=6) enabling to obtain data with statically relevance. For the treated group (i), on the first day post irradiation, we observed strong inflammation of the irradiated area resulting in a formation of a local edema and on the second day post-treatment tumor necrosis was noted. In the first seven days-post treatment we observed progressive scab formation indicating the destruction of the tumor. For the first two weeks post-treatment, we did not observe any signs of tumor growth and the post-therapeutic wound gradually healed, which indicated a successful outcome. Photographs of animals on the 2nd, 7th and 14th days post PDT treatment are presented in **Figure 5.12**. No signs of mechanically induced necrosis were observed for the non-irradiated animal group. Nevertheless, in the third week, tumor regrowth was observed at the treatment site. The survival analysis of the treated groups is presented in **Figure 5.13**. Considering the complexity of the processes responsible for the success of PDT, we can state several hypotheses that may explain the recurrence of the tumors. First, despite the superficial signs of necrosis, there is a risk that the therapy did not destroy the entire population of tumor cells and did not impact the network of blood vessels. Considering the local application of the formulation, the vascular effect of the PDT treatment is considered to be limited. Additionally, melanoma is characterized as highly aggressive and exhibits low immunogenicity.[460] Finally, the presence of melanin can partially impact light penetration.[457,463]

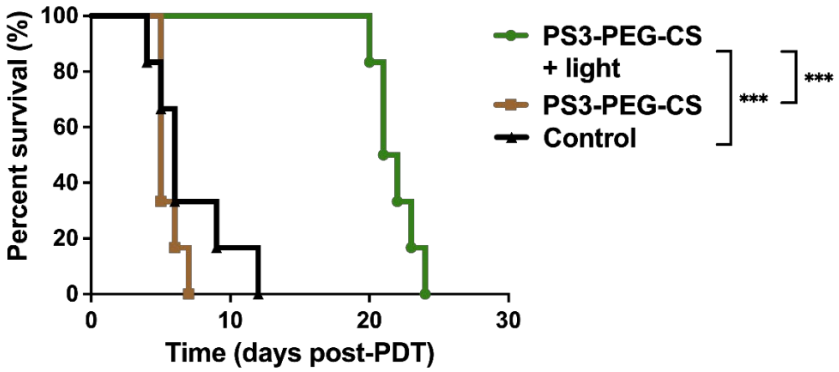

Figure 5.12. *Kaplan–Meier survival analysis of female C57BL/6J mice bearing melanoma tumors. A single irradiation protocol for PDT treatment using the* ***PS3-PEG-CS*** *hydrogel. Each treatment group consists of 6 mice (DLI = 24 h, drug dose = 0.08 mg, LD = 36 J/cm², λ = 660 nm). *** p<0.001.*

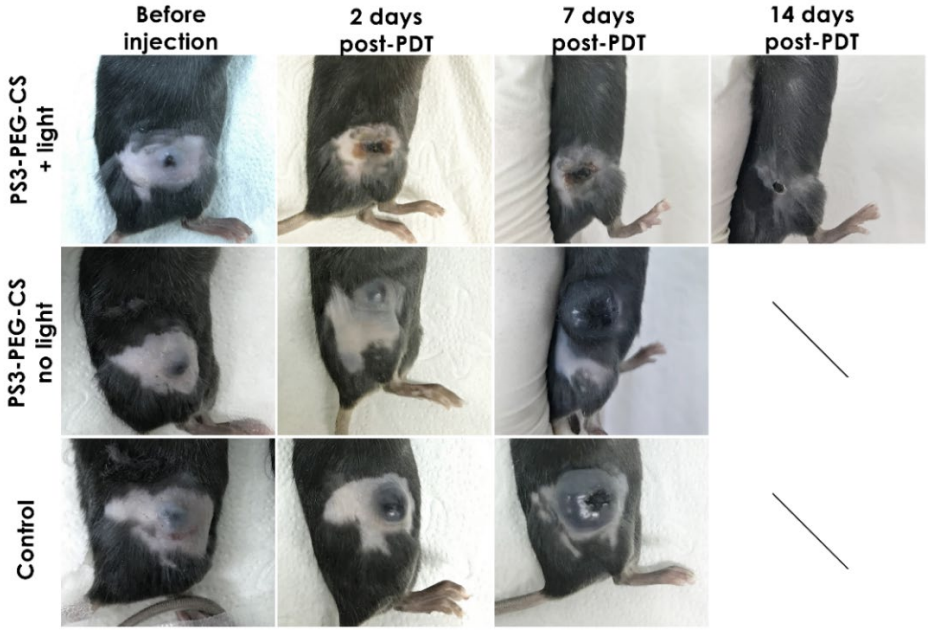

Figure 5.13. *Post PDT images of BL57C/6J mice bearing B16F10 tumors undergoing PDT with* ***PS3-PEG-CS*** *hydrogel formulation (DLI = 24 h, drug dose = 0.08 mg, LD = 36 J/cm², λ = 660 nm).*

In order to obtain a better therapeutic result, we decided to take advantage of the sustained **PS 3** release from the hydrogel matrix and performed multiple tumor irradiations.

5.3.3.3.Multiple treatment protocol

It has been reported that multiple irradiation PDT treatments yield a more robust immune response.[464] Therefore, considering the prolonged release of the PS from the hydrogel network, we propose that better treatment efficacy and an enhanced immune response will be achieved by multiround light stimulation.[465] Consequently, we surmise that this approach could allow us to decrease the dose of the PS and/or light intensity, without affecting the immune response. There are literature reports confirming the enhanced impact of multiple light irradiations in the red or infrared region and/ or fractionated light on PDT treatment.[466,467] It has been proved that low light therapy can lead to increased ATP levels, which enhances the uptake of the PS and results in more efficient apoptosis.[468] Moreover, the influence of low dose PDT *in vivo* has been suggested to stimulate tumoricidal activity of macrophages.[469] In a first set of experiments, mice were divided into three groups among which different intensities of light irradiation, 5, 10, and 15 J/cm^2, were applied at time intervals of 24, 48, and 72 h after injection of **PS3-PEG-CS** (0.08 mg). These timepoints were selected based on the biodistribution study outlined in **Section 5.3.1**. LD of 5 and 10 J/cm^2 were not found to be effective. Similar behavior was noted for the LD = 15 J/cm^2 experimental group, however in this case we observed signs of edema at the irradiation area, confirming the presence of inflammatory processes. Nevertheless, there was no significant increase in survival time, which did exceed 10 days post-treatment (**Figure 5.14**). Due to the ineffective therapeutic response, a further optimization study with increased irradiation intensities was required.

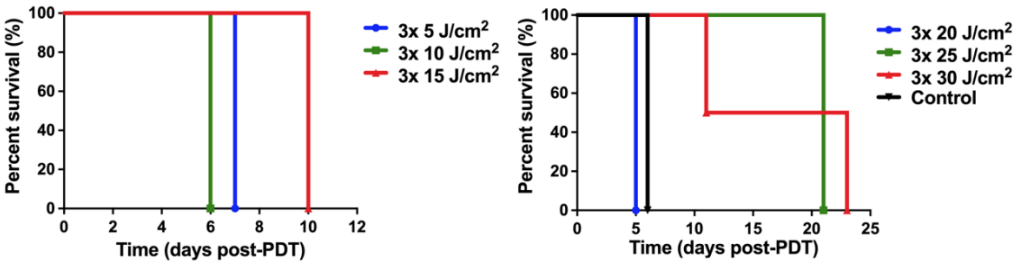

Figure 5.14. *Kaplan–Meier survival analysis of female C57BL/6J mice bearing melanoma tumors. An optimization experiment applying a multiple irradiation protocol for the PDT treatment using the* ***PS3-PEG-CS*** *hydrogel. Each treatment groups contains 1-2 mice (DLI = 24, 48 and 72 h, drug dose = 0.08 mg, LD = 5–30 J/cm^2, λ = 660 nm).*

Increasing the LD to 20, 25 and 30 J/cm^2 yielded better therapeutic outcomes. For doses of 25 and 30 J/cm^2, it was possible to extend the survival rate of the treated groups two-fold with respect to the maximum survival time obtained for the previously applied protocol (15 J/cm^2) (**Figure 5.14**). Although strong oedema and progressive necrosis of the tumor tissue was observed (**Figure 5.15**), tumor regrowth was observed in the second week post-treatment, which was similar to the single protocol treatment. Animals that received an applied LD of 20 J/cm^2 did not respond to the treatment.

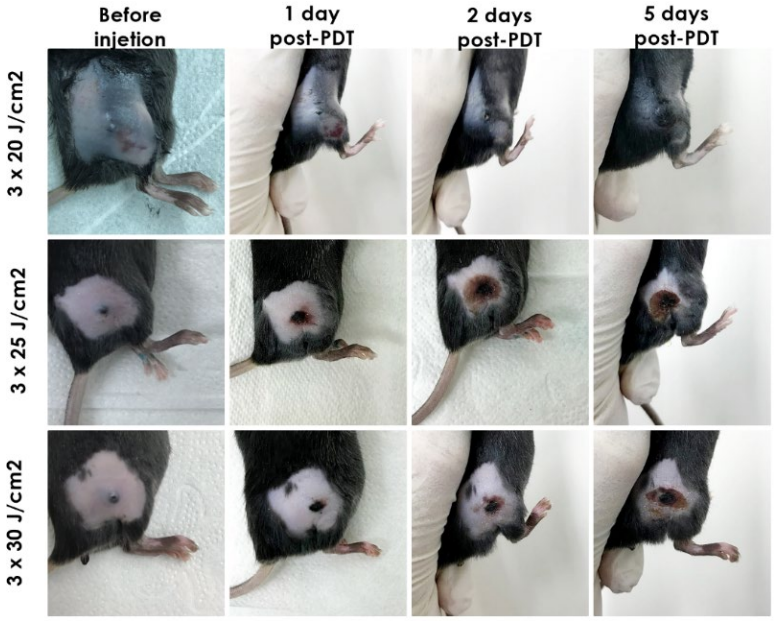

***Figure 5.15**. Post-PDT images of C57BL/6J mice undergoing a multiple irradiation protocol using the **PS3-PEG-CS** hydrogel formulation (DLI = 24, 48 and 72 h, drug dose = 0.08 mg, LD = 20–30 J/cm^2, λ = 660 nm).*

Considering that no significant differences were observed in the therapeutic response in the melanoma tumors between the single and multiple irradiation protocols, a final study of the multiple irradiation approach was performed by applying 35, 40, and 45 J/cm^2 LD. Although necrosis of tumors was observed for all treatment conditions, we did not observe significant differences in the long-term survival rate between the treated groups. Approximately 3 weeks of survival was noted (compared to 7 days of untreated mice) although, tumor regrowth was still observed (**Figure 5.16 and 5.17**). Additionally, logical approach of increasing even more the LD was not possible as at 45 J/cm^2 mice already exhibited some signs of stress (*e.g.*, long post-PDT recovery time as a result of long-lasting irradiations).

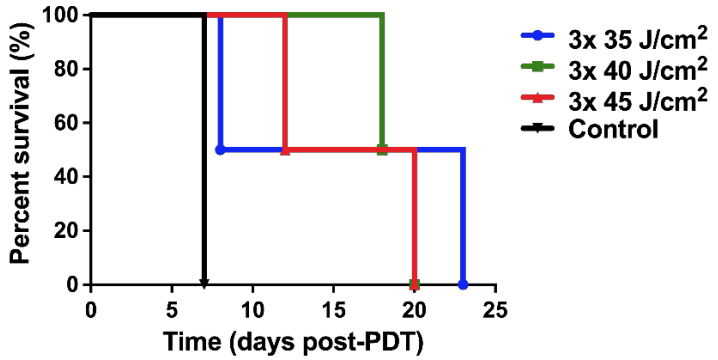

Figure 5.16. *Kaplan–Meier survival analysis of female C57BL/6J mice bearing melanoma tumors. An optimization experiment applying a multiple irradiation protocol for the PDT treatment using the* ***PS3-PEG-CS*** *hydrogel. Each treatment groups contains 1-2 mice (DLI = 24, 48 and 72 h, drug dose = 0.08 mg, LD = 35–45 J/cm^2, λ = 660 nm).*

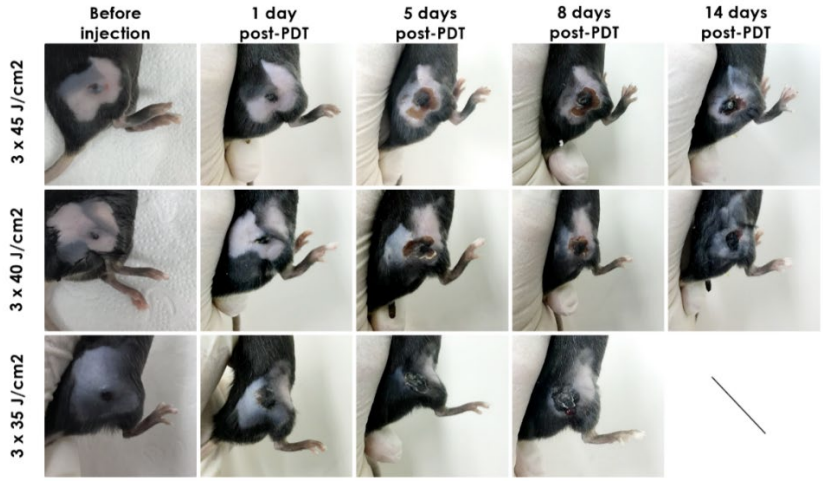

Figure 5.17. *Post-PDT images of C57BL/6J mice undergoing the multiple irradiation protocol using the* ***PS3-PEG-CS*** *hydrogel formulation (DLI = 24, 48 and 72 h, drug dose = 0.08 mg, LD = 35–45 J/cm^2, λ = 660 nm).*

Then, to obtain data with higher statistical power, a large-scale experiment including 6 animals for each treatment condition was performed. In this experiment, 0.1 mg **PS 3/** mouse was intratumorally injected followed by three irradiation (40 J/cm^2) at 24, 48 and 72 h post-injection. Furthermore, in this study, the advantage of the hydrogel formulation over a **PS3-PBS** solution was also evaluated. Herein, a therapeutic response was observed for all treatment conditions and the survival rate was significantly increased in comparison to the control group. Moreover, the fastest tumor regrowth occurred for the animals treated with the **PS3-PBS** formulation. This is a combined effect of the non-homogenous distribution of the PS at the injection site and the rapid clearance

of the PS from the injected compartment. For the **PS3-PBS** group the average post-PDT survival was 2 weeks, reaching a maximum of 22 days (**Figure 5.18**). A comparable outcome was observed for the **PS3-PEG-CS** treated mice using single irradiation protocol. For this group, animals experienced a better response to the applied treatment due to the homogenous distribution of the formulation at the injection site and tumor regrowth was only observed third-week post treatment. the. The average survival time for this group was 15 days, while the maximum survival reached over 25 days. Importantly, a noticeable increase in the treatment efficacy was observed for the mice treated with the hydrogel using the multiple irradiation protocol. This protocol resulted in an average survival of two-weeks but at least one mouse survived until 40 days after PDT.

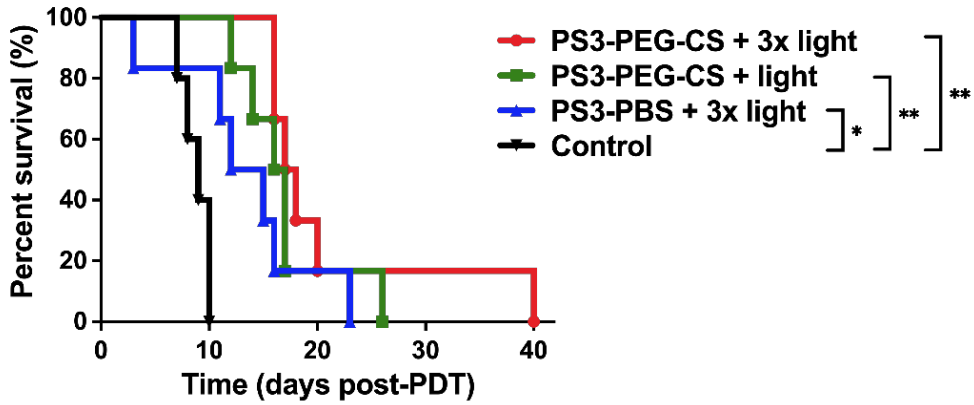

Figure 5.18. *Kaplan–Meier survival analysis of female C57BL/6J mice bearing melanoma tumors. A comparison between the single and multiple irradiation protocols for the PDT treatment using the* ***PS3-PEG-CS*** *or* ***PS3-PBS*** *formulation. Each treatment groups contains 6 mice (DLI = 24–72 h, drug dose = 0.1, LD = 40 J/cm^2, λ = 660 nm). *** $p<0.001$, ** $p<0.01$, * $p<0.05$.*

Oedema and necrosis at the area of irradiation were observed in the first- and second-day post treatment (**Figure 5.19**). Signs of tumor regrowth were delayed in comparison to the single irradiation group. Although the significant increase in the survival rate confirms the efficacy of the treatment, further optimization of the formulation and treatment conditions are required to achieve complete tumor remission. Considering the low immunogenicity and highly aggressive nature of melanoma, a combination therapy including immunostimulating agents or tumor-targeting ligands could be one solution to improve the treatment efficacy.

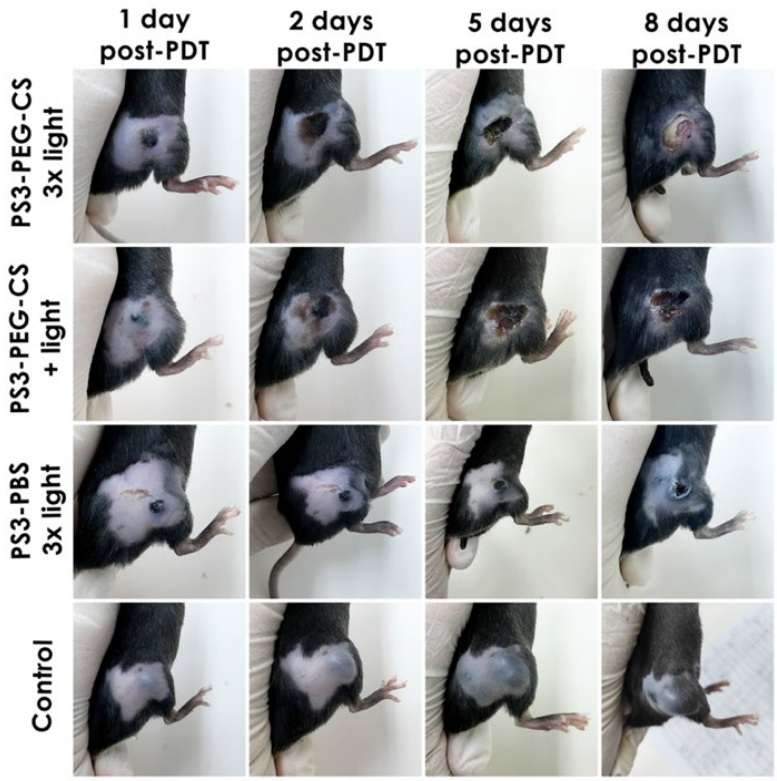

Figure 5.19. *Post-PDT images of C57BL/6J mice undergoing single and multiple irradiation protocols using the* ***PS3-PEG-CS*** *or* ***PS3-PEG-CS*** *formulation (DLI = 24–72 h, drug dose = 0.1 mg, LD = 40 J/cm^2, λ = 660 nm).*

5.3.4. Evaluation of the PDT-induced immune system response

5.3.4.1. Antitumor immune memory experiment

Considering that the immune cells of a host animal strongly impact the success of the therapy, we evaluated if our local PDT treatment protocol could induce a systemic immune response and activate the adaptive immune system, thus creating anti-tumor memory. Therefore, 60 days post treatment, cured mice were rechallenged by the subcutaneous injection of 350,000 of CT26 cancer cells. Over the next 60 days, tumor growth was monitored and compared with the control group. The results revealed that 75% of the cured mice completely rejected the second rechallenged with cancer cells, while all control animals exhibited continuous tumor growth (**Figure 5.20**). Furthermore, in those cured mice that did not reject the cancer cells, the tumor growth kinetic was much slower than the one observed in the control group. The present study shows that **PS3-PEG-CS**-based PDT can induce a highly potent antigen specific immune response capable of inducing immune memory that enables mice to reject a tumor rechallenge with the same tumor model from which they were cured.

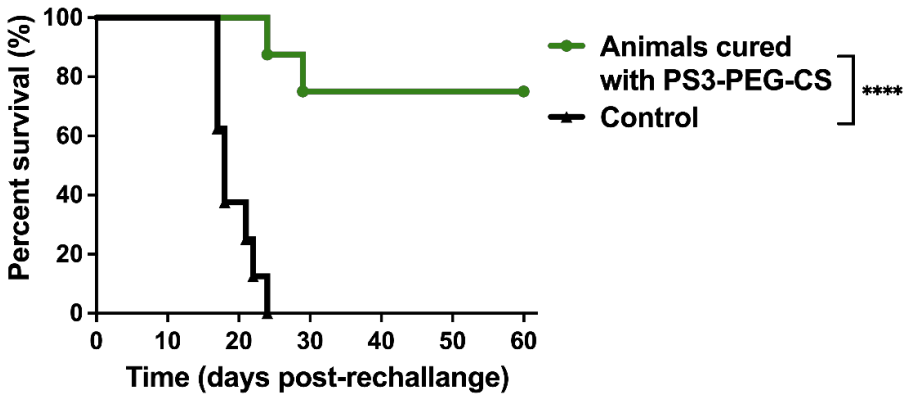

Figure 5.20. *Tumor protection observed in male BALB/c mice that were previously cured, from CT26 tumors, with PDT using the* ***PS3-PEG-CS*** *hydrogel. These tumor-free mice were submitted to a second rechallenge with live CT26 cells 60 days pos-PDT. (Drug dose = 0.07 mg, DLI = 24 h, LD = 20 J/cm^2). **** $p<0.0001$.*

Previously, Preise *et al*. proved that vascular PDT with WST11 resulted in the strong induction of the immune system giving protection not only against the same cell line it was cured (4T1) from but was also found to be cross-protective against mismatched tumors (CT26).[470] This phenomenon might be explained by the antigenic similarity between the two cancer cell models. Another explanation relies on the damaged endothelial cells, which could be an additional source of common antigens between the two tumor models. Moreover, Rodeberg *et al*. reported, based on *in vitro* results, that helper T-lymphocytes obtained from alveolar rhabdomyosarcoma exhibited activity against prostate cancer and melanoma cells.[471]

Therefore, we also exposed cured animals, to 4T1 cells 60 days post-PDT. Tumor growth was compared between three groups: i) mice that were cured with the single irradiation protocol (0.07 mg **PS 3** and 20 J/cm^2), ii) mice that were cured with the multiple irradiation protocol (0.07 mg **PS 3** and 3x 20 J/cm^2) and, iii) mice that were never in contact with any cancer cells. We obtained very promising results indicating a significant involvement of the immune system. The average and individual kinetics of tumor growth are presented in **Figure 5.21**. Although tumor growth was observed in both previously treated groups, the kinetics were noticeably slower in the animals that had previously undergone the multiple irradiation treatment. Moreover, the Kaplan-Meier survival analysis shows that all rechallenged animals in this group

exceeded 30 days of survival (**Figure 5.21**). In contrast, the average survival time for the control group and animals treated with a single irradiation was 22 days. This statistically significant difference in survival between the two treatment groups may indicate the impact of the potent immune system response upon multiple light stimulations.

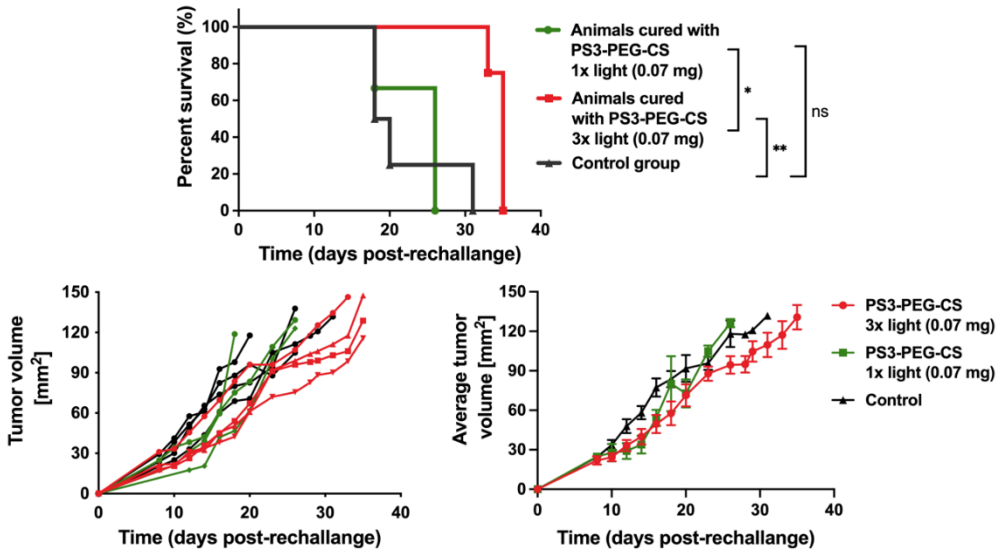

Figure 5.21. *Cross-tumor protection observed in male BALB/c mice that were previously cured, from CT26 tumors, with single or multiple PDT using the* ***PS3-PEG-CS*** *hydrogel. These tumor-free mice were submitted to a second rechallenge with live 4T1 cells 60 days pos-PDT. (Drug dose = 0.07 mg, DLI = 24 or 24, 48 and 72 h, LD = 20 J/cm^2). Kaplan–Meier survival analysis* ***(top)*** *individual tumor volume* ***(bottom left)*** *and average tumor volume* ***(bottom right)*** *of the rechallenged mice. ** p<0.01, * p<0.05, ns – p>0.05.*

5.3.4.2. Evaluation of PDT-mediated abscopal effects on a pseudo-metastatic CT26 tumor model

PDT exhibits the ability to recruit immune cells not only to the irradiated area but also to metastasized tumors.[472] Several works suggest that PDT-mediated antitumor immune stimulation is strong enough to inhibit the growth of distant, and non-illuminated, tumors.[473,474] Pseudo-metastatic models obtained upon the induction of multiple and distant tumors are an useful tool to investigate the abscopal effects of PDT.[433] For instance, a study using a *redaporfin*-PDT protocol to treat subcutaneous CT26 tumors also inhibited the number and size of lung pseudo-metastatic lesions that were induced by *I.V.* injection of the tumor cells.[433] Comparably, a study by Mroz *et al*. showed complete growth inhibition of secondary, and non-irradiated, CT26.CL25

tumors in 78% of mice, which primary tumor was submitted to *verteporfin*-PDT.[475] Moreover, the impact of the PDT treatment on distant metastasis was also observed when the animals were treated using intratumorally injection of PS formulated in a hydrogel formulation. For instance, Liu *et al*. observed that 4T1 tumors treated by PDT using an alginate hydrogel containing Pp IX conjugated with manganese oxide (MnO_2) induced abscopal inhibition of lung metastasis were observed by histopathological evaluation. In contrast, obvious pulmonary tumor metastases were detected for the control groups.[476]

In our study, CT26 tumors were established subcutaneously and 10 days later a hydrogel formulation was injected intratumorally, while the secondary tumors were inoculated subcutaneously in the left flank of the animals. Next, the animals were exposed to PDT using the previously described multiple irradiation protocol. The growth of secondary tumors was compared between the studied groups. The schematic representation of the performed treatment is shown in **Figure 5.22**.

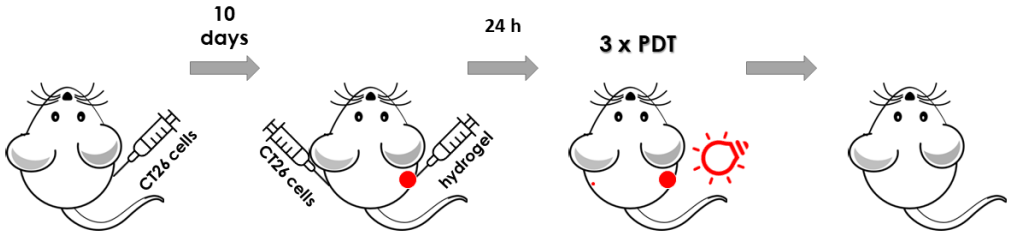

Figure 5.22. *Schematic representation of the PDT protocol towards primary and secondary (pseudo-metastatic) CT26 tumors.*

It was found that the multiple irradiation protocol applied after the intratumoral injection of **PS3-PEG-CS** could more efficiently inhibit the growth of the secondary tumor that when **PS3-PBS** was used. This suggests that PDT with **PS3-PEG-CS** generates a stronger immune response than PDT with **PS3-PBS**. Moreover, this was reflected in the growth kinetic of secondary tumors which was observed to be slower for animals treated with **PS3-PEG-CS** in comparison with **PS3-PBS** solution (**Figure 5.23**). We observed complete inhibition of secondary tumor growth in 3 out of 8 animals in both the **PS3-PEG-CS** and **PS3-PBS** treatment groups. In comparison, only 1 out of 8 animals in the control group did not exhibit secondary tumor growth. Inhibition of the secondary tumors could be affected by a variety of factors and such a case can

be considered as an outlier. Due to the primary tumor growth the survival rate is in agreement with previous data.

Interestingly, although the same rate of inhibition of secondary tumors was observed for both treatment groups, the survival rate of the **PS3-PBS** group did not increase due to the continuous growth of the primary tumors. The survival analysis presented in **Figure 5.23** shows that the average survival of the **PS3-PBS** and control group remain below 20 days. Although not all the animals from the **PS3-PEG-CS** treated group successfully respond to the treatment and inhibition of pseudo-metastatic tumors was not achieved, the survival rate was longer, reaching at least 40 days. This highlights the advantages of the hydrogel formulations over the **PS3-PBS** solution. Finally, the obtained data indicates that PDT-mediate anti-tumor immunity trigger by our hydrogel system can have a positive impact in metastasis outside of the field of illumination. Therefore, our therapeutic approach offers a new strategy to control not only primary but also metastatic tumors upon local delivery of a PS.

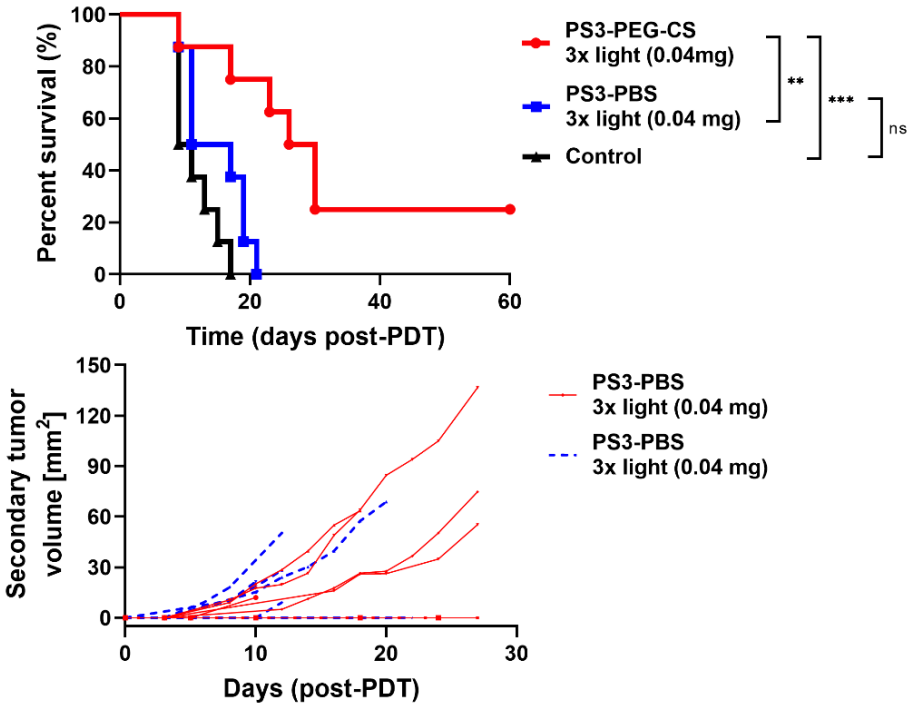

Figure 5.23. *Kaplan–Meier survival analysis of male Balb/c mice bearing two CT26 tumors. Evaluation of the multiple irradiation protocol for the PDT treatment using the* ***PS3-PEG-CS*** *or* ***PS3-PBS*** *formulation on the growth kinetics of secondary tumors. Each treatment groups contains 8 mice (DLI = 24, 48 and 72 h, drug dose = 0.07 mg, LD = 20 J/cm², λ = 660 nm). *** $p<0.001$, ** $p<0.01$, ns – $p>0.05$.*

5.3.4.3. Evaluation of PS3-PEG-CS-based PDT on immunocompromised mice

To confirm the importance of an intact immune system for the success of the PDT herein proposed, immunocompromised mice bearing CT26 tumors were included in our studies. Balb/c nude mice lack the thymus, which is one of the main organs of the lymphatic system being responsible for the production of T lymphocytes.[477] T-cell- mediated responses are involved in the development of acquired immunity, which is of the upmost importance to prevent local relapses and to control distant metastasis. Herein, to evaluate the involvement of T-cells, we tested the multi-irradiation PDT protocol, using the **PS3-PEG-CS** formulation, on Balb/c nude mice. The hydrogel formulation was injected intratumorally and was followed by three light irradiations at a dose of 20 J/cm^2. The survival analysis presented in **Figure 5.24** shows that the survival of nude mice, treated with PDT using **PS3-PEG-CS** hydrogel, dropped from 67% (obtained previously for the Balb/c mice using the same treatment conditions – **Section 5.3.2.3**) to zero.

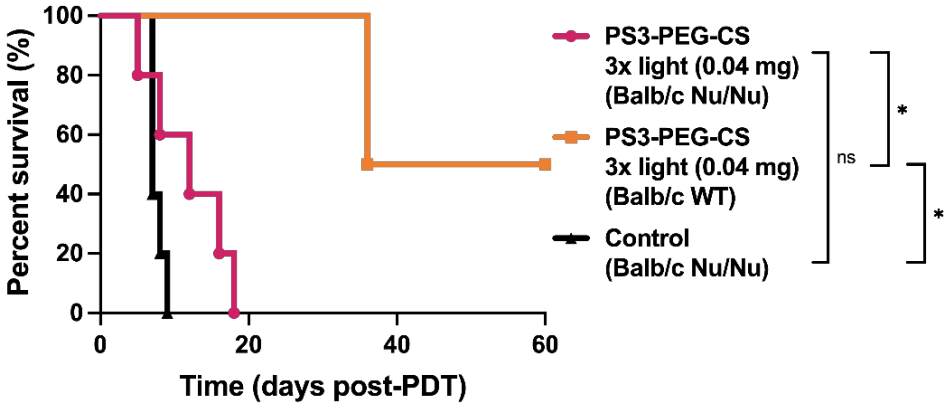

Figure 5.24. *Kaplan–Meier survival analysis of male Balb/c and male Balb/c nude mice bearing CT26 tumors, which were submitted to the PDT multiple irradiation protocol using the* ***PS3-PEG-CS*** *formulation. Each treatment groups contains 2-5 mice (DLI = 24, 48 and 72 h, drug dose = 0.04 mg, LD = 20 J/cm^2, λ = 660 nm). * $p<0.05$, ns – $p>0.05$.*

Less signs of inflammation (edema) were observed after light irradiation for the Balb/c nude mice. Additionally, the necrotic area at the site of irradiation was also significantly smaller in the nude mice than in the wild type (WT) (**Figure 5.25**). The differences listed clearly indicate the importance of an intact immune system, namely the presence of T cells, for the long-term effect of PDT.

Many comparable results have been published in the literature. For example, the PDT protocol used by Korbelik *et al*. with Photofrin reached 100% remission in the immunocompetent mice, but this was reduced to 0% in the immunocompromised animal model.[431] Similarly, to investigate the role of adaptive immunity in the activity of *verteporfin*-PDT towards CT26 tumors, studies were carried out in both immunocompetent and immunodeficient mice models. Again, a drastic decrease in the survival rate was observed, from over 70% to only 20% or 11% for immunodeficient animals, respectively.[470] Summarizing, cell-mediated immunity assumes a critical role on the PDT efficacy.

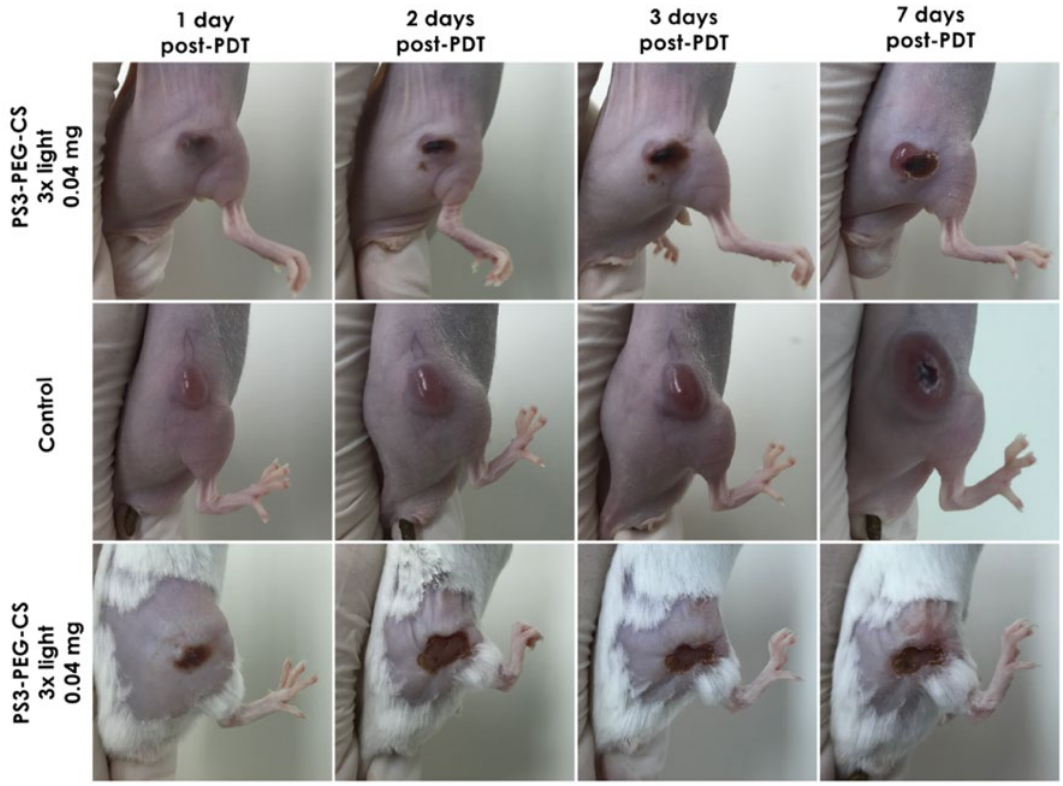

Figure 5.25. *Post-PDT images of nude Balb/c and WT Balb/c mice undergoing the multiple irradiation protocol using the* ***PS3-PEG-CS*** *formulation (DLI = 24, 48 and 72 h, drug dose = 0.04 mg, LD = 20 J/cm^2, λ = 660 nm).*

5.4. Conclusions and outlook

In this chapter, the activity of the **PS3-PEG-CS** hydrogel formulation was tested *in vivo* against two tumor models – B16F10 melanoma and CT26 colon carcinoma. The results of the biodistribution study showed the presence of **PS 3** in the tumor for up to 72 h post-injection. This suggests prolonged and sustained release of the drug molecule from the hydrogel network. In comparison, administration of **PS 3** in PBS would only allow for treatment within 24 h post injection, as at longer timepoints no **PS 3** is detected at tumor sites. The maximum accumulation of the PS at the tumor site was observed within 6 h post-injection, for both the **PS3-PEG-CS** hydrogel and **PS3-PBS** solution. However, for higher timepoints (24-72 h), **PS 3** is only observed when the hydrogel formulation was used. This agrees with the results obtained in the multiple irradiation protocol that shows better therapeutic results with the hydrogel formulation than with the free **PS 3**. We showed that hydrogel-based PDT against melanoma tumors allowed to duplicate the overall survival of treated mice though, no total tumor remission was observed. For CT26, 50 % of cures were obtained. While a small improvement was observed in the melanoma model, more significant effects were attained in the CT26 tumors (67% cures). The discrepancy between the two models can be explained by the negative interference of melanin as well as differences on their intrinsic immunogenicity.

The contribution of the immune system to the treatment efficacy was further evaluated in three independent approaches: i) rechallenge of cured mice, ii) evaluation of the abscopal effects on untreated metastasis and ii) PDT efficacy in immunocompromised mice. The immune response triggered by the PDT using **PS3-PEG-CS** (and applying single irradiation) allowed to reject the formation of CT26 tumors in 75% of animals rechallenged two months later. Much smaller protection was observed when a cell line of different histological origin (4T1) was used. The impact of the immune system was also observed in mice bearing two tumors (pseudo-metastatic model), in which the treatment of only the primary tumor resulted in the abscopal protection against a secondary tumor. Finally, the contribution of T cell mediated immunity was evaluated by the treatment of immunocompromised Balb/c nude mice. A decrease in the

inflammatory processes, together with less superficial tumor necrosis did not result in efficient PDT.

To conclude, in recent years injectable CS hydrogels for intratumoral drug delivery are gaining increasing attention in the field of anti-cancer PDT. The range of possible medical applications of hydrogels constantly expands. This might be among other things due to the chemical, physical and biological flexibility of these systems, which makes them the material of choice for a broad range of applications. Our CS-based hydrogel formulation containing **PS 3** as a photosensitizing agent remains at the tumor site for at least 72 h *in vivo* showing that after a single injection, multiround treatment sessions were possible. The multiple treatment protocol allows to achieve better treatment efficacy due to enhanced stimulation of the immune system. Therefore, recently this approach more often finds its application in protocols for hydrogel-based drug delivery in the field of PDT. Several examples were extensively described in the introduction (**Section 1.4.4.**). Additionally, our therapeutic approach offers a new strategy to control not only primary but also metastatic tumors through local, intratumoral delivery of the **PS3**-based hydrogel formulation. The observed anti-tumor immunity is possibly linked with the necrotic cell death triggered by the photo-activated **PS 3** at the vicinity of the cancer cells. With a different mechanism of action, lack of cytotoxicity, and more homogenous PS distribution at the injection site, the **PS3-PEG-CS** formulation effectively decreases side effects (*e.g.*, skin photosensitivity) related to convectional Foscan therapy. Pointing to the significant influence of the immune system on the success of anti-cancer therapies, we open a door to further improvements on the formulation and/or the PS itself. For instance, combinational therapies involving the incorporation of immune system adjuvants or conjugation of a targeting ligands to the PS to enhance uptake and specific colocalization may be one of the many potential modifications necessary to achieve the desired therapeutic outcome.

5.5. Experimental

General information

Unless otherwise specified, all chemicals were commercially sourced and used without further purification. CT26 cells (ATCC CRL-2638) and B16F10 (given by IPO, Porto, Portugal) were cultured in Dulbecco's Modified Eagle's medium (DMEM, Sigma-Aldrich) supplemented with 10% (v/v) heat-inactivated fetal bovine serum, 100 U/mL penicillin, and 100 ng/ml streptomycin (Invitrogen).

Animal experiments were performed in compliance with The Portuguese Animal Health Authority under individual approved animal experiment authorization number (Direção-Geral da Alimentação e Veterinária authorization 0421/000/000/2020). C57BL/6J (female), BALB/c (male), or BALB/c nude mice (male) were provided by Charles River Laboratories. Mice were sex- and age- matched, with most mice at 8-12 weeks of age and approximately 20 – 25 g of weight. All mice were housed in a Specific Pathogen-Free (SPF) animal facility in individually ventilated cages (IVC) and maintained in accordance with EU legislation (2010/63/EU). Continuous light – dark cycles (12:12 h) were maintained in the facility. The animals were kept under anesthesia during the inoculation and treatment protocols, with an inhalation anesthetic (isoflurane) using an XGI-8 gas anesthesia delivery system (PerkinElmer, USA). Mice hair in the tumor area was removed with commercial hair removal cream 4 to 6 days post-inoculation. The irradiation area was selected to be 15 nm diameter for all PDT protocols. Tumor growth was followed two times per week using a Vernier caliper until the animals reached the humane endpoint. The experimental endpoint of the tumor growth was selected as 12 mm diameter of the tumor size. Animals were irradiated using 660 nm LED light (mW/cm^2) source for all applied treatments.

Non-invasive *in vivo* fluorescence imaging

Tumors were established by subcutaneous injection of 350.000 CT26 cells to Balb/c mice or 500.000 B16F10 cells to C57BL6 mice. **PS3-PEG-CS** hydrogel (prepared as mentioned in **Chapter 3**) and **PS3-PBS** solution (5.6% DMSO) were injected intratumorally into B16F10 or CT26 tumor bearing mice

when the tumor volume reached 5 × 5 mm diameter. The applied **PS 3** dose was 0.08 mg mimicking conditions used for the PDT. Tumor retention of the PS was observed using an *in vivo* imaging system (IVIS Lumina XR, Caliper Life-sciences) monitoring the fluorescence of **PS 3** ($\lambda_{exc.}$ = 430 nm, $\lambda_{em.}$ = 600 -700 nm). The *in vivo* images were acquired at the time points of 0 h (before and immediately after injection), 3 h, 6 h, 24 h, 48 h, 72 h, and 7 days. Hydrogel formulation **PEG-CS**, which does not contain the PS in the structure, was used as negative control. **PS3-PEG-CS** hydrogel and **PS3-PBS** groups included three animals, except for the control group, which had one animal. All images were taken in the automatic mode and are presented in the same color scale (independent for both tumor models). Bioluminescent signals were quantified using the Living Image 4.5.2 software (IVIS Imaging Systems) and were expressed as radiant efficiency (p/s/cm^2/sr)/(μW/cm^2). A region-of-interest (ROI) was selected in the flank area of each animal and was applied for all images and compared over time and between treatment groups.

Optimization of PDT using PS-PEG-CS hydrogel for the treatment of CT26 tumors

Balb/c male mice (n=9) were inoculated *via* subcutaneous injection of 350 000 cells in the right flank in 50 μL FBS free DMEM. The mice were divided into five groups of 1 to 2 animals, which were submitted to increased doses of PS and/ or DL. When the tumors reached the size of *ca*. 5 mm diameter, **PS 3** formulation was injected intratumorally. Treatment conditions are presented in **Table 5.1**.

Table 5.1. *Details of PDT treatment conditions applied for the optimization protocol against CT26 tumors.*

No. of animals	Formulation	Drug dose [mg]	LD [J/cm^2]	DLI [h]
2	PS3-PEG-CS	0.04	20	24
2	PS3-PEG-CS	0.07	20	24
2	PS3-PEG-CS	0.04	30	24
2	PS3-PEG-CS	0.07	30	24
1	Control	-	-	24

Single intratumoral administration of PS3-PEG-CS with single irradiation (CT26 tumor model)

Balb/c male mice (n=43) were inoculated with CT26 cells following the optimization protocol described above. **PS 3** formulation was injected intratumorally when the tumor reached *ca*. 5 mm in diameter. Treatment conditions are presented in **Table 5.2**.

Table 5.2. *Details of treatment conditions applied for PDT against CT26 tumors using a single irradiation protocol.*

No. of animals	Formulation	Drug dose [mg]	LD [J/cm^2]	DLI [h]
15	PS3-PEG-CS	0.07	20	24
11	PS3-PEG-CS	0.07	-	24
6	PS3-PBS	0.07	20	24
11	Control		-	-

Single intratumoral administration of PS3-PEG-CS with multiple irradiations (CT26 tumor model)

Balb/c male mice (n=24) were inoculated with CT26 cells following the optimization protocol described above. Hydrogel was injected intratumorally when the tumor reached *ca*. 5 mm in diameter. Treatment conditions are presented in **Table 5.3**.

Table 5.3*. Details of treatment conditions applied for PDT against B16F10 tumors using a multiple irradiation protocol.*

No. of animals	Formulation	Drug dose [mg]	LD [J/cm^2]	DLI [h]
6	PS3-PEG-CS	0.07	20	24
6	PS3-PEG-CS	0.07	20	24, 48, 72
6	PS3-PEG-CS	0.04	20	24, 48, 72
6	PS3-PBS	0.07	20	24, 48, 72
6	Control	-	-	-

Optimization of PDT using PS-PEG-CS hydrogel for the treatment of B16F10 tumors

C57BL/6J female mice (n=16) were inoculated *via* subcutaneous injection with 500 000 B16F10 cells in the right flank in 50 µL 1:1 mixture of Matrigel and PBS. The mice were divided into groups of 1 to 2 animals, which were submitted to increased doses of PS and/ or DL and different DLI. The **PS1-PEG-CS** or **PS3-PEG-CS** hydrogel was injected intratumorally when the tumor reached *ca*. 6 mm in diameter. The untreated group of animals was used as a control. Treatment conditions are presented in **Table 5.4**.

Table 5.4. *Details of PDT treatment conditions applied for the optimization protocol against B16F10 tumors.*

No. of animals	Formulation	Drug dose [mg]	LD [J/cm^2]	DLI [h]
1	PS1-PEG-CS	0.03	20	24
1	PS1-PEG-CS	0.03	30	24
1	PS1-PEG-CS	0.055	20	24
1	PS1-PEG-CS	0.055	30	24
1	PS3-PEG-CS	0.03	30	24
1	PS3-PEG-CS	0.03	20	24
2	PS3-PEG-CS	0.08	36	24
1	PS1-PEG-CS	0.08	36	0
1	PS1-PEG-CS	0.08	36	7
1	PS1-PEG-CS	0.08	36	24
1	PS3-PEG-CS	0.08	36	0
1	PS3-PEG-CS	0.08	36	7
1	PS3-PEG-CS	0.08	36	24
2	Control	-	-	-

Single intratumoral administration of PS3-PEG-CS with single irradiation (B16F10 tumor model)

C57BL/6J female mice (n=18) were inoculated with B16F10 cells following the optimization protocol described above. **PS3-PEG-CS** hydrogel was injected intratumorally when the tumor reached *ca*. 5 mm in diameter. Treatment conditions are presented in **Table 5.5**.

Table 5.5. *Details of treatment conditions applied for PDT against B16F10 tumors using a single irradiation protocol.*

No. of animals	Formulation	Drug dose [mg]	LD [J/cm^2]	DLI [h]
6	PS3-PEG-CS	0.08	36	24
6	PS3-PEG-CS	0.08	-	24
6	Control	-	-	24

Single intratumoral administration of PS3-PEG-CS with multiple irradiations (B16F10 tumor model)

C57BL/6J female mice (n=24) were inoculated with B16F10 cells following the optimization protocol described above. **PS 3** formulation was injected intratumorally when the tumor reached *ca*. 5 mm in diameter. Treatment conditions are presented in **Table 5.6**.

Table 5.6*. Details of treatment conditions applied for PDT against B16F10 tumors using a multiple irradiation protocol.*

No. of animals	Formulation	Drug dose [mg]	LD [J/cm^2]	DLI [h]
6	PS3-PEG-CS	0.1	40	24, 48, 72
6	PS3-PEG-CS	0.1	40	24
6	PS3-PBS	0.1	40	24, 48, 72
6	Control		-	-

Evaluation of PDT-mediated antitumor immune memory

Balb/c mice that were cured by **PS3-PEG-CS**-based PDT against the CT26 tumors were re-challenged with subcutaneous inoculation of 350 000 CT26 cells (n=8), or with 350 000 4T1 cells (n=7) in 50 µM FBS free DMEM in the previously untreated flank, approximately 60 days after PDT treatment. Age-matched group of naive Balb/c male mice were used as negative control for both CT26 and 4T1 tumor growth.

Evaluation of PDT-mediated abscopal effects on a pseudo-metastatic CT26 tumor model.

Balb/c male mice were inoculated *via* subcutaneous injection of 350 000 CT26 cancer cells in 50 µL of FBS free DMEM in the right flank of each animal. A secondary tumor was inoculated in a similar way 10 days later on the left flank of each animal. On the same day, intratumoral injection of the **PS3-PEG-CS** hydrogel (0.04 mg/ mouse) or **PS3-PBS** solution (0.04 mg/ mouse) was performed. After 24, 48 and 72 h, tumor irradiation was performed and a DL = 20 J/cm^2 was delivered at each time. An untreated group of animals was used as negative control. Tumor growth of the primary and secondary tumors was followed until the animals reached the humane endpoint.

Efficacy of PS3-PEG-CS -based PDT in immunocompromised mice

Male Balb/c nude mice were inoculated *via* subcutaneous injection of 350 000 CT26 cancer cells in the right flank in 50 µL of FBS free DMEM. **PS3-PEG-CS** hydrogel (0.04 mg) was injected intratumorally when the tumors reached ca. 5 mm in diameter. After 24, 48 and 72 h, tumor irradiation was performed and a DL=20 J/cm^2 was delivered at each time. Untreated mice were used as negative control. An additional control group included 2 WT mice bearing CT26 tumors that were submitted to the optimized protocol. The latter serve as positive control for PDT.

Statistical analysis

The results are presented as the mean ± standard error (SEM). One-way ANOVA with Dunnett´s post-test was used to determine statistically significant differences of the means between the control group and the treated groups. Statistical differences were presented at probability levels of $p < 0.05$ *, $p < 0.01$ **, $p < 0.001$ *** and $p < 0.0001$ ****.

Chapter 6 References

1. R. L. Siegel, K. D. Miller, A. Jemal, Cancer Statistics, 2017, *CA Cancer J. Clin.*, **2017**, *67*, 7–30.C. Mattiuzzi, G. Lippi, Current Cancer Epidemiology, *J. Epidemiol. Glob. Health*, **2019**, *9*, 217–222.
2. C. Mattiuzzi and G. Lippi, Current Cancer Epidemiology, *J. Epidemiol. Glob. Health.*, **2019**, ***9***, 217–222.
3. J. Zugazagoitia, C. Guedes, S. Ponce, I. Ferrer, S. Molina-Pinelo, L. Paz-Ares, Current Challenges in Cancer Treatment, *Clin. Ther.*, **2016**, *38*, 1551–1566.
4. S. Tohme, R. L. Simmons, A. Tsung, Surgery for Cancer: A Trigger for Metastases, *Cancer Res.*, **2017**, *77*, 1548–1552.
5. B. A. Chabner, T. G. Roberts, Chemotherapy and the war on cancer, *Nat. Rev. Cancer*, **2005**, *5*, 65–72.
6. D. E. J. G. J. Dolmans, D. Fukumura, R. K. Jain, Photodynamic therapy for cancer, *Nat. Rev. Cancer*, **2003**, *3*, 380–387.
7. M. H. Abdel-Kader, in: *Photodynamic Medicine: From Bench to Clinic*, Ed. H. Kostron, T. Hasan, *Royal Society of Chemistry*, London, **2016**, Chapter 1, pp. 1–22.
8. T. A. Palm, The geographic distribution and etiology of rickets, *Practitioner*, **1890**, *45:270-279*, 321-342.
9. R. W. Chesney, Theobald Palm and His Remarkable Observation: How the Sunshine Vitamin Came to Be Recognized, *Nutrients*, **2012**, *4*, 42–51.
10. N. Finsen, Phototherapy, *Edward Arnold*, London, **1901**.
11. G. Lawrence, The Finsen Light, *The Lancet*, **2002**, *359*, 1784.
12. H. V Tappeiner, Therapeutische Versuche mit fluoreszierenden Stoffen., *Munch. Med. Wochenschr.*, **1903**, *1*, 2042–2044.

13. A. Jesionek, H. Von Tappeiner, Zur behandlung der hautcarcinome mit fluorescierenden stoffen, *Dtsch. Arch. Klin. Med.*, **1905**, *85*, 223–239.

14. W. Hausmann, Die sensibilisierende Wirkung tierischer Farbstoffe und ihre physiologische Bedeutung, *Wien. Klin. Wochenschr*, **1908**, ***21***, 1527–1528

15. W. Hausmann, Die sensibilisierende Wirkung des Hämatoporphyrins, *Biochem. Z,* **1911***, 30*, *276–316.*

16. H. Pfeiffer, *Der Nachweis photodynamischer Wirkungen fluorescierenden Stoffe am levenden Warmbluter. Handbuch der Eiochemischen,* Ed. E. Abderhaldan*,* Berlin, **1911**, pp. 563-571.

17. F. Meyer-Betz, Untersuchung uber die biologische (photodynamische) Wirkung des Hämatoporphyrins und anderer Derivate des Blut-und Gallenfarbstoffs, *Dtsch. Arch. Klin. Med.*, **1913**, *112*, 476–503.

18. A. Policard, Etude sur les aspects offerts par des tumeurs experimentales examinees a la limiere de wood, *Biologue Comptes Rendus*, **1924**, *91*, 1423.

19. T. J. Dougherty, G. B. Grindey, R. Fiel, K. R. Weishaupt, D. G. Boyle, Photoradiation Therapy. II. Cure of Animal Tumors With Hematoporphyrin and Light, *J. Natl. Cancer Inst.*, **1975**, *55*, 115–121.

20. T. J. Dougherty, J. E. Kaufman, A. Goldfarb, K. R. Weishaupt, D. Boyle, A. Mittleman, Photoradiation Therapy for the Treatment of Malignant Tumors, *Cancer Res.*, **1978**, *38*, 2628–2635.

21. S. H. Tomson, E. A. Emmett, S. H. Fox, Photodestruction of Mouse Epithelial Tumors after Oral Acridine Orange and Argon Laser, *Cancer Res.*, **1974**, ***34***, 3124–3127.

22. J. R. Benson, G. M. Farrow, J. H. Kinsey, D. A. Cortese, H. Zincke, D. C. Utz, Detection and localization of In situ carcinoma of the bladder with hematoporphyrin derivative., *Mayo Clin. Proc.*, **1982**, *57*, 548–555.

23. B. G. Ward, I. J. Forbes, P. A. Cowled, M. M. McEvoy, L. W. Cox, The treatment of vaginal recurrences of gynecologic malignancy with

phototherapy following hematoporphyrin derivative pretreatment, *Am. J. Obstet. Gynecol.*, **1982**, *142*, 356–357.

24. E. R. Laws, D. A. Cortese, J. H. Kinsey, R. T. Lagan, R. L. Anderson, Photoradiation Therapy in the Treatment of Malignant Brain Tumors A Phase I (Feasibility) Study, *Neurosurgery*, **1981**, *9*, 672–678.

25. B. W. Henderson, T. J. Dougherty, How Does Photodynamic Therapy Work? *Photochem. Photobiol.*, **1992**, *55*, 145–157.

26. J. M. Dąbrowski, L. G. Arnaut, Photodynamic therapy (PDT) of cancer: from local to systemic treatment, *Photochem. Photobiol. Sci.*, **2015**, *14*, 1765–1780.

27. Z. Melissari, R. M. Williams, M. O. Senge, in *Applications of Porphyrinoids as Functional Materials*, Ed. Heinrich Lang, Tobias Rüffer, *Royal Society of Chemistry*, Croydon, **2021**, pp. 252–291.

28. H. Abrahamse, M. R. Hamblin, New photosensitizers for photodynamic therapy, *Biochem. J.*, **2016**, *473*, 347–364.

29. M. O. Senge, Exercises in molecular gymnastics—bending, stretching and twisting porphyrins, *Chem. Comm.*, **2006**, 243–256.

30. E. Yang, C. Kirmaier, M. Krayer, M. Taniguchi, H.-J. Kim, J. R. Diers, D. F. Bocian, J. S. Lindsey, D. Holten, Photophysical Properties and Electronic Structure of Stable, Tunable Synthetic Bacteriochlorins: Extending the Features of Native Photosynthetic Pigments, *J. Phys. Chem. B*, **2011**, *115*, 10801–10816.

31. K. Plaetzer, B. Krammer, J. Berlanda, F. Berr, T. Kiesslich, Photophysics and photochemistry of photodynamic therapy: fundamental aspects, *Lasers Med. Sci.*, **2009**, *24*, 259–268.

32. C. S. Foote, Definition of type I and type II photosensitized oxidation, *Photochem. Photobiol.,* **1991**, *54*, 659–659

33. M. S. Baptista, J. Cadet, P. D. Mascio, A. A. Ghogare, A. Greer, M. R. Hamblin, C. Lorente, S. C. Nunez, M. S. Ribeiro, A. H. Thomas, M. Vignoni, T. M. Yoshimura, Type I and Type II Photosensitized

Oxidation Reactions: Guidelines and Mechanistic Pathways, *Photochem. Photobiol.*, **2017**, *93*, 912–919.

34. C. Tanielian, C. Wolff, M. Esch, Singlet Oxygen Production in Water: Aggregation and Charge-Transfer Effects, *J. Phys. Chem.*, **1996**, *100*, 6555–6560.

35. J. Moan, Properties for optimal PDT sensitizers, *J. Photochem. Photobiol. B: Biol.*, **1990**, *5*, 521–524.

36 A. P. Castano, T. N. Demidova, M. R. Hamblin, Mechanisms in photodynamic therapy: part one—photosensitizers, photochemistry and cellular localization, *Photodiagnosis Photodyn. Ther.*, **2004**, *1*, 279–293.

37. L. Christina Pires Gonçalves, Photophysical properties and therapeutic use of natural photosensitizers, *J. Photochem. Photobiol.*, **2021**, *7*, 100052.

38. E. Hemmer, A. Benayas, F. Légaré, F. Vetrone, Exploiting the biological windows: current perspectives on fluorescent bioprobes emitting above 1000 nm, *Nanoscale Horiz.*, **2016**, *1*, 168–184.

39. S. K. Pushpan, S. Venkatraman, V. G. Anand, J. Sankar, D. Parmeswaran, S. Ganesan, T. K. Chandrashekar, Porphyrins in photodynamic therapy - A search for ideal photosensitizers, *Curr. Med. Chem. - Anti-Cancer Agents*, **2002**, *2*, 187–207.

40. A. E. O'Connor, W. M. Gallagher, A. T. Byrne, Porphyrin and Nonporphyrin Photosensitizers in Oncology: Preclinical and Clinical Advances in Photodynamic Therapy, *Photochem. Photobiol.,* **2009**, *85*, 1053–1074.

41. M. Lan, S. Zhao, W. Liu, C.-S. Lee, W. Zhang, P. Wang, Photosensitizers for Photodynamic Therapy, *Adv. Healthc. Mater.*, **2019**, *8*, 1900132.

42. J. Zhang, C. Jiang, J. P. Figueiró Longo, R. B. Azevedo, H. Zhang, L. A. Muehlmann, An updated overview on the development of new photosensitizers for anticancer photodynamic therapy, *Acta Pharm. Sin. B.*, **2018**, *8*, 137–146.

43. S. Kwiatkowski, B. Knap, D. Przystupski, J. Saczko, E. Kędzierska, K. Knap-Czop, J. Kotlińska, O. Michel, K. Kotowski, J. Kulbacka, Photodynamic therapy – mechanisms, photosensitizers and combinations, *Biomed. Pharmacother.*, **2018**, *106*, 1098–1107.

44. C. J. Gomer, Preclinical Examination Of First and Second Generation Photosensitizers Used in Photodynamic Therapy, *Photochem. Photobiol.*, **1991**, *54*, 1093–1107.

44. I. Yoon, J. Z. Li, Y. K. Shim, Advance in Photosensitizers and Light Delivery for Photodynamic Therapy, *Clin. Endosc.*, **2013**, *46*, 7–23.

46. G. C. Ferreira, R. Franco, S. G. Lloyd, I. Moura, J. J. G. Moura, B. H. Huynh, Structure and function of ferrochelatase, *J. Bioenerg. Biomembr.*, **1995**, *27*, 221–229.

47. Q. Peng, T. Warloe, K. Berg, J. Moan, M. Kongshaug, K.-E. Giercksky, J. M. Nesland, 5-Aminolevulinic acid-based photodynamic therapy, *Cancer*, **1997**, *79*, 2282–2308.

48. C. Fenton, C. M. Perry, Verteporfin, *Drugs Aging.*, **2006**, *23*, 421–445.

49. T. Yano, T. Minamide, K. Takashima, K. Nakajo, T. Kadota and Y. Yoda, Clinical Practice of Photodynamic Therapy Using Talaporfin Sodium for Esophageal Cancer, *J. Clin. Med.*, **2021**, *10*, 2785.

50. A. M. Bugaj, Vascular targeted photochemotherapy using padoporfin and padeliporfin as a method of the focal treatment of localised prostate cancer - clinician's insight, *World J. Methodol.*, **2016**, *6*, 65–76.

51. M. O. Senge, J. C. Brandt, Temoporfin (Foscan®, 5,10,15,20-Tetra(m-hydroxyphenyl)chlorin)—A Second-generation Photosensitizer, *Photochem. Photobiol.*, **2011**, *87*, 1240–1296.

52. J. S. Friedberg, R. Mick, J. Stevenson, J. Metz, T. Zhu, J. Buyske, D. H. Sterman, H. I. Pass, E. Glatstein, S. M. Hahn, A phase I study of Foscan-mediated photodynamic therapy and surgery in patients with mesothelioma, *Ann. Surg.*, **2003**, *75*, 952–959.

53. I. S. Mfouo-Tynga, L. D. Dias, N. M. Inada, C. Kurachi, Features of third generation photosensitizers used in anticancer photodynamic therapy: Review, *Photodiagnosis Photodyn. Ther.*, **2021**, *34*, 102091.

54. P. Gierlich, A. I. Mata, C. Donohoe, R. M. M. Brito, M. O. Senge, L. C. Gomes-da-Silva, Ligand-Targeted Delivery of Photosensitizers for Cancer Treatment, *Molecules*, **2020**, *25*, 5317.

55. S. Callaghan, M. O. Senge, The good, the bad, and the ugly – controlling singlet oxygen through design of photosensitizers and delivery systems for photodynamic therapy, *Photochem. Photobiol. Sci.*, **2018**, *17*, 1490–1514.

56. A.-R. Azzouzi, S. Vincendeau, E. Barret, A. Cicco, F. Kleinclauss, H. G. van der Poel, C. G. Stief, J. Rassweiler, G. Salomon, E. Solsona, A. Alcaraz, T. T. Tammela, D. J. Rosario, F. Gomez-Veiga, G. Ahlgren, F. Benzaghou, B. Gaillac, B. Amzal, F. M. J. Debruyne, G. Fromont, C. Gratzke, M. Emberton, Padeliporfin vascular-targeted photodynamic therapy versus active surveillance in men with low-risk prostate cancer (CLIN1001 PCM301): an open-label, phase 3, randomised controlled trial, *Lancet Oncol.*, **2017**, *18*, 181–191.

57. A. Pece, P. Milani, V. Isola, L. Pierro, A Long-Term Study of Photodynamic Therapy with Verteporfin for Choroidal Neovascularization at the Edge of Chorioretinal Atrophy in Pathologic Myopia, *Ophthalmologica*, **2011**, *225*, 161–168.

58. M. M. Attwood, M. Rask-Andersen and H. B. Schiöth, Orphan Drugs and Their Impact on Pharmaceutical Development, *Trends Pharmacol. Sci.*, **2018**, *39*, 525–535.

59. L. L. Santos, J. Oliveira, E. Monteiro, J. Santos, C. Sarmento, Treatment of Head and Neck Cancer with Photodynamic Therapy with Redaporfin: A Clinical Case Report, *Case Rep. Oncol.*, **2018**, *11*, 769–776.

60. A. C. S. Lobo, L. C. Gomes-da-Silva, P. Rodrigues-Santos, A. Cabrita, M. Santos-Rosa, L. G. Arnaut, Immune Responses after Vascular Photodynamic Therapy with Redaporfin, *J. Clin. Med.*, **2020**, *9*, 104.

61. F. E. Fox, Z. Niu, A. Tobia, A. H. Rook, Photoactivated Hypericin is an Anti-Proliferative Agent that Induces a High Rate of Apoptotic Death of Normal, Transformed, and Malignant T Lymphocytes: Implications for the Treatment of Cutaneous Lymphoproliferative and Inflammatory Disorders, *J. Invest. Dermatol.*, **1998**, *111*, 327–332.

62. A. H. Rook, G. S. Wood, M. Duvic, E. C. Vonderheid, A. Tobia, B. Cabana, A phase II placebo-controlled study of photodynamic therapy with topical hypericin and visible light irradiation in the treatment of cutaneous T-cell lymphoma and psoriasis, *J. Am. Acad. Dermatol.*, **2010**, *63*, 984–990.

63. M. Triesscheijn, P. Baas, J. H. M. Schellens, F. A. Stewart, Photodynamic Therapy in Oncology, *The Oncologist*, **2006**, *11*, 1034–1044.

64. M. S. Nestor, B. Berman, J. Patel, A. Lawson, Safety and Efficacy of Aminolevulinic Acid 10% Topical Gel versus Aminolevulinic Acid 20% Topical Solution Followed by Blue-light Photodynamic Therapy for the Treatment of Actinic Keratosis on the Face and Scalp: A Randomized, Double-blind Study, *J. Clin. Aesthet. Dermatol.*, **2019**, *12*, 32–38.

65. S. Radakovic, M. Dangl, A. Tanew, 5-Aminolevulinic acid patch (Alacare) photodynamic therapy for actinic cheilitis: data from a prospective 12-month follow-up study on 21 patients, *J. Eur. Acad. Dermatol. Venereol.*, **2020**, *34*, 2011–2015.

66. C. Morton, Methyl aminolevulinate (Metvix®) photodynamic therapy - practical pearls, *J. Dermatol. Treat.*, **2003**, *14*, 23–26.

67. G. B., M. R., G. D., G. P., Hexvix blue light fluorescence cystoscopy – a promising approach in superficial bladder tumors diagnosis, *J. Med. Life*, **2008**, *1*, 355–362.

68. C. Hopper, C. Niziol, M. Sidhu, The cost-effectiveness of Foscan mediated photodynamic therapy (Foscan-PDT) compared with extensive palliative surgery and palliative chemotherapy for patients with advanced head and neck cancer in the UK, *Oral Oncol.*, **2004**, *40*, 372–382.

69. R. A. Weersink, A. Bogaards, M. Gertner, S. R. H. Davidson, K. Zhang, G. Netchev, J. Trachtenberg and B. C. Wilson, Techniques for delivery and monitoring of TOOKAD (WST09)-mediated photodynamic therapy of the prostate: Clinical experience and practicalities, *J. Photochem. Photobiol. B: Biol.*, **2005**, *79*, 211–222.

70. V. R. Participants, Guidelines for using verteporfin (Visudyne) in photodynamic therapy for choroidal neovascularization due to age-related macular degeneration and other causes: update, *Retina*, **2005**, *25*, 119–134.

71. L. R. Carobeli, L. E. de F. Meirelles, G. M. Z. F. Damke, E. Damke, M. V. F. de Souza, N. L. Mari, K. H. Mashiba, C. S. Shinobu-Mesquita, R. P. Souza, V. R. S. da Silva, R. S. Gonçalves, W. Caetano, M. E. L. Consolaro, Phthalocyanine and Its Formulations: A Promising Photosensitizer for Cervical Cancer Phototherapy, *Pharmaceutics*, **2021**, *13*, 2057.

72. P. Hillemanns, F. Garcia, K. U. Petry, V. Dvorak, O. Sadovsky, O.-E. Iversen, M. H. Einstein, A randomized study of hexaminolevulinate photodynamic therapy in patients with cervical intraepithelial neoplasia 1/2, *Am. J. Obstet. Gynecol.*, **2015**, *212*, 465.e1-465.e7.

73. H. R. Nava, S. S. Allamaneni, T. J. Dougherty, M. T. Cooper, W. Tan, G. Wilding and B. W. Henderson, Photodynamic Therapy (PDT) Using HPPH for the Treatment of Precancerous Lesions Associated with Barrett's Esophagus, *Lasers Surg. Med.*, **2011**, *43*, 705–712.

74. N. Rigual, G. Shafirstein, M. T. Cooper, H. Baumann, D. A. Bellnier, U. Sunar, E. C. Tracy, D. J. Rohrbach, G. Wilding, W. Tan, M. Sullivan, M. Merzianu, B. W. Henderson, Photodynamic Therapy with 3-(1′-Hexyloxyethyl) Pyropheophorbide a for Cancer of the Oral Cavity, *Clin. Cancer Res.*, **2013**, *19*, 6605–6613.

75. G. Shafirstein, A. Battoo, K. Harris, H. Baumann, S. O. Gollnick, J. Lindenmann, C. E. Nwogu, Photodynamic Therapy of Non–Small Cell Lung Cancer. Narrative Review and Future Directions, *Ann. Am. Thorac. Soc.*, **2016**, *13*, 265–275.

76. A. F. D. Di Stefano, M. M. Radicioni, A. Vaccani, A. Fransioli, L. Longo, L. Moro, A. Repici, Methylene blue MMX® tablets for chromoendoscopy. Bioavailability, colon staining and safety in healthy volunteers undergoing a full colonoscopy, *Contemp. Clin. Trials*, **2018**, *71*, 96–102.

77. K. Berg, M. Folini, L. Prasmickaite, P. K. Selbo, A. Bonsted, B. O. Engesaeter, N. Zaffaroni, A. Weyergang, A. Dietzea, G. M. Maelandsmo, E. Wagner, O.-J. Norum, A. Hogset, Photochemical Internalization: A New Tool for Drug Delivery, *Curr. Pharm. Biotechnol.*, **2007**, *8*, 362–372.

78. K. Berg, S. Nordstrand, P. K. Selbo, D. T. T. Tran, E. Angell-Petersen, A. Høgset, Disulfonated tetraphenyl chlorin (TPCS2a), a novel photosensitizer developed for clinical utilization of photochemical internalization, *Photochem. Photobiol. Sci.*, **2011**, *10*, 1637–1651.

79. B. Rodríguez-Amigo, O. Planas, R. Bresolí-Obach, J. Torra, R. Ruiz-González, S. Nonell, in: *Photodynamic Medicine: From Bench to Clinic*, Ed. H. Kostron, T. Hasan, *Royal Society of Chemistry*, London, **2016**, pp. 23-62.

80. Q. Zhang, X. Tian, H. Zhou, J. Wu, Y. Tian, Lighting the Way to See Inside Two-Photon Absorption Materials: Structure–Property Relationship and Biological Imaging, *Materials*, **2017**, *10*, 223.

81. M. Rumi, J. W. Perry, Two-photon absorption: an overview of measurements and principles, *Adv. Opt. Photon.,* **2010**, *2*, 451–518.

82. M. Göppert-Mayer, Über Elementarakte mit zwei Quantensprüngen, *Ann. Phy.*, **1931**, *401*, 273–294.

83. W. Kaiser, C. G. B. Garrett, Two-Photon Excitation in CaF2: Eu^{2+}, *Phys. Rev. Lett.*, **1961**, *7*, 229–231.

84. W. Denk, J. H. Strickler, W. W. Webb, Two-Photon Laser Scanning Fluorescence Microscopy, *Science*, **1990**, *248*, 73–76.

85. F. Bolze, S. Jenni, A. Sour, V. Heitz, Molecular photosensitisers for two-photon photodynamic therapy, *Chem. Comm.*, **2017**, *53*, 12857–12877.

86. B. H. Cumpston, S. P. Ananthavel, S. Barlow, D. L. Dyer, J. E. Ehrlich, L. L. Erskine, A. A. Heikal, S. M. Kuebler, I.-Y. S. Lee, D. McCord-Maughon, J. Qin, H. Röckel, M. Rumi, X.-L. Wu, S. R. Marder, J. W. Perry, Two-photon polymerization initiators for three-dimensional optical data storage and microfabrication, *Nature*, **1999**, *398*, 51–54.

87. Q. Zhang, X. Tian, H. Zhou, J. Wu, Y. Tian, Lighting the Way to See Inside Two-Photon Absorption Materials: Structure–Property Relationship and Biological Imaging, *Materials*, **2017**, ***10***, 223.

88. M. Pawlicki, H. A. Collins, R. G. Denning, H. L. Anderson, Two-Photon Absorption and the Design of Two-Photon Dyes, *Angew. Chem. Int. Ed.*, **2009**, *48*, 3244–3266.

89. E. Robbins, S. Leroy-Lhez, N. Villandier, M. Samoć, K. Matczyszyn, Prospects for More Efficient Multi-Photon Absorption Photosensitizers Exhibiting Both Reactive Oxygen Species Generation and Luminescence, *Molecules*, **2021**, *26*, 6323.

90. Y. Shen, A. J. Shuhendler, D. Ye, J.-J. Xu and H.-Y. Chen, Two-photon excitation nanoparticles for photodynamic therapy, *Chem. Soc. Rev.*, **2016**, *45*, 6725–6741.

91. H. A. Collins, M. Khurana, E. H. Moriyama, A. Mariampillai, E. Dahlstedt, M. Balaz, M. K. Kuimova, M. Drobizhev, V. X. D. Yang, D. Phillips, A. Rebane, B. C. Wilson, H. L. Anderson, Blood-vessel closure using photosensitizers engineered for two-photon excitation, *Nat. Photon.*, **2008**, *2*, 420–424.

92. M. Gary-Bobo, Y. Mir, C. Rouxel, D. Brevet, I. Basile, M. Maynadier, O. Vaillant, O. Mongin, M. Blanchard-Desce, A. Morère, M. Garcia, J.-O. Durand, L. Raehm, Mannose-Functionalized Mesoporous Silica Nanoparticles for Efficient Two-Photon Photodynamic Therapy of Solid Tumors, *Angew. Chem. Int. Ed.*, **2011**, *50*, 11425–11429.

93. Y. Li, R. Tang, X. Liu, J. Gong, Z. Zhao, Z. Sheng, J. Zhang, X. Li, G. Niu, R. T. K. Kwok, W. Zheng, X. Jiang, B. Z. Tang, Bright Aggregation-Induced Emission Nanoparticles for Two-Photon Imaging and Localized Compound Therapy of Cancers, *ACS Nano*, **2020**, *14*, 16840–16853.

94. F. Helmchen, W. Denk, Deep tissue two-photon microscopy, *Nat. Methods*, **2005**, *2*, 932–940.

95. A. Zoumi, X. Lu, G. S. Kassab, B. J. Tromberg, Imaging Coronary Artery Microstructure Using Second-Harmonic and Two-Photon Fluorescence Microscopy, *Biophys. J.*, **2004**, *87*, 2778–2786.

96. J. Wu, Y. Liang, S. Chen, C.-L. Hsu, M. Chavarha, S. W. Evans, D. Shi, M. Z. Lin, K. K. Tsia, N. Ji, Kilohertz two-photon fluorescence microscopy imaging of neural activity *in vivo*, *Nat. Methods*, **2020**, *17*, 287–290.

97. C.-L. Sun, J. Li, X.-Z. Wang, R. Shen, S. Liu, J.-Q. Jiang, T. Li, Q.-W. Song, Q. Liao, H.-B. Fu, J.-N. Yao, H.-L. Zhang, Rational Design of Organic Probes for Turn-On Two-Photon Excited Fluorescence Imaging and Photodynamic Therapy, *Chem*, **2019**, *5*, 600–616.

98. Z. Sun, L.-P. Zhang, F. Wu, Y. Zhao, Photosensitizers for Two-Photon Excited Photodynamic Therapy, *Adv. Funct. Mater.*, **2017**, *27*, 1704079.

99. L. Brancaleon, H. Moseley, Laser and Non-laser Light Sources for Photodynamic Therapy, *Lasers Med. Sci.*, **2002**, *17*, 173–186.

100. P. R. Ogilby, Singlet oxygen: there is indeed something new under the sun, *Chem. Soc. Rev.*, **2010**, *39*, 3181–3209.

101. X. Ragàs, A. Jiménez-Banzo, D. Sánchez-García, X. Batllori, S. Nonell, Singlet oxygen photosensitisation by the fluorescent probe Singlet Oxygen Sensor Green®, *Chem. Comm.*, **2009**, 2920–2922.

102. S. Hatz, L. Poulsen, P. R. Ogilby, Time-resolved Singlet Oxygen Phosphorescence Measurements from Photosensitized Experiments in

Single Cells: Effects of Oxygen Diffusion and Oxygen Concentration, *Photochem. Photobiol.*, **2008**, *84*, 1284–1290.

103. Y. You, Chemical tools for the generation and detection of singlet oxygen, *Org. Biomol. Chem.*, **2018**, *16*, 4044–4060.

104. T. Grune, L.-O. Klotz, J. Gieche, M. Rudeck, H. Sies, Protein oxidation and proteolysis by the nonradical oxidants singlet oxygen or peroxynitrite, *Free Radic. Biol. Med.*, **2001**, *30*, 1243–1253.

105. C. Donohoe, M. O. Senge, L. G. Arnaut, L. C. Gomes-da-Silva, Cell death in photodynamic therapy: From oxidative stress to anti-tumor immunity, *Biochim. Biophys. Acta – Rev. Cancer*, **2019**, *1872*, 188308.

106. L. Kelbauskas, W. Dietel, Internalization of Aggregated Photosensitizers by Tumor Cells: Subcellular Time-resolved Fluorescence Spectroscopy on Derivatives of Pyropheophorbide-a Ethers and Chlorin e6 under Femtosecond One- and Two-photon Excitation, *Photochem. Photobiol.*, **2002**, *76*, 686–694.

107. J. G. Ğb, D. Nowis, M. Skrzycki, H. Czeczot, A. Barańczyk-Kuźma, G. M. Wilczyński, M. Makowski, P. Mróz, K. Kozar, R. Kamiński, A. Jalili, M. Kopeć, T. Grzela, M. Jakóbisiak, Antitumor Effects of Photodynamic Therapy Are Potentiated by 2-Methoxyestradiol: A Superoxide Dismutase Inhibitor, *J. Biol. Chem.*, **2003**, *278*, 407–414.

108. E. Buytaert, M. Dewaele, P. Agostinis, Molecular effectors of multiple cell death pathways initiated by photodynamic therapy, *Biochim. Biophys. Acta Rev. Cancer*, **2007**, *1776*, 86–107.

109. G. Kroemer, L. Galluzzi, O. Kepp, L. Zitvogel, Immunogenic Cell Death in Cancer Therapy, *Annu. Rev. Immunol.*, **2013**, *31*, 51–72.

110. L. Bezu, L. C. Gomes-da-Silva, H. Dewitte, K. Breckpot, J. Fucikova, R. Spisek, L. Galluzzi, O. Kepp, G. Kroemer, Combinatorial Strategies for the Induction of Immunogenic Cell Death, *Front. Immunol.*, **2015**, *6*, 187.

111. J. Folkman, Tumor angiogenesis: therapeutic implications, *N. Engl. J. Med.*, **1971**, *285*, 1182–1186.

112. J. Zhou, T. Schmid, S. Schnitzer, B. Brüne, Tumor hypoxia and cancer progression, *Cancer Lett.*, **2006**, *237*, 10–21.

113. Z. Ji, G. Yang, S. Shahzidi, K. Tkacz-Stachowska, Z. Suo, J. M. Nesland, Q. Peng, Induction of hypoxia-inducible factor-1α overexpression by cobalt chloride enhances cellular resistance to photodynamic therapy, *Cancer Lett.*, **2006**, *244*, 182–189.

114. A. Castelani, G. P. Pace, M. Concioli, Photodynamic effect of haematoporphyrin on blood microcirculation, *J. Pathol. Bacteriol.*, **1963**, *86*, 99–102.

115. B. W. Henderson, V. H. Fingar, Oxygen Limitation of Direct Tumor Cell Kill During Photodynamic Treatment of a Murine Tumor Model, *Photochem. Photobiol.*, **1989**, *49*, 299–304.

116. P. J. Delves, I. M. Roitt, The Immune System, *N. Engl. J. Med.*, **2000**, *343*, 37–49.

117. J. Seita, I. L. Weissman, Hematopoietic stem cell: self-renewal versus differentiation, *WIREs Syst. Biol. Med.*, **2010**, *2*, 640–653.

118. R. Medzhitov, C. Janeway, Innate Immunity, *N. Engl. J. Med.*, **2000**, *343*, 338–344.

119. Z. Pancer, M. D. Cooper, The Evolution of Adaptive Immunity, *Annu. Rev. Immunol.*, **2006**, *24*, 497–518.

120. A. P. Castano, P. Mroz, M. R. Hamblin, Photodynamic therapy and anti-tumour immunity, *Nat. Rev. Cancer*, **2006**, *6*, 535–545.

121. M. Korbelik, PDT-associated host response and its role in the therapy outcome, *Lasers Surg. Med.*, **2006**, *38*, 500–508.

122. D. Nowis, T. Stokłosa, M. Legat, T. Issat, M. Jakóbisiak, J. Gołąb, The influence of photodynamic therapy on the immune response, *Photodiagnosis Photodyn. Ther.*, **2005**, *2*, 283–298.

123. N. Maeding, T. Verwanger, B. Krammer, Boosting Tumor-Specific Immunity Using PDT, *Cancers*, **2016**, *8*, 91.

124. R. Bonnett, R. D. White, U. J. Winfield, M. C. Berenbaum, Hydroporphyrins of the *meso*-tetra(hydroxyphenyl)porphyrin series as tumour photosensitizers, *Biochem. J.*, **1989**, *261*, 277–280.

125. E. B. Chevretton, M. C. Berenbaum, R. Bonnett, The effect of photodynamic therapy on normal skeletal muscle in an animal model, *Laser Med. Sci.*, **1992**, *7*, 103–110.

126. M. C. Berenbaum, S. L. Akande, R. Bonnett, H. Kaur, S. Ioannou, R. D. White, U. J. Winfield, *Meso*-Tetra(hydroxyphenyl)porphyrins, a new class of potent tumour photosensitisers with favourable selectivity, *Br. J. Cancer*, **1986**, *54*, 717–725.

127. R. M. Jones, J. H. Lamb, C. K. Lim, 5,10,15,20-*meso*-tetra(hydroxyphenyl)chlorin as a matrix for the analysis of low molecular weights compounds by matrix-assisted laser desorption/ionization time-of-flight mass spectrometry, *Rapid Commun. Mass Spectrom.*, **1995**, *9*, 968–969.

128. R. Bonnett, B. D. Djelal, G. E. Hawkes, P. Haycock, F. Pont, Fine structure of 5,10,15,20-tetrakis(*m*-hydroxyphenyl)chlorin (*m*-THPC): a ^{1}H, ^{13}C and ^{15}N NMR study, *J. Chem. Soc., Perkin Trans. 2*, **1994**, 1839–1843.

129. R. Bonnett, D. J. McGarvey, A. Harriman, E. J. Land, T. G. Truscott, U.-J. Winfield, Photophysical Properties of *meso*-tetraphenylporphyrin and some *meso*-tetra(hydroxyphenyl)porphyrins, *Photochem. Photobiol.*, **1988**, *48*, 271–276.

130. R. Bonnett, B. D. Djelal, P. A. Hamilton, G. Martinez, F. Wierrani, Photobleaching of 5,10,15,20-tetrakis(*m*-hydroxyphenyl)porphyrin (*m*-THPP) and the corresponding chlorin (*m*-THPC) and bacteriochlorin (*m*-THPBC). A comparative study, *J. Photochem. Photobiol. B: Biol.*, **1999**, *53*, 136–143.

131. H.-B. Ris, H. J. Altermatt, C. M. Stewart, T. Schaffner, Q. Wang, C. K. Lim, R. Bonnett, U. Althaus, Photodynamic therapy with *m*-tetrahydroxyphenylchlorin *in vivo*: Optimization of the therapeutic index, *Int. J. Cancer*, **1993**, *55*, 245–249.

132. S. A. Blant, A. Woodtli, G. Wagnières, C. Fontolliet, H. van den Bergh, P. Monnier, *In Vivo* Fluence Rate Effect in Photodynamic Therapy of Early Cancers with Tetra(*m*-hydroxyphenyl)chlorin, *Photochem. Photobiol.*, **1996**, *64*, 963–968.

133. S. Coutier, L. N. Bezdetnaya, T. H. Foster, R.-M. Parache, F. Guillemin, Effect of Irradiation Fluence Rate on the Efficacy of Photodynamic Therapy and Tumor Oxygenation in *meta*-Tetra(Hydroxyphenyl)Chlorin (*m*THPC)-Sensitized HT29 Xenografts in Nude Mice1, *rare*, **2002**, *158*, 339–345.

134. D. Kessel, Transport and localisation of *m*-THPC *in vitro*, *Int. J. Clin. Pract.*, **1999**, *53*, 263–267.

135. V. O. Melnikova, L. N. Bezdetnaya, C. Bour, E. Festor, M.-P. Gramain, J.-L. Merlin, A. Ya. Potapenko, F. Guillemin, Subcellular localization of *meta*-tetra(hydroxyphenyl)chlorin in human tumor cells subjected to photodynamic treatment, *J. Photochem. Photobiol. B: Biol.*, **1999**, *49*, 96–103.

136. M.-H. Teiten, L. Bezdetnaya, P. Morlière, R. Santus, F. Guillemin, Endoplasmic reticulum and Golgi apparatus are the preferential sites of Foscan® localisation in cultured tumour cells, *Br. J. Cancer*, **2003**, *88*, 146–152.

137. E. G. Friberg, B. Čunderlíková, E. O. Pettersen, J. Moan, pH effects on the cellular uptake of four photosensitizing drugs evaluated for use in photodynamic therapy of cancer, *Cancer Lett.*, **2003**, *195*, 73–80.

138. S. Thibaut, L. Bourré, D. Hernot, N. Rousset, Y. Lajat, T. Patrice, Effects of BAPTA-AM, Forskolin, DSF and Z.VAD.fmk on PDT-induced apoptosis and *m*-THPC phototoxicity on B16 cells, *Apoptosis*, **2002**, *7*, 99–106.

139. Z. Yuan, G. Fan, H. Wu, C. Liu, Y. Zhan, Y. Qiu, C. Shou, F. Gao, J. Zhang, P. Yin, K. Xu, Photodynamic therapy synergizes with PD-L1 checkpoint blockade for immunotherapy of CRC by multifunctional nanoparticles, *Mol. Ther.*, **2021**, *29*, 2931–2948.

140. J. Garrier, A. Bressenot, S. Gräfe, S. Marchal, S. Mitra, T. H. Foster, F. Guillemin, L. Bezdetnaya, Compartmental Targeting for *m*THPC-Based Photodynamic Treatment *In Vivo*: Correlation of Efficiency, Pharmacokinetics, and Regional Distribution of Apoptosis, *Int. J. Radiat. Oncol. Biol. Phys.*, **2010**, *78*, 563–571.

141. Q. Peng, J. Moan, L. W. Ma, J. M. Nesland, Uptake, localization, and photodynamic effect of *meso*-tetra(hydroxyphenyl)porphine and its corresponding chlorin in normal and tumor tissues of mice bearing mammary carcinoma, *Cancer Res.*, **1995**, *55*, 2620–2626.

142. M. Triesscheijn, M. Ruevekamp, M. Aalders, P. Baas, F. A. Stewart, Outcome of *m*THPC Mediated Photodynamic Therapy is Primarily Determined by the Vascular Response, *Photochem. Photobiol.*, **2005**, *81*, 1161–1167.

143. H. Cai, Q. Wang, J. Luo, C. K. Lim, Study of temoporfin metabolism by HPLC and electrospray mass spectrometry, *Biomed. Chromatogr.*, **1999**, *13*, 354–359.

144. A. M. Ronn, M. Nouri, L. A. Lofgren, B. M. Steinberg, A. Westerborn, T. Windahl, M. J. Shikowitz, A. L. Abramson, Human tissue levels and plasma pharmacokinetics of temoporfin (Foscan®, *m*THPC), *Laser Med. Sci.*, **1996**, *11*, 267–272.

145. T. Glanzmann, C. Hadjur, M. Zellweger, P. Grosjean, M. Forrer, J.-P. Ballini, P. Monnier, H. van den Bergh, C. K. Lim, G. Wagnières, Pharmacokinetics of Tetra (m-hydroxyphenyl)chlorin in Human Plasma and Individualized Light Dosimetry in Photodynamic Therapy, *Photochem. Photobiol.*, **1998**, *67*, 596–602.

146. H. J. Hopkinson, D. I. Vernon, S. B. Brown, Identification and Partial Characterization of an Unusual Distribution of the Photosensitizer *meta*-

Tetrahydroxyphenyl Chlorin (Temoporfin) in Human Plasma, *Photochem. Photobiol.*, **1999**, *69*, 482–488.

147. A. K. D'Cruz, M. H. Robinson, M. A. Biel, *m*THPC-mediated photodynamic therapy in patients with advanced, incurable head and neck cancer: a multicenter study of 128 patients, *Head Neck*, **2004**, *26*, 232–240.

148. K. J. Lorenz, H. Maier, Squamous cell carcinoma of the head and neck. Photodynamic therapy with Foscan, *HNO*, **2008**, *56*, 402–409.

149. D. J. Ball, D. I. Vernon, S. B. Brown, Research Note: The High Photoactivity of *m*-THPC in Photodynamic Therapy. Unusually Strong Retention of *m*-THPC by RIF-1 Cells in Culture, *Photochem. Photobiol.*, **1999**, *69*, 360–363.

150. C. A. Morton, Treating basal cell carcinoma: has photodynamic therapy come of age?, *Br. J. Dermatol.*, **2001**, *145*, 1–2.

151. R. R. Allison, C. Sibata, T. S. Mang, V. S. Bagnato, G. H. Downie, X. H. Hu, R. Cuenca, Photodynamic therapy for chest wall recurrence from breast cancer, *Photodiagn. Photodyn. Ther.*, **2004**, *1*, 157–171.

152. N. E. Martin, S. M. Hahn, Interstitial photodynamic therapy for prostate cancer: a developing modality, *Photodiagn. Photodyn. Ther.*, **2004**, *1*, 123–136.

153. S. Sasnouski, V. Zorin, I. Khludeyev, M.-A. D'Hallewin, F. Guillemin, L. Bezdetnaya, Investigation of Foscan® interactions with plasma proteins, *Biochim. Biophys. Acta Gen. Subj.*, **2005**, *1725*, 394–402.

154. I. Opitz, T. Krueger, Y. Pan, H.-J. Altermatt, G. Wagnières, H.-B. Ris, Preclinical Comparison of *m*THPC and Verteporfin for Intracavitary Photodynamic Therapy of Malignant Pleural Mesothelioma, *Eur. Surg. Res.*, **2006**, *38*, 333–339.

155. A. C. Kübler, J. de Carpentier, C. Hopper, A. G. Leonard, G. Putnam, Treatment of squamous cell carcinoma of the lip using Foscan-mediated

Photodynamic Therapy, *Int. J. Oral Maxillofac. Surg.*, **2001**, *30*, 504–509.

156. R. Baskaran, J. Lee, S.-G. Yang, Clinical development of photodynamic agents and therapeutic applications, *Biomater. Res.*, **2018**, *22*, 25.

157. V. A. Schwarz, S. D. Klein, R. Hornung, R. Knochenmuss, P. Wyss, D. Fink, U. Haller, H. Walt, Skin protection for photosensitized patients, *Lasers Surg. Med.*, **2001**, *29*, 252–259.

158. E. Gaio, D. Scheglmann, E. Reddi and F. Moret, Uptake and photo-toxicity of Foscan®, Foslip® and Fospeg® in multicellular tumor spheroids, *J. Photochem. Photobiol. B: Biol.*, **2016**, *161*, 244–252.

159. A. Petri, D. Yova, E. Alexandratou, M. Kyriazi, M. Rallis, Comparative characterization of the cellular uptake and photodynamic efficiency of Foscan® and Fospeg in a human prostate cancer cell line, *Photodiagn. Photodyn. Ther.,* **2012**, 9, 344–354.

160. J. Buchholz, B. Kaser-Hotz, T. Khan, C. Rohrer Bley, K. Melzer, R. A. Schwendener, M. Roos, H. Walt, Optimizing Photodynamic Therapy: *In vivo* Pharmacokinetics of Liposomal *meta*-(Tetrahydroxyphenyl)Chlorin in Feline Squamous Cell Carcinoma, *Clin. Cancer Res.*, **2005**, *11*, 7538–7544.

161. V. Reshetov, D. Kachatkou, T. Shmigol, V. Zorin, M.-A. D'Hallewin, F. Guillemin, L. Bezdetnaya, Redistribution of *meta*-tetra(hydroxyphenyl)chlorin (*m*-THPC) from conventional and PEGylated liposomes to biological substrates, *Photochem. Photobiol. Sci.*, **2011**, *10*, 911–919.

162. L. B. Josefsen, R. W. Boyle, Photodynamic therapy: novel third-generation photosensitizers one step closer?, *Br. J. Pharmacol.*, **2008**, *154*, 1–3.

163. M. O. Senge, *m*THPC – A drug on its way from second to third generation photosensitizer?, *Photodiagn. Photodyn. Ther.*, **2012**, *9*, 170–179.

164. A. Wiehe, E. J. Simonenko, M. O. Senge, B. Röder, Hydrophilicity vs hydrophobicity—varying the amphiphilic structure of porphyrins related to the photosensitizer *m*-THPC, *J. Porphyrins Phthalocyanines*, **2001**, *5*, 758–761.

165. I. Laville, T. Figueiredo, B. Loock, S. Pigaglio, P. Maillard, D. S. Grierson, D. Carrez, A. Croisy, J. Blais, Synthesis, cellular internalization and photodynamic activity of glucoconjugated derivatives of tri and tetra(*meta*-hydroxyphenyl)chlorins, *Bioorg. Med. Chem.*, **2003**, *11*, 1643–1652.

166. L. Rogers, F. Majer, N. N. Sergeeva, E. Paszko, J. F. Gilmer, M. O. Senge, Synthesis and biological evaluation of Foscan® bile acid conjugates to target esophageal cancer cells, *Bioorg. Med. Chem. Lett.*, **2013**, *23*, 2495–2499.

167. L. Rogers, N. N. Sergeeva, E. Paszko, G. M. F. Vaz, M. O. Senge, Lead Structures for Applications in Photodynamic Therapy. 6. Temoporfin Anti-Inflammatory Conjugates to Target the Tumor Microenvironment for *In Vitro* PDT, *PLOS ONE*, **2015**, *10*, e0125372.

168. M. B. Vrouenraets, G. W. M. Visser, F. A. Stewart, M. Stigter, H. Oppelaar, P. E. Postmus, G. B. Snow, G. A. M. S. van Dongen, Development of *meta*-Tetrahydroxyphenylchlorin-Monoclonal Antibody Conjugates for Photoimmunotherapy, *Cancer Res.*, **1999**, *59*, 1505–1513.

169. I. Yakavets, M. Millard, V. Zorin, H.-P. Lassalle, L. Bezdetnaya, Current state of the nanoscale delivery systems for temoporfin-based photodynamic therapy: Advanced delivery strategies, *J. Control. Release*, **2019**, *304*, 268–287.

170. F. Moret, D. Scheglmann, E. Reddi, Folate-targeted PEGylated liposomes improve the selectivity of PDT with *meta*-tetra(hydroxyphenyl)chlorin (*m*-THPC), *Photochem. Photobiol. Sci.*, **2013**, *12*, 823–834.

171. Y. Liu, L. Scrivano, J. D. Peterson, M. H. A. M. Fens, I. B. Hernández, B. Mesquita, J. S. Toraño, W. E. Hennink, C. F. van Nostrum, S. Oliveira, EGFR-Targeted Nanobody Functionalized Polymeric Micelles Loaded with mTHPC for Selective Photodynamic Therapy, *Mol. Pharm.*, **2020**, *17*, 1276–1292.

172. S. J. Buwalda, K. W. M. Boere, P. J. Dijkstra, J. Feijen, T. Vermonden, W. E. Hennink, Hydrogels in a historical perspective: From simple networks to smart materials, *J. Control. Release*, **2014**, *190*, 254–273.

173. Y. Qiu, K. Park, Environment-sensitive hydrogels for drug delivery, *Adv. Drug Deliv. Rev.*, **2001**, *53*, 321–339.

174. S. Belali, H. Savoie, J. M. O'Brien, A. A. Cafolla, B. O'Connell, A. R. Karimi, R. W. Boyle, M. O. Senge, Synthesis and Characterization of Temperature-Sensitive and Chemically Cross-Linked Poly(N-isopropylacrylamide)/Photosensitizer Hydrogels for Applications in Photodynamic Therapy, *Biomacromolecules*, **2018**, *19*, 1592–1601.

175. S. Belali, A. R. Karimi, M. Hadizadeh, Cell-specific and pH-sensitive nanostructure hydrogel based on chitosan as a photosensitizer carrier for selective photodynamic therapy, *Int. J. Biol. Macromol.*, **2018**, *110*, 437–448.

176. F. Bayat, A. R. Karimi, Design of photodynamic chitosan hydrogels bearing phthalocyanine-colistin conjugate as an antibacterial agent, *Int. J. Biol. Macromol.*, **2019**, *129*, 927–935.

177. J. M. van Bemmelen, Second Mŕmoire. L'hydrogel de l'acide siliciqne, *Rec. Trav. Chim. Pays Bas*, **1888**, *7*, 69–74.

178. W. Y. Seow, C. A. E. Hauser, Short to ultrashort peptide hydrogels for biomedical uses, *Mater. Today*, **2014**, *17*, 381–388.

179. J. H. Grindlay, O. T. Clagett, A plastic sponge prosthesis for use after pneumonectomy; preliminary report of an experimental study, *Proc. Staff Meet. Mayo Clin.*, **1949**, *24*, 538.

180. C. M. Kirschner, K. S. Anseth, Hydrogels in healthcare: From static to dynamic material microenvironments, *Acta Mater.*, **2013**, *61*, 931–944.

181. S. M. Tadavarthy, J. H. Moller, K. Amplatz, Polyvinyl alcohol (Ivalon)—a new embolic material, *Am. J. Roentgenol.*, **1975**, *125*, 609–616.

182. O. Wichterle, D. Lím, Hydrophilic Gels for Biological Use, *Nature*, **1960**, *185*, 117–118.

183. M. Rizwan, R. Yahya, A. Hassan, M. Yar, A. D. Azzahari, V. Selvanathan, F. Sonsudin, C. N. Abouloula, pH Sensitive Hydrogels in Drug Delivery: Brief History, Properties, Swelling, and Release Mechanism, Material Selection and Applications, *Polymers*, **2017**, *9*, 137.

184. T. Ren, Z. Mao, J. Guo, C. Gao, Directional Migration of Vascular Smooth Muscle Cells Guided by a Molecule Weight Gradient of Poly(2-hydroxyethyl methacrylate) Brushes, *Langmuir*, **2013**, *29*, 6386–6395.

185. C.-C. Lin, K. S. Anseth, PEG Hydrogels for the Controlled Release of Biomolecules in Regenerative Medicine, *Pharm. Res.*, **2009**, *26*, 631–643.

186. G. Rivera-Hernández, M. Antunes-Ricardo, P. Martínez-Morales, M. L. Sánchez, Polyvinyl alcohol based-drug delivery systems for cancer treatment, *Int. J. Pharm.*, **2021**, *600*, 120478.

187. R. M. Trigo, M. D. Blanco, J. M. Teijón, R. Sastre, Anticancer drug, ara-C, release from pHEMA hydrogels, *Biomaterials*, **1994**, *15*, 1181–1186.

188. W. Wei, H. Li, C. Yin, F. Tang, Research progress in the application of in situ hydrogel system in tumor treatment, Drug Deliv., **2020**, *27*, 460–468.

189. H. Huang, X. Qi, Y. Chen, Z. Wu, Thermo-sensitive hydrogels for delivering biotherapeutic molecules: A review, *Saudi Pharm. J.*, **2019**, *27*, 990–999.

190. N. B. Graham, M. E. McNeill, Hydrogels for controlled drug delivery, *Biomaterials*, **1984**, *5*, 27–36.

191. F. Ullah, M. B. H. Othman, F. Javed, Z. Ahmad, H. Md. Akil, Classification, processing and application of hydrogels: A review, *Mater. Sci. Eng. C.*, **2015**, *57*, 414–433.

192. M. C. Catoira, L. Fusaro, D. Di Francesco, M. Ramella, F. Boccafoschi, Overview of natural hydrogels for regenerative medicine applications, *J. Mater. Sci: Mater. Med.*, **2019**, *30*, 115.

193. Q. Wei, N.-N. Deng, J. Guo, J. Deng, Synthetic Polymers for Biomedical Applications, *Int. J. Biomater.*, **2018**, *2018*, e7158621.

194. W. Zhu, J. Ding, Synthesis and characterization of a redox-initiated, injectable, biodegradable hydrogel, *J. Appl. Polym. Sci.*, **2006**, *99*, 2375–2383.

195. M. Deshmukh, Y. Singh, S. Gunaseelan, D. Gao, S. Stein, P. J. Sinko, Biodegradable poly(ethylene glycol) hydrogels based on a self-elimination degradation mechanism, *Biomaterials*, **2010**, *31*, 6675–6684.

196. T. Miyazaki, K. Yamaoka, J. P. Gong, Y. Osada, Hydrogels with Crystalline or Liquid Crystalline Structure, *Macromol. Rapid Commun.*, **2002**, *23*, 447–455.

197. S. Khan, A. Ullah, K. Ullah, N. Rehman, Insight into hydrogels, *Des. Monomers Polym.*, **2016**, *19*, 456–478.

198. G. R. Deen, X. J. Loh, Stimuli-Responsive Cationic Hydrogels in Drug Delivery Applications, *Gels*, **2018**, *4*, 13.

199. K. Varaprasad, G. M. Raghavendra, T. Jayaramudu, M. M. Yallapu, R. Sadiku, A mini review on hydrogels classification and recent developments in miscellaneous applications, *Mater. Sci. Eng. C*, **2017**, *79*, 958–971.

200. X. Ding, Y. Wang, Weak bond-based injectable and stimuli responsive hydrogels for biomedical applications, *J. Mater. Chem. B*, **2017**, *5*, 887–906.

201. J. L. West, J. A. Hubbell, Comparison of covalently and physically cross-linked polyethylene glycol-based hydrogels for the prevention of postoperative adhesions in a rat model, *Biomaterials*, **1995**, *16*, 1153–1156.

202. C. K. Kuo, P. X. Ma, Maintaining dimensions and mechanical properties of ionically crosslinked alginate hydrogel scaffolds *in vitro*, *J. Biomed. Mater. Res. A*, **2008**, *84A*, 899–907.

203. R. Ricciardi, F. Auriemma, C. De Rosa, F. Lauprêtre, X-ray Diffraction Analysis of Poly(vinyl alcohol) Hydrogels, Obtained by Freezing and Thawing Techniques, *Macromolecules*, **2004**, *37*, 1921–1927.

204. K. Trabbic-Carlson, L. A. Setton, A. Chilkoti, Swelling and Mechanical Behaviors of Chemically Cross-Linked Hydrogels of Elastin-like Polypeptides, *Biomacromolecules*, **2003**, *4*, 572–580.

205. K.-J. Kim, S.-B. Lee, N.-W. Han, Kinetics of crosslinking reaction of PVA membrane with glutaraldehyde, *Korean J. Chem. Eng.*, **1994**, *11*, 41–47.

206. O. A. C. Monteiro, C. Airoldi, Some studies of crosslinking chitosan–glutaraldehyde interaction in a homogeneous system, *Int. J. Biol. Macromol.*, **1999**, *26*, 119–128.

207. W. E. Hennink, C. F. van Nostrum, Novel crosslinking methods to design hydrogels, *Adv. Drug Deliv. Rev.*, **2012**, *64*, 223–236.

208. Y.-C. Nho, J.-S. Park, Y.-M. Lim, Preparation of Poly(acrylic acid) Hydrogel by Radiation Crosslinking and Its Application for Mucoadhesives, *Polymers*, **2014**, *6*, 890–898.

209. S. Ida, Structural design of vinyl polymer hydrogels utilizing precision radical polymerization, *Polym. J.*, **2019**, *51*, 803–812.

210. J. Li, D. J. Mooney, Designing hydrogels for controlled drug delivery, *Nat. Rev. Mater.*, **2016**, *1*, 1–17.

211. Z. Sun, C. Song, C. Wang, Y. Hu, J. Wu, Hydrogel-Based Controlled Drug Delivery for Cancer Treatment: A Review, *Mol. Pharm.*, **2020**, *17*, 373–391.

212. J. Zhu, R. E. Marchant, Design properties of hydrogel tissue-engineering scaffolds, *Expert Rev. Med. Devices*, **2011**, *8*, 607–626.

213. X. Hong, Z. Wu, L. Chen, F. Wu, L. Wei, W. Yuan, Hydrogel Microneedle Arrays for Transdermal Drug Delivery, *Nano-Micro Lett.*, **2014**, *6*, 191–199.

214. G. R. Shin, H. E. Kim, J. H. Kim, S. Choi, M. S. Kim, Advances in Injectable In Situ-Forming Hydrogels for Intratumoral Treatment, *Pharmaceutics*, **2021**, *13*, 1953.

215. B. Stawicki, T. Schacher, H. Cho, Nanogels as a Versatile Drug Delivery System for Brain Cancer, *Gels*, **2021**, *7*, 63.

216. J. K. Oh, R. Drumright, D. J. Siegwart, K. Matyjaszewski, The development of microgels/nanogels for drug delivery applications, *Prog. Polym. Sci.*, **2008**, *33*, 448–477.

217. K. R. Kamath, K. Park, Biodegradable hydrogels in drug delivery, *Adv. Drug Deliv. Rev.*, **1993**, *11*, 59–84.

218. S. Merino, C. Martín, K. Kostarelos, M. Prato, E. Vázquez, Nanocomposite Hydrogels: 3D Polymer–Nanoparticle Synergies for On-Demand Drug Delivery, *ACS Nano*, **2015**, *9*, 4686–4697.

219. A. Ahsan, W.-X. Tian, M. A. Farooq, D. H. Khan, An overview of hydrogels and their role in transdermal drug delivery, *Int. J. Polym. Mater. Polym. Biomater.*, **2021**, *70*, 574–584.

220. K. Zhang, X. Shi, X. Lin, C. Yao, L. Shen, Y. Feng, Poloxamer-based in situ hydrogels for controlled delivery of hydrophilic macromolecules after intramuscular injection in rats, *Drug Deliv.*, **2015**, *22*, 375–382.

221. L. A. Sharpe, A. M. Daily, S. D. Horava, N. A. Peppas, Therapeutic applications of hydrogels in oral drug delivery, *Expert Opin. Drug Deliv.*, **2014**, *11*, 901–915.

222. F. Andrade, M. M. Roca-Melendres, E. F. Durán-Lara, D. Rafael, S. Schwartz, Stimuli-Responsive Hydrogels for Cancer Treatment: The Role of pH, Light, Ionic Strength and Magnetic Field, *Cancers*, **2021**, *13*, 1164.

223. F. Raza, Y. Zhu, L. Chen, X. You, J. Zhang, A. Khan, M. W. Khan, M. Hasnat, H. Zafar, J. Wu, L. Ge, Paclitaxel-loaded pH responsive hydrogel based on self-assembled peptides for tumor targeting, *Biomater. Sci.*, **2019**, *7*, 2023–2036.

224. L. Zhao, L. Zhu, F. Liu, C. Liu, Shan-Dan, Q. Wang, C. Zhang, J. Li, J. Liu, X. Qu, Z. Yang, pH triggered injectable amphiphilic hydrogel containing doxorubicin and paclitaxel, *Int. J. Pharm.*, **2011**, *410*, 83–91.

225. M. Singh, S. Kundu, A. R. M, V. Sreekanth, R. K. Motiani, S. Sengupta, A. Srivastava, A. Bajaj, Injectable small molecule hydrogel as a potential nanocarrier for localized and sustained in vivo delivery of doxorubicin, *Nanoscale*, **2014**, *6*, 12849–12855.

226. M. Norouzi, B. Nazari, D. W. Miller, Injectable hydrogel-based drug delivery systems for local cancer therapy, *Drug Discov. Today*, **2016**, *21*, 1835–1849.

227. B. Khurana, P. Gierlich, A. Meindl, L. C. Gomes-da-Silva, M. O. Senge, Hydrogels: soft matters in photomedicine, *Photochem. Photobiol. Sci.*, **2019**, *18*, 2613–2656.

228. D. Gao, H. Xu, M. A. Philbert, R. Kopelman, Ultrafine Hydrogel Nanoparticles: Synthetic Approach and Therapeutic Application in Living Cells, *Angew. Chem. Int. Ed.*, **2007**, *46*, 2224–2227.

229. N. Dragicevic-Curic, S. Winter, M. Stupar, J. Milic, D. Krajišnik, B. Gitter, A. Fahr, Temoporfin-loaded liposomal gels: Viscoelastic properties and *in vitro* skin penetration, *Int. J. Pharm.*, **2009**, *373*, 77–84.

230. N. Dragicevic-Curic, S. Winter, D. Krajisnik, M. Stupar, J. Milic, S. Graefe, A. Fahr, Stability evaluation of temoporfin-loaded liposomal gels for topical application, *J. Liposome Res.*, **2010**, *20*, 38–48.

231. D. Zhu, Z. Zheng, G. Luo, M. Suo, X. Li, Y. Duo, B. Z. Tang, Single injection and multiple treatments: An injectable nanozyme hydrogel as AIEgen reservoir and release controller for efficient tumor therapy, *Nano Today*, **2021**, *37*, 101091.

232. H. Wang, Z. Fu, W. Li, Y. Li, L. Zhao, L. Wen, J. Zhang, N. Wen, The synthesis and application of nano doxorubicin-indocyanine green matrix metalloproteinase-responsive hydrogel in chemophototherapy for head and neck squamous cell carcinoma, *Int. J. Nanomed.*, **2019**, *14*, 623–638.

233. L. Zhang, M. Yang, Y. Ji, K. Xiao, J. Shi, L. Wang, UCPs/Zn_2GeO_4:Mn^{2+}/g-C_3N_4 heterojunction engineered injectable thermosensitive hydrogel for oxygen independent breast cancer neoadjuvant photodynamic therapy, *Biomater. Sci.*, **2021**, *9*, 2124–2136.

234. L. Luo, Q. Zhang, Y. Luo, Z. He, X. Tian, G. Battaglia, Thermosensitive nanocomposite gel for intra-tumoral two-photon photodynamic therapy, *J. Control. Release*, **2019**, *298*, 99–109.

235. E. Paszko, C. Ehrhardt, M. O. Senge, D. P. Kelleher, J. V. Reynolds, Nanodrug applications in photodynamic therapy, *Photodiagnosis Photodyn. Ther.*, **2011**, *8*, 14–29.

236. H. J. Hah, G. Kim, Y.-E. K. Lee, D. A. Orringer, O. Sagher, M. A. Philbert, R. Kopelman, Methylene Blue-Conjugated Hydrogel Nanoparticles and Tumor-Cell Targeted Photodynamic Therapy, *Macromol. Biosci.*, **2011**, *11*, 90–99.

237. F. Khoushab, M. Yamabhai, Chitin Research Revisited, *Mar. Drugs*, **2010**, *8*, 1988–2012.

238. I. Younes, M. Rinaudo, Chitin and Chitosan Preparation from Marine Sources. Structure, Properties and Applications, *Mar. Drugs*, **2015**, *13*, 1133–1174.

239. K. Kurita, Chitin and Chitosan: Functional Biopolymers from Marine Crustaceans, *Mar. Biotechnol*, **2006**, *8*, 203.

240. K. V. Harish Prashanth, R. N. Tharanathan, Chitin/chitosan: modifications and their unlimited application potential—an overview, *Trends Food Sci. Technol.*, **2007**, *18*, 117–131.

241. V. K. Mourya, N. N. Inamdar, Chitosan-modifications and applications: Opportunities galore, *React. Funct. Polym.*, **2008**, *68*, 1013–1051.

242. M. Rinaudo, Chitin and chitosan: Properties and applications, *Prog. Polym. Sci.*, **2006**, *31*, 603–632.

243. I. A. Sogias, V. V. Khutoryanskiy, A. C. Williams, Exploring the Factors Affecting the Solubility of Chitosan in Water, *Macromol. Chem. Phys.*, **2010**, *211*, 426–433.

244. I. Aranaz, M. Mengibar, R. Harris, I. Panos, B. Miralles, N. Acosta, G. Galed, A. Heras, Functional Characterization of Chitin and Chitosan, *Curr. Chem. Biol.,* **2009**, *3*, 203–230.

245. S. (Gabriel) Kou, L. M. Peters, M. R. Mucalo, Chitosan: A review of sources and preparation methods, *Int. J. Biol. Macromol.*, **2021**, *169*, 85–94.

246. H. Zhang, S. H. Neau, *In vitro* degradation of chitosan by a commercial enzyme preparation: effect of molecular weight and degree of deacetylation, *Biomaterials*, **2001**, *22*, 1653–1658.

247. S. Hirano, H. Tsuchida, N. Nagao, N-acetylation in chitosan and the rate of its enzymic hydrolysis, *Biomaterials*, **1989**, *10*, 574–576.

248. M. Dash, F. Chiellini, R. M. Ottenbrite, E. Chiellini, Chitosan - A versatile semi-synthetic polymer in biomedical applications, *Prog. Polym. Sci.*, **2011**, *36*, 981–1014.

249. I. Wedmore, J. G. McManus, A. E. Pusateri, J. B. Holcomb, A Special Report on the Chitosan-based Hemostatic Dressing: Experience in Current Combat Operations, *J. Trauma Acute Care Surg.*, **2006**, *60*, 655–658.

250. P. Baldrick, The safety of chitosan as a pharmaceutical excipient, *Regul. Toxicol. Pharmacol.*, **2010**, *56*, 290–299.

251. S. B. Rao, C. P. Sharma, Use of chitosan as a biomaterial: Studies on its safety and hemostatic potential, *J. Biomed. Mater. Res.*, **1997**, *34*, 21–28.

252. S. Hirano, M. Iwata, K. Yamanaka, H. Tanaka, T. Toda, H. Inui, Enhancement of Serum Lysozyme Activity by Injecting a Mixture of Chitosan Oligosaccharides Intravenously in Rabbits, *Agric. Biol. Chem.*, **1991**, *55*, 2623–2625.

253. S. H. Pangburn, P. V. Trescony, J. Heller, Lysozyme degradation of partially deacetylated chitin, its films and hydrogels, *Biomaterials*, **1982**, *3*, 105–108.

254. K. Tsukada, T. Matsumoto, K. Aizawa, A. Tokoro, R. Naruse, S. Suzuki, M. Suzuki, Antimetastatic and Growth-inhibitory Effects of N-Acetylchitohexaose in Mice Bearing Lewis Lung Carcinoma, *Jpn. J. Cancer Res.*, 1990, **81**, 259–265.

255. A. Saber, S. P. Strand, M. Ulfendahl, Use of the biodegradable polymer chitosan as a vehicle for applying drugs to the inner ear, *Eur. J. Pharm. Sci.*, **2010**, *39*, 110–115.

256. I. M. van der Lubben, J. C. Verhoef, A. C. van Aelst, G. Borchard, H. E. Junginger, Chitosan microparticles for oral vaccination: preparation, characterization and preliminary *in vivo* uptake studies in murine Peyer's patches, *Biomaterials*, **2001**, *22*, 687–694.

257. R. Fernández-Urrusuno, P. Calvo, C. Remuñán-López, J. L. Vila-Jato, M. José Alonso, Enhancement of Nasal Absorption of Insulin Using Chitosan Nanoparticles, *Pharm. Res.*, **1999**, *16*, 1576–1581.

258. M. N. V. Ravi Kumar, A review of chitin and chitosan applications, *React. Funct. Polym.*, **2000**, *46*, 1–27.

259. T. Kean, M. Thanou, Biodegradation, biodistribution and toxicity of chitosan, *Adv. Drug Deliv. Rev.*, **2010**, *62*, 3–11.

260. N. Bhattarai, J. Gunn, M. Zhang, Chitosan-based hydrogels for controlled, localized drug delivery, *Adv. Drug Deliv. Rev.*, **2010**, *62*, 83–99.

261. X. Bai, An injectable self-healing hydrogel “Trojan Horse” for adjunctive therapy of colon cancer recurrence, *New J. Chem.*, **2021**, *45*, 20818–20824.

262. J. Zhan, Y. Wu, H. Wang, J. Liu, Q. Ma, K. Xiao, Z. Li, J. Li, F. Luo, H. Tan, An injectable hydrogel with pH-sensitive and self-healing properties based on 4armPEGDA and N-carboxyethyl chitosan for local treatment of hepatocellular carcinoma, *Int. J. Biol. Macromol.*, **2020**, *163*, 1208–1222.

263. L.-Y. Xia, X. Zhang, M. Cao, Z. Chen, F.-G. Wu, Enhanced Fluorescence Emission and Singlet Oxygen Generation of Photosensitizers Embedded in Injectable Hydrogels for Imaging-Guided Photodynamic Cancer Therapy, *Biomacromolecules*, **2017**, *18*, 3073–3081.

264. F. Azadikhah, A. R. Karimi, G. H. Yousefi, M. Hadizadeh, Dual antioxidant-photosensitizing hydrogel system: Cross-linking of chitosan with tannic acid for enhanced photodynamic efficacy, *Int. J. Biol. Macromol.*, **2021**, *188*, 114–125.

265. G. M. F. Calixto, S. R. de Annunzio, F. D. Victorelli, M. L. Frade, P. S. Ferreira, M. Chorilli, C. R. Fontana, Chitosan-Based Drug Delivery Systems for Optimization of Photodynamic Therapy: a Review, *AAPS Pharm. Sci. Tech.*, **2019**, *20*, 253.

266. P. T. C. So, C. Y. Dong, B. R. Masters, K. M. Berland, Two-Photon Excitation Fluorescence Microscopy, *Annu. Rev. Biomed. Eng.,* **2000**, *2*, 399–429.

267. P. Lenz, *In vivo* Excitation of Photosensitizers by Infrared Light, *Photochem. Photobiol.,* **1995**, *62*, 333–338.

268. C. Rimington, Spectral-absorption coefficients of some porphyrins in the Soret-band region, *Biochem. J.*, **1960**, *75*, 620–623.

269. J.-L. Ravant, T. Douki, J. Cadet, Direct and indirect effects of UV radiation on DNA and its components, *J. Photochem. Photobiol. B: Biol.*, **2001**, *63*, 88–102.

270. J. D. Bhawalkar, N. D. Kumar, C.-F. Zhao, P. N. Pasad, Two-Photon Photodynamic Therapy, *J. Clin. Laser Med. Surg.,* **1997**, *15*, 201–204.

271. M. O. Senge, M. Fazekas, E. G. A. Notaras, W. J. Blau, M. Zawadzka, O. B. Locos, E. M. Ni Mhuircheartaigh, Nonlinear Optical Properties of Porphyrins, *Adv. Mater.*, **2007**, *19*, 2737–2774.

272. S. G. Mucha, L. Firlej, J.-L. Bantignies, A. Żak, M. Samoć, K. Matczyszyn, Acetone-derived luminescent polymer dots: a facile and low-cost synthesis leads to remarkable photophysical properties, *RSC Adv.*, **2020**, *10*, 38437–38445.

273. I. Maliszewska, E. Wanarska, A. C. Thompson, I. D. W. Samuel, K. Matczyszyn, Biogenic Gold Nanoparticles Decrease Methylene Blue Photobleaching and Enhance Antimicrobial Photodynamic Therapy, *Molecules*, 2021, **26**, 623.

274. I. Maliszewska, B. Lisiak, K. Popko, K. Matczyszyn, Enhancement of the Efficacy of Photodynamic Inactivation of Candida albicans with the Use of Biogenic Gold Nanoparticles, *Photochem. Photobiol.*, **2017**, *93*, 1081–1090.

275. I. Maliszewska, A. Leśniewska, J. Olesiak-Bańska, K. Matczyszyn, M. Samoć, Biogenic gold nanoparticles enhance methylene blue-induced phototoxic effect on Staphylococcus epidermidis, *J. Nanopart. Res.*, **2014**, *16*, 2457.

276. L. Rogers, E. Burke-Murphy and M. O. Senge, Simple Porphyrin Desymmetrization: 5,10,15,20-Tetrakis(3-hydroxyphenyl)porphyrin (*m*THPP) as a Gateway Molecule for Peripheral Functionalization, *Eur. J. Org. Chem.*, **2014**, 4283–4294.

277. A. Wiehe, Y. M. Shaker, J. C. Brandt, S. Mebs, M. O. Senge, Lead structures for applications in photodynamic therapy. Part 1: Synthesis and variation of *m*-THPC (Temoporfin) related amphiphilic A_2BC-type porphyrins, *Tetrahedron*, **2005**, *61*, 5535–5564.

278. M. B. Bakar, M. Oelgemöller, M. O. Senge, Lead structures for applications in photodynamic therapy. Part 2: Synthetic studies for

photo-triggered release systems of bioconjugate porphyrin photosensitizers, *Tetrahedron*, **2009**, *65*, 7064–7078.

279. M. Drobizhev, Y. Stepanenko, Y. Dzenis, A. Karotki, A. Rebane, P. N. Taylor, H. L. Anderson, Understanding Strong Two-Photon Absorption in π-Conjugated Porphyrin Dimers *via* Double-Resonance Enhancement in a Three-Level Model, *J. Am. Chem. Soc.*, **2004**, *126*, 15352–15353.

280. L. M. Mazur, T. Roland, S. Leroy-Lhez, V. Sol, M. Samoc, I. D. W. Samuel, K. Matczyszyn, Efficient Singlet Oxygen Photogeneration by Zinc Porphyrin Dimers upon One- and Two-Photon Excitation, *J. Phys. Chem. B*, **2019**, *123*, 4271–4277.

281. X. Liang, Q. Zhang, Recent progress on intramolecular charge-transfer compounds as photoelectric active materials, *Sci. China Mater.*, **2017**, *60*, 1093–1101.

282. N. Sheng, D. Liu, J. Wu, B. Gu, Z. Wang, Y. Cui, Donor-π-acceptor type porphyrins with large two-photon absorption cross section, *Dyes Pigm.*, **2015**, *119*, 116–121.

283. Ò. Rubio-Pons, Y. Luo, H. Ågren, Effects of conjugation length, electron donor and acceptor strengths on two-photon absorption cross sections of asymmetric zinc-porphyrin derivatives, *J. Chem. Phys.*, **2006**, *124*, 094310.

284. Y. Zheng, S. Sun, L. Xu, S. Ni, W. Liu, B. Huang, Q. Huang, Q. Zhang, F. Lu, M.-D. Li, Arylamine-coumarin based donor-acceptor dyads: Unveiling the relationship between two-photon absorption cross-section and lifetime of singlet excited state intramolecular charge separation, *Dyes Pigm.*, **2019**, 165, 301–307.

285. T. Xiong, M. Li, X. Zhao, Y. Zou, J. Du, J. Fan, X. Peng, Functional two-photon cationic targeted photosensitizers for deep-seated tumor imaging and therapy, *Sens. Actuators B: Chem.*, **2020**, *304*, 127310.

286. R. Han, M. Zhao, Z. Wang, H. Liu, S. Zhu, L. Huang, Y. Wang, L. Wang, Y. Hong, Y. Sha, Y. Jiang, Super-efficient in Vivo Two-Photon

Photodynamic Therapy with a Gold Nanocluster as a Type I Photosensitizer, *ACS Nano*, **2020**, *14*, 9532–9544.

287. B. Hamed, T. von Haimberger, V. Kozich, A. Wiehe, K. Heyne, Two-photon cross-sections of the photosensitizers *m*-THPC and *m*-THPP in the 1.05–1.45μm range, *J. Photochem. Photobiol. A: Chem.*, **2014**, *295*, 53–56.

288. M. Atif, P. E. Dyer, T. A. Paget, H. V. Snelling, M. R. Stringer, Two-photon excitation studies of m-THPC photosensitizer and photodynamic activity in an epithelial cell line, *Photodiagn. Photodyn. Ther.*, **2007**, *4*, 106–111.

289. M. Schneider, G. Graschew, T. A. Roelofs, E. Balanos, S. Rakowsky, H. Sinn, P. M. Schlag, in *Optical Methods for Tumor Treatment and Detection: Mechanisms and Techniques in Photodynamic Therapy IX*, Proc. SPIE, 2000, vol. 3909, pp. 60–65.

290. A. Gandioso, K. Purkait, G. Gasser, Recent Approaches towards the Development of Ru(II) Polypyridyl Complexes for Anticancer Photodynamic Therapy, *CHIMIA*, **2021**, *75*, 845–855.

291. J. Karges, S. Kuang, F. Maschietto, O. Blacque, I. Ciofini, H. Chao, G. Gasser, Rationally designed ruthenium complexes for 1- and 2-photon photodynamic therapy, *Nat. Commun.*, **2020**, *11*, 3262.

292. L. Arnaut, in *Chemical Kinetics (Second Edition)*, ed. L. Arnaut, *Elsevier*, The Netherlands, **2021**, pp. 317–342.

293. B. Neises, W. Steglich, Simple Method for the Esterification of Carboxylic Acids, *Angew. Chem. Int. Ed.*, **1978**, *17*, 522–524.

294. R. Chinchilla, C. Nájera, The Sonogashira reaction: A booming methodology in synthetic organic chemistry, *Chem. Rev.,* **2007**, *107*, 874–922.

295. C. Petrou, Y. Sarigiannis, in *Peptide Applications in Biomedicine, Biotechnology and Bioengineering*, ed. S. Koutsopoulos, Woodhead Publishing, United Kingdom, **2018**, pp. 1–21.

296. D. Lankhorst, J. Schriever, J. C. Leyte, An NMR relaxation study of hydrogen exchange and its deuterium isotope effects in aqueous carboxylic acid solutions, *Chem. Phys.*, **1983**, *77*, 319–340.

297. R. Bonnett, P. Charlesworth, B. D. Djelal, S. Foley, D. J. McGarvey, T. G. Truscott, Photophysical properties of 5,10,15,20-tetrakis(m-hydroxyphenyl)porphyrin (*m*-THPP), 5,10,15,20-tetrakis(m-hydroxyphenyl)chlorin (*m*-THPC) and 5,10,15,20-tetrakis(m-hydroxyphenyl)bacteriochlorin (*m*-THPBC): a comparative study, *J. Chem. Soc., Perkin Trans. 2*, **1999**, 325–328.

298. K. Zhang, J. Liu, Y. Zhang, J. Fan, C.-K. Wang, L. Lin, Theoretical Study of the Mechanism of Aggregation-Caused Quenching in Near-Infrared Thermally Activated Delayed Fluorescence Molecules: Hydrogen-Bond Effect, *J. Phys. Chem. C*, **2019**, *123*, 24705–24713.

299. R. Bonnett, B. D. Djelal, A. Nguyen, Physical and chemical studies related to the development of *m*-THPC (FOSCAN®) for the photodynamic therapy (PDT) of tumours, *J. Porphyrins Phthalocyanines*, **2001**, *05*, 652–661.

300. D. M. Fiedler, F. Wierrani, G. Schnitzhofer, J. C. M. Stewart, K. Gharehbaghi, W. Grünberger, B. Krammer, Does the in-vitro efficiency of *meso*-tetrahydroxy-phenyl-chlorin depend on pre-treatment of sensitizer?, *J. Photochem. Photobiol. B: Biol.*, **1997**, *38*, 241–244.

301. W. I. White, in: *The Porphyrins*; Ed. D. Dolphin, *Academic Press,* New York, **2012**, *Vol. 5*, pp. 303– 335.

302. D. F. Swinehart, The Beer-Lambert law, *J. Chem. Ed.*, **1962**, 39, 333–335.

303. P. R. Ogilby, C. S. Foote, Chemistry of singlet oxygen. 42. Effect of solvent, solvent isotopic substitution, and temperature on the lifetime of singlet molecular oxygen ($^1\Delta_g$), *J. Am. Chem. Soc.*, **1983**, *105*, 3423–3430.

304. M. A. J. Rodgers, Solvent-induced deactivation of singlet oxygen, *J. Am. Chem. Soc.*, **1983**, *105*, 6201–6205.

305. W. Spiller, H. Kliesch, D. Wöhrle, S. Hackbarth, B. Röder, G. Schnurpfeil, Singlet Oxygen Quantum Yields of Different Photosensitizers in Polar Solvents and Micellar Solutions, *J. Porphyrins Phthalocyanines*, **1998**, *02*, 145–158.

306. H. Mojzisova, S. Bonneau, P. Maillard, K. Berg,D. Brault, Photosensitizing properties of chlorins in solution and in membrane-mimicking systems, *Photochem. Photobiol. Sci.*, **2009**, *8*, 778–787.

307. Y. Chen, S. Xu, L. Li, M. Zhang, J. Shen, T. Shen, Active oxygen generation and photo-oxygenation involving temporfin (*m*-THPC), *Dyes Pigm.*, **2001**, *51*, 63–69.

308. B. Aveline, O. Delgado, D. Brault, Reaction of singlet oxygen with vinyl-substituted porphyrins. A kinetic study by laser flash photolysis, *J. Chem. Soc., Faraday Trans.*, **1992**, *88*, 1971–1976.

309. P. R. Ogilby, J. Sanetra, Magnetic field effects on excited-state oxygen-organic molecule interactions, *J. Phys. Chem.*, **1993**, *97*, 4689–4694.

310. J. Varchola, K. Želonková, D. Chorvat Jr, D. Jancura, P. Miskovsky, G. Bánó, Singlet oxygen produced by quasi-continuous photo-excitation of hypericin in dimethyl-sulfoxide, *J. Lumin.*, **2016**, *177*, 17–21.

311. A. Staicu, A. Pascu, M. Boni, M. L. Pascu, M. Enescu, Photophysical study of Zn phthalocyanine in binary solvent mixtures, *J. Mol. Struct.*, **2013**, *1044*, 188–193.

312. M. Hajimohammadi, N. Safari, H. Mofakham, A. Shaabani, A new and efficient aerobic oxidation of aldehydes to carboxylic acids with singlet oxygen in the presence of porphyrin sensitizers and visible light, *Tetrahedron Lett.*, **2010**, *51*, 4061–4065.

313. S. Oelckers, T. Hanke, B. Röder, Quenching of singlet oxygen in dimethylformamide, *J. Photochem. Photobiol. A: Chem.*, **2000**, *132*, 29–32.

314. R. Datta, T. M. Heaster, J. T. Sharick, A. A. Gillette, M. C. Skala, Fluorescence lifetime imaging microscopy: fundamentals and advances

in instrumentation, analysis, and applications, *J. Biomed. Opt.*, **2020**, *25*, 071203.

315. D. Wawrzyńczyk, Two-photon absorption in penicillamine capped CdS tetrapods, *J. Mater. Chem. C*, **2017**, *5*, 1724–1729.

316. S. Hei Yau, N. Abeyasinghe, M. Orr, L. Upton, O. Varnavski, J. H. Werner, H.-C. Yeh, J. Sharma, A. P. Shreve, J. S. Martinez, T. G. Iii, Bright two- photon emission and ultra-fast relaxation dynamics in a DNA-templated nanocluster investigated by ultra-fast spectroscopy, *Nanoscale*, **2012**, *4*, 4247–4254.

317. J. Arnbjerg, A. Jiménez-Banzo, M. J. Paterson, S. Nonell, J. I. Borrell, O. Christiansen, P. R. Ogilby, Two-Photon Absorption in Tetraphenylporphycenes: Are Porphycenes Better Candidates than Porphyrins for Providing Optimal Optical Properties for Two-Photon Photodynamic Therapy? *J. Am. Chem. Soc.*, **2007**, *129*, 5188–5199.

318. T. Li, F. Li, C. Altuzarra, A. Classen, G. S. Agarwal, Squeezed light induced two-photon absorption fluorescence of fluorescein biomarkers, *Appl. Phys. Lett.*, **2020**, *116*, 254001.

319. N. S. Makarov, J. Campo, J. M. Hales and J. W. Perry, Rapid, broadband two-photon-excited fluorescence spectroscopy and its application to red-emitting secondary reference compounds, *Opt. Mater. Express*, **2011**, *1*, 551–563.

320. X. Long, J. Wu, S. Yang, Z. Deng, Y. Zheng, W. Zhang, X.-F. Jiang, F. Lu, M.-D. Li and L. Xu, Discovery of and insights into one-photon and two-photon excited ACQ-to-AIE conversion via positional isomerization, *J. Mater. Chem. C*, **2021**, *9*, 11679–11689.

321. C.-K. Wang, P. Macak, Y. Luo, H. Ågren, Effects of π centers and symmetry on two-photon absorption cross sections of organic chromophores, *J. Chem. Phys.*, **2001**, *114*, 9813–9820.

322. O. Mongin, V. Hugues, M. Blanchard-Desce, A. Merhi, S. Drouet, D. Yao, C. Paul-Roth, Fluorenyl porphyrins for combined two-photon

excited fluorescence and photosensitization, *Chem. Phys. Lett.*, **2015**, *625*, 151–156.

323. S. Sumalekshmy, M. M. Henary, N. Siegel, P. V. Lawson, Wu, K. Schmidt, J.-L. Brédas, J. W. Perry, C. J. Fahrni, Design of Emission Ratiometric Metal-Ion Sensors with Enhanced Two-Photon Cross Section and Brightness, *J. Am. Chem. Soc.*, **2007**, *129*, 11888–11889.

324. E. F. F. Silva, F. A. Schaberle, C. J. P. Monteiro, J. M. Dąbrowski, L. G. Arnaut, The challenging combination of intense fluorescence and high singlet oxygen quantum yield in photostable chlorins – a contribution to theranostics, *Photochem. Photobiol. Sci.*, **2013**, *12*, 1187–1192.

325. D. Wöhrle, M. Shopova, S. Müller, A. D. Milev, V. N. Mantareva, K. K. Krastev, Liposome-delivered Zn(II)-2,3-naphthalocyanines as potential sensitizers for PDT: synthesis, photochemical, pharmacokinetic and phototherapeutic studies, *J. Photochem. Photobiol. B: Biol.*, **1993**, *21*, 155–165.

326. U. Michelsen, G. Schnurpfeil, A. K. Sobbi, D. Wöhrle, H. Kliesch, Unsymmetrically Substituted Benzonaphthoporphyrazines: A New Class of Cationic Photosensitizers for the Photodynamic Therapy of Cancer*, *Photochem. Photobiol.*, **1996**, *64*, 694–701.

327. R. Medishetty, J. K. Zaręba, D. Mayer, M. Samoć, R. A. Fischer, Nonlinear optical properties, upconversion and lasing in metal–organic frameworks, *Chem. Soc. Rev.*, **2017**, *46*, 4976–5004.

328. L. Xu, W. Lin, B. Huang, J. Zhang, X. Long, W. Zhang, Q. Zhang, The design strategies and applications for organic multi-branched two-photon absorption chromophores with novel cores and branches: a recent review, *J. Mater. Chem. C*, **2021**, *9*, 1520–1536.

329. C. Hopper, A. Kübler, H. Lewis, I. B. Tan, G. Putnam, the Foscan 01 Study Group, mTHPC-mediated photodynamic therapy for early oral squamous cell carcinoma, *Int. J. Cancer*, **2004**, *111*, 138–146.

330. Y. N. Konan, R. Gurny, E. Allémann, State of the art in the delivery of photosensitizers for photodynamic therapy, *J. Photochem. Photobiol. B: Biol.*, **2002**, *66*, 89–106.

331. B. Tan, L. Huang, Y. Wu, J. Liao, Advances and trends of hydrogel therapy platform in localized tumor treatment: A review, *J. Biomed. Mater. Res. A*, **2021**, *109*, 404–425.

332. A. Reza Karimi, A. Khodadadi, M. Hadizadeh, A nanoporous photosensitizing hydrogel based on chitosan cross-linked by zinc phthalocyanine: an injectable and pH-stimuli responsive system for effective cancer therapy, *RSC Adv.*, **2016**, *6*, 91445–91452.

333. A. Wiehe, J. M. O'Brien, M. O. Senge, Trends and targets in antiviral phototherapy, *Photochem. Photobiol. Sci.*, **2019**, *18*, 2565–2612.

334. G. M. F. Calixto, J. Bernegossi, L. M. De Freitas, C. R. Fontana, M. Chorilli, Nanotechnology-Based Drug Delivery Systems for Photodynamic Therapy of Cancer: A Review, *Molecules*, **2016**, *21*, 342.

335. C. K. S. Pillai, W. Paul, C. P. Sharma, Chitin and chitosan polymers: Chemistry, solubility and fiber formation, *Prog. Pol. Sci.*, **2009**, *34*, 641–678.

336. M. Sepantafar, R. Maheronnaghsh, H. Mohammadi, F. Radmanesh, M. M. Hasani-sadrabadi, M. Ebrahimi, H. Baharvand, Engineered Hydrogels in Cancer Therapy and Diagnosis, *Trends Biotechnol.*, **2017**, *35*, 1074–1087.

337. S. Mura, J. Nicolas, P. Couvreur, Stimuli-responsive nanocarriers for drug delivery, *Nature Mater.*, **2013**, *12*, 991–1003.

338. S. Anjum, A. Arora, M. S. Alam, B. Gupta, Development of antimicrobial and scar preventive chitosan hydrogel wound dressings, *Int. J. Pharm.*, **2016**, *508*, 92–101.

339. W. Li, S. Wang, D. Zhong, Z. Du, M. Zhou, A Bioactive Living Hydrogel: Photosynthetic Bacteria Mediated Hypoxia Elimination and

Bacteria-Killing to Promote Infected Wound Healing, *Adv. Ther.*, **2021**, *4*, 2000107.

340. X. Wang, B. Ma, J. Xue, J. Wu, J. Chang, C. Wu, Defective Black Nano-Titania Thermogels for Cutaneous Tumor-Induced Therapy and Healing, *Nano Lett.*, **2019**, *19*, 2138–2147.

341. Z. Zhang, A. Li, X. Min, Q. Zhang, J. Yang, G. Chen, M. Zou, W. Sun, G. Cheng, An ROS-sensitive tegafur-PpIX-heterodimer-loaded in situ injectable thermosensitive hydrogel for photodynamic therapy combined with chemotherapy to enhance the tegafur-based treatment of breast cancer, *Biomater. Sci.*, **2021**, *9*, 221–237.

342. S. Campbell, D. Maitland, T. Hoare, Enhanced Pulsatile Drug Release from Injectable Magnetic Hydrogels with Embedded Thermosensitive Microgels, *ACS Macro Lett.*, **2015**, *4*, 312–316.

343. R. K. Korhonen, M. S. Laasanen, J. Töyräs, J. Rieppo, J. Hirvonen, H. J. Helminen, J. S. Jurvelin, Comparison of the equilibrium response of articular cartilage in unconfined compression, confined compression and indentation, *J. Biomech.*, **2002**, *35*, 903–909.

344. A. E. Forte, F. D'Amico, M. N. Charalambides, D. Dini, J. G. Williams, Modelling and experimental characterisation of the rate dependent fracture properties of gelatine gels, *Food Hydrocoll.*, **2015**, *46*, 180–190.

345. P. Gupta, K. Vermani, S. Garg, Hydrogels: from controlled release to pH-responsive drug delivery, *Drug Discov. Today*, **2002**, *7*, 569–579.

346. J. Ye, S. Fu, S. Zhou, M. Li, K. Li, W. Sun, Y. Zhai, Advances in hydrogels based on dynamic covalent bonding and prospects for its biomedical application, *Eur. Polym. J.*, **2020**, *139*, 110024.

347. S. J. Rowan, S. J. Cantrill, G. R. L. Cousins, J. K. M. Sanders, J. F. Stoddart, Dynamic Covalent Chemistry, *Angew. Chem. Int. Ed.*, **2002**, *41*, 898–952.

348. Y. Zhang, L. Tao, S. Li, Y. Wei, Synthesis of Multiresponsive and Dynamic Chitosan-Based Hydrogels for Controlled Release of Bioactive Molecules, *Biomacromolecules*, **2011**, *12*, 2894–2901.

349. H. Tan, C. R. Chu, K. A. Payne, K. G. Marra, Injectable in situ forming biodegradable chitosan-hyaluronic acid based hydrogels for cartilage tissue engineering, *Biomaterials*, **2009**, *30*, 2499–2506.

350. H. Chen, J. Cheng, L. Ran, K. Yu, B. Lu, G. Lan, F. Dai, F. Lu, An injectable self-healing hydrogel with adhesive and antibacterial properties effectively promotes wound healing, *Carbohydr. Polym.*, **2018**, *201*, 522–531.

351. H. Sadeghi-Abandansari, S. Pakian, M.-R. Nabid, M. Ebrahimi, A. Rezalotfi, Local co-delivery of 5-fluorouracil and curcumin using Schiff's base cross-linked injectable hydrogels for colorectal cancer combination therapy, *Eur. Polym. J.*, **2021**, *157*, 110646.

352. J. Qu, X. Zhao, Y. Liang, T. Zhang, P. X. Ma, B. Guo, Antibacterial adhesive injectable hydrogels with rapid self-healing, extensibility and compressibility as wound dressing for joints skin wound healing, *Biomaterials*, **2018**, *183*, 185–199.

353. J. Qu, X. Zhao, P. X. Ma, B. Guo, pH-responsive self-healing injectable hydrogel based on N-carboxyethyl chitosan for hepatocellular carcinoma therapy, *Acta Biomater.*, **2017**, *58*, 168–180.

354. M. Patenaude, N. M. B. Smeets, T. Hoare, Designing Injectable, Covalently Cross-Linked Hydrogels for Biomedical Applications, *Macromol. Rapid Commun.*, **2014**, *35*, 598–617.

355. M. Mahinroosta, Z. Jomeh Farsangi, A. Allahverdi and Z. Shakoori, Hydrogels as intelligent materials: A brief review of synthesis, properties and applications, *Mater. Today Chem.*, **2018**, *8*, 42–55.

356. B. Leung, P. Dharmaratne, W. Yan, B. C. L. Chan, C. B. S. Lau, K.-P. Fung, M. Ip, S. S. Y. Leung, Development of thermosensitive hydrogel containing methylene blue for topical antimicrobial photodynamic therapy, *J. Photochem. Photobiol. B: Biol.*, **2020**, *203*, 111776.

357. C.-H. Wu, M.-K. Sun, J. Shieh, C.-S. Chen, C.-W. Huang, C.-A. Dai, S.-W. Chang, W.-S. Chen, T.-H. Young, Ultrasound-responsive NIPAM-based hydrogels with tunable profile of controlled release of large molecules, *Ultrasonics*, **2018**, *83*, 157–163.

358. W. Qing, X. Xing, D. Feng, R. Chen, Z. Liu, Indocyanine green loaded pH-responsive bortezomib supramolecular hydrogel for synergistic chemo-photothermal/photodynamic colorectal cancer therapy, *Photodiagn. Photodyn. Ther.*, **2021**, *36*, 102521.

359. M. Li, P. He, S. Li, X. Wang, L. Liu, F. Lv and S. Wang, Oligo(p-phenylenevinylene) Derivative-Incorporated and Enzyme-Responsive Hybrid Hydrogel for Tumor Cell-Specific Imaging and Activatable Photodynamic Therapy, *ACS Biomater. Sci. Eng.*, **2018**, *4*, 2037–2045.

360. S. Gou, D. Xie, Y. Ma, Y. Huang, F. Dai, C. Wang, B. Xiao, Injectable, Thixotropic, and Multiresponsive Silk Fibroin Hydrogel for Localized and Synergistic Tumor Therapy, *ACS Biomater. Sci. Eng.*, **2020**, *6*, 1052–1063.

361. E. Boedtkjer, S. F. Pedersen, The Acidic Tumor Microenvironment as a Driver of Cancer, *Annu. Rev. Physiol.*, **2020**, *82*, 103–126.

362. W. Wang, Q. Meng, Q. Li, J. Liu, M. Zhou, Z. Jin, K. Zhao, Chitosan Derivatives and Their Application in Biomedicine, *Int. J. Mol. Sci.*, **2020**, *21*, 487.

363. L. L. Chaves, A. Silveri, A. C. C. Vieira, D. Ferreira, M. C. Cristiano, D. Paolino, L. Di Marzio, S. C. Lima, S. Reis, B. Sarmento, C. Celia, pH-responsive chitosan based hydrogels affect the release of dapsone: Design, set-up, and physicochemical characterization, *Int. J. Biol. Macromol.*, **2019**, *133*, 1268–1279.

364. K. Lavanya, S. V. Chandran, K. Balagangadharan, N. Selvamurugan, Temperature- and pH-responsive chitosan-based injectable hydrogels for bone tissue engineering, *Mater. Sci. Eng. C*, **2020**, *111*, 110862.

365. R. Jayakumar, D. Menon, K. Manzoor, S. V. Nair, H. Tamura, Biomedical applications of chitin and chitosan based nanomaterials - A short review, *Carbohydr. Polym.*, **2010**, *82*, 227–232.

366. A. Ali, S. Ahmed, A review on chitosan and its nanocomposites in drug delivery, *Int. J. Biol. Macromol.*, **2018**, *109*, 273–286.

367. Q. Z. Wang, X. G. Chen, N. Liu, S. X. Wang, C. S. Liu, X. H. Meng, C. G. Liu, Protonation constants of chitosan with different molecular weight and degree of deacetylation, *Carbohydr. Polym.*, **2006**, *65*, 194–201.

368. L. H. H. Olde Damink, P. J. Dijkstra, M. J. A. van Luyn, P. B. van Wachem, P. Nieuwenhuis, J. Feijen, Cross-linking of dermal sheep collagen using a water-soluble carbodiimide, *Biomaterials*, **1996**, *17*, 765–773.

369. J. Desbrieres, Viscosity of Semiflexible Chitosan Solutions: Influence of Concentration, Temperature, and Role of Intermolecular Interactions, *Biomacromolecules*, **2002**, *3*, 342–349.

370. S. Peers, A. Montembault, C. Ladavière, Chitosan hydrogels for sustained drug delivery, *J. Control. Release*, **2020**, *326*, 150–163.

371. Q. G. Fan, D. M. Lewis, K. N. Tapley, Characterization of cellulose aldehyde using Fourier transform infrared spectroscopy, *J. Appl. Polym. Sci.*, **2001**, *82*, 1195–1202.

372. M. Ray, K. Pal, A. Anis, A. K. Banthia, Development and Characterization of Chitosan-Based Polymeric Hydrogel Membranes, *Des. Monomers Polym.*, **2010**, *13*, 193–206.

373. A. Boskey, N. Pleshko Camacho, FT-IR imaging of native and tissue-engineered bone and cartilage, *Biomaterials*, **2007**, *28*, 2465–2478.

374. H. A. Barnes, J. F. Hutton, K. Walters, An Introduction to Rheology, *Elsevier*, Amsterdam, **1989**.

375. T. G. Mezger, The Rheology Handbook: For Users of Rotational and Oscillatory Rheometers, 2nd revised edition; *Vincentz Network GmbH & Co KG*, Hannover, **2006**.

376. C. Yan, A. Altunbas, T. Yucel, R. P. Nagarkar, J. P. Schneider, D. J. Pochan, Injectable solid hydrogel: mechanism of shear-thinning and immediate recovery of injectable β-hairpin peptide hydrogels, *Soft Matter*, **2010**, *6*, 5143–5156.

377. C. Yan, D. J. Pochan, Rheological properties of peptide -based hydrogels for biomedical and other applications, *Chem. Soc. Rev.*, **2010**, *39*, 3528–3540.

378. F. Bayat, A. R. Karimi, Design of photodynamic chitosan hydrogels bearing phthalocyanine-colistin conjugate as an antibacterial agent, *Int. J. Biol. Macromol.*, **2019**, *129*, 927–935.

379. F. Bayat, A. R. Karimi, T. Adimi, Design of nanostructure chitosan hydrogels for carrying zinc phthalocyanine as a photosensitizer and difloxacin as an antibacterial agent, *Int. J. Biol. Macromol.*, **2020**, *159*, 598–606.

380. S. W. Kim, Y. H. Bae, T. Okano, Hydrogels: Swelling, Drug Loading, and Release, *Pharm. Res.*, **1992**, *9*, 283–290.

381. J. Fu, M. in het Panhuis, Hydrogel properties and applications, *J. Mater. Chem. B*, **2019**, *7*, 1523–1525.

382. M. Reza Saboktakin, R. M. Tabatabaie, F. Satarzade Amini, A. Maharramov, M. Ali Ramazanov, Synthesis and In-vitro Photodynamic Studies of the Superparamagnetic Chitosan Hydrogel/Chlorin E6 Nanocarriers, *Med. Chem.*, **2013**, *9*, 112–117.

383. F. Ricchelli, Photophysical properties of porphyrins in biological membranes, *J. Photochem. Photobiol. B: Biol.*, **1995**, *29*, 109–118.

384. S. Bonneau, C. Vever-Bizet, Tetrapyrrole photosensitisers, determinants of subcellular localisation and mechanisms of photodynamic processes in therapeutic approaches, *Expert Opin. Ther. Pat.*, **2008**, *18*, 1011–1025.

385. A. F. Uchoa, K. T. de Oliveira, M. S. Baptista, A. J. Bortoluzzi, Y. Iamamoto, O. A. Serra, Chlorin Photosensitizers Sterically Designed To Prevent Self-Aggregation, *J. Org. Chem.*, **2011**, *76*, 8824–8832.

386. N. J. Hestand and F. C. Spano, Expanded Theory of H- and J-Molecular Aggregates: The Effects of Vibronic Coupling and Intermolecular Charge Transfer, *Chem. Rev.*, **2018**, *118*, 7069–7163.

387. E. Skovsen, J. W. Snyder, J. D. C. Lambert, P. R. Ogilby, Lifetime and Diffusion of Singlet Oxygen in a Cell, *J. Phys. Chem. B*, **2005**, *109*, 8570–8573.

388. F. Wilkinson, W. P. Helman, A. B. Ross, Rate Constants for the Decay and Reactions of the Lowest Electronically Excited Singlet State of Molecular Oxygen in Solution. An Expanded and Revised Compilation, *J. Phys. Chem. Ref. Data*, **1995**, *24*, 663–677.

389. D. P. Valenzeno, Photomodification of Biological Membranes with Emphasis on Singlet Oxygen Mechanisms, *Photochem. Photobiol.*, **1987**, *46*, 147–160.

390. J. Moan, K. Berg, The Photodegradation of Porphyrins in Cells Can Be Used to Estimate the Lifetime of Singlet Oxygen, *Photochem. Photobiol.*, **1991**, *53*, 549–553.

391. D. Kessel, Subcellular Targeting as a Determinant of the Efficacy of Photodynamic Therapy, *Photochem. Photobiol.*, **2017**, *93*, 609–612.

392. N. Vanlangenakker, T. V. Berghe, D. V. Krysko, N. Festjens, P. Vandenabeele, Molecular Mechanisms and Pathophysiology of Necrotic Cell Death, *Curr. Mol. Med.,* **2008**, *8*, 207–220.

393. S. Rowan, D. E. Fisher, Mechanisms of apoptotic cell death, *Leukemia*, **1997**, *11*, 457–465.

394. G. Kroemer, B. Levine, Autophagic cell death: the story of a misnomer, *Nat. Rev. Mol. Cell. Biol.*, **2008**, *9*, 1004–1010.

395. P. Lei, T. Bai, Y. Sun, Mechanisms of Ferroptosis and Relations with Regulated Cell Death: A Review, *Front. Physiol.*, **2019**, *10*, 139.

396. S. Kesavardhana, R. K. S. Malireddi, T.-D. Kanneganti, Caspases in Cell Death, Inflammation, and Pyroptosis, *Annu. Rev. Immunol.*, **2020**, *38*, 567–595.

397. L. Galluzzi, I. Vitale, S. A. Aaronson, J. M. Abrams, D. Adam, P. Agostinis, E. S. Alnemri, L. Altucci, I. Amelio, D. W. Andrews, M. Annicchiarico-Petruzzelli, A. V. Antonov, E. Arama, E. H. Baehrecke, N. A. Barlev, N. G. Bazan, F. Bernassola, M. J. M. Bertrand, K. Bianchi, M. V. Blagosklonny, K. Blomgren, C. Borner, P. Boya, C. Brenner, M. Campanella, E. Candi, D. Carmona-Gutierrez, F. Cecconi, F. K.-M. Chan, N. S. Chandel, E. H. Cheng, J. E. Chipuk, J. A. Cidlowski, A. Ciechanover, G. M. Cohen, M. Conrad, J. R. Cubillos-Ruiz, P. E. Czabotar, V. D'Angiolella, T. M. Dawson, V. L. Dawson, V. De Laurenzi, R. De Maria, K.-M. Debatin, R. J. DeBerardinis, M. Deshmukh, N. Di Daniele, F. Di Virgilio, V. M. Dixit, S. J. Dixon, C. S. Duckett, B. D. Dynlacht, W. S. El-Deiry, J. W. Elrod, G. M. Fimia, S. Fulda, A. J. García-Sáez, A. D. Garg, C. Garrido, E. Gavathiotis, P. Golstein, E. Gottlieb, D. R. Green, L. A. Greene, H. Gronemeyer, A. Gross, G. Hajnoczky, J. M. Hardwick, I. S. Harris, M. O. Hengartner, C. Hetz, H. Ichijo, M. Jäättelä, B. Joseph, P. J. Jost, P. P. Juin, W. J. Kaiser, M. Karin, T. Kaufmann, O. Kepp, A. Kimchi, R. N. Kitsis, D. J. Klionsky, R. A. Knight, S. Kumar, S. W. Lee, J. J. Lemasters, B. Levine, A. Linkermann, S. A. Lipton, R. A. Lockshin, C. López-Otín, S. W. Lowe, T. Luedde, E. Lugli, M. MacFarlane, F. Madeo, M. Malewicz, W. Malorni, G. Manic, J.-C. Marine, S. J. Martin, J.-C. Martinou, J. P. Medema, P. Mehlen, P. Meier, S. Melino, E. A. Miao, J. D. Molkentin, U. M. Moll, C. Muñoz-Pinedo, S. Nagata, G. Nuñez, A. Oberst, M. Oren, M. Overholtzer, M. Pagano, T. Panaretakis, M. Pasparakis, J. M. Penninger, D. M. Pereira, S. Pervaiz, M. E. Peter, M. Piacentini, P. Pinton, J. H. M. Prehn, H. Puthalakath, G. A. Rabinovich, M. Rehm, R. Rizzuto, C. M. P. Rodrigues, D. C. Rubinsztein, T. Rudel, K. M. Ryan, E. Sayan, L. Scorrano, F. Shao, Y. Shi, J. Silke, H.-U. Simon, A. Sistigu, B. R. Stockwell, A. Strasser, G. Szabadkai, S. W. G. Tait, D. Tang, N. Tavernarakis, A. Thorburn, Y. Tsujimoto, B. Turk, T. Vanden Berghe, P. Vandenabeele, M. G. Vander Heiden, A. Villunger, H. W. Virgin, K. H. Vousden, D. Vucic, E. F. Wagner, H. Walczak, D. Wallach, Y. Wang, J. A. Wells, W. Wood, J. Yuan, Z. Zakeri, B. Zhivotovsky, L. Zitvogel, G. Melino, G. Kroemer, Molecular mechanisms of cell death:

recommendations of the Nomenclature Committee on Cell Death 2018, *Cell Death Differ.*, **2018**, *25*, 486–541.

398. H. Rezzoug, L. Bezdetnaya, O. A'amar, J. L. Merlin, F. Guillemin, Parameters Affecting Photodynamic Activity of Foscan® or Meta-tetra(hydroxyphenyl)chlorin (*m*THPC) In Vitro and In Vivo, *Lasers Med. Sci.*, **1998**, *13*, 119–125.

399. C. Lange, P. J. Bednarski, Evaluation for Synergistic Effects by Combinations of Photodynamic Therapy (PDT) with Temoporfin (mTHPC) and Pt(II) Complexes Carboplatin, Cisplatin or Oxaliplatin in a Set of Five Human Cancer Cell Lines, *Int. J. Mol. Sci.*, **2018**, *19*, 3183.

400. G. Bœuf-Muraille, G. Rigaux, M. Callewaert, N. Zambrano, L. Van Gulick, V. G. Roullin, C. Terryn, M.-C. Andry, F. Chuburu, S. Dukic and M. Molinari, Evaluation of mTHPC-loaded PLGA nanoparticles for in vitro photodynamic therapy on C6 glioma cell line, *Photodiagnosis Photodyn. Ther.*, 2019, **25**, 448–455.

401. S. Marchal, A. Fadloun, E. Maugain, M.-A. D'Hallewin, F. Guillemin, L. Bezdetnaya, Necrotic and apoptotic features of cell death in response to Foscan® photosensitization of HT29 monolayer and multicell spheroids, *Biochem. Pharmacol.*, **2005**, *69*, 1167–1176.

402. A. Sasnauskiene, J. Kadziauskas, N. Vezelyte, V. Jonusiene, V. Kirveliene, Apoptosis, autophagy and cell cycle arrest following photodamage to mitochondrial interior, *Apoptosis*, **2009**, *14*, 276–286.

403. W. Zhong, J. S. Myers, F. Wang, K. Wang, J. Lucas, E. Rosfjord, J. Lucas, A. T. Hooper, S. Yang, L. A. Lemon, M. Guffroy, C. May, J. R. Bienkowska, P. A. Rejto, Comparison of the molecular and cellular phenotypes of common mouse syngeneic models with human tumors, *BMC Genomics*, **2020**, *21*, 2.

404. E. H. W. Pap, G. P. C. Drummen, V. J. Winter, T. W. A. Kooij, P. Rijken, K. W. A. Wirtz, J. A. F. Op den Kamp, W. J. Hage, J. A. Post, Ratio-fluorescence microscopy of lipid oxidation in living cells using C11-BODIPY581/591, *FEBS Lett.*, **1999**, *453*, 278–282.

405. P. Kumar, A. Nagarajan and P. D. Uchil, Analysis of Cell Viability by the alamar Blue Assay, *Cold Spring Harb Protoc*, 2018, **2018**, pdb.prot095489.

406. R. J. Gonzalez, J. B. Tarloff, Evaluation of hepatic subcellular fractions for Alamar blue and MTT reductase activity, *Toxicol. In Vitro*, **2001**, *15*, 257–259.

407. S. Suresh, Biomechanics and biophysics of cancer cells, *Acta Biomater.*, **2007**, *3*, 413–438.

408. G. Palumbo, Photodynamic therapy and cancer: a brief sightseeing tour, *Expert Opin. Drug Deliv.*, **2007**, *4*, 131–148.

409. R. W. Boyle, D. Dolphin, Structure and Biodistribution Relationships of Photodynamic Sensitizers, *Photochem. Photobiol.*, **1996**, *64*, 469–485.

410. B. W. Pedersen, L. E. Sinks, T. Breitenbach, N. B. Schack, S. A. Vinogradov, P. R. Ogilby, Single Cell Responses to Spatially Controlled Photosensitized Production of Extracellular Singlet Oxygen, *Photochem. Photobiol.*, **2011**, *87*, 1077–1091.

411. P. R. Ogilby, Singlet oxygen: there is still something new under the sun, and it is better than ever, *Photochem. Photobiol. Sci.*, **2010**, *9*, 1543–1560.

412. R. H. Weiss, R. W. Estabrook, The mechanism of cumene hydroperoxide-dependent lipid peroxidation: The function of cytochrome P-450, *Arch. Biochem. Biophys*, **1986**, *251*, 348–360.

413. C. Dive, C. D. Gregory, D. J. Phipps, D. L. Evans, A. E. Milner, A. H. Wyllie, Analysis and discrimination of necrosis and apoptosis (programmed cell death) by multiparameter flow cytometry, *Biochim. Biophys. Acta Mol. Cell Res.*, **1992**, *1133*, 275–285.

414. P. Vandenabeele, T. Vanden Berghe, N. Festjens, Caspase Inhibitors Promote Alternative Cell Death Pathways, *Science's STKE*, **2006**, *2006*, pe44.

415. M. B. Collatz, R. Rüdel, H. Brinkmeier, Intracellular calcium chelator BAPTA protects cells against toxic calcium overload but also alters physiological calcium responses, *Cell Calcium*, **1997**, *21*, 453–459.

416. R. Skouta, S. J. Dixon, J. Wang, D. E. Dunn, M. Orman, K. Shimada, P. A. Rosenberg, D. C. Lo, J. M. Weinberg, A. Linkermann, B. R. Stockwell, Ferrostatins Inhibit Oxidative Lipid Damage and Cell Death in Diverse Disease Models, *J. Am. Chem. Soc.*, **2014**, *136*, 4551–4556.

417. P. Vandenabeele, S. Grootjans, N. Callewaert, N. Takahashi, Necrostatin-1 blocks both RIPK1 and IDO: consequences for the study of cell death in experimental disease models, *Cell Death Differ.*, **2013**, *20*, 185–187.

418. K. Nakajima, M. Ogawa, Phototoxicity in near-infrared photoimmunotherapy is influenced by the subcellular localization of antibody-IR700, *Photodiagnosis Photodyn. Ther.*, **2020**, *31*, 101926.

419. N. Atale, S. Gupta, U. C. S. Yadav, V. Rani, Cell-death assessment by fluorescent and nonfluorescent cytosolic and nuclear staining techniques, *J. Microsc.*, **2014**, *255*, 7–19.

420. G. Ciancio, A. Pollack, M. A. Taupier, N. L. Block, G. L. Irvin, Measurement of cell-cycle phase-specific cell death using Hoechst 33342 and propidium iodide: preservation by ethanol fixation., *J. Histochem. Cytochem.*, **1988**, *36*, 1147–1152.

421. D. Kessel, R. D. Poretz, Sites of Photodamage Induced by Photodynamic Therapy with a Chlorin e6 Triacetoxymethyl Ester (CAME), *Photochem. Photobiol.,* **2000**, *71*, 94–96.

422. C. Fabris, G. Valduga, G. Miotto, L. Borsetto, G. Jori, S. Garbisa, E. Reddi, Photosensitization with Zinc (II) Phthalocyanine as a Switch in the Decision between Apoptosis and Necrosis1, *Cancer Res.*, **2001**, *61*, 7495–7500.

423. F. A. Schaberle, Assessment of the actual light dose in photodynamic therapy, *Photodiagnosis Photodyn. Ther.*, **2018**, *23*, 75–77.

424. D. Antoni, H. Burckel, E. Josset, G. Noel, Three-Dimensional Cell Culture: A Breakthrough in Vivo, *Int. J. Mol. Sci.*, **2015**, *16*, 5517–5527.

425. Z. S. Silva Jr, S. K. Bussadori, K. P. S. Fernandes, Y.-Y. Huang, M. R. Hamblin, Animal models for photodynamic therapy (PDT), *Biosci. Rep.*, **2015**, *35*, e00265.

426. G. Gunaydin, M. E. Gedik, S. Ayan, Photodynamic Therapy—Current Limitations and Novel Approaches, *Front. Chem.*, **2021**, *9*, 691697.

427. J. F. Algorri, M. Ochoa, P. Roldán-Varona, L. Rodríguez-Cobo, J. M. López-Higuera, Light Technology for Efficient and Effective Photodynamic Therapy: A Critical Review, *Cancers*, **2021**, *13*, 3484.

428. B. Chen, B. W. Pogue, P. J. Hoopes, T. Hasan, Vascular and cellular targeting for photodynamic therapy, *Crit. Rev. Eukaryot. Gene. Expr.*, **2006**, *16*, 279–305.

429. T.-J. Zhou, L. Xing, Y.-T. Fan, P.-F. Cui, H.-L. Jiang, Inhibition of breast cancer proliferation and metastasis by strengthening host immunity with a prolonged oxygen-generating phototherapy hydrogel, *J. Control. Release*, **2019**, *309*, 82–93.

430. G. Canti, D. Lattuada, A. Nicolin, P. Taroni, G. Valentini, R. Cubeddu, Antitumor immunity induced by photodynamic therapy with aluminum disulfonated phthalocyanines and laser light, *Anticancer Drugs*, **1994**, *5*, 443–447.

431. M. Korbelik, G. Krosl, J. Krosl, G. J. Dougherty, The Role of Host Lymphoid Populations in the Response of Mouse EMT6 Tumor to Photodynamic Therapy, *Cancer Res.*, **1996**, *56*, 5647–5652.

432. M. Korbelik, G. J. Dougherty, Photodynamic Therapy-mediated Immune Response against Subcutaneous Mouse Tumors, *Cancer Res.*, **1999**, *59*, 1941–1946.

433. L. B. Rocha, L. C. Gomes-da-Silva, J. M. Dąbrowski, L. G. Arnaut, Elimination of primary tumours and control of metastasis with rationally

designed bacteriochlorin photodynamic therapy regimens, *Eur. J. Cancer*, **2015**, *51*, 1822–1830.

434. I. Cecic, M. Korbelik, Mediators of peripheral blood neutrophilia induced by photodynamic therapy of solid tumors, *Cancer Lett.*, **2002**, *183*, 43–51.

435. B. W. Henderson, S. O. Gollnick, J. W. Snyder, T. M. Busch, P. C. Kousis, R. T. Cheney, J. Morgan, Choice of Oxygen-Conserving Treatment Regimen Determines the Inflammatory Response and Outcome of Photodynamic Therapy of Tumors, *Cancer Res.*, **2004**, *64*, 2120–2126.

436. E. Reginato, P. Wolf, M. R. Hamblin, Immune response after photodynamic therapy increases anti-cancer and anti-bacterial effects, *World J. Immunol.*, **2014**, *4*, 1–11.

437. T. Yamaguchi, F. Takizawa, U. Fischer, J. M. Dijkstra, Along the Axis between Type 1 and Type 2 Immunity; Principles Conserved in Evolution from Fish to Mammals, *Biology*, **2015**, *4*, 814–859.

438. A. L. Franks and J. E. Slansky, Multiple Associations Between a Broad Spectrum of Autoimmune Diseases, Chronic Inflammatory Diseases and Cancer, *Anticancer Res.*, **2012**, *32*, 1119–1136.

439. B. F. Zamarron, W. Chen, Dual roles of immune cells and their factors in cancer development and progression, *Int. J. Biol. Sci.*, **2011**, *7*, 651–658.

440. K. E. de Visser, A. Eichten, L. M. Coussens, Paradoxical roles of the immune system during cancer development, *Nat. Rev. Cancer*, **2006**, *6*, 24–37.

441. T. H. Foster, B. R. Giesselman, R. Hu, M. E. Kenney, S. Mitra, Intratumor Administration of the Photosensitizer Pc 4 Affords Photodynamic Therapy Efficacy and Selectivity at Short Drug-Light Intervals, *Transl. Oncol.*, **2010**, *3*, 135–141.

442. S. L. Gibson, K. R. van der Meid, R. S. Murant, R. Hilf, Increased efficacy of photodynamic therapy of R3230AC mammary adenocarcinoma by intratumoral injection of Photofrin II, *Br. J. Cancer*, **1990**, *61*, 553–557.

443. A. Fakhari, J. Anand Subramony, Engineered in-situ depot-forming hydrogels for intratumoral drug delivery, *J. Control. Release*, **2015**, *220*, 465–475.

444. A. C. Marques, P. J. Costa, S. Velho, M. H. Amaral, Stimuli-responsive hydrogels for intratumoral drug delivery, *Drug Discov. Today*, **2021**, *26*, 2397–2405.

445. S. Coutier, L. Bezdetnaya, S. Marchal, V. Melnikova, I. Belitchenko, J. L. Merlin, F. Guillemin, Foscan® (mTHPC) photosensitized macrophage activation: enhancement of phagocytosis, nitric oxide release and tumour necrosis factor-α-mediated cytolytic activity, *Br. J. Cancer*, **1999**, *81*, 37–42.

446. I. Cecic, C. S. Parkins, M. Korbelik, Induction of Systemic Neutrophil Response in Mice by Photodynamic Therapy of Solid Tumors, *Photochem. Photobiol.*, **2001**, *74*, 712–720.

447. J. Sun, I. Cecic, C. S. Parkins, M. Korbelik, Neutrophils as inflammatory and immune effectors in photodynamic therapy-treated mouse SCCVII tumours, *Photochem. Photobiol. Sci.*, **2002**, *1*, 690–695.

448. M. Korbelik, J. Sun, Cancer treatment by photodynamic therapy combined with adoptive immunotherapy using genetically altered natural killer cell line, *Int. J. Cancer*, **2001**, *93*, 269–274.

449. D. Separovic, J. Bielawski, J. S. Pierce, S. Merchant, A. L. Tarca, G. Bhatti, B. Ogretmen, M. Korbelik, Enhanced tumor cures after Foscan photodynamic therapy combined with the ceramide analog LCL29. Evidence from mouse squamous cell carcinomas for sphingolipids as biomarkers of treatment response, *Int. J. Oncol.*, **2011**, *38*, 521–527.

450. M. Korbelik, J. Banáth, W. Zhang, K. M. Saw, Z. M. Szulc, A. Bielawska, D. Separovic, Interaction of acid ceramidase inhibitor

LCL521 with tumor response to photodynamic therapy and photodynamic therapy-generated vaccine, *Int. J. Cancer*, **2016**, *139*, 1372–1378.

451. M. N. Theodoraki, K. Lorenz, R. Lotfi, D. Fürst, C. Tsamadou, S. Jaekle, J. Mytilineos, C. Brunner, J. Theodorakis, T. K. Hoffmann, S. Laban, P. J. Schuler, Influence of photodynamic therapy on peripheral immune cell populations and cytokine concentrations in head and neck cancer, *Photodiagn. Photodyn. Ther.*, **2017**, *19*, 194–201.

452. I. Beltrán Hernández, Y. Yu, F. Ossendorp, M. Korbelik, S. Oliveira, Preclinical and Clinical Evidence of Immune Responses Triggered in Oncologic Photodynamic Therapy: Clinical Recommendations, *J. Clin. Med.*, **2020**, *9*, 333.

453. P. Sharma, J. P. Allison, Immune Checkpoint Targeting in Cancer Therapy: Toward Combination Strategies with Curative Potential, *Cell*, **2015**, *161*, 205–214.

454. I. Böhme, A. K. Bosserhoff, Acidic tumor microenvironment in human melanoma, *Pigment Cell Melanoma Res.*, **2016**, *29*, 508–523.

455. A. De Milito, R. Canese, M. L. Marino, M. Borghi, M. Iero, A. Villa, G. Venturi, F. Lozupone, E. Iessi, M. Logozzi, P. D. Mina, M. Santinami, M. Rodolfo, F. Podo, L. Rivoltini, S. Fais, pH-dependent antitumor activity of proton pump inhibitors against human melanoma is mediated by inhibition of tumor acidity, *Int. J. Cancer*, **2010**, *127*, 207–219.

456. T. F. Sergeeva, M. V. Shirmanova, O. A. Zlobovskaya, A. I. Gavrina, V. V. Dudenkova, M. M. Lukina, K. A. Lukyanov, E. V. Zagaynova, Relationship between intracellular pH, metabolic co-factors and caspase-3 activation in cancer cells during apoptosis, *Biochim. Biophys. Acta – Mol. Cell Res.*, **2017**, *1864*, 604–611.

457. V. V. Barun, A. P. Ivanov, A. V. Volotovskaya, V. S. Ulashchik, Absorption spectra and light penetration depth of normal and pathologically altered human skin, *J. Appl. Spectrosc.*, **2007**, *74*, 430–439.

458. S. Premi, Role of Melanin Chemiexcitation in Melanoma Progression and Drug Resistance, *Front. Oncol*., **2020**, *10*, 1305.

459. B. Pucelik, L. G. Arnaut, G. Stochel, J. M. Dąbrowski, Design of Pluronic-Based Formulation for Enhanced Redaporfin-Photodynamic Therapy against Pigmented Melanoma, *ACS Appl. Mater. Interfaces*, **2016**, *8*, 22039–22055.

460. M. G. Lechner, S. S. Karimi, K. Barry-Holson, T. E. Angell, K. A. Murphy, C. H. Church, J. R. Ohlfest, P. Hu, A. L. Epstein, Immunogenicity of Murine Solid Tumor Models as a Defining Feature of In Vivo Behavior and Response to Immunotherapy, *J. Immunother.*, **2013**, *36*, 477–489.

461. W. Chen, K. Achazi, B. Schade, R. Haag, Charge-conversional and reduction-sensitive poly(vinyl alcohol) nanogels for enhanced cell uptake and efficient intracellular doxorubicin release, *J. Control. Release*, **2015**, *205*, 15–24.

462. R. A. Craig, C. P. McCoy, Á. T. De Baróid, G. P. Andrews, S. P. Gorman, D. S. Jones, Quantification of singlet oxygen generation from photodynamic hydrogels, *React. Funct. Polym.*, **2015**, *87*, 1–6.

463. J. Riesz, J. Gilmore, P. Meredith, Quantitative Scattering of Melanin Solutions, *Biophys. J.*, **2006**, *90*, 4137–4144.

464. W. Ngwa, O. C. Irabor, J. D. Schoenfeld, J. Hesser, S. Demaria, S. C. Formenti, Using immunotherapy to boost the abscopal effect, *Nat. Rev. Cancer*, **2018**, *18*, 313–322.

465. K. Lu, C. He, N. Guo, C. Chan, K. Ni, R. R. Weichselbaum, W. Lin, Chlorin-Based Nanoscale Metal–Organic Framework Systemically Rejects Colorectal Cancers via Synergistic Photodynamic Therapy and Checkpoint Blockade Immunotherapy, *J. Am. Chem. Soc.*, **2016**, *138*, 12502–12510.

466. D. Luo, X. Wang, E. Walker, J. Wang, S. Springer, J. Lou, G. Ramamurthy, C. Burda, J. P. Basilion, Nanoparticles Yield Increased

Drug Uptake and Therapeutic Efficacy upon Sequential Near-Infrared Irradiation, *ACS Nano*, **2020**, *14*, 15193–15203.

467. J. Sun, Y. Guo, R. Xing, T. Jiao, Q. Zou, X. Yan, Synergistic in vivo photodynamic and photothermal antitumor therapy based on collagen-gold hybrid hydrogels with inclusion of photosensitive drugs, *Colloids Surf. A: Physicochem. Eng. Asp.*, **2017**, *514*, 155–160.

468. S.-R. Tsai, R. Yin, Y.-Y. Huang, B.-C. Sheu, S.-C. Lee, M. R. Hamblin, Low-level light therapy potentiates NPe6-mediated photodynamic therapy in a human osteosarcoma cell line via increased ATP, *Photodiagn. Photodyn. Ther.*, **2015**, *12*, 123–130.

469. R. Li, Y. Zhang, M. A. Mohamed, X. Wei, C. Cheng, Macrophages play an essential role in the long effects of low-dose photodynamic therapy on vessel permeability, *Int. J. Biochem. Cell Biol.*, **2016**, *71*, 55–61.

470. D. Preise, R. Oren, I. Glinert, V. Kalchenko, S. Jung, A. Scherz, Y. Salomon, Systemic antitumor protection by vascular-targeted photodynamic therapy involves cellular and humoral immunity, *Cancer Immunol. Immunother.*, **2009**, *58*, 71–84.

471. D. A. Rodeberg, C. Erskine, E. Celis, In vitro induction of immune responses to shared tumor-associated antigens in rhabdomyosarcoma, *J. Pediatr. Surg.*, **2007**, *42*, 1396–1402.

472. H. S. Hwang, H. Shin, J. Han, K. Na, Combination of photodynamic therapy (PDT) and anti-tumor immunity in cancer therapy, *J. Pharm. Investig.*, **2018**, *48*, 143–151.

473. G. Yang, L. Xu, J. Xu, R. Zhang, G. Song, Y. Chao, L. Feng, F. Han, Z. Dong, B. Li, Z. Liu, Smart Nanoreactors for pH-Responsive Tumor Homing, Mitochondria-Targeting, and Enhanced Photodynamic-Immunotherapy of Cancer, *Nano Lett.*, **2018**, *18*, 2475–2484.

474. C. He, X. Duan, N. Guo, C. Chan, C. Poon, R. R. Weichselbaum, W. Lin, Core-shell nanoscale coordination polymers combine chemotherapy and photodynamic therapy to potentiate checkpoint blockade cancer immunotherapy, *Nat. Commun.*, **2016**, *7*, 12499.

475. P. Mroz, A. Szokalska, M. X. Wu, M. R. Hamblin, Photodynamic Therapy of Tumors Can Lead to Development of Systemic Antigen-Specific Immune Response, *PLOS ONE*, **2010**, *5*, e15194.

476. J. Liu, X. Qing, Q. Zhang, N. Yu, M. Ding, Z. Li, Z. Zhao, Z. Zhou, J. Li, Oxygen-producing proenzyme hydrogels for photodynamic-mediated metastasis-inhibiting combinational therapy, *J. Mater. Chem. B*, **2021**, *9*, 5255–5263.

477. I. Szadvari, O. Krizanova, P. Babula, Athymic nude mice as an experimental model for cancer treatment, *Physiol. Res.*, **2016**, *65*, S441–S453.

Appendix

1. NMR data

Minor traces of impurities present on the H^1 NMR spectra of **PS 1** and **5** are insignificant and do not overlap with the peaks inherent in the molecule being characterized.

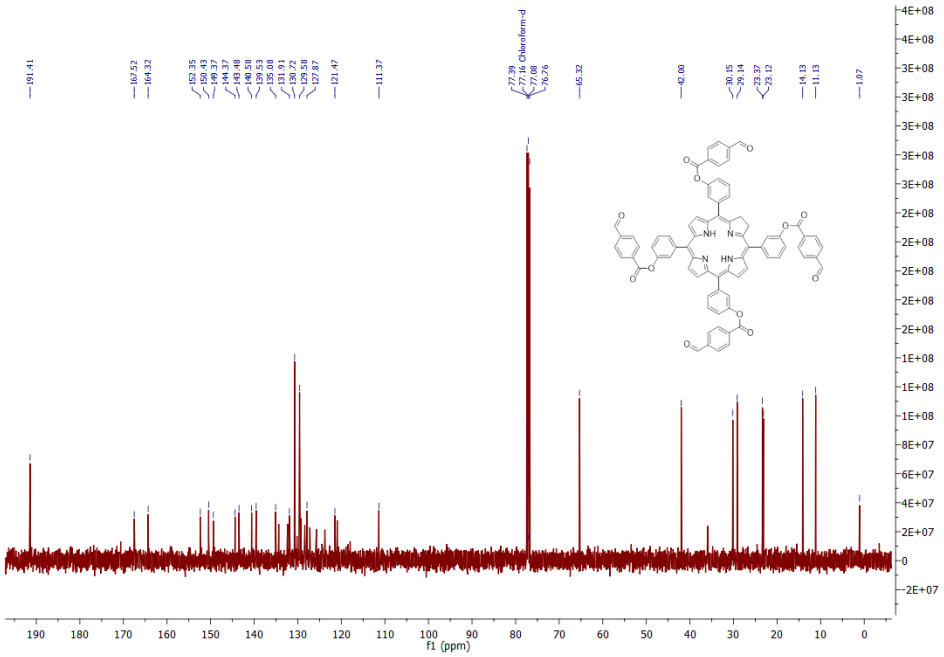

Figure A1. *C^{13} NMR spectrum of* ***PS 1*** *in $CDCl_3$*

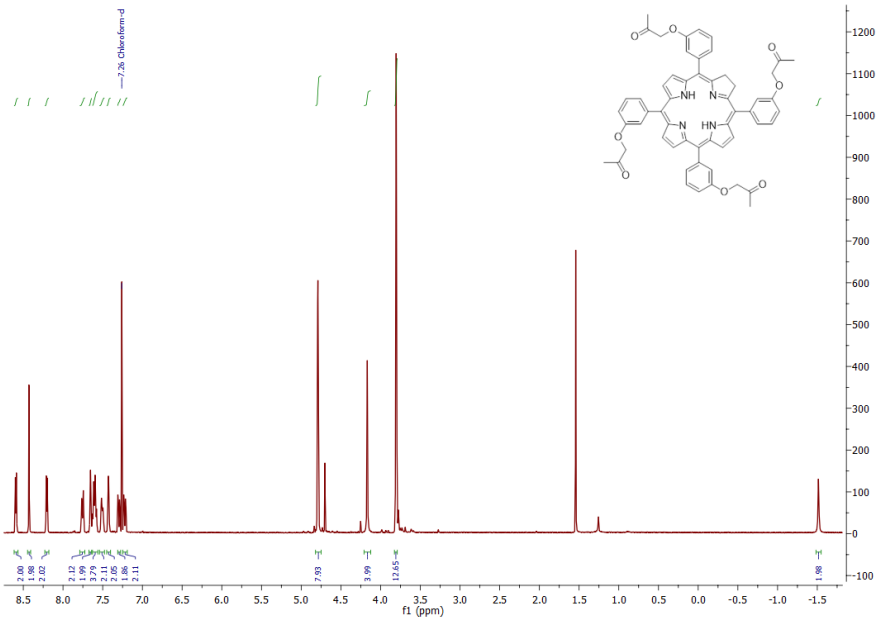

Figure A2. *H^1 NMR spectrum of PS **2** in $CDCl_3$*

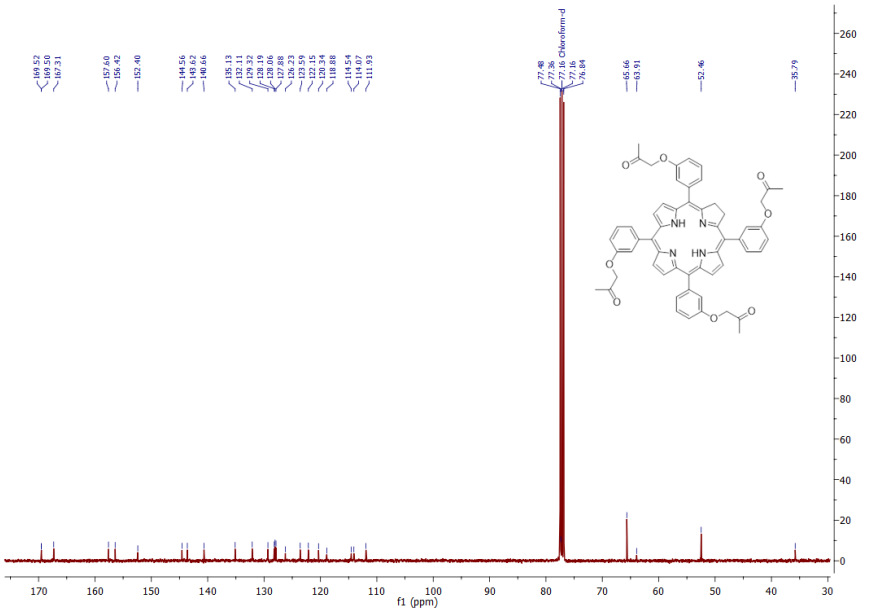

Figure A3. *C^{13} NMR spectrum of PS **2** in $CDCl_3$*

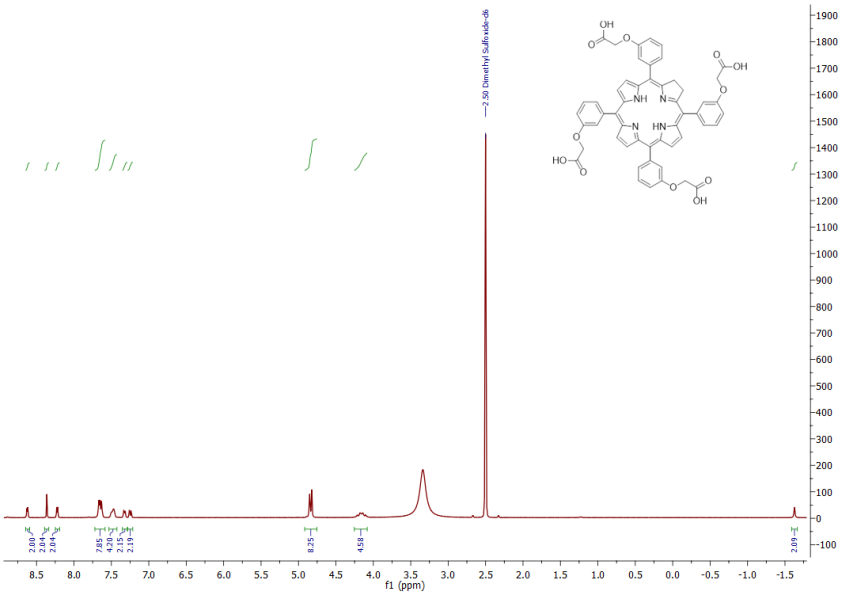

Figure A4. *H^1 NMR spectrum of* ***PS 3*** *in DMSO-D_6*

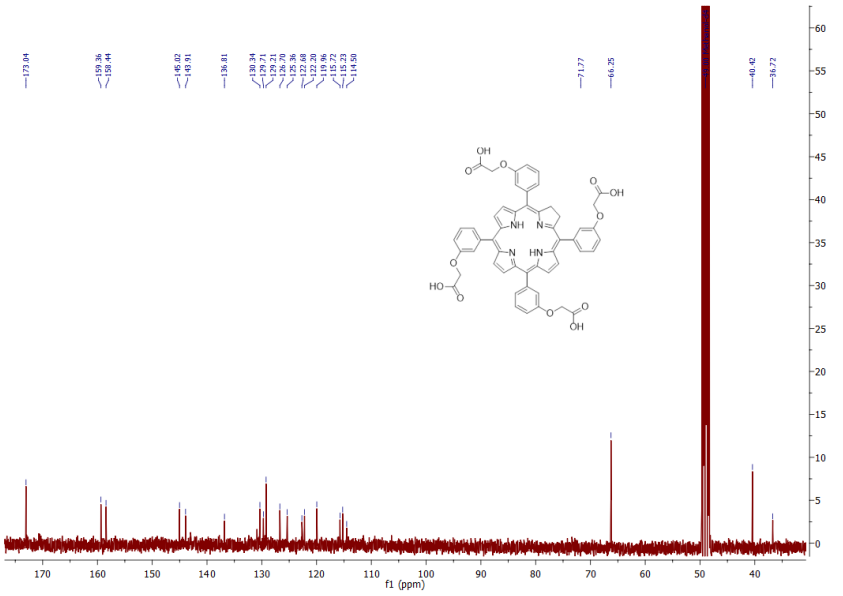

Figure A5. *C^{13} NMR spectrum of* ***PS 3*** *in DMSO-D_6*

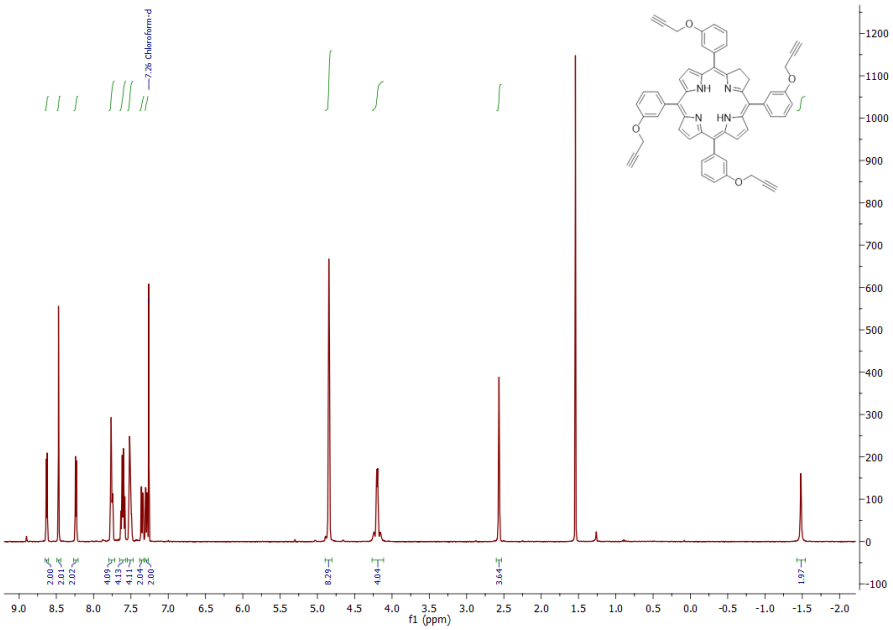

Figure A6. *H^1 NMR spectrum of* ***PS 3*** *in $CDCl_3$.*

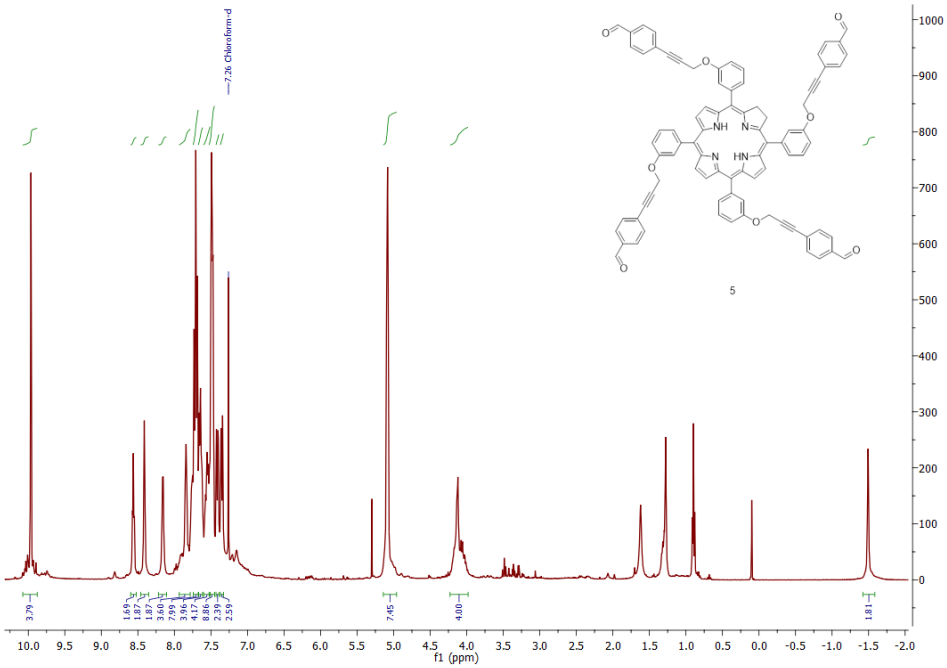

Figure A7. *H^1 NMR spectrum of* ***PS 5*** *in $CDCl_3$*

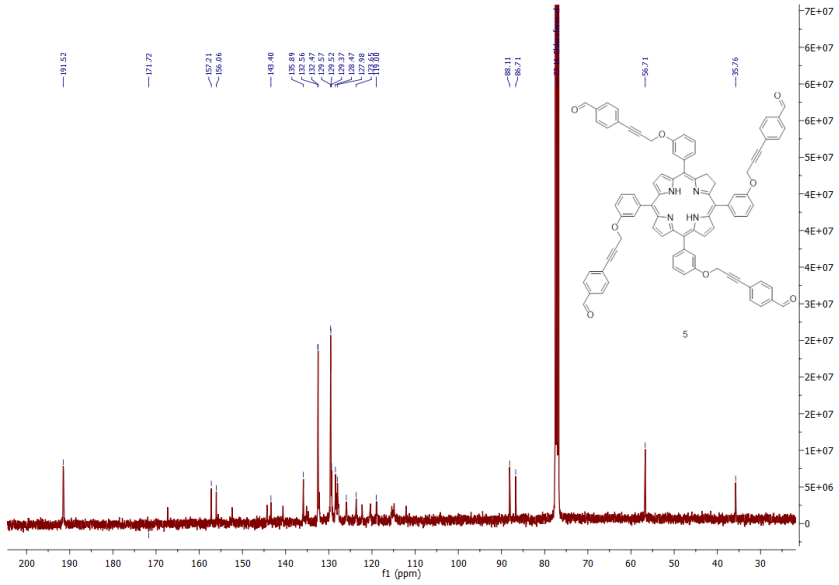

Figure A8. *C^{13} NMR spectrum of* ***PS 5*** *in $CDCl_3$.*

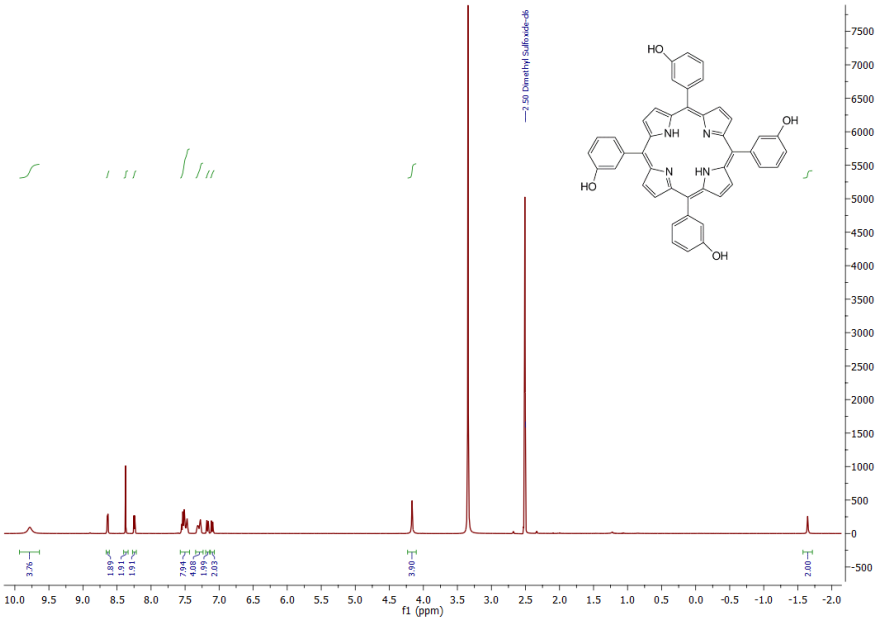

Figure A9. *H^1 NMR spectrum of m-THPC in DMSO-D_6.*

2. Mass spectrometry data

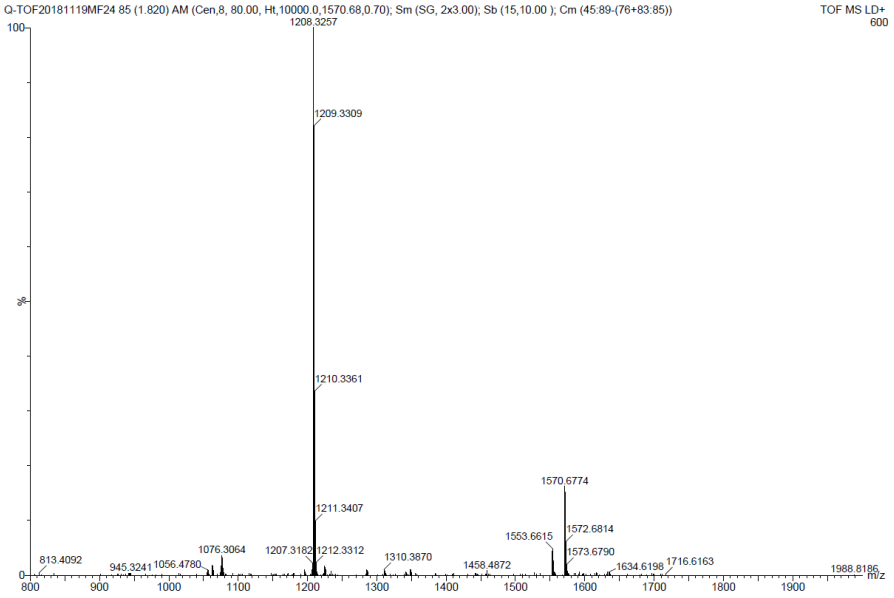

Figure A10. *MALDI-TOF Mass spectrum of* ***PS 1****.*

Elemental Composition Report **Page 1**

Single Mass Analysis
Tolerance = 100.0 PPM / DBE: min = -1.5, max = 400.0
Element prediction: Off
Number of isotope peaks used for i-FIT = 5

Monoisotopic Mass, Odd and Even Electron Ions
36 formula(e) evaluated with 1 results within limits (up to 10 closest results for each mass)
Elements Used:
C: 0-76 H: 0-48 N: 0-4 O: 0-12

Piotr Gierlich (MSe), PG8.7
Q-TOF20181119MF24 85 (1.820) AM (Cen,8, 80.00, Ht,10000.0,1570.68,0.70); Sm (SG, 2x3.00); Sb (15,10.00); Cm (45:89-(76+83:85))
TOF MS LD+
6.00e+002

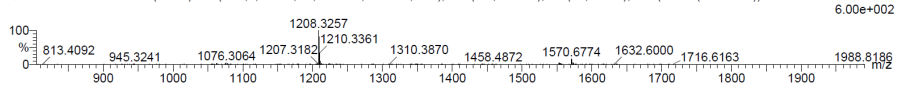

Minimum:				-1.5			
Maximum:		5.0	100.0	400.0			
Mass	Calc. Mass	mDa	PPM	DBE	i-FIT	i-FIT (Norm)	Formula
1208.3257	1208.3269	-1.2	-1.0	55.0	31.0	0.0	C76 H48 N4 O12

Figure A11. *Single-Probe mass spectrometry of* ***PS 1****.*

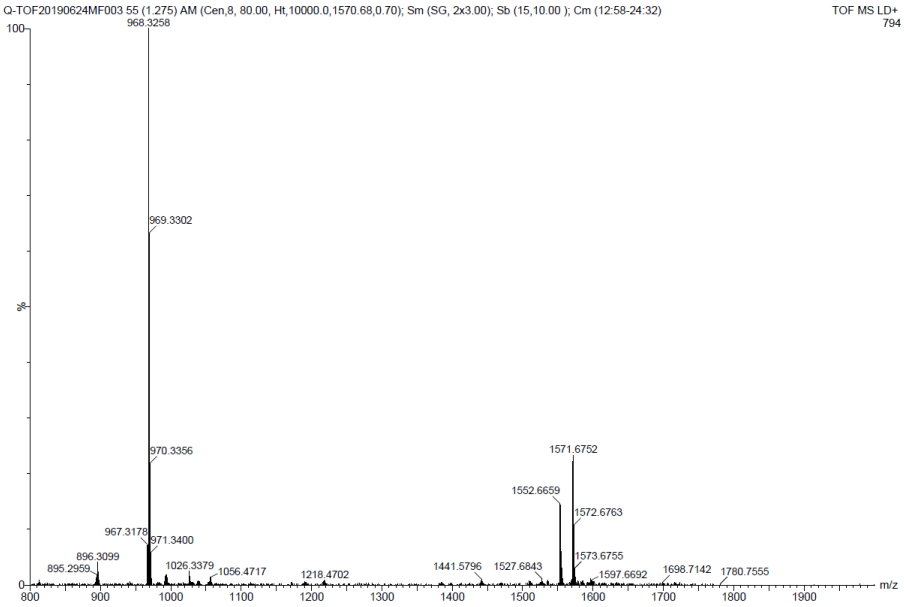

Figure A12. *MALDI-TOF mass spectrum of PS* ***2****.*

Elemental Composition Report **Page 1**

Single Mass Analysis
Tolerance = 50.0 PPM / DBE: min = -1.5, max = 400.0
Element prediction: Off
Number of isotope peaks used for i-FIT = 5

Monoisotopic Mass, Odd and Even Electron Ions
46 formula(e) evaluated with 1 results within limits (up to 10 closest results for each mass)
Elements Used:
C: 0-56 H: 0-48 N: 0-4 O: 0-12

Piotr Gierlich (MSe), PG27.1
Q-TOF20190624MF003 55 (1.275) AM (Cen,8, 80.00, Ht,10000.0,1570.68,0.70); Sm (SG, 2x3.00); Sb (15,10.00); Cm (12:58-24:32)
TOF MS LD+
7.94e+002

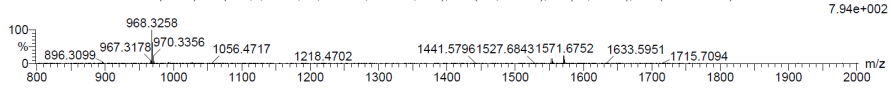

Minimum:				-1.5			
Maximum:		5.0	50.0	400.0			
Mass	Calc. Mass	mDa	PPM	DBE	i-FIT	i-FIT (Norm)	Formula
968.3258	968.3269	-1.1	-1.1	35.0	22.9	0.0	C56 H48 N4 O12

Figure A13. *Single-Probe mass spectrometry of PS* ***2****.*

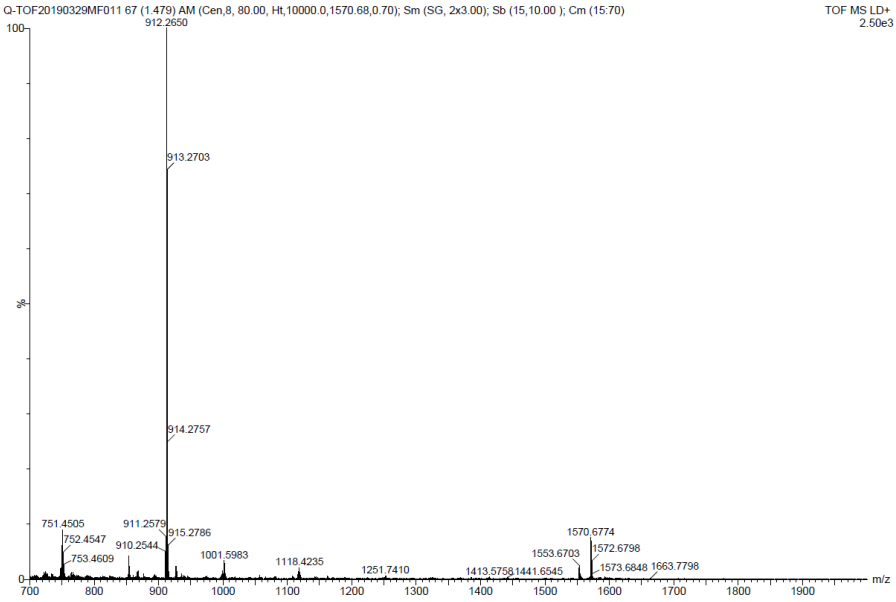

Figure A14. *MALDI-TOF mass spectrum of* ***PS 3****.*

Elemental Composition Report **Page 1**

Single Mass Analysis
Tolerance = 100.0 PPM / DBE: min = -1.5, max = 400.0
Element prediction: Off
Number of isotope peaks used for i-FIT = 5

Monoisotopic Mass, Odd and Even Electron Ions
46 formula(e) evaluated with 1 results within limits (up to 10 closest results for each mass)
Elements Used:
C: 0-52 H: 0-40 N: 0-4 O: 0-12

Piotr Gierlich (MSe), PG29
Q-TOF20190329MF011 67 (1.479) AM (Cen,8, 80.00, Ht,10000.0,1570.68,0.70); Sm (SG, 2x3.00); Sb (15,10.00); Cm (15:70)
TOF MS LD+
2.50e+003

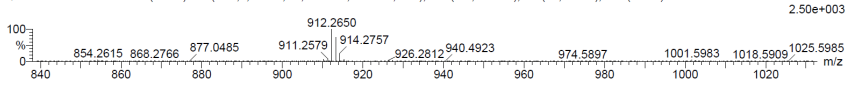

Minimum:				-1.5			
Maximum:		5.0	100.0	400.0			
Mass	Calc. Mass	mDa	PPM	DBE	i-FIT	i-FIT (Norm)	Formula
912.2650	912.2643	0.7	0.8	35.0	74.7	0.0	C52 H40 N4 O12

Figure A15. *Single-Probe mass spectrometry of* ***PS 3****.*

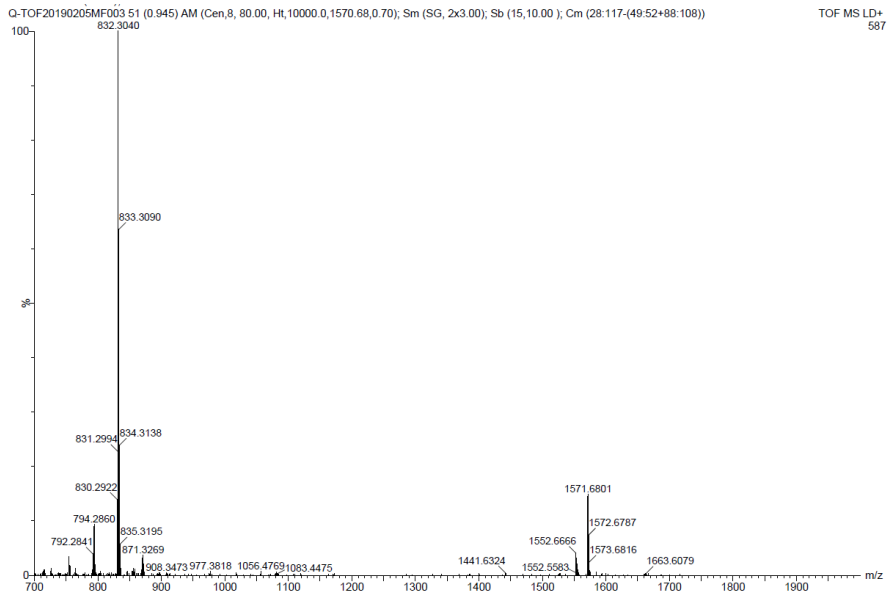

Figure A16. *MALDI-TOF mass spectrum of PS* ***4****.*

Elemental Composition Report **Page 1**

Single Mass Analysis
Tolerance = 100.0 PPM / DBE: min = -1.5, max = 400.0
Element prediction: Off
Number of isotope peaks used for i-FIT = 5

Monoisotopic Mass, Odd and Even Electron Ions
7 formula(e) evaluated with 1 results within limits (up to 10 closest results for each mass)
Elements Used:
C: 0-56 H: 0-40 N: 0-4 O: 0-4

Piotr Gierlich (MSe), PG17.1
Q-TOF20190205MF003 51 (0.945) AM (Cen,8, 80.00, Ht,10000.0,1570.68,0.70); Sm (SG, 2x3.00); Sb (15,10.00); Cm (28:117-(49:52+88:108)) TOF MS LD+
5.87e+002

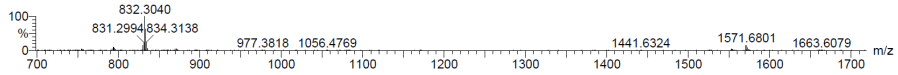

Minimum:				-1.5			
Maximum:		5.0	100.0	400.0			
Mass	Calc. Mass	mDa	PPM	DBE	i-FIT	i-FIT (Norm)	Formula
832.3040	832.3050	-1.0	-1.2	39.0	16.3	0.0	C56 H40 N4 O4

Figure A17. *Single-Probe mass spectrometry of PS* ***4****.*

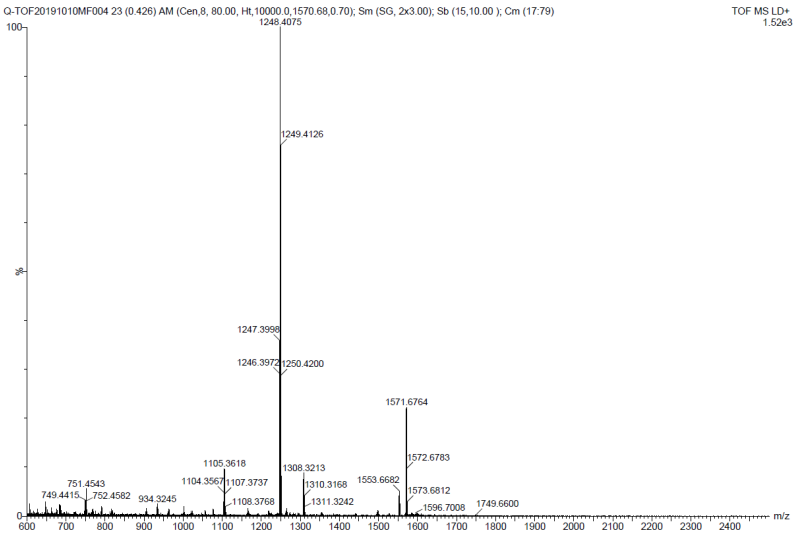

Figure A18. *MALDI-TOF mass spectrum of* ***PS 5****.*

Elemental Composition Report **Page 1**

Single Mass Analysis
Tolerance = 50.0 PPM / DBE: min = -1.5, max = 400.0
Element prediction: Off
Number of isotope peaks used for i-FIT = 5

Monoisotopic Mass, Odd and Even Electron Ions
11 formula(e) evaluated with 1 results within limits (up to 10 closest results for each mass)
Elements Used:
C: 0-84 H: 0-56 N: 0-4 O: 0-8

Piotr Gierlich (MSe), PG68_1
Q-TOF20190903MF007 112 (2.335) AM (Cen,8, 80.00, Ht,10000.0,1570.68,0.70); Sm (SG, 2x3.00); Sb (15,10.00); Cm (10:113)
TOF MS LD+
2.54e+003

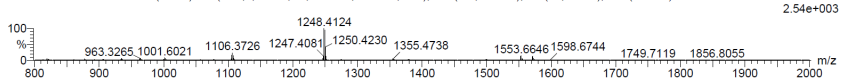

Minimum:				-1.5			
Maximum:		5.0	50.0	400.0			
Mass	Calc. Mass	mDa	PPM	DBE	i-FIT	i-FIT (Norm)	Formula
1248.4124	1248.4098	2.6	2.1	59.0	83.8	0.0	C84 H56 N4 O8

Figure A19. *Single-Probe mass spectrometry of* ***PS 5****.*

3. **UV- Vis visible absorption, excitation, and emission spectra**

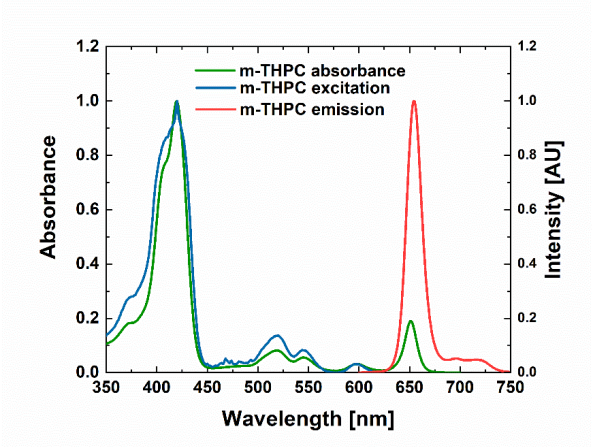

Figure A20. *Absorption, excitation for 650 nm emission wavelength and emission for the 420 nm excitation wavelength spectra of m-THPC in DMF.*

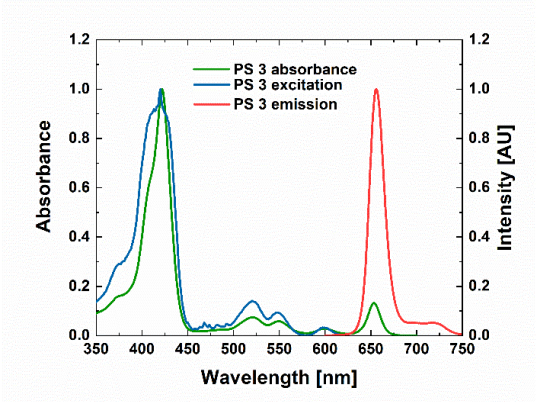

Figure A21. *Absorption, excitation for 650 nm emission wavelength and emission for the 420 nm excitation wavelength spectra of* ***PS 3*** *in DMF.*

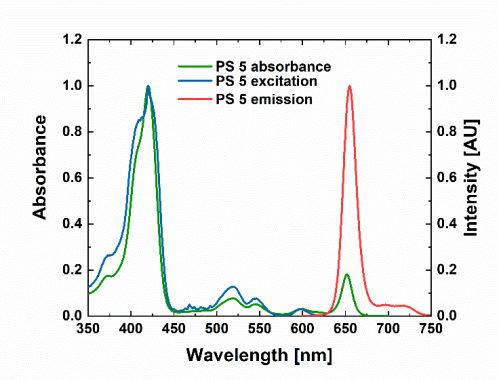

Figure A22. *Absorption, excitation for 650 nm emission wavelength and emission for the 420 nm excitation wavelength spectra of* ***PS 5*** *in DMF.*

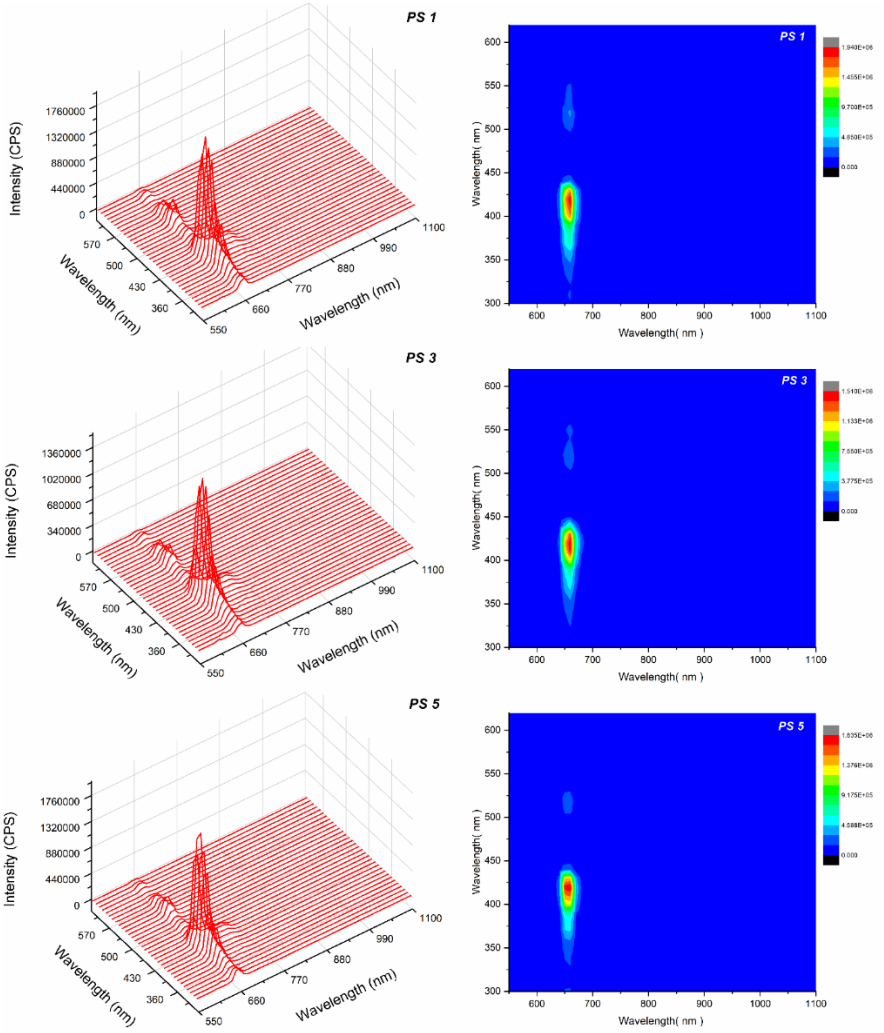

Figure A23. *One-photon excitation (350 – 600 nm) – emission (550 – 1100) spectra (left) and maps (right) of* ***PS 1****,* ***3*** *and* ***5*** *in DMF.*

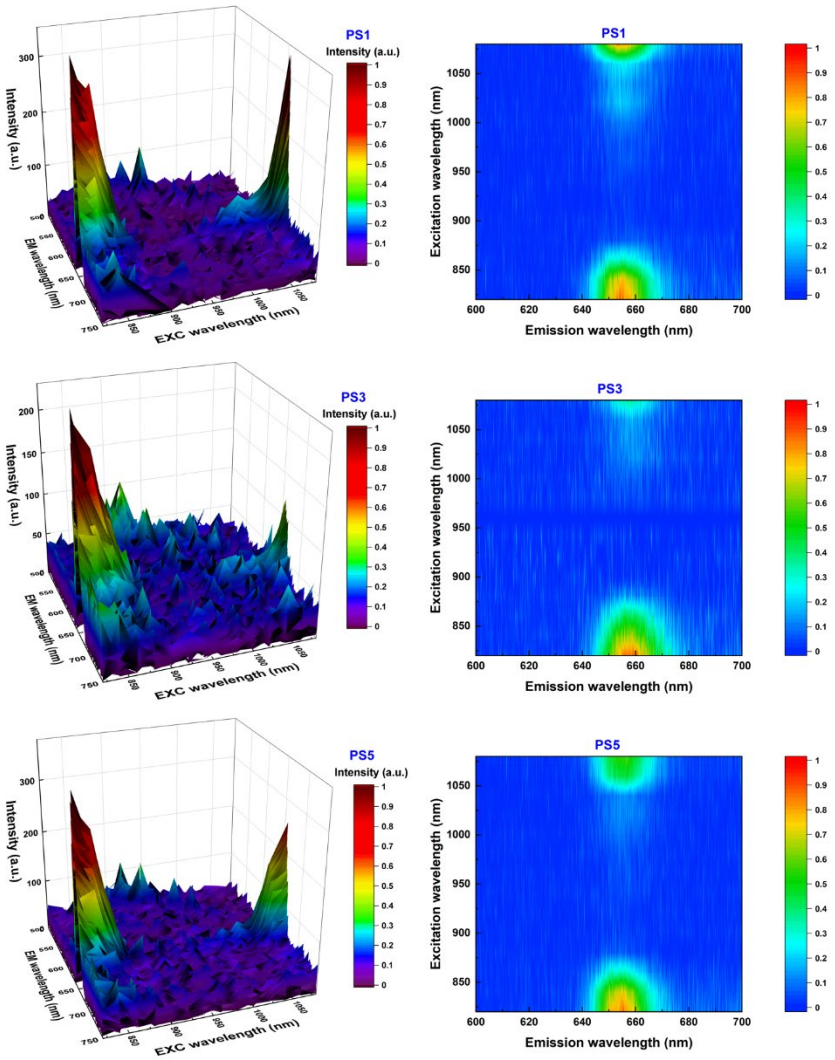

Figure A24. *Two-photon excitation (350 – 600 nm) – emission (550 – 1100) spectra (left) and maps (right) of* ***PS 1****,* ***3*** *and* ***5*** *in DMF.*

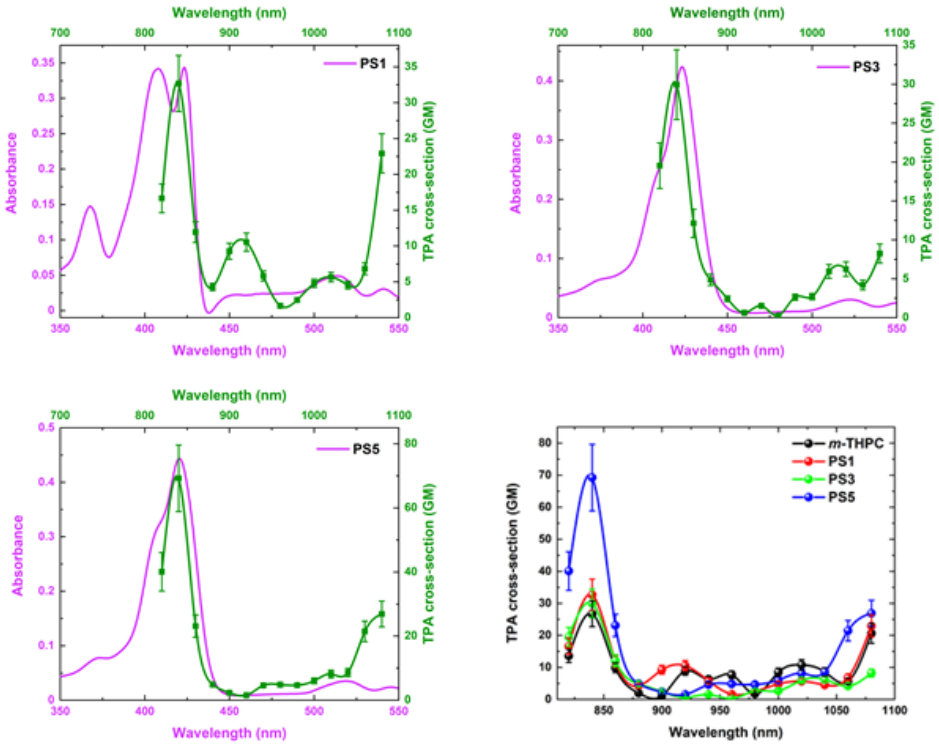

Figure A25. *Comparison of OPA and TPA spectra of temoporfin derivatives (a-c). Normalized TPA spectra (d) recorded in DMF.*